Numerical Study of Quiescent and Sheared Sedimenting Suspensions

Thesis by

Hong-Man Chan

in Partial Fulfillment of the Requirements

for the Degree of

Doctor of Philosophy

California Institute of Technology

Pasadena, California

1988

(Submitted September 30, 1987)

Abstract

In this thesis we reported the results of our investigation into the behavior of particles settling in a quiescent and sheared suspensions using a molecular-dynamics-type simulator. The effects of varying the concentration over the range of 0.0025 to 0.05, and the shear rate between 0.0 and 20.0 on the average particle velocity, the diffusion coefficient, the variance of the particle velocity, the average particle-distribution function, the particle-distribution-correlation time, and the average velocity and variance autocorrelation times are reported. We found that the first correction to the sedimentation velocity for concentration (c) depended upon c rather than $c^{\frac{1}{3}}$, and that no structure with a length scale of $O(ac^{\frac{-1}{3}})$ developed in the particle-distribution function. Shearing the suspension caused a nonuniform particle-angular distribution to form, and the particle correlation times and the diffusion coefficients to decrease. Using the diffusion coefficient from the simulations, we modelled the spreading of the interface between the supension and the clear fluid region. We found that the spreading of the interface could cause misinterpretation of the experimental measurements of the sedimentation velocity, and that this might explain the discrepancies among the experimental data.

In building the simulator, we needed to determine what effects N, the number of particles used in the simulator, have on the simulation results. Neither the sedimentation velocity, nor the average particle-distribution function changed when N varied from 27 to 125. However, we found that both the variance of the particle velocity and the diffusion coefficent grew with N. We have shown that for an homogeneous suspension, these statistics will converge, although the number of particles needed may still be very large, especially in the low concentration range which we are interested in.

Acknowledgment

I wish to express my gratitude to all those who have helped make this work possible. Foremost on this list is my advisor, Eric Herbolzheimer, who gave me much needed encouragement and advice, and who did not lose interest in me or my work even after he had left Caltech. I wish to thank John Brady and Lou Durlofsky for their help in incorporating part of their work into my simulator, and also for the many useful discussions on the theory of suspensions. This project is a continuation of the work of Doug Lynch. He laid down much of the ground work for this project. I want to express my appreciation toward Gary Leal for filling in as my advisor, and toward the chemical engineering department for providing financial assistance after Eric left. I also wish to mention Chris Chow, Julia Lester, Enrique Geffroy-Aguilar, Ardith El-Kareh, Eliana Makhlouf, Ed Ascoli, Howard Stone, Jim Stoos, Bob Hauenstein, John Klemic, John Bauer, Dave Loren, and Ann Heil who maded my stay at Caltech more enjoyable.

Table of Contents

1. Introduction

Many applications require an understanding of the sedimentation process. Examples include sizing sedimentation tanks, determining the fluidization velocity, and characterizing the sizes of particles. Another reason the sedimentation velocity is of interest is that it provides one of the constitutive relationships needed in the averaged equation approach to predicting suspension flows. With this method, the suspension, which is a dispersion of many particles in a fluid, is viewed as a single phase material composed of two or more species. This is possible whenever the length scale over which the properties of the suspension changes is large compared to the inter-particle spacing. When this occurs, the conservation equations governing the motion of the fluid and particles can be averaged over a volume whose size is in between these two length scales to yield a set of averaged equations of motion (e.g., Anderson and Jackson 1967, and Drew 1983). This approach represents a significant simplification since the details of the flow around each individual particle are no longer necessary. These averaged equations are, however, incomplete, and constitutive relationships are needed to close this set of equations; e.g., for an isothermal flow one constitutive relationship is needed for the average suspension stress (suspension viscosity) and another is needed for the average force exerted on the particles by the suspending fluid (sedimentation velocity). Clearly these quantities depend on the details of the flow around the particles, so an additional source of information is needed before flows can be calculated.

A theoretical basis now exists for predicting these constitutive relations for the limiting case when the particle Reynolds number is small and the suspension is relatively dilute (Batchelor 1972, Batchelor and Green 1972, Batchelor 1982, Batchelor and Wen 1982, and Feuillebois 1984). The problem can be broken down into two parts. First, given a set of flow conditions and the average relative positions of the particles, determine the average suspension property of interest. Second, since the particles move in response to the imposed flow (and to the motions of each other) we must determine the statistics of the particle positions. Indeed, the microscale structure can be dominant in determining the dependence of a property

on the particle concentrations (Saffman 1973, Jeffrey 1974).

To illustrate this, let us consider a dilute suspension of particles and determine the sedimentation velocity relative to the average suspension velocity. Since the suspension is dilute, one can consider only the two-particle interactions since configurations where three-particle interactions are significant occur with the probability of $O(c^2)$, an $O(c)$ smaller than the two-body interactions. Since we are interested only in the leading order solution, we can simplify the problem further by treating the particles as point forces. Neglecting the finite size of the particles leads to an error of $O((\frac{a}{r})^3)$, where r is the particles' separation. A point particle α in this suspension will settle with the velocity,

$$\mathbf{U}_p^\alpha = \mathbf{U}_s + \frac{3}{4} a \mathbf{U}_s \left[\frac{\mathbf{I}}{r} + \frac{\mathbf{rr}}{r^3} \right] + O(1/r^3), \tag{1.1}$$

where $\mathbf{U}_s$ is the Stokes's velocity, a is the particle radius, $\mathbf{r}$ is the vector connecting particle α with the second particle, and r is $|\mathbf{x}|$. Equation (1.1) gives the velocities of particle α for a particular arrangement of the two particles. To obtain the average particle velocity, we average (1.1) over all possible configurations, leading to,

$$< \mathbf{U}_p^\alpha > = \mathbf{U}_s + \frac{3}{4} \mathbf{U}_s a \int \left[\frac{\mathbf{I}}{r} + \frac{\mathbf{rr}}{r^3} \right] P(\mathbf{x} + \mathbf{r}|\mathbf{x}) d\mathbf{r}, \tag{1.2}$$

where the pair-particle distribution, $P(\mathbf{x} + \mathbf{r}|\mathbf{x})$, is the probability of finding the second particle at $\mathbf{x} + \mathbf{r}$ when particle α is at $\mathbf{x}$. Similarly, the average suspension velocity $\mathbf{u}_{susp}$ is obtained by averaging,

$$\mathbf{u}_{susp} = \frac{3}{4} \mathbf{U}_{sj} a \left[\frac{\mathbf{I}}{r} + \frac{\mathbf{rr}}{r^3} \right] + O(c), \tag{1.3}$$

giving,

$$< \mathbf{u}_{susp} > = \frac{3}{4} \mathbf{U}_s a \int \left[\frac{\mathbf{I}}{r} + \frac{\mathbf{rr}}{r^3} \right] P(\mathbf{x} + \mathbf{r}) d\mathbf{r} + O(c), \tag{1.4}$$

where $P(\mathbf{x} + \mathbf{r})$ is the probability of finding a particle at $\mathbf{r}$, regardless of whether there is a particle at $\mathbf{x}$ or not. This probability is equal to n, the particle number

concentration of the suspension. The desired result is given by,

$$< \mathbf{U}_p^{\alpha} > - < \mathbf{u}_{susp} > = \mathbf{U}_s \left[1 + \frac{3}{4} a \int \left(\frac{\mathbf{I}}{r} + \frac{\mathbf{rr}}{r^3} \right) \Big(P(\mathbf{x}+\mathbf{r}|\mathbf{x}) - n \Big) d\mathbf{r} \right] + O(c). \quad (1.5)$$

The exact behavior of $P(\mathbf{x}+\mathbf{r}|\mathbf{x})$ is not known, but we expect it to approach n as r increases since we do not expect the particles' positions to be correlated over a long distance. For convenience, a step function depicted in figure 1.1 is used for the conditional probability with the length scale of the pair-distribution function given by $2a\lambda$. Using this distribution function, and assuming that the average suspension velocity is zero, the average sedimentation velocity is

$$\frac{< \mathbf{U}_p > - \mathbf{U}_s}{\mathbf{U}_s} = -6\lambda^2 c + O(c). \quad (1.6)$$

The constant -6 is the result of the particular choice of the shape of the pair-distribution between $r = 0$ and $2\lambda a$. Another choice will lead to a different constant but the same dependence on λ and c. If the suspension is random, λ equals one and the correction to the sedimentation velocity is of $O(c)$. If on the other hand λ is dependent on $O(c^{-\frac{1}{3}})$, as is the case where particles are arranged in a cubic array, this correction to Stokes's velocity is of $O(c^{\frac{1}{3}})$. For other choices of the concentration dependence of the length scale, this correction can depend on concentration in a variety of ways.

The above example demonstrates the sensitivity of the sedimentation velocity to the structure of the suspension. Batchelor (1972) made the ***ad hoc*** assumption that the distribution is random and found that,

$$< \mathbf{U}_p > = \mathbf{U}_s(1.0 - 6.55c). \quad (1.7)$$

Saffman (1973) found that for a suspension of point forces,

$$< \mathbf{U}_p > = \mathbf{U}_s(1 - \beta c^{\frac{1}{3}} + O(c)), \quad (1.8)$$

where β is a constant which is 1.76 for a cubic array of point particles and vanishes for a random distribution.

Instead of making *ad hoc* assumptions concerning the particle-distribution functions needed in (1.5), this distribution can be obtained in principle using the conservation equation for pairs of particles. Batchelor (1982) solved the two-particle approximation of this continuity equation,

$$\frac{\partial P(\mathbf{x}+\mathbf{r}|\mathbf{x})}{\partial t} = -\nabla\cdot(\mathbf{V}P(\mathbf{x}+\mathbf{r}|\mathbf{x})) + \nabla\cdot\{P(\mathbf{x}+\mathbf{r}|\mathbf{x})\mathbf{D}\cdot\nabla(\frac{\phi}{kt})\} \qquad (1.9)$$
$$+ \nabla(\mathbf{D}\cdot\nabla P(\mathbf{x}+\mathbf{r}|\mathbf{x})),$$

where $\mathbf{V}$ is the relative velocity between the two particles due to gravitational forces, D is the diffusion coefficient, and ϕ is the force potential (e.g., inter-particle forces and Brownian motion). The first term on the right hand side represents the effect of gravity on the pair-probability function. For the case of monodispersed, non-Brownian particles with no inter-particle forces, the case which we are interested in, the first term on the right hand side of (1.9) disappears because there is no relative motion for two identical spheres settling under the influence of gravity. Equation (1.9) reduces to,

$$\frac{\partial P}{\partial t} = 0, \qquad (1.10)$$

showing that the pair-probability function remains equal to the initial distribution, and thus the assumption made in obtaining (1.9) is inadequate. In principle one can use the three-particle approximation to the particle-continuity equation, but this problem is much more difficult, and there is no guarantee that the three-particle approximation is sufficient to determine the particle-distribution function either.

An alternative to using (1.9) is to determine the structure experimentally. One can deduce the structure of the suspension from the concentration dependence of the sedimentation velocity. Barnea and Mizrahi (1973) correlated numerous sets of experimental sedimentation data and found that they could be best fitted by the equation,

$$< \mathbf{U}_p >= \mathbf{U}_s \frac{(1.0-c)}{(1.0+c^{\frac{1}{3}})e^{\frac{5c}{3(1-c)}}}, \qquad (1.11)$$

which for low concentration reduces to,

$$< \mathbf{U}_p >= \mathbf{U}_s(1-c^{\frac{1}{3}}). \qquad (1.12)$$

From these experiments we would infer that at low concentration, on the average, particles are further apart than they would be if arranged in a random hard-sphere-type distribution, and that the microscale structure has a length scale which depends on $ac^{\frac{-1}{3}}$. There are, however, other experiments, (e.g., Chen and Schachman 1955, Kops-Werkhoven and Fijnaut 1981, and Buscall *et al.* 1982), where the best fit to the data are of the form

$$\mathbf{U}_p = \mathbf{U}_s(1 - \beta c), \tag{1.13}$$

where β is about 5. These experiments indicate a random hard sphere type distribution. Lynch (1985) noted that the experiments used to obtain equation (1.12) were performed using large particles ($a > 5\mu$m) while those used for equation (1.13) were small particles ($a < 1\mu$m). To resolve the discrepancy between the two sets of data, he proposed that there is a competition between multi-particle-hydrodynamic interactions which for some reason tend to cause microscale structure with a length scale of $O(ac^{-\frac{1}{3}})$ to form, and Brownian motion which tends to randomize the particle distribution. For large particles, the hydrodynamic effects are predominant and thus the sedimentation velocity behaves as described by equation (1.12). On the other hand, for small particles, Brownian motion is more important and a random particle distribution results, so the sedimentation velocity is described by equation (1.13). In fact, he found that the two sets of data did split into high and low Peclet number conditions.

To further investigate this hypothesis, he conducted a set of experiments using a couette device to measure the sedimentation velocity with and without shear applied to the suspension. If particles tend to be well spaced in the quiescent sedimentation case, shearing the suspension should bring the particles closer together on the average, and the sedimentation velocity should increase. This enhancement of the sedimentation velocity was observed. The experimental data are reproduced in figure 1.2. These measurements imply that in sedimenting suspensions of large particles the pair probabilty distribution has a length scale $O(ac^{\frac{-1}{3}})$.

Attempts have also been made to measure this structure directly. Smith (1968),

took pictures of a low Reynolds number fluidized bed from two perpendicular directions. He divided the domain into cubes, and using the particles' positions extracted from the photographs, assigned the particles to one of these cells. His conclusion was that the distribution in the suspension is random. Makhlouf (1988), took holograms of sedimenting spheres and extracted the particles' positions from them. She divided the space about a particle into spherical shells and determined the number of particles in each of these shells. In the shells that are near twice the particle radius from the center of a particle, she found more particles than would have been expected if the distribution was uniform. The remaining shells showed no excess (figure 1.3). Due to the suspension becoming opaque at very low concentration, these measurements were taken at 0.1% by volume. Also only one hologram was analyzed. Her results therefore should be considered tentative only. These direct measurements of the structure suggest that the particle distributions in these systems are random.

A third way to determine the particle-distribution function is through the use of a molecular-dynamics-type simulator. Bossis and Brady (1985), used this approach to examine the suspension viscosity and particle-distribution function for a monolayer of particles undergoing a shearing motion. More recently, Lester (1987) examined the particle distribution in a sedimenting monolayer of particles using this approach. Lynch (1985) constructed a simulator to examine the sedimentation velocity and particle distribution for a three dimensional system. In his simulator, the motions of the particles are governed strictly by multi-particle-hydrodynamic interactions. The pair-probability distribution obtained showed a slight deficit of close pairs. He also found that the sedimentation velocity depended on $c^{\frac{1}{3}}$, and thus concluded that multi-particle-hydrodynamic interactions can lead to structures in the suspension with length scale of $O(ac^{\frac{-1}{3}})$. As we shall show in chapter 2, the method he used in determining the sedimentation velocity is sensitive to the number of particles he used in the simulation. Furthermore the error is large for a small number of particles and it scales with $c^{\frac{1}{3}}$, which accounts for the results he obtained. The problem was not detected by him because he lacked the computer resources to

vary the number of particles extensively.

This review of the literature concerning whether structures with length scale of $O(ac^{\frac{-1}{3}})$ exist in a sedimenting suspension of large particles shows conflicting results. The sedimentation velocity data suggest that these structures do exist, while direct measurements of the pair distribution indicate that they do not exist. The computer simulation results are inconclusive. One goal of this thesis is to resolve this discrepancy.

This discrepancy may be due to the dispersive behavior of the particles in the suspension. By dispersive behavior we mean that if we draw an imaginary box in the suspension and move it with the average particle velocity, after a while, the particles originally inside the box will have drifted out of the box and other particles will have drifted in. This dispersive behavior occurs because at any instance in time, some particles will have close pairs and they will tend to settle faster than the average particle, while some particles will have no near neighbors and they will tend to move slower than the average particle. Clusters of particles tend to settle faster than the average because when a particle settles, it drags down with it a large volume of fluid. If a second particle comes sufficiently close to the first, the two particles will be in each other's downdraft, and both particles will settle faster than if they are far apart. The arrangement of particles is dynamic; clusters of particles do not remain together indefinitely. After breaking up, these particles will then settle slower than the average particle. On the other hand, particles which do not have near neighbors may come close to the other particles and they will now settle faster than the average particle. This mechanism may lead to a diffusive type behavior. This diffusive behavior causes the boundary between the suspension and the clear fluid region to spread, and causes a concentration gradient ranging from the bulk concentration at the true interface to zero concentration at some distance above the true interface to develop. This surface region continues to spread as the suspension settles. In the experiments, the sedimentation velocities are measured by the rate of fall of the boundary. The exact position in the surface region which the eyes pick as the boundary depends on the concentration at which the suspension appears

opague. This need not be at the true interface. As the experiment progresses, this false interface will lag further and further behind the true interface, and the measured sedimentation velocity will be less than that in the bulk.

There is experimental evidence that a concentration gradient at the interface exists and that it leads to a significant error in the measured sedimentation velocity. Lynch (1985) filled a beaker with a 10% suspension. He suspended vertically a blackened plate 1 to 2 cm from the wall of the beaker. The sedimentation velocity measured when the suspension is viewed directly at the plate was 10 to 20% faster than that measured when viewed on either side of the blackened plate. This is comparable to the difference between the c and $c^{\frac{1}{3}}$ velocity correlations. Furthermore, when the interface observed while looking directly at the blackened plate reached the bottom of the plate, the interface remained there until the interfaces on either side of the plate caught up with it. Afterward, all three settled as one. One way to interpret the results of this experiment is that when he was viewing the suspension on either side of the blackened plate, he was looking through more suspension. The suspension therefore appeared opaque at a lower concentration. The difference in the sedimentation velocities is due to choosing a different constant concentration level as the interface.

To explore this hypothesis, we have built a molecular-dynamics-type simulator to model sedimentation in a quiescent and sheared suspension. This simulator approach allows us to obtain suspension statistics (e.g., sedimentation velocity, pair-particle distribution, diffusion coefficient) relatively easily. We wish to model Lynch's couette device experiment to examine the differences in the suspension statistics when the suspension is being sheared and when it is not. In particular we wish to see whether there are any differences in the particle distribution, average sedimentation velocity, and the diffusion coefficient between the two cases. In chapter 3 we will describe the simulator, and in chapter 4 we will present the results of the simulation. In Chapter 5 we will use these results to model the spreading of the interface to show that this spreading may account for the experimental observations.

We will solve the one dimensional macroscopic continuity equation,

$$\frac{\partial c}{\partial t} + \frac{\partial c U_p}{\partial x} - \frac{\partial \mathcal{D}}{\partial x}\frac{\partial c}{\partial x} = 0, \tag{1.14}$$

where t is time, U_p is the average particle velocity, x is the vertical distance, and $\mathcal{D}$ is the diffusion coefficient.

In performing the simulation, we are limited to modeling the motion of a relatively small number of particles because the cost of performing the simulation increases rapidly with N, the number of particle used. The most we have used is 192. Due to this limitation, it is desirable that the statistics we are interested in to converge rapidly with N. Unfortunately this is not generally true because of the slow decay of the velocity field due to a sedimenting sphere. In fact some statistics may actually diverge. Consider a volume of radius R containing a fluid in which N particles have been uniformly distributed. From (1.1), we note that the contribution from the particles at the edge of this volume to the velocity at the center of the volume decays as $O(\frac{1}{R})$ as we increase R. However in order to maintain a constant concentration when we increase the size of this volume, we must also increase N. The number of particles increases as $O(R^3)$, and therefore the velocity at the center of the volume grows as $O(R^2)$, or equivalently as $O(N^{\frac{2}{3}})$. If we now reexamine (1.2), we will notice that the equation is incomplete since the integral diverges with increasing size of the volume. The average particle velocity determined in this fashion diverges. This is known as the Smoluchowski paradox. To avoid obscuring the main issue at that time, we did not point this out. (The average particle velocity relative to the suspension velocity, however, is free from this difficulty, and the analysis concerning the relationship between the length scale of the particle distribution and the concentration dependence of the sedimentation velocity is correct.) The resolution of the Smoluchowski paradox is well known (Batchelor 1972, Saffman 1973). When a particle settles, it drags down with it a large volume of fluid. Since the bottom of the container does not permit the fluid to pass through, the fluid must percolate back up through the suspension. This back flow which decreases the particle velocity has not been accounted for in (1.2), which accounts for the

divergence of average particle velocity. We will elaborate further on this problem in chapter 2. Caflisch and Luke (1985) pointed out another problem that this long range interaction causes. They noted that if N particles are randomly placed into a box many times, the variance of the particles' velocities diverges with increasing number of particles. The divergence of the variance implies that there are many configurations in which particles move with infinite velocities. (He had taken into account the back flow.) This is not physically possible. One explanation for this is that the suspension is not random, but is homogeneous. By homogeneous we mean that if we draw a sufficiently large box anywhere in the suspension, it will contain the same number of particles. In chapter 2 we will show that this can eliminate this divergence difficulty. In chapter 2 we will also examine whether we can obtain the correct particle distribution function, sedimentation velocity and the diffusion coefficient from our simulator despite the slow decay of the velocity field due to a settling particle.

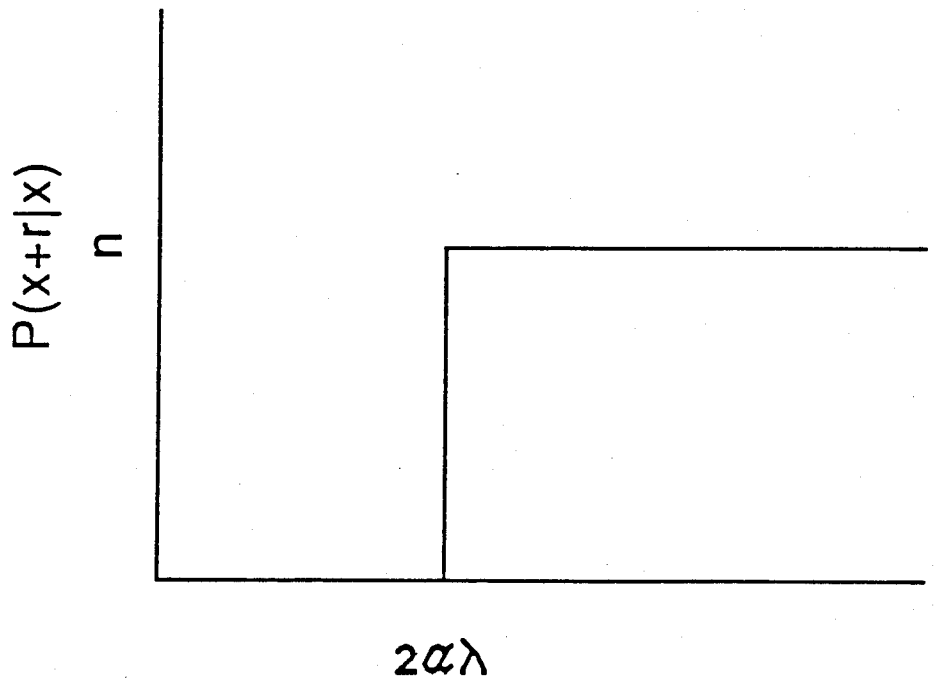

Figure 1.1 Idealized particle distribution. $2a\lambda$ is the the length scale of this particle distribution.

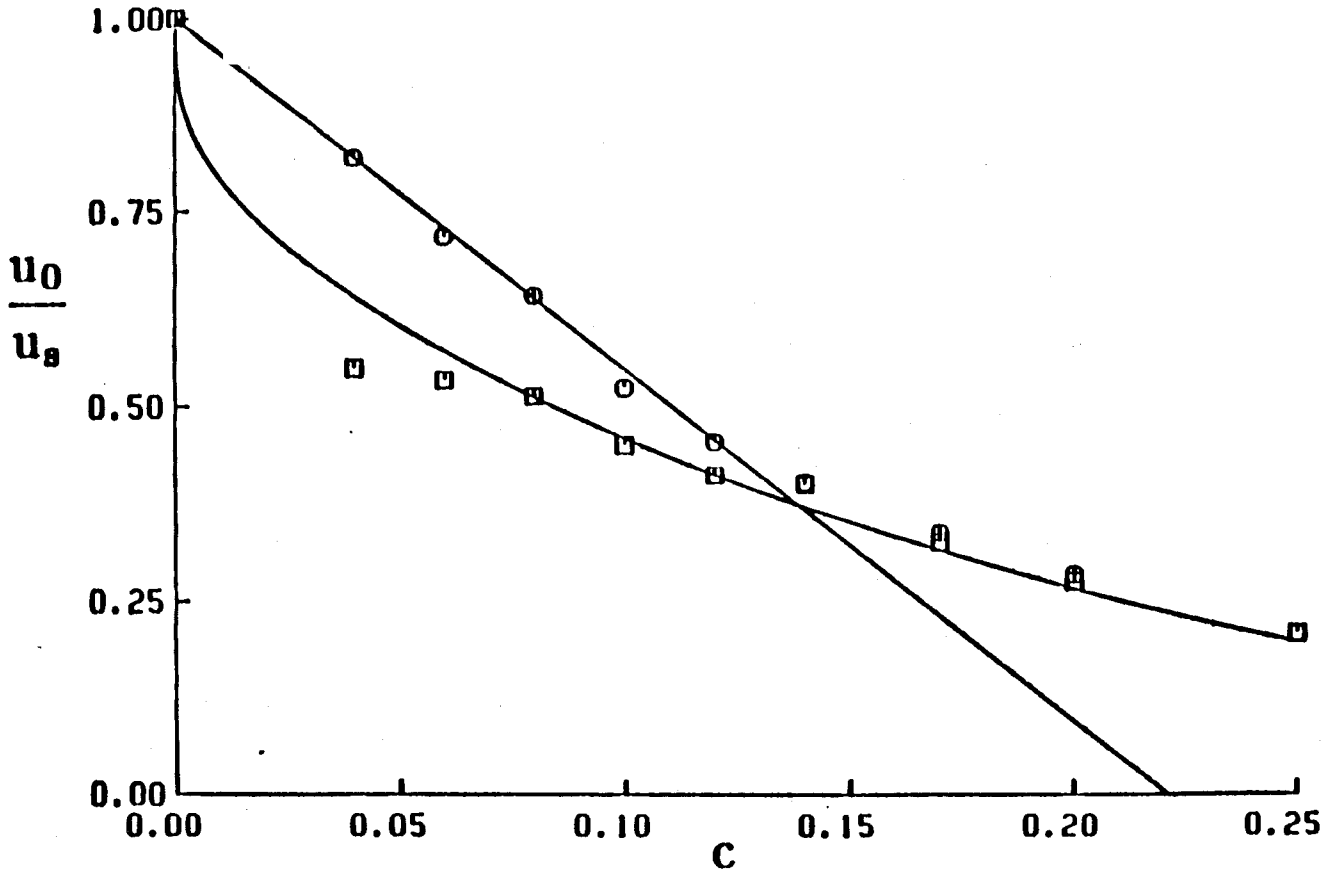

Figure 1.2 Lynch's (1985) couette device experiments. The square symbols are for the quiescent sedimentation experiments. The curved line is the correlation of Barnea and Misrahi (1973) $1.0 - c^{\frac{1}{3}}$. The circle symbols are for the sheared sedimentation experiments. The straight line is the theoretical predictions for sedimentation velocity in a straining flow.

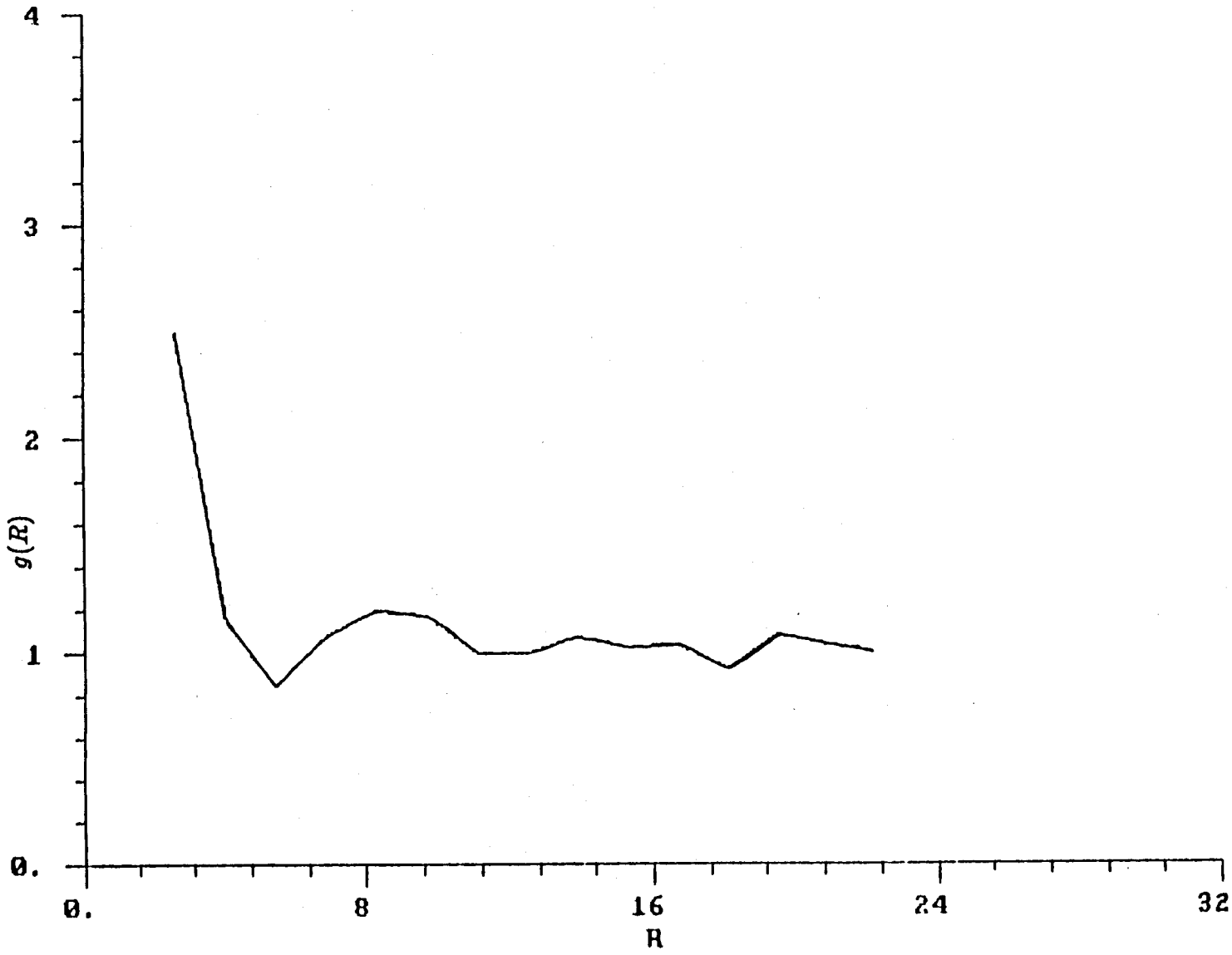

Figure 1.3 The radial distribution of Makhlouf's (1988) holography experiments.

2. Divergence Difficulties

The velocity field due to a settling sphere decays slowly, which implies that we need to include the effects of a large number of particles. This poses a problem to constructing our simulator because the cost of simulating the suspension grows quadratically with the number of particles used. In this chapter we will explore how this difficulty will affect the results of our simulations and examine methods which can be used to overcome some of the problems that arise. We will show that we can obtain the correct sedimentation velocity if we have the correct particle-distribution function. We will also consider the divergence of the velocity variance which Caflisch and Luke (1985) have noted and the implications it has on the diffusion coefficient which we wish to determine. (The diffusion coefficient is proportional to the variance.) Even though we are interested in the problem of sedimentation in a sheared suspension, we will restrict the discussion mainly to the quiescent sedimentation case. The velocity field due to a particle immersed in a shear flow decays as $O((\frac{1}{r})^2)$ for large r. This velocity field decays faster than the flow field generated by a settling particle, and therefore we do not expect that including the shear flow will cause any additional divergence difficulty.

We have pointed out that the average particle velocity as defined by (1.2) diverges with increasing number of particles. The physical interpretation is that the bottom of the container forces a large volume of fluid to move upward to satisfy the no flux condition there. This contribution from the back flow has not been included in (1.2). There are two ways to resolve this divergence difficulty. The effects of the container bottom can be included explicitly (Beenakker and Mazur 1985), or they can be included through the use of known bulk properties of the suspension (Batchelor 1972, Saffman 1973, Mazaika 1974, and O'Brien 1979). The two methods have been shown to give equivalent results. The latter method, however, is simpler, and it is the approach we will use. A review will be given below. The following derivation is essentially that given by Batchelor (1972), and by Mazaika (1974). We will first properly formulate the solution for a finite system and then take the

limit as the volume and the number of particles increase to infinity to recover the solution for the unbounded sedimentation problem.

There are several techniques which can be used to define the average particle velocity. In presenting the theory of suspensions, the ensemble average (denoted by $< >_E$) is most convenient. In the literature this is the approach generally used and it is the method we will follow here. However in the simulator we will use the particle number average (denoted by $< >_N$), and the time average (denoted by $< >_T$) instead because they are simpler to obtain during the simulation. All three methods are equivalent provided that the number of particles is large and the averaging time period is long.

The average particle velocity is given by

$$< \mathbf{U}_p(\mathbf{x}) >= \frac{1}{N!} \int \mathbf{U}_p(\mathcal{C}_N, \mathbf{x}) P(\mathcal{C}_N|\mathbf{x}) d\mathcal{C}_N, \tag{2.1}$$

where the conditional probability, $P(\mathcal{C}_N|\mathbf{x})$, is the probability of finding the other particles distributed in configuration $\mathcal{C}_N$, given that there is a particle centered at $\mathbf{x}$, and $\mathbf{U}_p(\mathcal{C}_N, \mathbf{x})$ is the particle velocity at the point $\mathbf{x}$ when the other particles are arranged in configuration $\mathcal{C}_N$. The particle velocity in (2.1) can be related to the fluid velocity by the Faxen's law,

$$\mathbf{U}_p(C_N, \mathbf{x}) - U_s \mathbf{e} = \left(1 + \frac{a^2}{6}\nabla^2\right) \mathbf{u}_f^*(C_N, \mathbf{x}), \tag{2.2}$$

where $\mathbf{u}_f^*$ satisfies

$$\nabla^2 \mathbf{u}_f^* = \nabla p^*, \tag{2.3}$$

$$\nabla \cdot \mathbf{u}_f^* = 0, \tag{2.4}$$

$$\mathbf{u}_f^* = \mathbf{U_0}^i + \mathbf{\Omega_0}^i \wedge \mathbf{r} \quad \text{on the i}^{\text{th}} \text{ particle's surface}, \tag{2.5}$$

$$< \mathbf{U}_{susp} > = \frac{1}{N!} \int_{\mathbf{x} \in f} \mathbf{u}_f^*(\mathcal{C}_N, \mathbf{x}) P(\mathcal{C}_N) d\mathcal{C}_N \tag{2.6}$$

$$+ \frac{1}{N!} \int_{\mathbf{x} \in p} \mathbf{U}_p(\mathcal{C}_N, \mathbf{x}) P(\mathcal{C}_N) d\mathcal{C}_N = \text{constant},$$

where $\mathbf{U}_0{}^i$, and $\mathbf{\Omega}_0{}^i$ are chosen such that the force on a particle is given by the bouyancy force $\frac{4}{3}\pi a^3 \Delta\rho g \mathbf{e}_1$, and the torque is zero, and $P(\mathcal{C}_N)$ is the probability of finding the particles in configuration $\mathcal{C}_N$ about point $\mathbf{x}$ regardless of whether there is a particle there or not (unconditional probability). The first integral in (2.6) is over all configurations with $\mathbf{x}$ in the fluid while the second is over all configurations with $\mathbf{x}$ in a particle. The fluid velocity field which satisfies this set of equations is

$$\mathbf{u}_f^* = \mathbf{u}_f(\mathcal{C}_N, \mathbf{x}) - \frac{1}{N!}\int \mathbf{u}'(\mathcal{C}_N, \mathbf{x}) P(\mathcal{C}_N) d\mathcal{C}_N + < \mathbf{u}_{susp} >, \tag{2.7}$$

where $\mathbf{u}_f$ is the fluid velocity which satisfies (2.2) to (2.5) but not (2.6), and $\mathbf{u}'$ is the fluid velocity, $\mathbf{u}_f$, if $\mathbf{x}$ is in the fluid, and is the particle velocity if $\mathbf{x}$ is in a particle. It should be noted that $\mathbf{u}_f^*$ in (2.7) is not necessarily bounded as $N \to \infty$. There are configurations which will give unbounded velocity. This problem does not arise because we have used the macroscopic constraint instead of requiring the suspension to satisfy the no-slip condition at the container walls explicitly, but it is due to the slow decay of the zero Reynolds number solutions. Substituting (2.7) into (2.2) and averaging gives

$$< \mathbf{U}_p(\mathbf{x}) > - U_s \mathbf{e} = \frac{1}{N!}\int \left(1 + \frac{a^2}{6}\nabla^2\right)\mathbf{u}'(C_N, \mathbf{x}) \left[P(C_N|\mathbf{x}) - P(C_N)\right] dC_N + < \mathbf{U}_{susp} > . \tag{2.8}$$

We have assumed that the average suspension velocity varies on a length scale which is large compared to the inter-particle spacing, and therefore $\nabla^2 < \mathbf{u}_{susp} >$ is negligible. To obtain the $O(c)$ solution, we neglect all but the two-particle interactions. The term $\mathbf{u}'$ is approximated by

$$\mathbf{u}' = \sum^N \frac{3}{4} U_j \left[a\left(\frac{\delta_{ij}}{r} + \frac{x_i x_j}{r^3}\right) + \frac{a^3}{3}\left(\frac{\delta_{ij}}{r^3} - \frac{3x_i x_j}{r^5}\right)\right] \text{ if } \mathbf{x} \text{ is in the fluid,} \tag{2.9}$$

$$= U_s \qquad \text{if } \mathbf{x} \text{ is in the particle,}$$

and $\mathbf{u}_f^*$ is given by,

$$u_{fi}^*(\mathbf{x}+\mathbf{r}, \mathbf{x}) = \sum^N \frac{3}{4} U_j \left[a\left(\frac{\delta_{ij}}{r} + \frac{x_i x_j}{r^3}\right) + \frac{a^3}{3}\left(\frac{\delta_{ij}}{r^3} - \frac{3x_i x_j}{r^5}\right)\right] \tag{2.10}$$

$$- n \int \frac{3}{4} U_j \left[a\left(\frac{\delta_{ij}}{r} + \frac{x_i x_j}{r^3} \right) + \frac{a^3}{3}\left(\frac{\delta_{ij}}{r^3} - \frac{3x_i x_j}{r^5} \right) \right] dr$$
$$+ < u_{susp} >$$

Equation (2.8) now becomes,

$$< U_p > = \left(1 + \frac{a^2}{6}\nabla^2\right) \int_{r>a} \frac{3}{4} U_j \left[a\left(\frac{\delta_{ij}}{r} + \frac{x_i x_j}{r^3} \right) + \frac{a^3}{3}\left(\frac{\delta_{ij}}{r^3} - \frac{3x_i x_j}{r^5} \right) \right] \quad (2.11)$$
$$\Big[P(\mathbf{x}+\mathbf{r}|\mathbf{x}) - P(\mathbf{x}+\mathbf{r}) \Big] dr$$
$$- .5cU_s + < u_{susp} > + U_s.$$

(The term involving the Laplacian is singular at $r = a$ because the velocity gradient changes from zero to a non-zero value there. This singularity integrates to $0.5c\mathbf{U}_s$.) If the difference in the two probabilities decays faster than $O(\frac{1}{r^{2+\epsilon}})$, the integral converges. For a random hard-sphere type distribution (2.11) becomes

$$< \mathbf{U}_p >= (1 - 5.0c)\mathbf{U}_s. \quad (2.12)$$

Equation (2.12) is incomplete. When the test particle settles, it induces a flow field which the second particle must respond to. The second particle responds by generating an additional flow field which is $O((\frac{a}{r})^4)$ for large r. These terms have been neglected. Batchelor (1972) has found that they contribute an additional $-1.55cU_s$ to the sedimentation velocity, and that the sedimentation velocity is now

$$< \mathbf{U}_p >= (1 - 6.55c)\mathbf{U}_s. \quad (2.13)$$

The same technique can be used for the shear flow problem. In place of a constant average suspension velocity constraint, we require that

$$< U_{susp} >= E_{ij} R_j + \varepsilon_{ijk} \Omega_j R_k, \quad (2.14)$$

where E_{ij} is the bulk strain rate, Ω_j is the bulk vorticity, ε_{ijk} is the permutation tensor. To satisfy (2.14) we add to (2.11) the disturbance velocity field generated

by a particle immersed in a shear flow (Batchelor and Green 1972),

$$= \sum^{N-1} E_{jk}x_k\left[-\delta_{ij}\frac{a^5}{r^6} + \frac{x_ix_j}{r^2}\left(-\frac{5a^3}{2r^3} + \frac{5a^5}{2r^5}\right)\right] \tag{2.15}$$

$$+ n\int E_{jk}x_k\left[-\delta_{ij}\frac{a^5}{r^6} + \frac{x_ix_j}{r^2}\left(-\frac{5a^3}{2r^3} + \frac{5a^5}{2r^5}\right)\right]dr$$

$$+ E_{ij}R_j + \varepsilon_{ijk}\Omega_jR_k.$$

The terms in the sum in (2.15) are the disturbance velocity due to a particle in a shear flow, and the remaining terms are that which are needed to statisfy the constraint (2.14). For a random hard-sphere distribution the average particle velocity is

$$< U_p > -U_s = E_{ij}R_j + \varepsilon_{ijk}\Omega_jR_k + (1. - 5.0c)U_s. \tag{2.16}$$

Equation (2.11) can be used to obtain the sedimentation velocity if the pair-probability distribution is known, but it is not known. However we can approximate the integral in (2.11) using our simulator. The simulator consists of a volume within which N particles are placed. The motion of these particles is obtained with (2.10) along with Faxen's law. We allow the structure in this simulator to evolve over a long period of time, and at every instance in time we determine the number average of the particle velocities in the simulator. We then time average these instantaneous number averages to obtain

$$< U_p > = \left\langle\left\langle\sum^{N-1}\frac{3}{4}U_j\left[a\left(\frac{\delta_{ij}}{r} + \frac{x_ix_j}{r^3}\right) + \frac{2a^3}{3}\left(\frac{\delta_{ij}}{r^3} - \frac{3x_ix_j}{r^5}\right)\right]\right.\right. \tag{2.17}$$

$$\left.\left. - n\int\frac{3}{4}U_j\left[a\left(\frac{\delta_{ij}}{r} + \frac{x_ix_j}{r^3}\right) + \frac{a^3}{3}\left(\frac{\delta_{ij}}{r^3} - \frac{3x_ix_j}{r^5}\right)\right]dr\right\rangle_N\right\rangle_T + cU_s.$$

Provided that the simulator yields the correct particle distribution and that we average over a sufficiently long period of time and over a sufficiently large volume, this average particle velocity should be equivalent to that given by (2.11).

In our simulator, we can only use a small number of particles. The finite size of our simulator may change the particle distribution. Whether this is true or not can

be tested by varying the number of particles in the simulator and then comparing the resulting distributions. The details of this test are given in chapter 4. It appears that the particle distribution is unaffected by the size of the simulator. Even if the distribution is unaffected by the size of the simulator, we may still need a large number of particles before the velocity given by (2.17) will converge to a constant value. How many particles are needed depends on the definition of n, the particle-number concentration. If it is defined as $\frac{N}{V}$, the average velocity decays slowly with N. On the other hand if it is defined as $\frac{N-1}{V}$, the velocity converges rapidly with N. This is demonstrated in figure 2.1. We randomly placed N particles into a box many times and determined the average velocity of a hypothetical particle located in the middle of the box using (2.17). To simplify the problem we kept only terms that are of $O(\frac{1}{r})$ (i.e., we treated the particles as point forces). The exact solution for this problem is zero (Saffman 1973). If n is defined as $\frac{N}{V}$, it takes over 10^4 particles to converge to the correct solution, while with the other definition it has already converged with 27 particles. The difference between the two definitions is

$$\frac{1}{V}\int \frac{3}{4}U_j a\left(\frac{\delta_{ij}}{r}+\frac{x_i x_j}{r^3}\right)dr, \tag{2.18}$$

which is of $O(N^{\frac{-1}{3}}c^{\frac{1}{3}})$. The error is large for a small number of particles and what is even worse, the error is proportional to $c^{\frac{1}{3}}$. Lynch chose to define n as $\frac{N}{V}$ and therefore he found a $c^{\frac{1}{3}}$ dependence for the sedimentation velocity. In our work we will define n as $\frac{N-1}{V}$. We believe this is more appropriate because the sedimentation velocity converges rapidly with N, and furthermore, it gives the correct sedimentation velocity for the random distribution case. Mathematically the reason why $\frac{N}{V}$ is the incorrect choice is because the sum in (2.17) is based on $(N-1)$ particles while the integral (the back flow) is based on N particles.

We next turn our attention to the variance of the velocity. The variance of the velocity is defined as

$$\mathbf{V}=\left\langle(\mathbf{U}_p-\overline{\mathbf{U}}_p)^2\right\rangle. \tag{2.19}$$

The variance measures the fluctuations of the particle velocities. Since large fluc-

tuations in the particle velocity have not been observed in the sedimentation experiments, one expects that the variance should be bounded. Unfortunately, the variance of the particles' velocities is not bounded as N approaches infinity for a random suspension. Caflish and Luke (1985) have pointed out this problem. The average variance for a volume randomly filled with point particles is given by

$$\mathbf{V} = \int (\mathbf{u}_f^*(\mathbf{x}+\mathbf{r},\mathbf{x}))^2 n d\mathbf{r}. \tag{2.20}$$

To leading order, u_f^* is of order $(\frac{1}{r})$, and therefore the variance grows as $O(r)$. The number of particles (N) increases as r^3 so the variance is of $O(N^{\frac{1}{3}})$ for large N. We have verified their observations with our Monte Carlo simulations. We created a configuration by randomly placing N particles into a cube with the restriction that no particles may come within two radii of the center of this cube. We then determined the velocity of a hypothetical particle located at the center of the box. Thousands of configurations were generated, and the variance of the particle velocity at the center of the cube for a 1% suspension was determined. This process can be expressed mathematically as,

$$V = \frac{1}{M}\sum_{j}^{M}(u_j - \overline{u})^2, \tag{2.21}$$

where M is the number of configurations, u_j is the velocity of the particle at the center of the cube for configuration j, and $\overline{u}$ is the velocity of the particle averaged over all configurations. The results are presented in figure 2.2. The variance for a small number of particles grows as $O(N^{\frac{1}{2}})$, and the variance eventually grows as $O(N^{\frac{1}{3}})$ for large N.

Infinite variance is not physically possible. One plausible explanation is that in a real suspension, a small amount of inertia invalidates the Stokes's solution at large r. The first correction for Reynolds number (Re) is given by Oseen's solution (Van Dyke 1975). For large r ($r \gg \frac{1}{Re}$), the velocity decays as $O(\frac{1}{r^2})$, and the integrand in (2.20) decays as $O(r^{-4})$ for large r. The variance converges. This explanation implies that there is no solution for the zero Reynolds number

sedimentation problem, a suprising result if it is true. Furthermore, this explanation predicts that significant variation in the particles' velocities will develop as the Reynolds number is reduced. This is because as the Reynolds number decreases, the region over which Stokes's solution is valid grows, and hence the variance will also grow. Sedimentation experiments for wide ranges of the Reynolds number have been reported in the literature, but this effect has not been observed.

An alternate explanation is that the suspension is not random, and therefore Caflisch and Luke's (1985) calculations, and our Monte Carlo simulations are invalid. When the point particles are randomly placed into the box during the Monte Carlo simulation, any configurations are possible, including configurations where a large portion of all the particles are clustered about one point. Particles in this type of configurations have a much larger velocity compared with particles in configurations which have no large clusters. It is the formation of these large clusters which lead to the large variances. For a random suspension, as the number of particles are increased, one can obtain increasingly larger clusters and therefore increasingly larger variances. The real suspension may not be random, but it may be homogeneous instead. By a homogeneous suspension, we mean that a sufficiently large volume drawn anywhere in the suspension will encompass an equal number of particles. A homogeneous suspension will not have large clusters of particles and the divergence problem will be eliminated. Using the Ewald sum method (Lester 1987), we can demonstrate that homogeneity can eliminate the divergence problem. We place N particles inside a cell and then replicate this parent cell periodically in all directions. The particles inside each of these cells can be arranged in any configurations, but all the cells must have the same configuration. The contributions to the particles' velocities inside the parent cell from all the particles in the other cells can be divided into a portion which decays rapidly and a portion which decays slowly with respect to the distance from the parent cell. Taking advantage of the periodicity of the system, the slowly convergent portion can be evaluated rapidly using the Poisson summation formula. Using this Ewald sum technique, one finds that the velocity is bounded for any configurations. From (2.21), since u_j is bounded,

$\overline{u}$ is bounded, and hence the variance is also bounded. The system contains an infinite number of particles, but we have restricted the inhomogeneity in the system to the size of a single cell. We can therefore conclude that introducing homogeneity into the suspension can eliminate the divergence problem. The requirement that the suspension be periodic facilitates the computation but is not essential for eliminating the divergence difficulty. We have tested this by performing the following Monte Carlo simulation. We begin by randomly placing M point particles into a cell and calculating the particle velocity at the center of the box. Next we surround this cell with 26 other cells. Into each of these 26 cells, M particles are randomly distributed, and again the velocity of the particle at the center of the inner cell is determined. We continue adding cells to the simulator a layer at a time until a desired number of layers are in place. This entire process is repeated many times and the variance as a function of the total number of particles (N) is obtained. Figure 2.3 shows the variance as a function of N for M ranging from one particle to 512 particles per cell, and for a 1% suspension. Figure 2.3 shows that the variance does not diverge with N. This proves our contention that the periodicity is not essential for eliminating the divergence problem. Figure 2.3 further shows that the variance however does depend on M. In other words, if we allow the size of the inhomogeneity to grow by increasing M, the variance will grow. If we allow M to grow to infinity, we will recover the random suspension, and the variance will be unbounded. In figure 2.3, the curves asymptote to a constant value. These values as a function of M are shown in figure 2.4; they grow approximately with $M^{0.4}$. The results of these Monte Carlo simulations show that if one can restrict the length scale of the inhomogeneity (i.e., M) in the suspension, the divergence problem will disappear.

The Monte Carlo simulation results shown thus far are for point particles, and as such, these particles are permitted to overlap with other particles. This model is realistic for only the very dilute suspensions. For more concentrated suspensions, volume exclusion effect reduces the number of particle configurations which can be realized, and this in turn can affect the variance. Before we examine this problem,

we will first determine the concentration dependence of the variance for a suspension of point particles. We will see later that volume exclusion affects this dependence. The velocity variance for a suspension of point particles is given by (2.20). Since the integral is $O(L)$, n is $\frac{N}{L^3}$ and c is $\frac{4}{3}\pi a^3 \frac{N}{L^3}$, the variance is proportional to $N^{\frac{1}{3}} c^{\frac{2}{3}}$.

To examine the effects of volume exclusion on the variance, we performed the Monte Carlo simulation exactly as before except now we do not allow particles to overlap. To accomplish this we need to check for overlaps not only between particles within a cell but also for overlaps between particles in adjacent cells. The latter is rather time consuming and we do this approximately. Note first that if we did not check for particle overlap between adjacent cells, the distribution will have more particles near the edge of the cell than if we did check. This is because particles jutting in from the adjacent cells exclude part of the volume at the cell's edges. If we allow overlaps at the edges to occur, this volume exclusion effect will disappear. This difference can be eliminated by applying the toroidal boundary condition (section 3.4). As the name implies, in this scheme, opposite faces of a cell are connected so a particle along the left face of the cell can exclude a volume along the right face of the same cell. This mimics the volume exclusion effect due to the presence of particles at the edges of the neighboring cells. When the number of particles per cell (M) is large, this scheme will exclude the same volume at the edges of each cell as if we have checked for overlap between adjacent cells. The reason the two methods are equivalent only when M is large can be understood if we examine the case when M is one. The toroidal boundary condition can not exclude any volume in this case because the length of the side of a cell is always greater than two particle radii. In general the toroidal boundary condition can only exclude $\frac{N-1}{N}$ of the volume excluded when we do check for overlap between adjacent cells. The toroidal boundary condition, though only approximate, is significantly faster and simpler to implement. It is the approach we have taken.

Besides the volume exclusion effect, we also wished to examine how the method of determining the particle velocity affects the variance. To accomplish this, we

performed the simulation using the stokeslet approximation,

$$u_p = \frac{3}{4} u_s a \left[\frac{\delta_{i1}}{r} + \frac{x_i x_j}{r^3} \right], \tag{2.22}$$

and the stokeslet-dipole approximation,

$$u_p = \frac{3}{4} u_s a \left[\left(\frac{\delta_{i1}}{r} + \frac{x_i x_j}{r^3} \right) + \frac{2a^2}{3} \left(\frac{\delta_{i1}}{r^3} - \frac{3 x_i x_1}{r^5} \right) \right]. \tag{2.23}$$

We performed the simulation described above for volume fractions ranging from 0.001 to 0.1 and values of M ranging from 1 to 512. The variance's dependence on the total number of particles, N, is shown in figures 2.5 through 2.16. Figures 2.5 through 2.10 were obtained using the stokeslet approximation, and figures 2.11 through 2.16 were obtained using the stokeslet-dipole approximation. These two sets of figures are the same, which means that the method of determining the particle velocity is unimportant, and that the contribution to the variance comes mainly from the stokeslet term. Figure 2.7 shows the variance as a function of N for a 1% suspension. This figure is nearly the same as figure 2.3, which was obtained without considering particle overlap. This implies that volume exclusion does not affect the divergence of the variance at a concentration of 0.01. Figures 2.17 and 2.18 show the growth of the variance with M for five different concentrations. The variances grow approximately with $M^{0.4}$, the same as when we did not take particle overlaps into account. The results from these simulations show that preventing particles from overlapping with each other does not eliminate the divergence problem, at least not for volume fractions of 0.1 or less.

Prohibiting particle overlaps, however, does have a significant effect on the concentration dependence of the variance. In figures 2.19 and 2.20, the maximum variance's dependence on concentration for various values of M is shown. For M of one, the variance depends on $c^{\frac{2}{3}}$. This is expected, since with one particle in a cell, this particle can not overlap with another particle. Therefore, whether we prohibit overlap or not should make no difference, and we should recover the point particle result. For values of M other than one, the variances asymptote to constant values

at a concentration between 0.05 and 0.1. At high concentration, volume exclusion forces particles to crowd around the particle at the center of the box. All the possible configurations are similar and yield similar velocities for the particle at the center of the box, and the variance decreases. An extreme example is when the suspension is at maximum packing, and all the particles are locked into one large cluster. In this configuration all the particles settle with the same velocity and the variance is zero.

If we know the length scale of the inhomogeneity, then the variance can be obtain from the Monte Carlo simulations. This length scale is also important because we need to make our simulator larger than it so as not to artifically restrict the size of the inhomogeneity which can develop. However this length scale is not known and the Monte Carlo simulation gives no basis for choosing this length scale. We can obtain an estimate of this length scale from (2.20) by solving for the size of the volume in terms of the variance,

$$\mathbf{V} = n \int (\mathbf{u}_f^* - \langle \mathbf{u}_f^* \rangle)^2 dr = kc\frac{L}{a}, \tag{2.24}$$

where k is a proportionality constant, and $\frac{L}{a}$ is the length scale which we are interested in,

$$\frac{L}{a} = \frac{V}{k} c^{-1}. \tag{2.25}$$

Similarly we can estimate the number of particles required,

$$N = (\frac{V}{k'})^3 c^{-2}, \tag{2.26}$$

where k' is another proportionality constant. If $\frac{V}{k}$ and $(\frac{V}{k'})^3$ are $O(1)$, then for a 1% suspension $\frac{L}{a}$ is $O(100)$ and N is of $O(10^4)$. This analysis suggests that we need a substantial number of particles in our simulator before we can capture the correct variance and also the correct diffusion coefficient. (The diffusion coefficient is proportional to the variance.) Unfortunately we can at most employ about a hundred particles. We therefore expect that our simulator will underestimate both the variance and the diffusion coefficient.

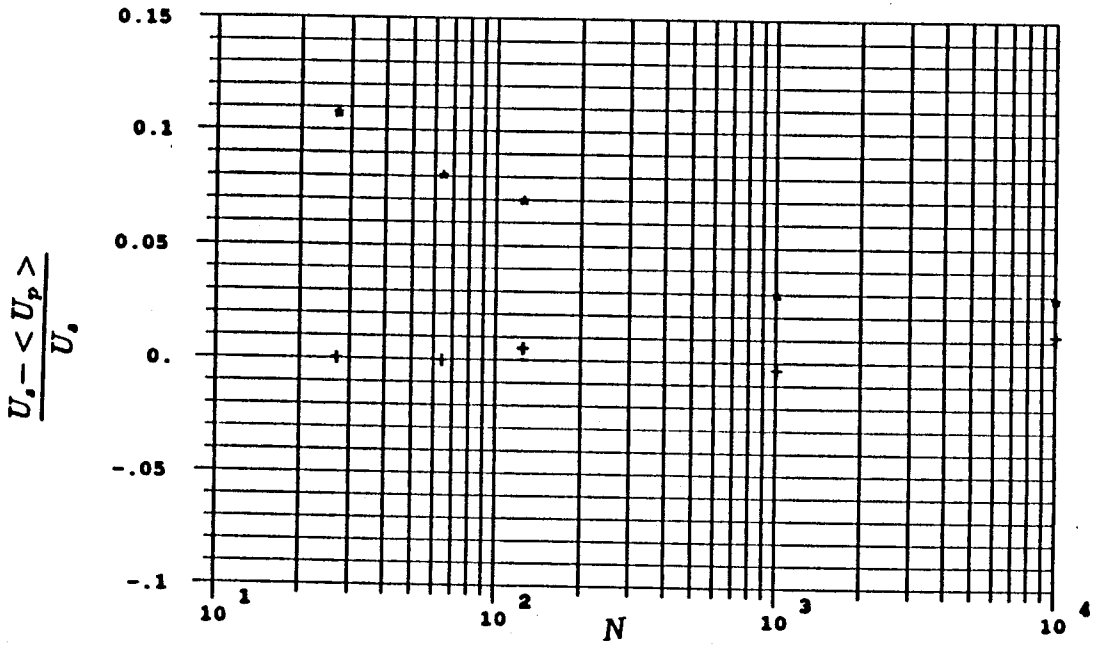

Figure 2.1 Sedimentation velocity's dependence on the number of particles used. The symbol + is for $n = \frac{N-1}{V}$, where n is the number concentration, N is the number of particles in the simulator, and V is the volume of the simulator. The symbol * is for $n = \frac{N}{V}$.

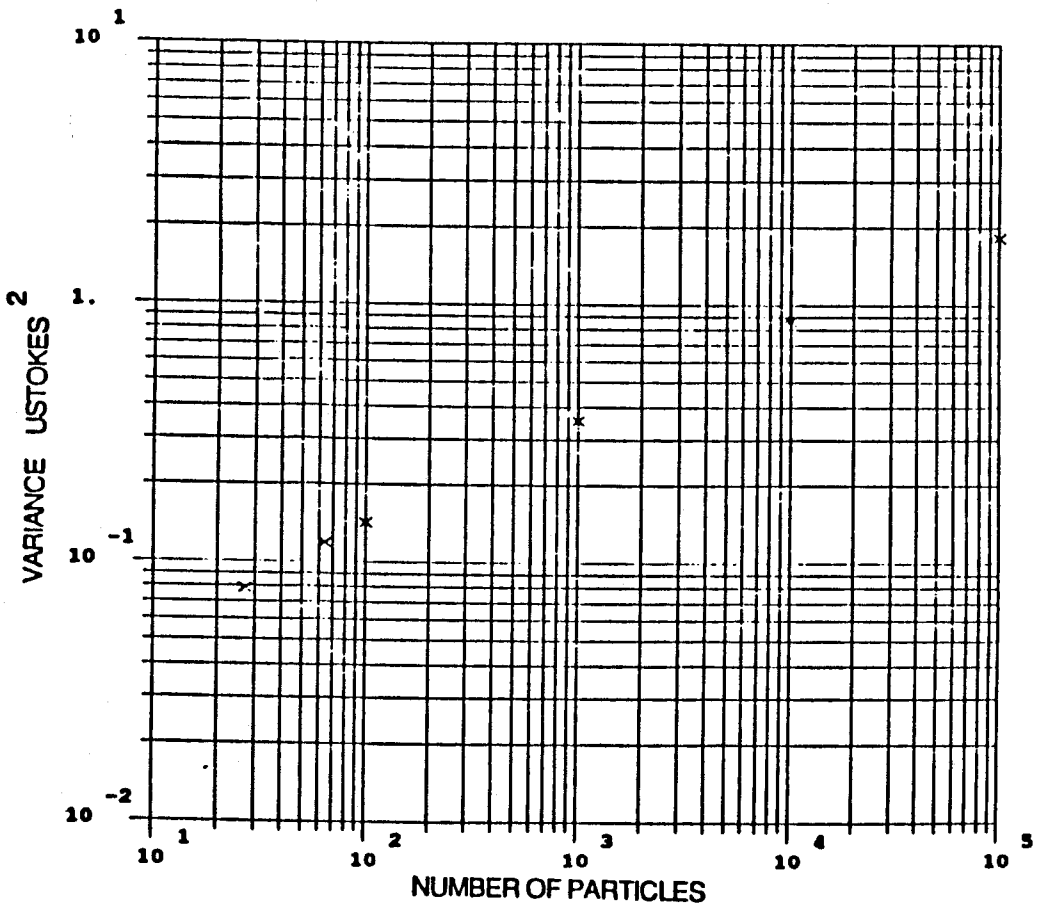

Figure 2.2 The dependence of the x velocity variance on the number of particles. The suspension concentration is 0.01 and the values are from the Monte Carlo simulations.

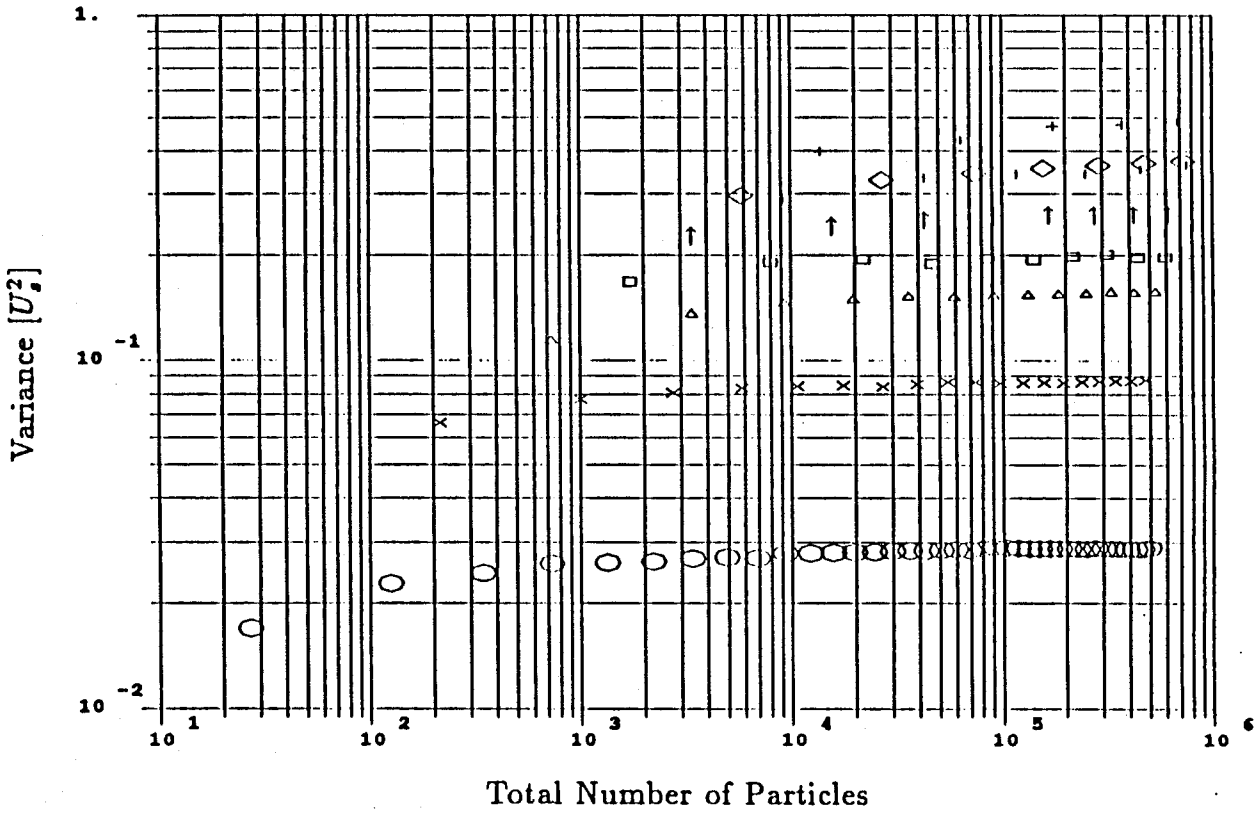

Figure 2.3 The variance of the velocity for different numbers of particles per cell. The concentration of the suspension is 1%. ○ is 1 particle per cell, △ is 27 particles per cell, □ is 64 particles per cell, ↑ is 125 particles per cell, ◇ is 216 particles per cell, | is 343 particles per cell, and + is 512 particles per cell.

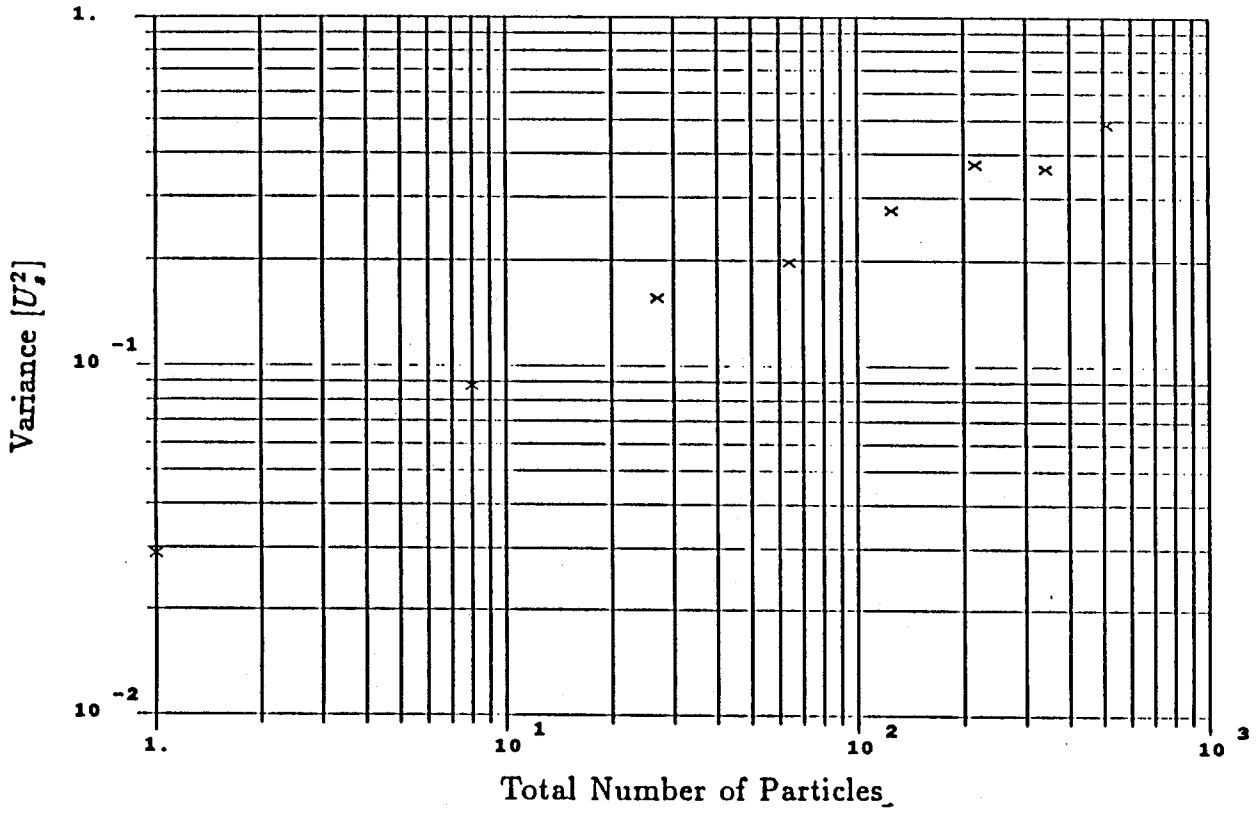

Figure 2.4 The asymptotic values of the velocity variance for different numbers of particles per cell. The results are for point particles and a 1% suspension.

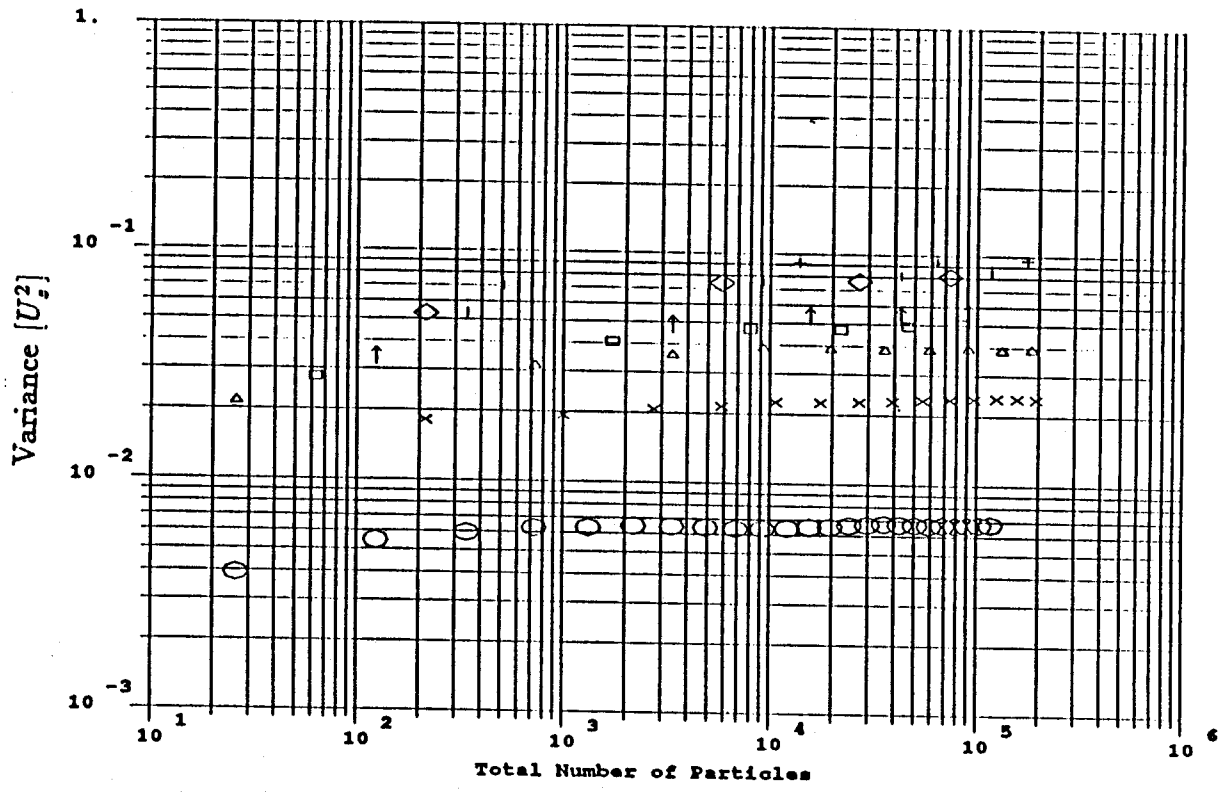

Figure 2.5 The variance of the velocity for different numbers of particles per cell. The particles are not permitted to overlap. The stokeslet approximation is used to determine the particle velocity. The concentration of the suspension is 0.001. ○ is 1 particle per cell, × is 8 particles per cell, △ is 27 particles per cell, □ is 64 particles per cell, ↑ is 125 particles per cell, ◇ is 216 particles per cell, | is 343 particles per cell, and + is 512 particles per cell.

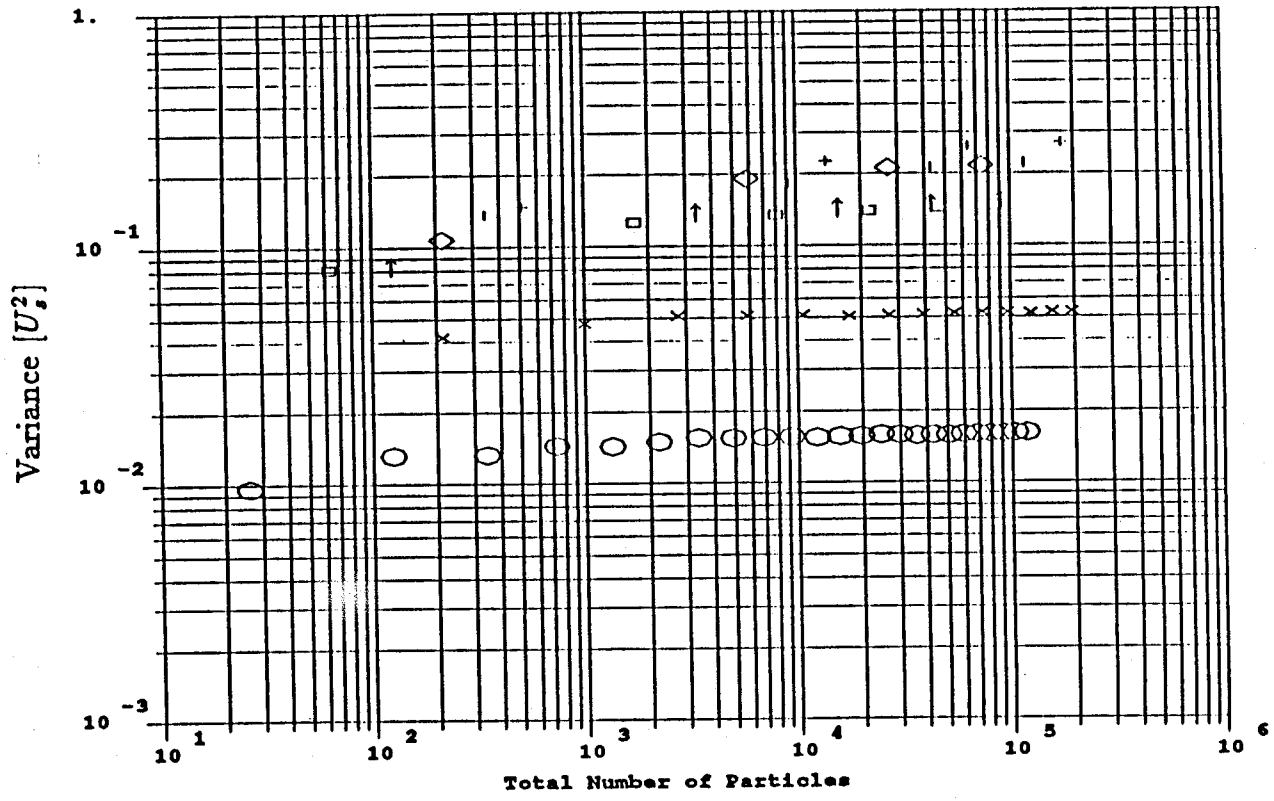

Figure 2.6 The variance of the velocity for different numbers of particles per cell. The particles are not permitted to overlap. The stokeslet approximation is used to determine the particle velocity. The concentration of the suspension is 0.005. ○ is 1 particle per cell, × is 8 particles per cell, △ is 27 particles per cell, □ is 64 particles per cell, ↑ is 125 particles per cell, ◇ is 216 particles per cell, | is 343 particles per cell, and + is 512 particles per cell.

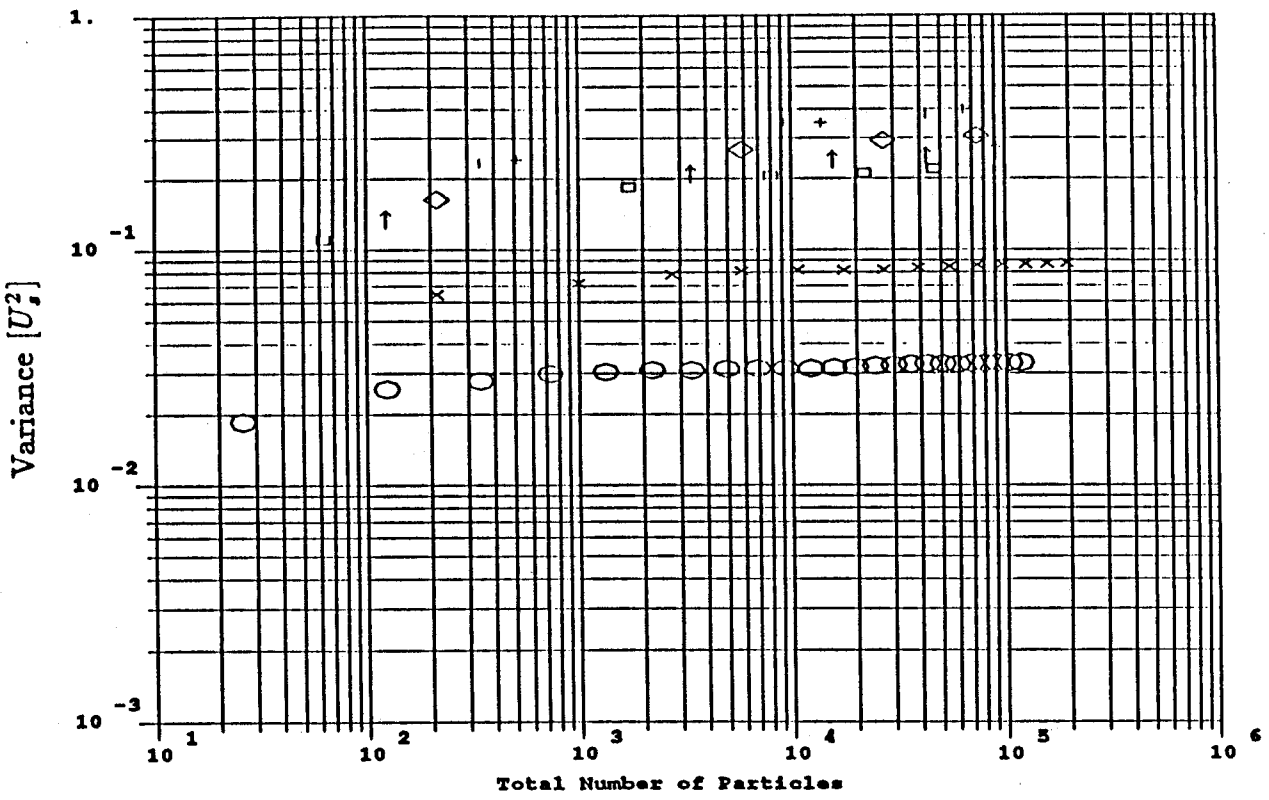

Figure 2.7 The variance of the velocity for different numbers of particles per cell. The particles are not permitted to overlap. The stokeslet approximation is used to determine the particle velocity. The concentration of the suspension is 0.01. ○ is 1 particle per cell, × is 8 particles per cell, △ is 27 particles per cell, □ is 64 particles per cell, ↑ is 125 particles per cell, ◇ is 216 particles per cell, | is 343 particles per cell, and + is 512 particles per cell.

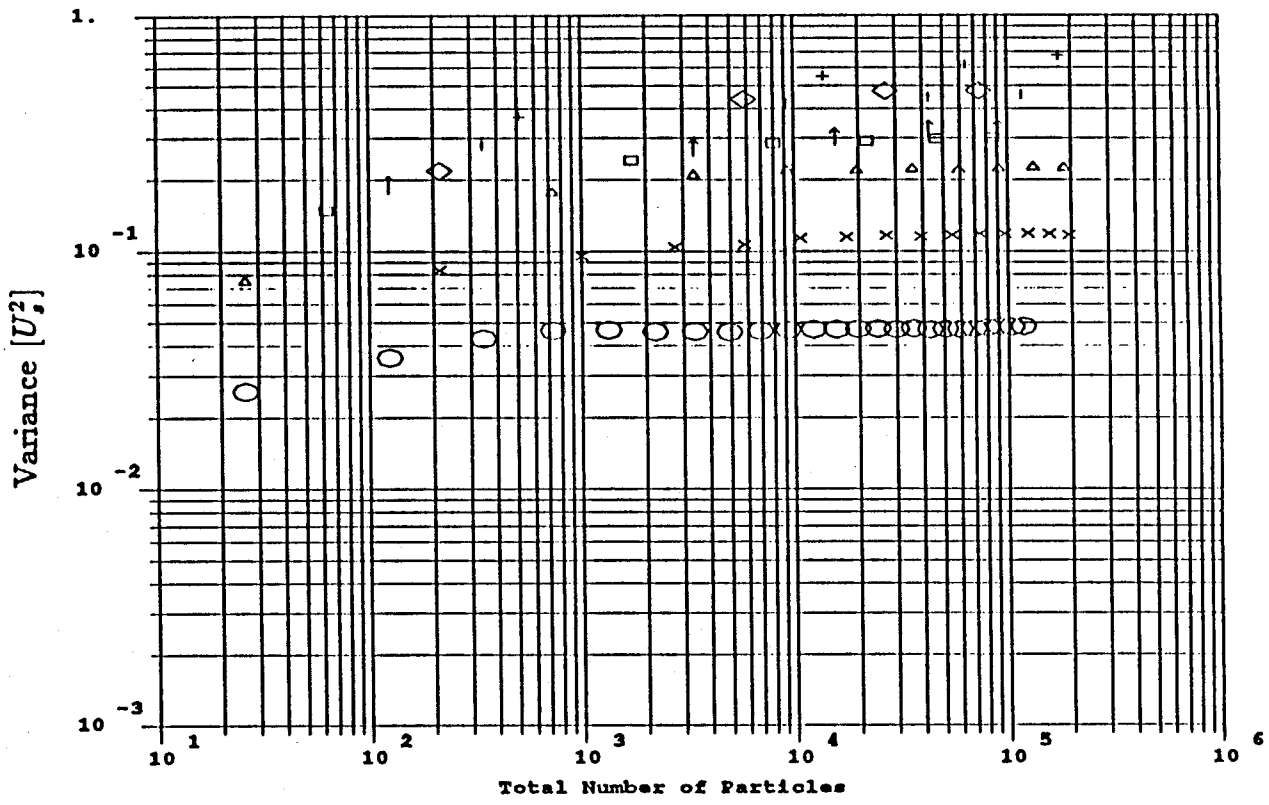

Figure 2.8 The variance of the velocity for different numbers of particles per cell. The particles are not permitted to overlap. The stokeslet approximation is used to determine the particle velocity. The concentration of the suspension is 0.02. ○ is 1 particle per cell, × is 8 particles per cell, △ is 27 particles per cell, □ is 64 particles per cell, ↑ is 125 particles per cell, ◇ is 216 particles per cell, | is 343 particles per cell, and + is 512 particles per cell.

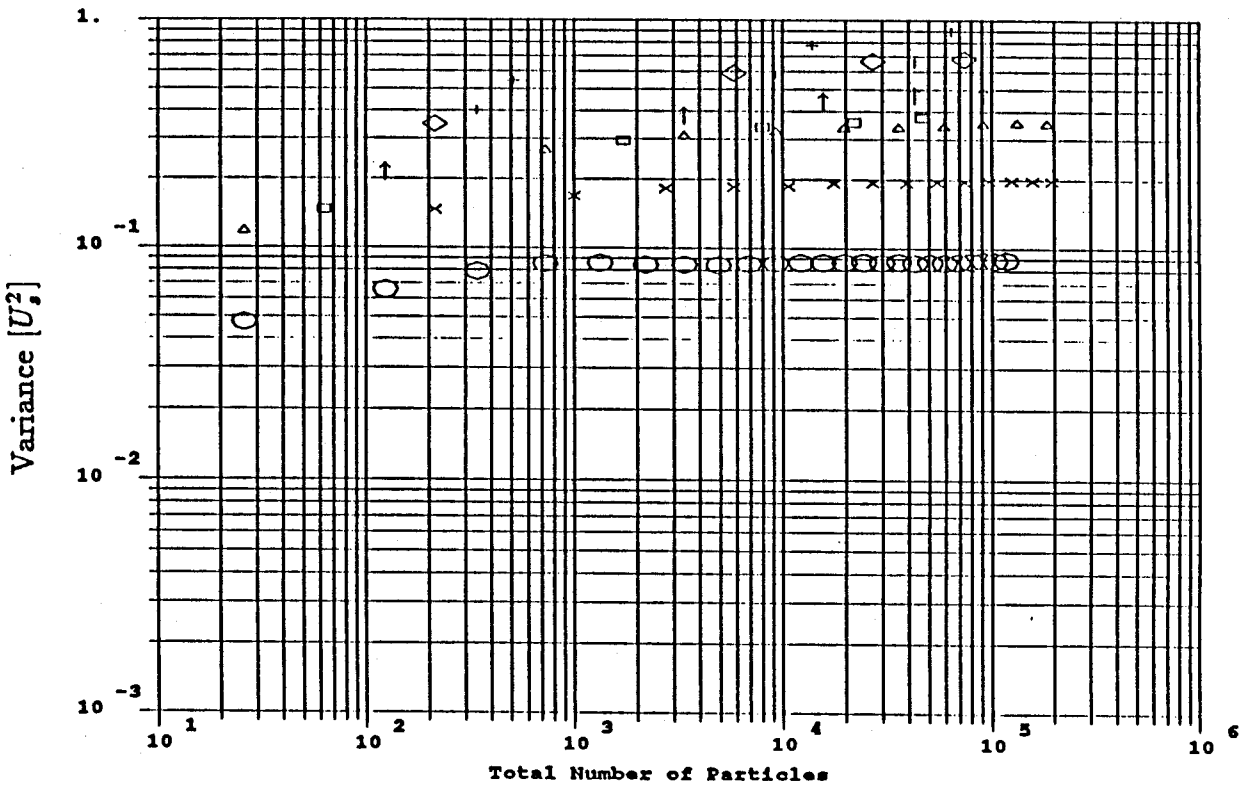

Figure 2.9 The variance of the velocity for different numbers of particles per cell. The particles are not permitted to overlap. The stokeslet approximation is used to determine the particle velocity. The concentration of the suspension is 0.05. ○ is 1 particle per cell, × is 8 particles per cell, △ is 27 particles per cell, □ is 64 particles per cell, ↑ is 125 particles per cell, ◇ is 216 particles per cell, | is 343 particles per cell, and + is 512 particles per cell.

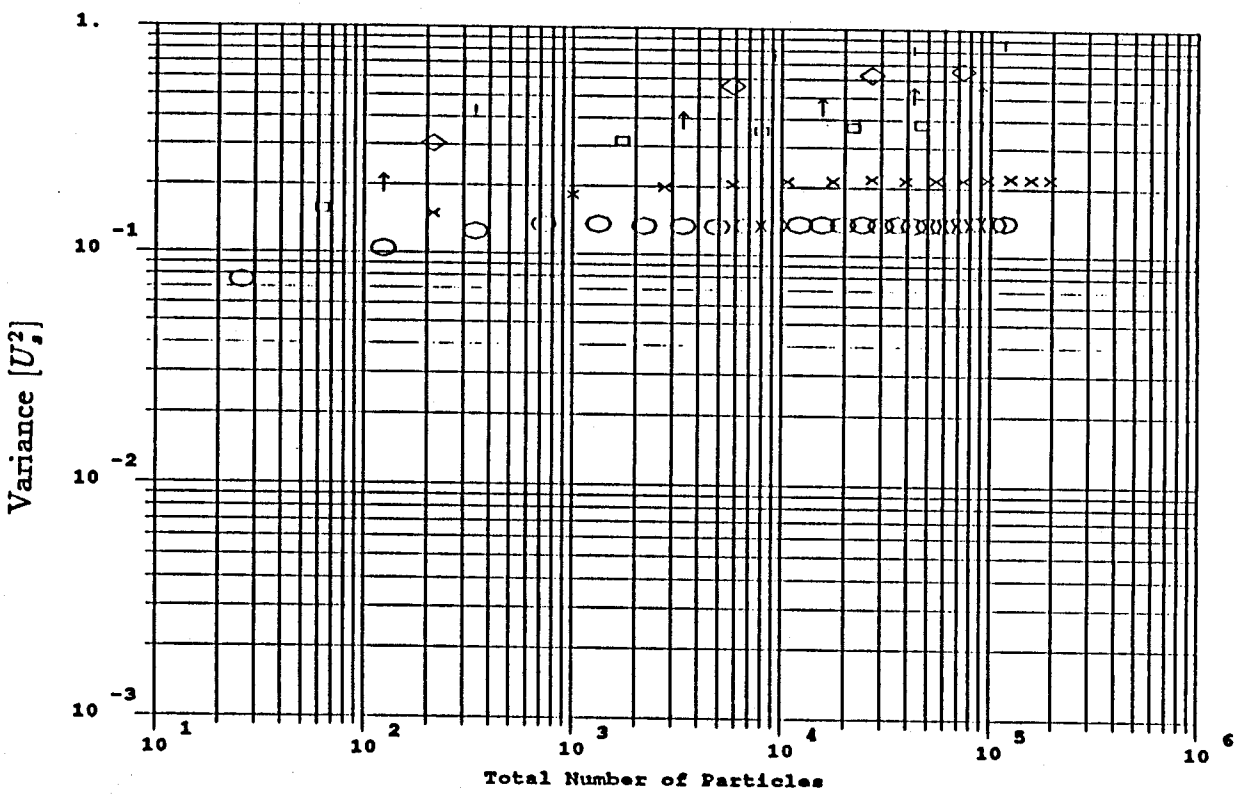

Figure 2.10 The variance of the velocity for different numbers of particles per cell. The particles are not permitted to overlap. The stokeslet approximation is used to determine the particle velocity. The concentration of the suspension is 0.1. ○ is 1 particle per cell, × is 8 particles per cell, △ is 27 particles per cell, □ is 64 particles per cell, ↑ is 125 particles per cell, ◇ is 216 particles per cell, | is 343 particles per cell, and + is 512 particles per cell.

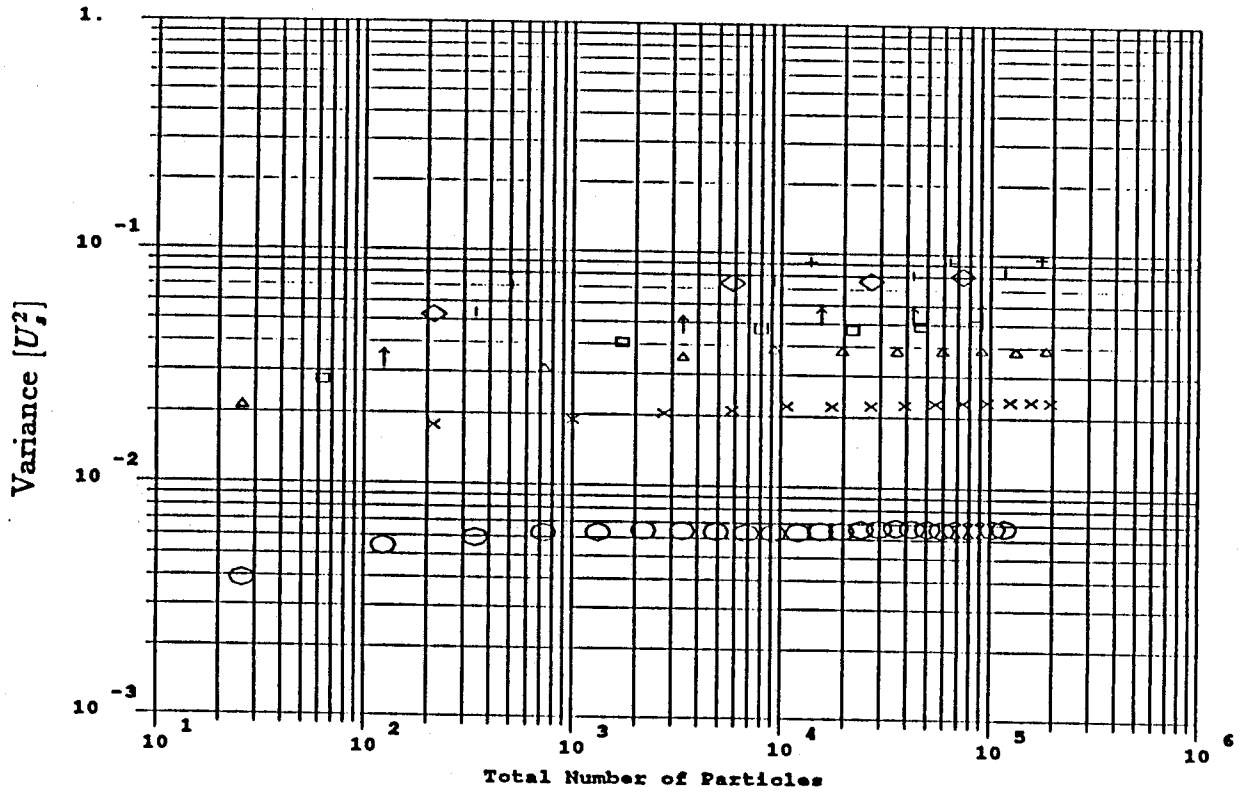

Figure 2.11 The variance of the velocity for different numbers of particles per cell. The particles are not permitted to overlap. The stokeslet-dipole approximation is used to determine the particle velocity. The concentration of the suspension is 0.001. ○ is 1 particle per cell, × is 8 particles per cell, △ is 27 particles per cell, □ is 64 particles per cell, ↑ is 125 particles per cell, ◇ is 216 particles per cell, | is 343 particles per cell, and + is 512 particles per cell.

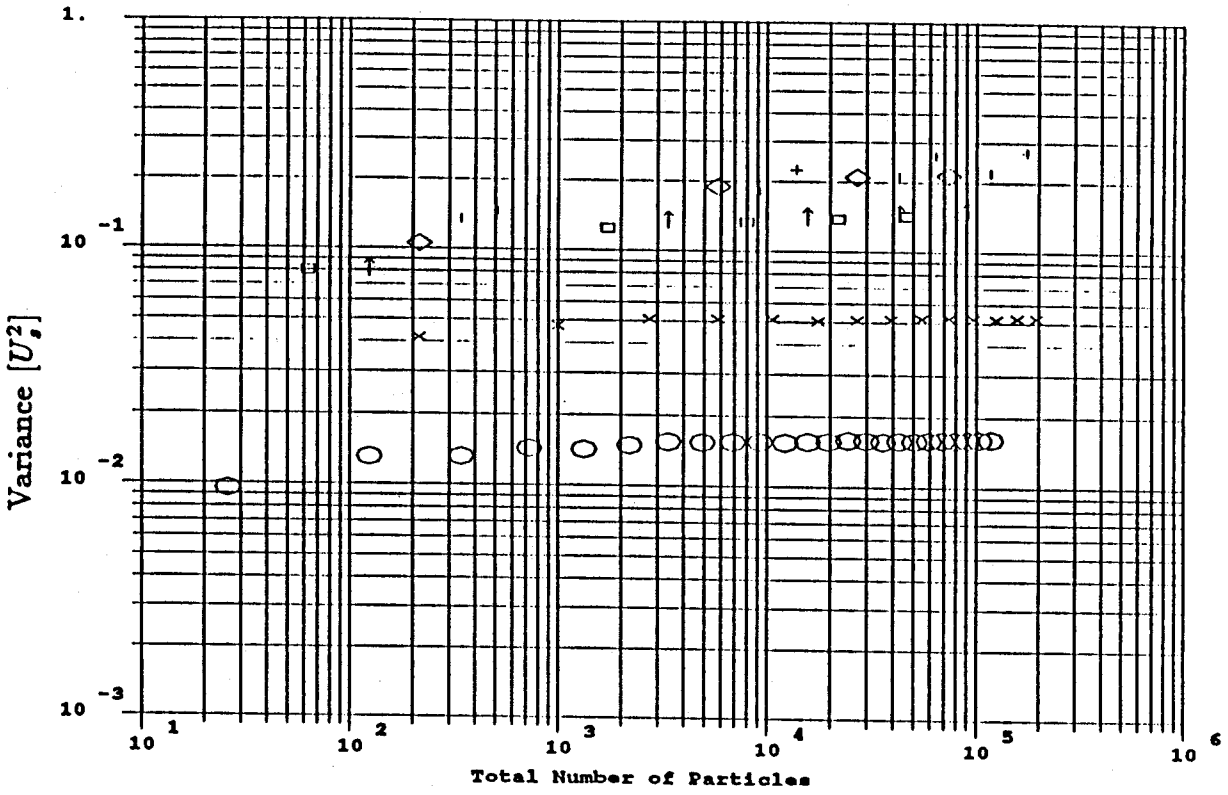

Figure 2.12 The variance of the velocity for different numbers of particles per cell. The particles are not permitted to overlap. The stokeslet-dipole approximation is used to determine the particle velocity. The concentration of the suspension is 0.005. ○ is 1 particle per cell, × is 8 particles per cell, △ is 27 particles per cell, □ is 64 particles per cell, ↑ is 125 particles per cell, ◇ is 216 particles per cell, | is 343 particles per cell, and + is 512 particles per cell.

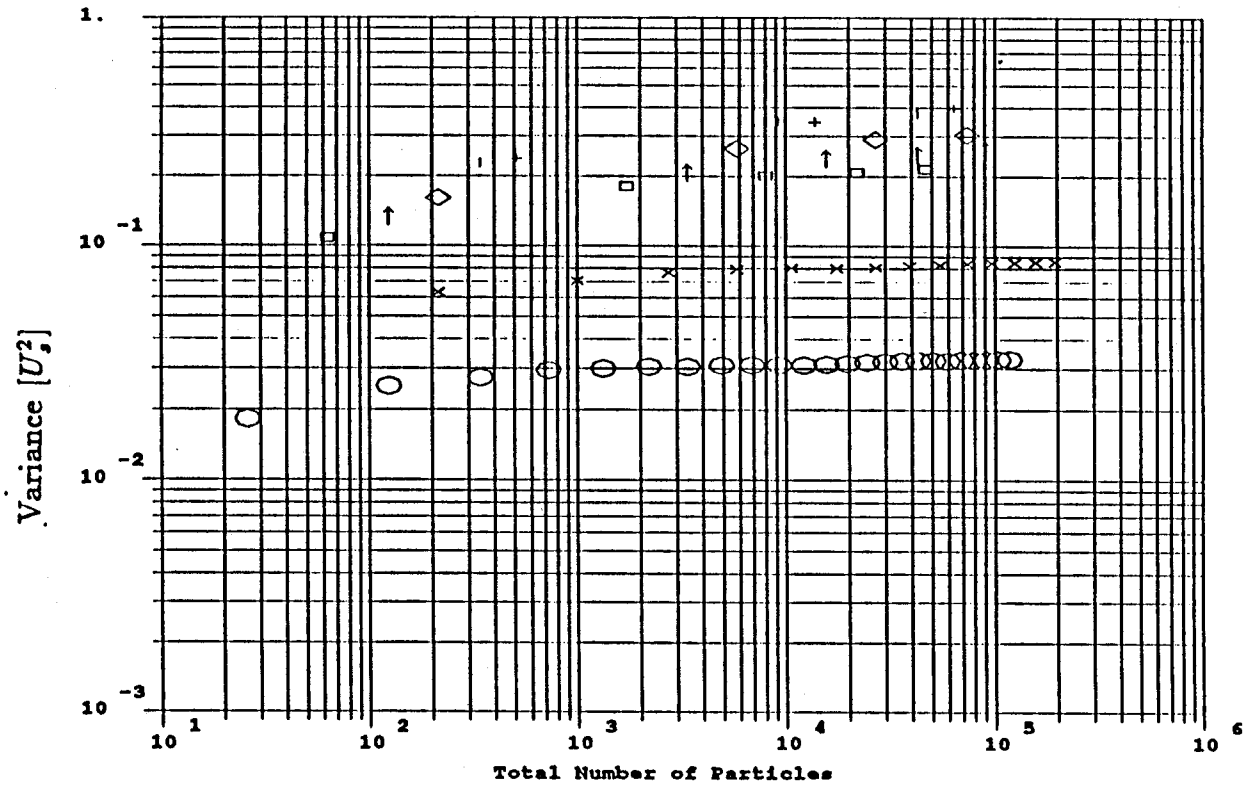

Figure 2.13 The variance of the velocity for different numbers of particles per cell. The particles are not permitted to overlap. The stokeslet-dipole approximation is used to determine the particle velocity. The concentration of the suspension is 0.01. ○ is 1 particle per cell, × is 8 particles per cell, △ is 27 particles per cell, □ is 64 particles per cell, ↑ is 125 particles per cell, ◇ is 216 particles per cell, | is 343 particles per cell, and + is 512 particles per cell.

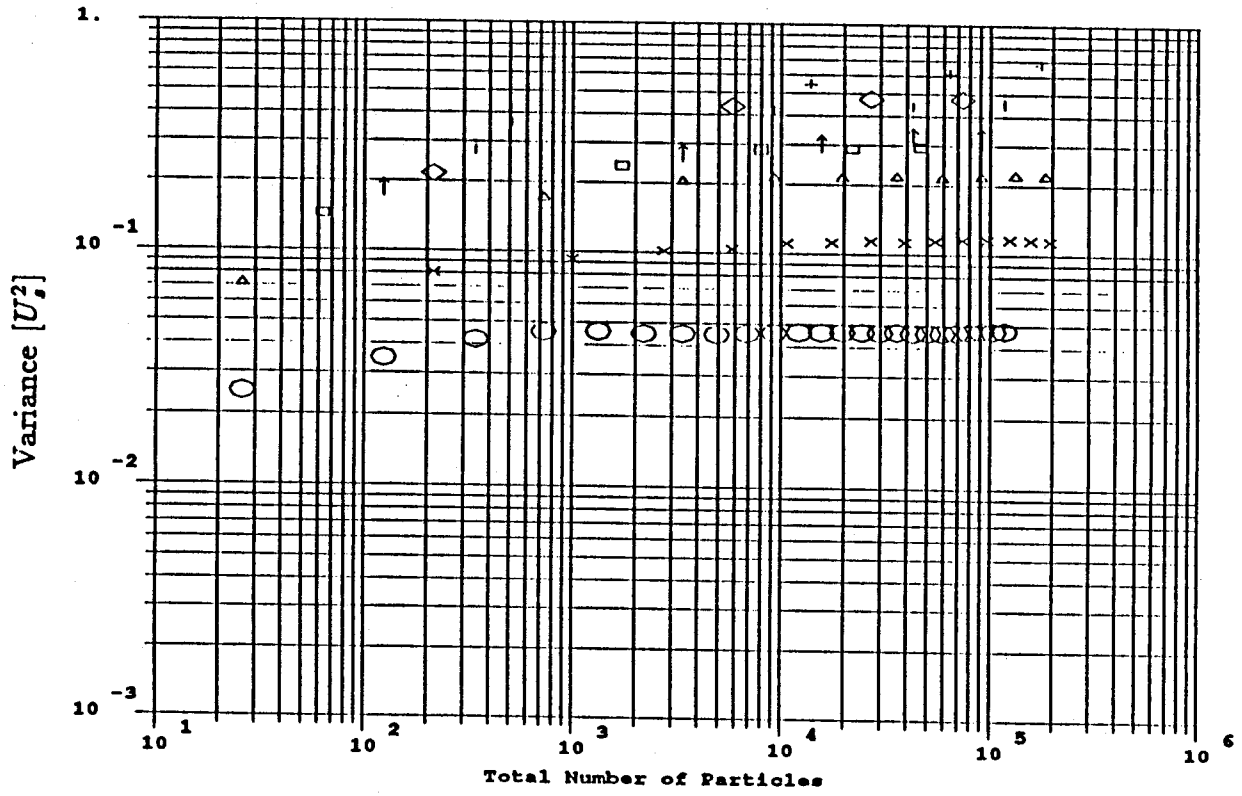

Figure 2.14 The variance of the velocity for different numbers of particles per cell. The particles are not permitted to overlap. The stokeslet-dipole approximation is used to determine the particle velocity. The concentration of the suspension is 0.02. ○ is 1 particle per cell, × is 8 particles per cell, △ is 27 particles per cell, □ is 64 particles per cell, ↑ is 125 particles per cell, ◇ is 216 particles per cell, | is 343 particles per cell, and + is 512 particles per cell.

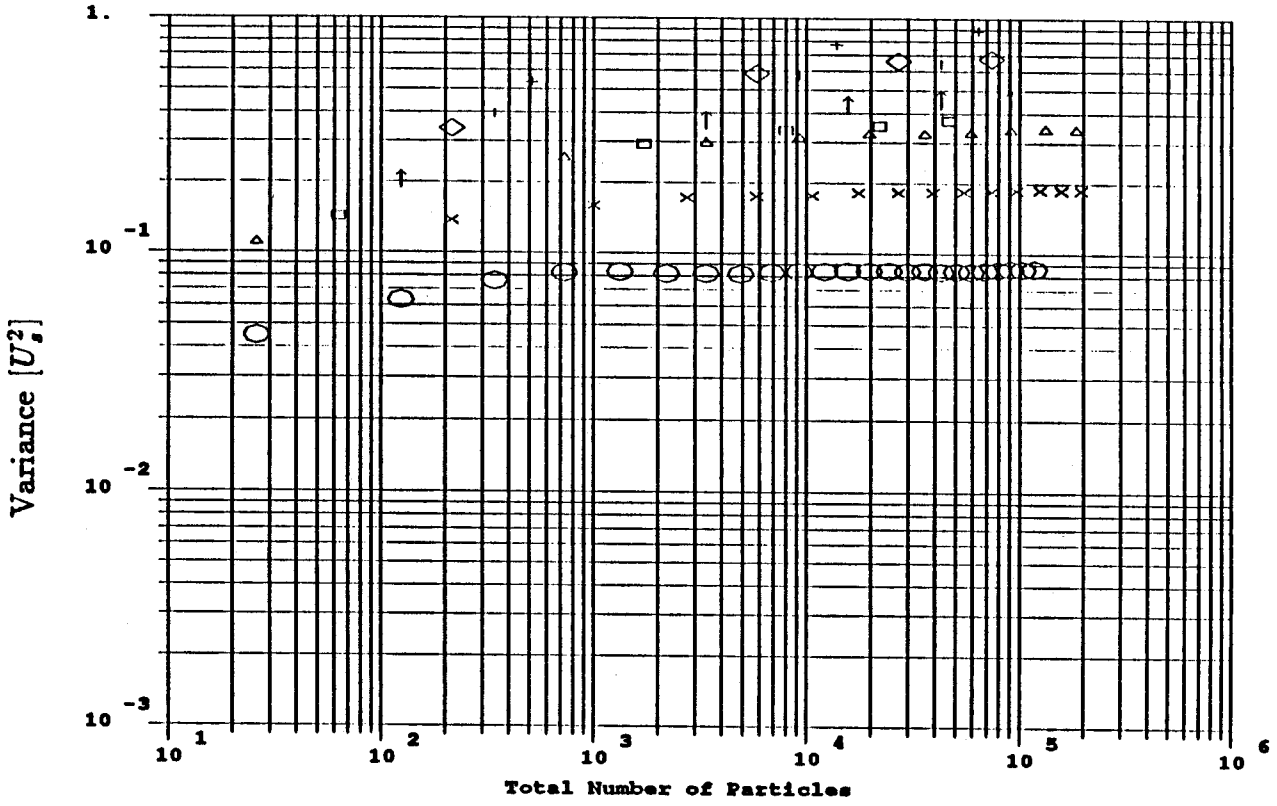

Figure 2.15 The variance of the velocity for different numbers of particles per cell. The particles are not permitted to overlap. The stokeslet-dipole approximation is used to determine the particle velocity. The concentration of the suspension is 0.05. ○ is 1 particle per cell, × is 8 particles per cell, △ is 27 particles per cell, □ is 64 particles per cell, ↑ is 125 particles per cell, ◇ is 216 particles per cell, | is 343 particles per cell, and + is 512 particles per cell.

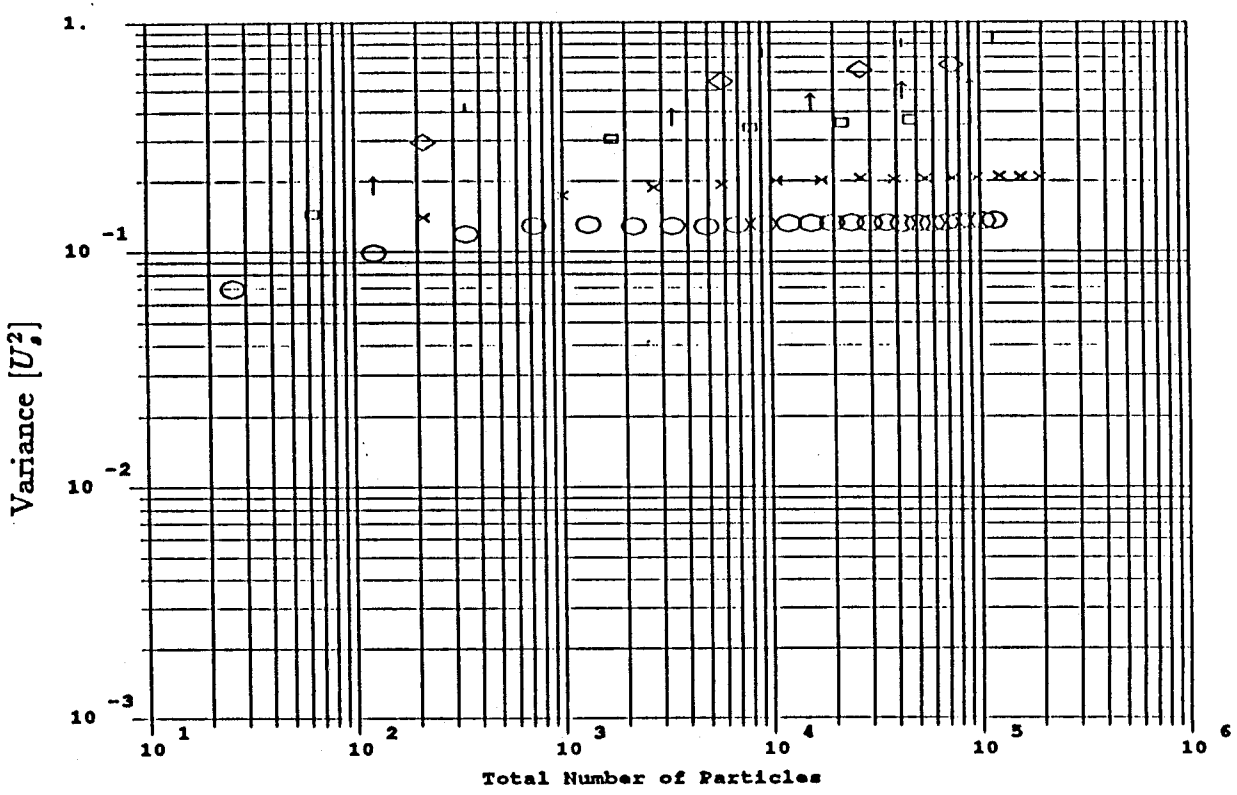

Figure 2.16 The variance of the velocity for different numbers of particles per cell. The particles are not permitted to overlap. The stokeslet-dipole approximation is used to determine the particle velocity. The concentration of the suspension is 0.1. ○ is 1 particle per cell, × is 8 particles per cell, △ is 27 particles per cell, □ is 64 particles per cell, ↑ is 125 particles per cell, ◇ is 216 particles per cell, | is 343 particles per cell, and + is 512 particles per cell.

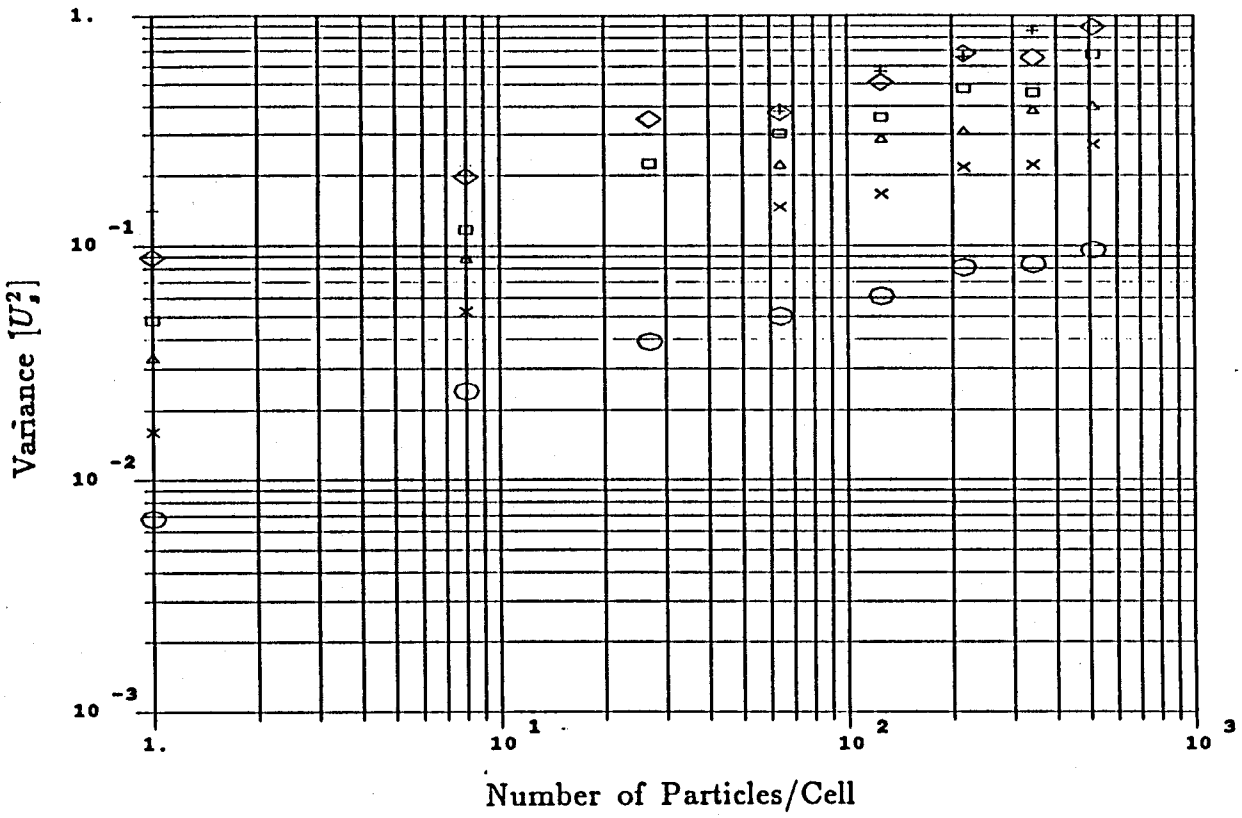

Figure 2.17 The asymptotic values of the velocity variance for different numbers of particles per cell. The particles are not permitted to overlap. The stokeslet approximation is used to determine the particle velocity. ○ is for $c = 0.001$, × is for $c = 0.005$, △ is for $c = 0.01$, □ is for $c = 0.02$, ↑ is for $c = 0.05$, and ◇ is for $c = 0.1$

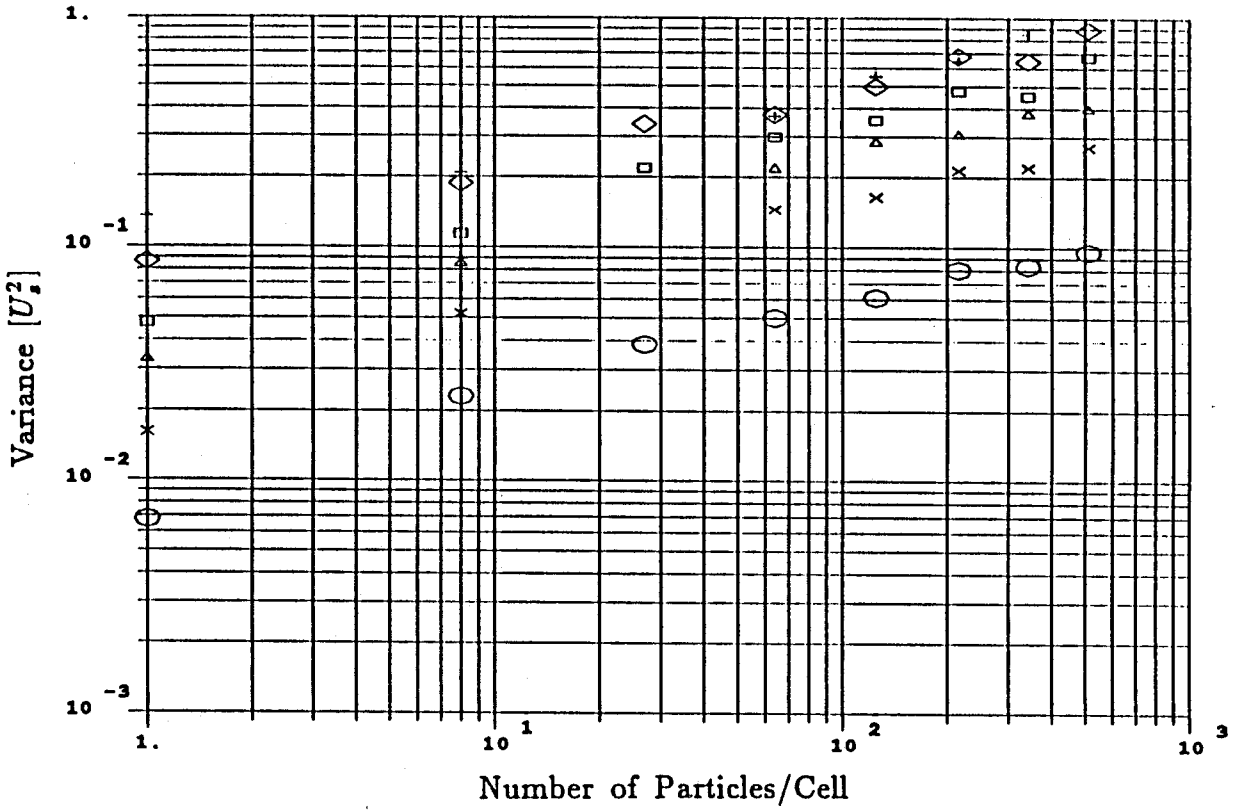

Figure 2.18 The asymptotic values of the velocity variance for different numbers of particles per cell. The particles are not permitted to overlap. The stokeslet-dipole approximation is used to determine the particle velocity. ○ is for $c = 0.001$, × is for $c = 0.005$, △ is for $c = 0.01$, □ is for $c = 0.02$, ↑ is for $c = 0.05$, and ◇ is for $c = 0.1$

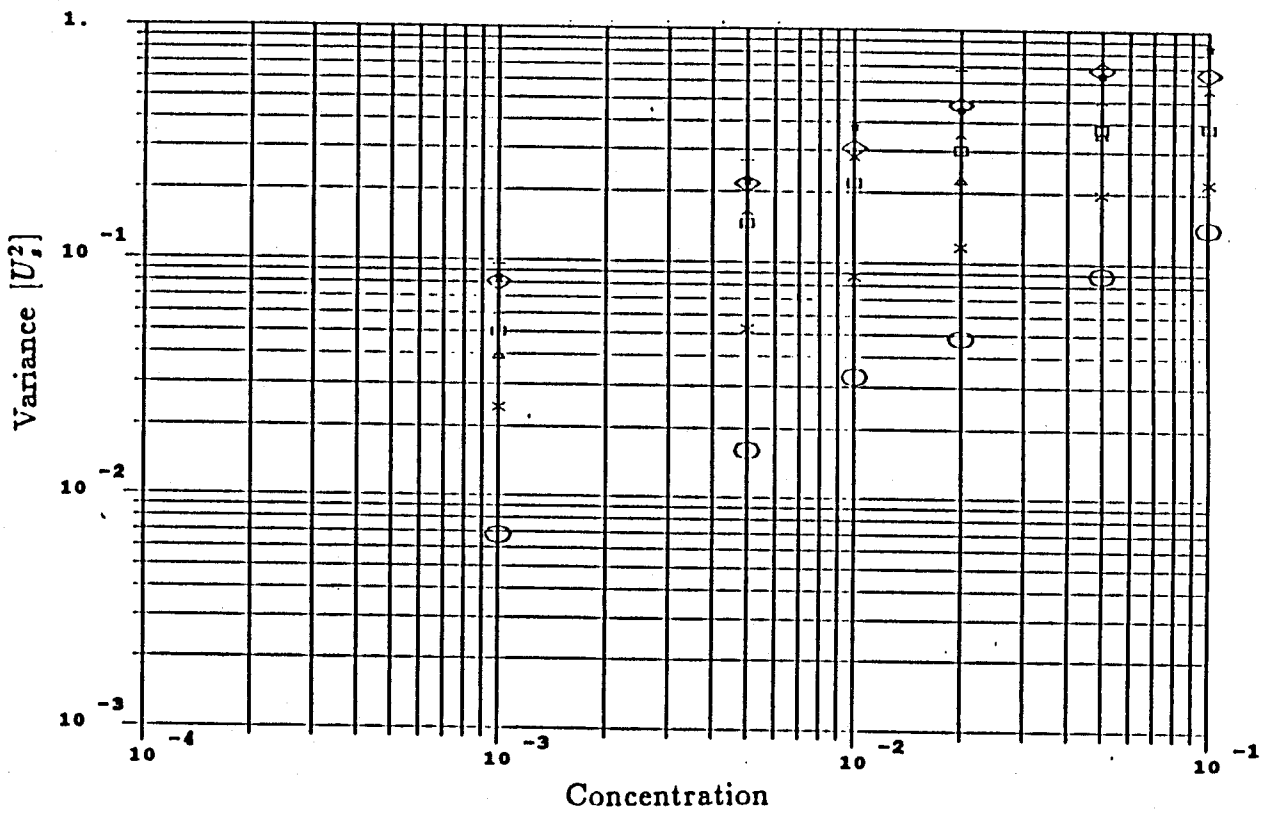

Figure 2.19 The dependence of the variance on the concentration for different number of particles per cell. The particles are not permitted to overlap. The stokeslet approximation is used to determine the particle velocity. ○ is 1 particle per cell, × is 8 particles per cell, △ is 27 particles per cell, □ is 64 particles per cell, ↑ is 125 particles per cell, ◇ is 216 particles per cell, | is 343 particles per cell, and + is 512 particles per cell.

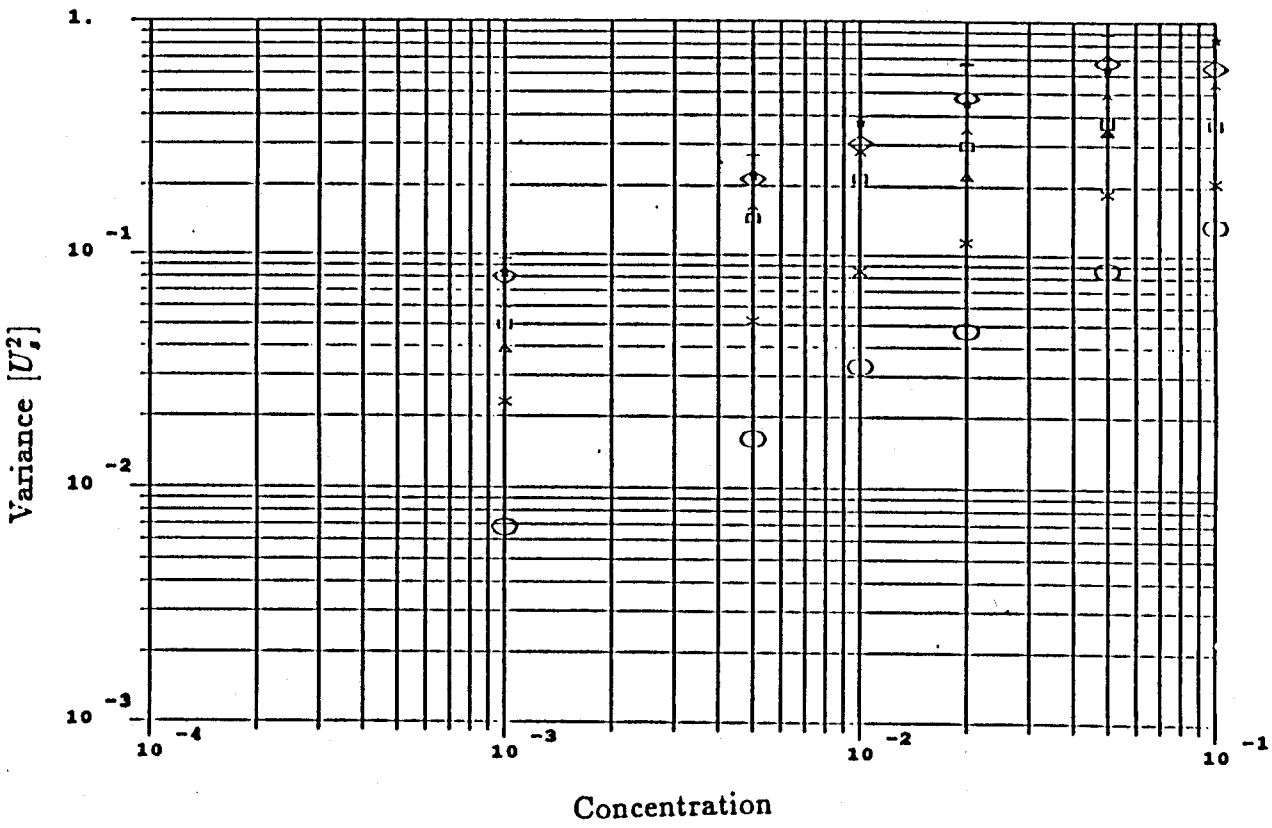

Figure 2.20 The dependence of the variance on the concentration for different number of particles per cell. The particles are not permitted to overlap. The stokeslet-dipole approximation is used to determine the particle velocity. ○ is 1 particle per cell, × is 8 particles per cell, △ is 27 particles per cell, □ is 64 particles per cell, ↑ is 125 particles per cell, ◇ is 216 particles per cell, | is 343 particles per cell, and + is 512 particles per cell.

3 Simulator

3.1 Introduction

In this chapter we will describe the simulator which we have built to model sedimentation in either a quiescent or sheared suspension (figure 3.1). The particles are settling in the e_1 direction while being sheared in the e_2, and e_3 plane. The suspension is assumed to be homogeneous and free from any convection in the direction of sedimentation. The particles are monodisperse and the problem's Reynolds number is assumed to be small. The latter is a reasonable assumption since in Lynch's experiments, the Reynolds number is $O(10^{-3})$. This assumption linearizes the governing equations and renders the problem tractable. We will further assume that quasi-steady state approximation is valid. This assumption is reasonable since the Reynolds number is small, and the fluid is incompressible. It allows us to determine the particles' velocities from knowing only their positions at that instant in time. The general scheme of the simulator is as follows. The simulator consists of a collection of particles inside a box. Initially we place these particles inside the box in any desired arrangement. Using the known particle positions, we determine their velocities, and integrating the velocities we obtain the new particles' positions. This process is repeated many times until steady state is reached in a statistical sense. Along the way, suspension statistics of interest (e.g., average particle velocity, variance of the velocity, particle diffusion coefficient, particle radial and angular distributions) are determined. Steady state is achieved when these statistics reach a constant value. There are two steps in building this simulator. First the true problem which involves infinitely many particles must be reduced to a N-particle problem. This will be discussed in section 3.4. The second step involves determining the velocity of the N particles given their positions. This will be described in the next section.

3.2 Determination of the Particles' Velocities

There are a variety of methods which can be used to determine the velocities of N particles moving in a fluid. However for use in the simulator, the method must not only be accurate, but must also be computationally fast. Before describing the approach we have used in our simulator, we will review the different ways to solve the N-particle problem. Our procedures are a combination of these methods.

One numerical technique for solving the N-particle problem is the collocation method developed by Ganatos, Pfeffer and Weinbaum (1978). The exact solution is assumed to be a linear combination of a set of basis functions and the weight for each of these basis functions is determined from requiring the solution to satisfy the boundary conditions at points on the particles' surfaces. Ganatos chose Lamb's solution as the set of basis functions. This method has been applied mainly to two dimensional or axisymmetric flow problems. In principle, this approach can determine the particles' velocities for any particle separation. However when the particles are close to each other, the number of collocation points (N_c) needed increases, and the computation time grows as ${N_c}^3$. This technique, applied in this fashion, cannot be used in the simulator because it requires excessive amount of computer time.

When the particles are well spaced, an alternate approach is the method of reflections (Happel and Brenner 1965). In this method, instead of requiring the solution to satisfy the boundary conditions on all the surfaces simultaneously, the solution is required to satisfy the boundary conditons at one surface at a time. This is an iterative scheme because when the solution satisfies the boundary conditions on one particle exactly, it will no longer satisfy the boundary conditions on the others. However, after each iteration, the error on each of the boundaries is smaller by a factor of $\frac{a}{R}$, where R is the distance to the nearest surface. If the particles are well spaced, a few iterations are sufficient to give a reasonable approximation. The main advantage of this method is that the solution can be obtained analytically.

A third approach is the method of multipole expansions (Jeffrey and Onishi 1984, Dabros 1985, and Durlofsky, Brady and Bossis 1987). The fundamental singu-

larity of the Stokes's equation is the stokeslet. The stokeslet along with its derivatives form a complete set of basis functions for any solution to a zero Reynolds number problem. The solution to the N-particle problem can be obtained by placing a set of these singularities at the center of each of the particles. The strength of these singularities can be determined using either the method of reflections or the collocation technique. One generally needs only the stokeslet and its first few derivatives to obtain a reasonable approximation to the particles' velocities, even when the particles are touching. For instance, for a horizontal chain of touching spheres, the errors are less than 10% (Dabros 1985). Because the strength of the stokeslet, the rotlet, and the stresslet have physical meaning (they are the force, torque and stress exerted by the particle on the fluid) one can often construct the leading order solution by inspection. For instance, a settling particle exerts a force on the fluid, and thus the leading term of the velocity field due to this particle is a stokeslet whose strength is equal to the weight of the particle.

Combining the ideas behind the method of reflections and the method of multipole expansion, we can develop the pairwise additivity in velocities approximation to the N-particle problem. At the center of each particle, we place a stokeslet and a potiential dipole (laplacian of the stokeslet). To the leading order, the velocity field $\mathbf{u}_f$ generated by a particle is,

$$u_{fi}(\mathbf{x}+\mathbf{r},\mathbf{x}) = \frac{F_j}{8\pi\mu}\left[\left(\frac{\delta_{ij}}{r}+\frac{r_i r_j}{r^3}\right)+\frac{a^2}{3}\left(\frac{\delta_{ij}}{r^3}-\frac{3r_i r_j}{r^5}\right)\right], \tag{3.1}$$

where F_j is the bouyancy force exerted by the particles on the fluid. It is equal to $6\pi\mu\mathbf{U}_s a$. In the suspension, the velocity field at a point in the fluid is approximately given by the sum of these velocity fields,

$$\mathbf{u}_{fi}(\mathbf{x}_0) = \sum_{q=1}^{N}\frac{F}{8\pi\mu}\mathbf{e}_1\left[\left(\frac{\delta_{i1}}{r}+\frac{r_i r_1}{r^3}\right)+\frac{a^2}{3}\left(\frac{\delta_{i1}}{r^3}-\frac{3r_i r_1}{r^5}\right)\right]. \tag{3.2}$$

By Faxen's law, a test particle immersed in this flow field will travel with the velocity,

$$U_p = \frac{F e_1}{8\pi\mu}\sum_{q=1}^{N}\left[\left(\frac{\delta_{i1}}{r}+\frac{r_i r_1}{r^3}\right)+\frac{2}{3}a^2\left(\frac{\delta_{i1}}{r_{ij}^3}-\frac{3r_i r_1}{r^5}\right)\right]. \tag{3.3}$$

The particle velocity given in the above equation depends on the velocity field generated by the other particles one at a time, and thus the name pairwise additivity in velocity. Terms involving reflections of one particle's velocity field off a second particle and then on to the test particle have been neglected. When the particles are well spaced, the terms neglected to the terms kept are of $O(\frac{a}{R^3})$ for large R, where R is the particle separation. One can in principle improve upon the estimate of the particle velocity given in (3.3) by applying the method of reflection again and by adding additional singularities to each of the particles (Burgers 1941, Mazur and Van Saarloos 1982). We will not do so.

Equation (3.3) relates the linear velocity of a particle to the forces on the other particles. Similarly we can relate the rotational velocities of a particle to the forces on the other particles,

$$\Omega_i = \frac{1}{2}\sum_{q=1}^{N} \frac{F_j}{8\pi\mu}\epsilon_{ijk}\frac{r_k}{r^3}, \tag{3.4}$$

the translational velocities to the torques on the other particles,

$$U_i = \sum_{q=1}^{N} \frac{T_j}{8\pi\mu}\epsilon_{ijk}\frac{r_k}{r^3}, \tag{3.5}$$

and the rotational velocities to the torques on the other particles,

$$\Omega_i = \frac{1}{2}\sum_{q=1}^{N} \frac{T_l}{8\pi\mu}\epsilon_{imk}\epsilon_{kln}\partial_m\frac{x_n}{r^3}. \tag{3.6}$$

Again these expressions are approximate since we have kept only the stokeslet plus its first two derivatives. These equations can be written in the matrix form,

$$\left[\mathbf{M}_{UF}\right]\begin{pmatrix}\mathbf{F}\\ \mathbf{T}\end{pmatrix} = \begin{pmatrix}\mathbf{U}\\ \mathbf{\Omega}\end{pmatrix}, \tag{3.7}$$

where $\left[M_{UF}\right]$ is the mobility matrix. This mobility matrix will be used later to obtain a more accurate approximation to the particles' velocities.

There is an alternate method of approximating the N-body problem. First the problem is cast in the matrix form,

$$[\mathbf{R}_{FU}]^{Nb} \cdot \begin{pmatrix} \mathbf{U} \\ \mathbf{\Omega} \end{pmatrix} = \begin{pmatrix} \mathbf{F} \\ \mathbf{T} \end{pmatrix}, \tag{3.8}$$

where $[\mathbf{R}_{FU}]^{Nb}$ is the N-body resistance matrix, $\mathbf{U}$ and $\mathbf{\Omega}$ are the translational and rotational velocities of the particles, and $\mathbf{F}$ and $\mathbf{T}$ are the known applied forces and torques. To approximate the N-body resistance matrix, one assumes that the particles' resistances to motion can be determined by considering pair interactions. For example, if particle α is in a cluster with particle β and γ, the force on particle α when it moves in the presence of these two other particles is approximated by the force on particle α in the presence of particle β with particle γ absent, plus the force on particle α in the presence of particle γ and in the absence of particle β, minus the force on particle α when both particle β and α are not there. The exact two-particle solutions needed to construct the resistance matrix are given by Jeffrey and Onishi (1984). Once the particles' resistances to motion are known, the particles' velocities can be determined by solving,

$$[\mathbf{R}_{FU}]^{Nb} \cdot \begin{pmatrix} \mathbf{U} \\ \mathbf{\Omega} \end{pmatrix} \sim [\mathbf{R}_{FU}]^{2b} \cdot \begin{pmatrix} \mathbf{U} \\ \mathbf{\Omega} \end{pmatrix} = \begin{pmatrix} \mathbf{F} \\ \mathbf{T} \end{pmatrix}, \tag{3.9}$$

where $[\mathbf{R}_{FU}]^{2b}$ is the pairwise additivity of forces (PAF) approximation to the N-body resistance matrix. The advantage of this approach is that the lubrication forces between particles are preserved, a feature which prevents particles from overlapping. This is not true in the PAV approximation, especially since we have kept only several terms of the series expansion in (3.3) through (3.6). The PAF approximation, however, is less accurate; the ratio of the terms neglected to the terms kept is of $O(\frac{a}{r})$ for large r. For a chain of six touching spheres, this method overestimates the settling velocity by a factor of two. This method is also more time consuming since it requires solving a set of simultaneous equations. As the number of particles (N) increases, the computation time required for the PAF method grows as N^3, while for the PAV method it grows only as N^2.

The source of the error in the PAF approximation can be seen from the following problem. Consider a cluster of three particles α, β, and γ. One piece of information needed in constructing the matrix $[\mathbf{R}_{FU}]^{2b}$ is the force on particle α when particle β is moved while keeping both particle α and γ fixed. To determine this force using the PAF approximation, we ignore the presence of particle γ. The force on particle α is approximately $O(\frac{a}{r})$. If we had solved this three-body problem exactly, we would have found that the motion of particle β induces a force on particle γ which in turn reduces the net effect that particle β has on particle α. If particles β and γ are nearly touching and particle α is far away, the force on α due to the motion of β is $O(\frac{a^2}{r^2})$. Only when particle β is very close to α so that the lubrication forces between particle α and β are much stronger than the contribution from the induced force at particle γ, will the PAF method give a good result.

Durlofsky, Brady and Bossis (1987) developed a method to overcome this problem. We will refer to their method as the FT method. Instead of using PAF to approximate the N-body resistance tensor, this resistance tensor is approximated by

$$\left[\mathbf{R}_{FU}\right]^{Nb} \sim \left[\mathbf{M}_{UF}\right]^{-1} + \left[\mathbf{R}_{FU}\right]^{2b} - \left[\mathbf{R}_{FU}\right]^{2b\infty}, \tag{3.10}$$

where $\left[\mathbf{M}_{UF}\right]$ is the mobility matrix given in (3.4), $\left[\mathbf{R}_{FU}\right]^{2b}$ is the PAF approximation to the N-body mobility matrix, and $\left[\mathbf{R}_{FU}\right]^{2b\infty}$ is constructed similar to $\left[\mathbf{R}_{FU}\right]^{2b}$ except that instead of using the exact two-body solutions, one uses the first few terms of the far-field expansion of the exact two-body solutions. $\left[\mathbf{R}_{FU}\right]^{2b\infty}$ does not contain the lubrication forces. When the mobility matrix is inverted, one in essence is solving a series of boundary value problems using the collocation method. One asks, what are the forces and torques on each of the particles when particle one moves in the x direction, when particle one moves in the y direction, etc. These forces and torques include the effects of all N particles simultaneously and not just one particle at a time. Due to this, the inverse of the mobility matrix gives a reasonable approximation of the exact N-body resistance matrix. The inverse of the mobility matrix, however, does not contain the lubrication forces. These terms

are introduced in $\left[\mathbf{R}_{FU}\right]^{2b}$. As was noted earlier, $\left[\mathbf{R}_{FU}\right]^{2b}$ formed using the PAF method is a poor approximation of the N-body resistance matrix when some of the particles are far apart. Furthermore, better estimates of these far field terms have been included in $\left[\mathbf{M}_{UF}\right]$. We therefore need to eliminate these terms from $\left[\mathbf{R}\right]^{2b}$ which is accomplished by subtracting $\left[\mathbf{R}\right]^{2b\infty}$ from $\left[\mathbf{R}\right]^{2b}$. In so doing, the far field terms are eliminated while leaving behind the lubrication terms.

At this point a question which may arise is, why not attempt to obtain an approximation to the N-body mobility matrix in an analogous fashion instead. The obvious advantage of this approach is that one can obtain the particles' velocities directly without having to solve another set of simultaneous equations by using (3.4). The reason is due to numerical accuracy considerations. If we consider the case when two particles are very close to one another, the forces required to move the two particles toward each other with a finite velocity is very large compared to the other resistances in the problem. Therefore, the terms in the resistance matrix associated with the lubrication forces are dominant, and their effects are preserved. On the other hand, from the mobility matrix point of view, the relative velocities of the two particles when they are subjected to a finite force is small relative to the other motions of these particles. The lubrication terms contribute little to the elements of the mobility matrix. If the particles are sufficiently close, the lubrication terms' contributions will be so small that they will be masked by the errors in the approximation made in the other parts of the problem. If we attempt to invert the PAF approximation of the N-body resistance matrix to obtain the mobility matrix, we can lose the lubrication terms due to numerical errors, especially since the matrix often becomes ill conditioned when the particles come very close to each other. To retain the effects of the lubrication forces, we must express the problem in the form of (3.9).

We have considered the case when these N particles are settling in the absence of a shear flow. If a shear flow is imposed, equations analogous to equations (3.3), (3.9), and (3.10) can be derived.

To account for the shear flow in the PAV approach, we need to add to equation

(3.2), a stresslet plus a potential quadrapole,

$$u_{fi}(\mathbf{x}_0) = \sum_{q=1}^{N} \frac{F_1}{8\pi\mu}\left[\left(\frac{\delta_{i1}}{r} + \frac{r_i r_1}{r^3}\right) + \frac{a^2}{3}\left(\frac{\delta_{i1}}{r^3} - \frac{3r_i r_1}{r^5}\right)\right] - cU_s e_i \tag{3.11}$$

$$+ E_{ij}R_j + \epsilon_{ijk}\Omega_j R_k + \sum_{q=1}^{N} \frac{S_{ij}}{\frac{20}{3}\pi\mu a} r_j \left[-\delta_{ik}\frac{a^5}{r^5} + \frac{r_i r_k}{r^2}\left(\frac{-5a^3}{2r^3} + \frac{5a^5}{2r^5}\right)\right].$$

After applying the Faxen's law, equation (3.3) becomes,

$$U_{pi} = \sum_{q=1}^{N} \frac{F}{8\pi\mu}\left[\left(\frac{\delta_{i1}}{r} + \frac{r_i r_1}{r^3}\right) + \frac{2}{3}a^2\left(\frac{\delta_{i1}}{{r_{ij}}^3} - \frac{3r_i r_1}{r^5}\right)\right] \tag{3.12}$$

$$- \frac{S_{23}}{\frac{20}{3}\pi\mu a^3} \sum_{q=1}^{N}\left[\frac{8}{3}a^5\frac{\left(\delta_{i2}r_3 + \delta_{i3}r_2\right)}{r^5} - \frac{r_i r_2 r_3}{r^2}\left(\frac{-5a^3}{r^3} + \frac{40}{3}\frac{a^5}{r^5}\right)\right] + \gamma R_3 e_2 - U_s,$$

where γ is the imposed shear rate. To the leading order, the stress S_{23} for a particle immersed in a shear flow is $\frac{20}{3}\pi\mu a^3 E_{23}$. Equation (3.10) relates the velocity to the force and the stress. Similar expressions can be written to relate the strain rate to the stress (Durlofsky, Brady and Bossis 1987). Just as before, these equations can be put in a matrix form,

$$\left[\mathcal{M}\right]\begin{pmatrix}\mathbf{F}\\ \mathbf{T}\\ \mathbf{S}\end{pmatrix} = \begin{pmatrix}\mathbf{U}\\ \mathbf{\Omega}\\ \mathbf{E}\end{pmatrix}, \tag{3.13}$$

where $\left[\mathcal{M}\right]$ is the grand mobility matrix, and it will be used later to obtain a more accurate approximation to the particle velocity.

In the PAF approximation, the effects of the shear flow enter as additional forces and torques ($\mathcal{F}$ and $\mathcal{T}$) on the right side of equation (3.9),

$$\left[\mathbf{R}_{FU}\right]^{Nb}\begin{pmatrix}\mathbf{U}\\ \mathbf{\Omega}\end{pmatrix} = \begin{pmatrix}\mathbf{F}\\ \mathbf{T}\end{pmatrix} + \begin{pmatrix}\mathcal{F}\\ \mathcal{T}\end{pmatrix}. \tag{3.14}$$

$\mathcal{F}$ and $\mathcal{T}$ are related to the strain rate by the shear resistance matrix $\mathbf{R}_{FE}$,

$$\begin{pmatrix}\mathcal{F}\\ \mathcal{T}\end{pmatrix} = \left[\mathbf{R}_{FE}\right]\left[\mathbf{E}\right]. \tag{3.15}$$

The shear resistance tensor can be obtained using the PAF approximation. The exact two-particle solutions that are needed are given by Arp and Mason (1977), and Kim and Mifflin (1985).

Finally, one can obtain a better approximation of the effects of the shear flow by using the method developed by Durlofsky, Brady and Bossis (1987). We first cast the problem into the matrix form,

$$\left[\mathcal{R}\right]^{Nb}\begin{pmatrix}\mathbf{U}\\ \mathbf{\Omega}\\ \mathbf{E}\end{pmatrix}=\begin{pmatrix}\mathbf{F}\\ \mathbf{T}\\ \mathbf{S}\end{pmatrix}, \tag{3.16}$$

where $\left[\mathcal{R}\right]^{Nb}$ is the N-body grand resistance tensor, and S is the stress tensor. The grand resistance matrix can be partitioned into submatrices,

$$\left[\mathcal{R}\right]^{Nb}=\begin{pmatrix}\mathbf{R}_{FU} & \mathbf{R}_{FE}\\ \mathbf{R}_{SU} & \mathbf{R}_{SE}\end{pmatrix}. \tag{3.17}$$

The scheme is to form $\mathcal{R}$, and then extract $\mathbf{R}_{FU}$ and $\mathbf{R}_{FE}$ from it. Finally using (3.14) and (3.15), the motions of the particles can be determined. Analogous to (3.10), we can approximate the N-body grand resistance matrix by,

$$\left[\mathcal{R}\right]^{Nb}\sim\left[\mathcal{M}\right]^{-1}+\left[\mathcal{R}\right]^{2b}-\left[\mathcal{R}\right]^{2b\infty}, \tag{3.18}$$

where $\left[\mathcal{M}\right]$ is the grand mobility matrix, $\left[\mathcal{R}\right]^{2b}$ is the grand resistance matrix formed using PAF approximation, and $\left[\mathcal{R}\right]^{2b\infty}$ is constructed similar to $\left[\mathcal{R}\right]^{2b}$ except that instead of using the exact two-body solutions, one uses only the leading terms of the expansion of the exact two-particle solutions. The elements of these matrices can be found in the reference just cited. We will refer to this method as the FTS method.

We have presented several ways for determining the motions of N particles. The PAV approximation is least costly in terms of computation time. The cost of this method grows with the the square of the number of particles (N). It is accurate when the particles are well spaced. However when particles are close, because this method does not preserve the lubrication forces, the particles tend to

overlap with one another. The PAF approximation, on the other hand, preserves the lubrication forces, and the particles are prevented from overlapping with each other. However this method is not as accurate as the PAV approximation when the particles are far apart. Since the PAF method requires the solution of a set of $6N$ simultaneous equations, the computation time needed by this method grows as $(6N)^3$, and therefore we cannot simulate as many particles with this method as with the PAV method. The FT and the FTS methods are the most accurate, but they are also the most expensive.

Since we will be modeling dilute suspensions, we expect that most of the particles to be far apart and that the PAV approximation will be adequate. However even at low concentration, particles do come together to form clusters, and (3.3) may not be sufficiently accurate to determine the velocities of these particles. One can in principle use the FT or FTS method, but the computation time required is large, and considering that the majority of the particles have no near neighbors, this approach is wasteful. A compromise developed by Lynch (1985) is to treat the particles in the cluster separate from the remaining particles. The velocities of the particles which have no near neighbors are calculated using (3.3), i.e., using the PAV approximation. The velocities of the particles in a cluster are approximated by treating the cluster as being immersed in a flow field generated by the remaining particles. This flow field is given by (3.11) with the sum performed over all particles not in the cluster. Suppose the cluster consists of two particles α and β. (The treatment of a cluster with more than two particles is identical.) We divide this problem into two sub-problems, the pair of particles settling in a quiescent fluid, and the pair (treated as being neutrally bouyant) immersed in the flow field (3.11). The solution of the former problem is given by (3.14) with $\mathcal{F}$, $\mathcal{T}$, and $\mathbf{T}$ set equal to zero, and $\mathbf{F}$ set equal to the buoyancy force. For the second problem, the velocity of particle α is obtained from applying Faxen's law to the velocity field given by (3.11) and evaluating the resulting expression at the center of particle α. Particle β's velocity can be obtained in a similar fashion. These velocities are incomplete because interactions between particles α and β have been neglected. To correct

for this, we approximate (3.11) as a linear shear flow and in this flow field, the additional forces on these particles are given by the product of the shear resistance matrix and the strain rate (3.15). With this force and equation (3.14) (setting **F** and **T** to zero) the additional velocity can be obtained.

The shear resistance matrix can be derived in two ways, either from using the PAF approximation or from extracting it from the grand resistance matrix formed using the FTS method. When there is no imposed shear flow, the forces due to the strain rate are small compared with the buoyancy forces ($O((\frac{a}{r})^2)$ versus $O(1)$), and the PAF approximation is adequate. However when there is an imposed shear flow, this will not be true, and we will obtain the shear resistance matrix from the grand resistance tensor (i.e., (3.17) and (3.18)). (For the two-particle case, the two methods are identical, but for more than two particles, they are not.)

The strain rate which is needed in (3.14) is obtained from taking the gradient of the velocity field given by (3.11),

$$
\begin{aligned}
\nabla \mathbf{u}_f \sim & \Bigg\{ \sum_{\substack{q=1 \\ q \notin \text{cluster}}}^{N} \frac{3}{4} U_s a \Bigg[\Big(\frac{\delta_{il}\mathbf{r}_1}{r^3} - \frac{3\mathbf{r}_i\mathbf{r}_l\mathbf{r}_1}{r^5} \Big) \\
& + \frac{1}{3}a^2 \Big(\frac{-3\mathbf{r}_l\delta_{il} + \mathbf{r}_1\delta_{il} + \mathbf{r}_i\delta_{l1}}{r^5} + \frac{15\mathbf{r}_i\mathbf{r}_l\mathbf{r}_1}{r^7} \Big) \Bigg] \\
& + \sum_{q=1}^{N} \Big[2\mathbf{E}_{23} \Big(\frac{\mathbf{r}_i\mathbf{r}_2\delta_{l3} + \mathbf{r}_l\mathbf{r}_2\delta_{i3}}{r^2} - \frac{2}{3}\delta_{il}\frac{\mathbf{r}_2\mathbf{r}_3}{r^2} \Big) \Big(-\frac{5}{2}\frac{(a)^3}{r^3} + 5\frac{(a)^5}{r^5} \Big) \Big] \\
& + 2\mathbf{E}_{23} \Big[\Big(\frac{\mathbf{r}_2\mathbf{r}_3}{r^2} \Big) \Big(\frac{\mathbf{r}_i\mathbf{r}_3}{r^2} - \frac{\delta_{il}}{3} \Big) \Big(\frac{25(a)^3}{2r^3} - \frac{35}{2}\frac{(a)^5}{r^5} \Big) \Big] \\
& + \mathbf{E}_{23}\big(\delta_{i2}\delta_{l3} + \delta_{i3}\delta_{l2}\big) \Bigg\} \\
& + \Bigg\{ \frac{3}{4} U_s a \epsilon_{i3l} \sum_{q=1}^{N} \frac{\mathbf{r}_l}{r^3} + \epsilon_{ikl} \sum_{q=1}^{N} \Big[\mathbf{E}_{23} \Big(\epsilon_{kj3}\frac{\mathbf{r}_j\mathbf{r}_2}{r^2}\frac{5(a)^3}{2r^3} + \epsilon_{kj2}\frac{\mathbf{r}_j\mathbf{r}_3}{r^2}\frac{5(a)^3}{2r^3} \Big) \Big] \\
& + \epsilon_{i1l}\mathbf{\Omega}_1 \Bigg\}.
\end{aligned}
\tag{3.19}
$$

The terms between the first set of curly braces is the strain rate, and those in the

second set of curly braces less the permutation tensor, ϵ_{ijk}, is the vorticity. Since the flow field about this pair of particles is not truly a linear shear flow, the value of the strain rate depends on where it is evaluated. (The difference however is no more than $O((\frac{a}{r})^2(\frac{R}{r}))$, where R is the separation between the two particles.) In determining the force and torque employing the PAF method, we use the average of the strain rates evaluated at the centers of particles α and β.

In the simulator, the method described above is only employed when the cluster contains more than two particles. (We have used the simple two-particle problem only to illustrate the method.) The velocity of particles in a doublet can be obtained more efficiently using the results of Batchelor and Green (1972). The velocities of two particles, α and β, in a shear flow are given by,

$$V_{\alpha i} = \left[(\lambda_1 - \lambda_2)R_iR_1 + \lambda_2\delta_{i1}\right]\cdot U_0 e_1 + \left(1 + \frac{a^2}{6}\partial_l\partial_l\right)u_{fi}|_\alpha \qquad (3.20)$$
$$- \frac{1}{2}\left\{A\frac{R_iR_j}{R^2} + B\left(\delta_{ij} - \frac{R_iR_j}{R^2}\right)\right\}R_kE_{jk},$$

$$V_{\beta i} = \left[(\lambda_1 - \lambda_2)R_iR_1 + \lambda_2\delta_{i1}\right]\cdot U_0 e_1 + \left(1 + \frac{a^2}{6}\partial_l\partial_l\right)u_{fi}|_\alpha \qquad (3.21)$$
$$+ \frac{1}{2}\left\{A\frac{R_iR_j}{R^2} + B\left(\delta_{ij} - \frac{R_iR_j}{R^2}\right\}R_kE_{jk},\right.$$

where R_i is the displacement vector between the two particles, and where λ_1, λ_2, A, and B are functions of $|R_i|$. These scalar functions can be found in Batchelor and Green (1972). The terms in the square brackets are the velocities of two particles settling in an unbounded quiescent fluid. The next term is the velocity of the particle due to the flow field generated by particles not in the cluster, and if the companion particle is not there. The terms in the curly brace are from the interactions of the two particles in the linear shear flow. This method allows us to obtain the particles' velocities without solving a set of simultaneous equations and therefore is faster.

To implement this hybrid method, we need to establish a criterion for deciding when particles are considered to be in a cluster. Our definition of a cluster is *ad hoc*. Particles are considered to be in a cluster if they are within a critical radius of each

other or if they share a common near neighbor. Thus for a linear chain of particles, the particles at each end of the chain are considered to be in a cluster even though they may be separated by more than one critical radius from each other. The choice of the critical radius is a compromise between speed and accuracy. A small critical radius will lead to fewer clusters and less computation time. However, it will also be less accurate. When the critical radius is increased, the opposite is true. The critical radius we have used is $4a$. To conserve computer memory, we have also placed a limit on the number of particles permitted in a cluster. In principle, all the particles in the simulator can be in one cluster. If we permit this to happen, for 125 particles, we must reserve at least 4 megabytes of memory just for the mobility matrix. Since large clusters of particles rarely appear at low concentration, this is wasteful. We generally set the limit at six particles. At a concentration of 1%, the number of times this limit is exceeded in 100,000 iterations is only several hundred times. When the maximum cluster size is exceeded, we change the definition of a cluster so that now only particles which are within the critical radius are considered to be near neighbors; long chains are broken up into smaller pieces. Breaking up a large cluster into smaller pieces also allows us to reach higher concentration. When we determine the velocity of a cluster of N particles, we need to invert a $11N$ by $11N$ matrix, which requires $O\big((11N)^3\big)$ operations. If the cluster is broken up into M smaller clusters, the operation count is $O(M^2)$ less. This increase in speed however, is also accompanied by lower accuracy. In the simulation we do not model suspension greater than 5%.

Up to now we have described how the motion of a finite system of particles is determined. Before these methods can be used to model an infinite suspension, they must be modified to satisfiy the macroscopic constraint on the suspension velocity,

$$< \mathbf{u}_{susp} >= \mathbf{E}_{ij}\mathbf{r}_j + \epsilon_{ijk}\mathbf{\Omega}_j\mathbf{r}_j, \tag{3.22}$$

where $\mathbf{E}_{ij}$ is the imposed bulk strain rate, $\mathbf{\Omega}_j$ is the bulk vorticity. Modifying (3.11)

to satisfy this contraint gives,

$$\mathbf{u}_f(\mathbf{x}_0) = \sum_{q=1}^{N} \frac{3}{4} a \mathbf{U}_s \mathbf{e}_1 \left[\left(\frac{\delta_{i1}}{r} + \frac{\mathbf{r}_i \mathbf{r}_1}{r^3} \right) + \frac{a^2}{3} \left(\frac{\delta_{i1}}{r^3} - \frac{3\mathbf{r}_i \mathbf{r}_1}{r^5} \right) \right] \tag{3.23}$$

$$- \int_{r>a} \frac{3}{4} a \mathbf{U}_s \mathbf{e}_1 \left[\left(\frac{\delta_{i1}}{r} + \frac{\mathbf{r}_i \mathbf{r}_1}{r^3} \right) + \frac{a^2}{3} \left(\frac{\delta_{i1}}{r^3} - \frac{3\mathbf{r}_i \mathbf{r}_1}{r^5} \right) \right] d\mathbf{r} - c \mathbf{U}_s \mathbf{e}_i$$

$$+ \mathbf{E}_{ij} \mathbf{r}_j + \epsilon_{ijk} \mathbf{\Omega}_j \mathbf{r}_k + \sum_{q=1}^{N} \mathbf{E}_{ij} \mathbf{r}_j \left[-\delta_{ik} \frac{a^5}{r^5} + \frac{\mathbf{r}_i \mathbf{r}_k}{r^2} \left(\frac{-5a^3}{2r^3} + \frac{5a^5}{2r^5} \right) \right]$$

$$- \int \mathbf{E}_{ij} \mathbf{r}_j \left[-\delta_{ik} \frac{a^5}{r^5} + \frac{\mathbf{r}_i \mathbf{r}_k}{r^2} \left(\frac{-5a^3}{2r^3} + \frac{5a^5}{2r^5} \right) \right] d\mathbf{r} + O(c^2).$$

The first integral on the right hand side is the familiar back flow term which is needed to satisfy the zero flux condition in the x direction. We have already seen the first two lines of (3.23) in chapter 2. The next line represents the effects of the linear shear flow. It, however, does not satisfy the constraint (3.22). The integral in the fourth line eliminates this problem. The new velocity gradient is obtained by differentiating (3.23), and the particle velocity is obtained by applying Faxen's law to (3.23). The complete set of equations used in the simulator will be presented later in section 3.4.

Before concluding this section, we will give an estimate of the error in the hybrid method. The error analysis for the hybrid method is complex because the largest error made depends on the configuration of the particles. If a cluster of particles is surrounded by a swarm of isolated particles, the largest error is due to the approximation of the strain rate discussed earlier. The error is $O((\frac{a}{r})^2(\frac{R}{r}))$. On the other hand if the particle configuration consists of a cluster located near a second cluster, the largest error is in the velocity field $\mathbf{u}_f$ given by (3.23). This equation neglects the effects of the interactions between the particles in the second clusters, and these effects are now important because the particles in the second cluster are close to each other. This error is of $O((\frac{a}{r})^2(\frac{a}{R'})^2)$, where R' is the particle separation in the second cluster. From these error analyses, we will expect the hybrid method to give good estimates of the velocities when the cluster is far

from the other particles, and we will expect this method to perform poorly when a second cluster is nearby. In the next section, where we compare the various methods, this will be shown to be true.

3.3 Comparison with Other Methods

In this section we will test the particle velocities predicted by the hybrid method described in the previous section against that of the FT and the FTS method, the latter two assumed to be nearly exact. (These methods give solutions which are very close to those obtained by Ganatos, Pfeffer and Weinbaum (1978) who used a collocation technique.) Comparisons will also be made with the PAV approximation (3.3) to demonstrate the advantages in using the hybrid method. In this test, six particles are placed in an arbitrary configuration. Their velocities are determined using the three different methods and then compared. We can obtain the three different methods from our computer code by simply adjusting the definition of when particles are considered to be in a cluster. By setting the critical distance to a large value, our computer program will consider all the particles to be in one cluster, and the velocities will be determined using the FT or the FTS method. By setting this distance to one particle radius, the program will estimate the particles' velocities using only the PAV approximation. To determine the particles' velocities that would have been obtained in the actual simulation, this critical distance is set to $4a$, the value used in the simulation.

The results of this test are recorded in tables 3.1 through 3.6. Tables 3.1, 3.2 and 3.3 are for sedimentation in a quiescent suspension, and the remainder are for sedimentation in a sheared suspension. For the first configuration (table 3.1), the velocities calculated using the three methods agree well. This is not suprising since the particles in this configuration are all well spaced. In the second configuration (Table 3.2), the particles are distributed with four particles close together surrounded by two other particles located far away. For this configuration, the hybrid method and the FT method show good agreement in the $\mathbf{e}_1$ direction, but in the $\mathbf{e}_2$, and $\mathbf{e}_3$ directions, while the errors are small compared with the Stokes's ve-

locity, they are large compared with the actual velocity in the appropriate direction. The PAV method overestimates the velocity in the $\mathbf{e}_1$ direction, and the agreements in the other two directions are worse. Finally in the third configuration (table 3.9), the particles are distributed in two clusters of three particles each. The difference between the hybrid method, and the FT method is about 12% in the $\mathbf{e}_1$ direction and substantially worse in the $\mathbf{e}_2$ and $\mathbf{e}_3$ directions. The PAV approximation again gives still poorer agreement.

When shear is introduced, similar results are obtained (tables 3.4 through 3.6). The dimensionless shear rate $\frac{\gamma a}{U_0}$ is 13, a typical maximum value used in the actual simulation. In determining the velocities of the close pairs in this test, the FTS method was used.

These tests indicate that the hybrid method is more accurate in general than the PAV approximation. Furthermore this hybrid method does not require much more computation time than the PAV method. For example, for a volume fraction of 0.01, the computation time increases less than 10%. This is not because there are few clusters (about 30% of the particles are typically found to be in clusters at 1%), but because the clusters tend to be small. This hybrid method thus gives us greater accuracy without extracting a heavy price in computation time.

3.4 Reduction to a N-Body-Problem and Other Details Needed to Construct the Simulator.

In the previous section, we described how the motion of a finite system of particles can be determined. In this section we will describe how we reduce the infinite suspension to a manageable problem involving a finite number of particles. Other details such as the integration method and size of the time step used in the integration will also be given here.

The suspension consists of many particles. However the number of particles (N) that we can use in the simulator is limited because the computation time required grows as N^2. We typically use 27, 64 or 125 particles. One problem that this causes is that the effects of the simulator's box edges are important. Recall that

the simulator consists of a box into which the N particles have been placed. Even with 125 particles, 78% of the particles are within one average particle spacing from the sides of the box. To minimize this problem, the toroidal boundary conditions are used. The main features of this model are depicted in figure 3.2. As the name implies, the opposite faces of the simulation box are connected. In essence the simulation cell finds itself surrounded by its own replicas. When particles leave one face of the box, they are returned to the box at the exact same point but on the opposite face. The periodicity of the torus is not used explicitly in calculating the particle velocities. Instead, in calculating the velocity of any given particle, say B, the effect of each of the other $N-1$ particles is considerred only once. However, if one of the images of particle A is closer to B than is the actual location of A in the simulator box, then A is considered to be at the image location when calculating the velocity of B. The simulation box is not restricted to a cube. In fact, for modeling sheared suspensions, the box is made longer in sheared direction (e2) than in the other two to ensure that when a pair of particles encounter each other a second time, the second encounter is not correlated with their previous meetings. Consider the following situation in a sheared suspension. Two particles, one moving faster in the e_2 direction than the other, meet. The faster-moving particle will leave the slower particle behind, go through the box and eventually overtake the slower particle. This second encounter in principle should represent the interaction between the slower particle with a new particle. Therefore the second encounter should not be correlated with the previous one. At low concentration, particles in a shear flow interact weakly, and encounters between particles remain correlated for a long time. This problem can be aleviated by increasing the concentration or the number of particles used. Either method will increase the likelihood that a particle will interact significantly with several other particles before meeting a particle for the second time. The concentration range is restricted by the method which we use to calculate the particle velocity, and thus we are left with the option of increasing the number of particles. The most efficient way to add particles to the simulator is to add them in the direction of shear, that is make the simulation box longer.

When a shear flow is imposed, we model this by shifting the adjacent box in the e_3 direction by an amount equal to the shear rate multiplied by the elapsed time. Since the adjacent boxes are shifted when shear is introduced, particles leaving the right face of the box are returned at a lower position along the left face of the box.

In applying the toroidal boundary conditions, the simulator is restricted to modeling the bulk of the suspension since the replication of the simulation box is unreasonable if boundaries are nearby.

The exact size of the simulation box needed to eliminate size effect is not known *a priori*. In chapter 2, we have shown that the sedimentation velocity converges with 27 particles. The number of particles needed before the variance converges depends on the homogeneity in the the suspension and it may be as many as $O(10^4)$. We will examine the effects of the box size on the simulation results further in chapter 4.

Besides the toroidal boundary condition, Another method for overcoming the box edge effects is to use true periodic boundary conditions. Lester (1987) made use of the Ewald sum method discussed in chapter 2. Instead of neglecting the contribution of particles outside of the simulation box, the simulation box is literally replicated periodically in all three dimensions in space. The contribution from these additional boxes are calculated using the Ewald sum method. In this method the contribution from all the boxes are divided into two parts; one part is rapidly convergent while the second portion converges slowly. Making use of the periodicity of the system, the slowly convergent portion can be calculated using the Poisson summation formula. This method is more time consuming. If we adopted this method, it would increase our computation time by a factor of 125 depending upon the accuracy desired. We prefer to expend the extra computer time in increasing the number of particles used in our simulation.

The toroidal boundary conditions allow us to simplify the expressions given in section 3.4 for the fluid velocity, velocity gradient, and the particle velocity. In using the toroidal boundary condition, we are in effect drawing an imaginary box inside the suspension centered about a particle. The effects that the particles outside the

simulator have on the particle at the middle of the box are neglected. This model implies that the summation in (3.23) is now over only particles inside the simulation box, and the the integral is over the volume of the simulator. Since the simulator cell has spherical symmetry, many of the integrals appearing in the expression for the fluid velocity, particle velocity and the velocity gradient vanish. After making these simplifications we obtain

$$
\begin{aligned}
u_f(x_0) = \sum_{q=1}^{N}\Bigg[&\Big(\frac{\delta_{i1}}{r} + \frac{r_i r_1}{r^3}\Big) + \frac{a^2}{3}\Big(\frac{\delta_{i1}}{r^3} - \frac{3r_i r_1}{r^5}\Big)\Bigg] \\
&- \frac{3}{4}aU_s \int \Bigg[\Big(\frac{\delta_{i1}}{r} + \frac{r_i r_1}{r^3}\Big)\Bigg] dr \\
&+ \gamma R_3 + \sum_{q=1}^{N} E_{ij} r_j \Bigg[-\delta_{ik}\frac{a^5}{r^5} + \frac{r_i r_k}{r^2}\Big(\frac{-5a^3}{2r^3} + \frac{5a^5}{2r^5}\Big)\Bigg],
\end{aligned}
\tag{3.24}
$$

the velocity gradient is given by

$$
\begin{aligned}
\nabla u_f \sim \Bigg\{ &\sum_{q=1}^{N} \frac{3}{4}aU_s \Bigg[\Big(\frac{\delta_{il} r_1}{r^3} - \frac{3r_i r_l r_1}{r^5}\Big) \\
&+ \frac{a^2}{3}\Big(\frac{-3r_l\delta_{il} + r_1\delta_{il} + r_i\delta_{l1}}{r^5} + \frac{15 r_i r_l r_1}{r^7}\Big)\Bigg] \\
&+ \sum_{q=1}^{N}\Bigg[2E_{23}\Big(\frac{r_i r_2 \delta_{l3} + r_l r_2 \delta_{i3}}{r^2} - \frac{2}{3}\delta_{il}\frac{r_2 r_3}{r^2}\Big)\Big(-\frac{5}{2}\frac{a^3}{r^3} + 5\frac{a^5}{r^5}\Big) \\
&+ 2E_{23}\Big(\frac{r_2 r_3}{r^2}\Big)\Big(\frac{r_i r_3}{r^2} - \frac{\delta_{il}}{3}\Big)\Big(\frac{25a^3}{2r^3} - \frac{35}{2}\frac{a^5}{r^5}\Big)\Bigg] \\
&+ E_{23}\big(\delta_{i2}\delta_{l3} + \delta_{i3}\delta_{l2}\big)\Bigg\} \\
&+ \Bigg\{\frac{3}{4}aU_s\epsilon_{i3l}\sum_{q=1}^{N}\frac{r_l}{r^3} + \epsilon_{ikl}\sum_{q=1}^{N}\Big[E_{23}\Big(\epsilon_{kj3}\frac{r_j r_2}{r^2}\frac{5a^3}{2r^3} + \epsilon_{kj2}\frac{r_j r_3}{r^2}\frac{5a^3}{2r^3}\Big)\Big] \\
&+ \epsilon_{i1l}\Omega_1\Bigg\}.
\end{aligned}
\tag{3.25}
$$

and the particle velocity is

$$U_p = \sum_{q=1}^{N}\left[\frac{3}{4}aU_s\left(\frac{\delta_{i1}}{r}+\frac{r_i r_1}{r^3}\right)+\frac{2}{3}a^2\left(\frac{\delta_{i1}}{r_{ij}}-\frac{3r_i r_1}{r^5}\right)\right] \tag{3.26}$$

$$-\frac{3}{4}aU_s\int\left(\frac{\delta_{i1}}{r}+\frac{r_i r_1}{r^3}\right)dr + U_s c e_1 + \gamma R_3 e_2$$

$$+E_{23}\sum_{q=1}^{N}\left[2a^5\frac{(\delta_{i2}r_3+\delta_{i3}r_2)}{r^5}+\frac{r_i r_2 r_3}{r^2}\left(\frac{-5a^3}{r^3}+\frac{40}{3}\frac{a^5}{r^5}\right)\right].$$

Finally we will nondimensionalize distance with the length of the box and time by τ_l, the time required for a particle to move relative to another particle an average particle separation, $(\frac{4}{3}\pi)^{\frac{1}{3}}ac^{-\frac{1}{3}}$. This time, τ_l, is obtained from considering the following. Suppose all the particles are well separated; then the relative velocity of two particles α and β is given by $\mathbf{R}_{\alpha\beta}\cdot\nabla\mathbf{u}_f$, where $\mathbf{R}_{\alpha\beta}$ is the vector connecting the two particles. If we take $\mathbf{R}_{\alpha\beta}$ to be the average particle spacing and the velocity gradient to be $\frac{3}{4}U_s\frac{a}{((\frac{4}{3}\pi)^{\frac{1}{3}}ac^{-\frac{1}{3}})^2}$, then the characteristic time is $\frac{\frac{4}{3}(\frac{4}{3}\pi)^{\frac{2}{3}}a^2c^{-\frac{2}{3}}}{aU_s}$ or $\frac{4}{3}\frac{L^2}{aU_sN^{\frac{2}{3}}}$. After performing these nondimensionalizations, the fluid velocity is given by

$$N^{\frac{-2}{3}}u_f(x_0) = \sum_{q=1}^{N}\left[\left(\frac{\delta_{i1}}{r}+\frac{r_i r_1}{r^3}\right)+\frac{(\frac{a}{L})^2}{3}\left(\frac{\delta_{i1}}{r^3}-\frac{3r_i r_1}{r^5}\right)\right] \tag{3.27}$$

$$-\int\left[\left(\frac{\delta_{i1}}{r}+\frac{r_i r_1}{r^3}\right)\right]dr$$

$$+\frac{4}{3}\frac{\gamma L}{\frac{a}{L}U_0}+\sum_{q=1}^{N}\frac{4}{3}\frac{L}{\frac{a}{L}U_0}E_{ij}r_j\left[-\delta_{ik}\frac{(\frac{a}{L})^5}{r^5}+\frac{r_i r_k}{r^2}\left(\frac{-5(\frac{a}{L})^3}{2r^3}+\frac{5(\frac{a}{L})^5}{2r^5}\right)\right],$$

the velocity gradient is given by

$$N^{\frac{-2}{3}}\nabla u_f \sim \left\{\sum_{q=1}^{N}\left[\left(\frac{\delta_{il}r_1}{r^3}-\frac{3r_i r_l r_1}{r^5}\right)\right.\right. \tag{3.28}$$

$$\left.\left.+\frac{1}{3}\frac{a^2}{L^2}\left(\frac{-3r_l\delta_{il}+r_1\delta_{il}+r_i\delta_{l1}}{r^5}+\frac{15r_i r_l r_1}{r^7}\right)\right]+\right.$$

$$+\sum_{q=1}^{N}\Bigg[\frac{8}{3}\frac{E_{23}L}{U_0}\Big(\frac{r_ir_2\delta_{l3}+r_lr_2\delta_{i3}}{r^2}-\frac{2}{3}\delta_{il}\frac{r_2r_3}{r^2}\Big)\Big(-\frac{5}{2}\frac{(\frac{a}{L})^3}{r^3}+5\frac{(\frac{a}{L})^5}{r^5}\Big)$$

$$+\frac{8}{3}\frac{E_{23}L}{U_0}\Big(\frac{r_2r_3}{r^2}\Big)\Big(\frac{r_ir_3}{r^2}-\frac{\delta_{il}}{3}\Big)\Big(\frac{25(\frac{a}{L})^3}{2r^3}-\frac{35}{2}\frac{(\frac{a}{L})^5}{r^5}\Big)\Bigg]$$

$$+\frac{4}{3}\frac{E_{23}L}{U_0}\big(\delta_{i2}\delta_{l3}+\delta_{i3}\delta_{l2}\big)\Bigg\}$$

$$+\Bigg\{\epsilon_{i3l}\sum_{q=1}^{N}\frac{r_l}{r^3}+\epsilon_{ikl}\sum_{q=1}^{N}\Big[\frac{4}{3}\frac{E_{23}L}{U_0}\Big(\epsilon_{kj3}\frac{r_jr_2}{r^2}\frac{5(\frac{a}{L})^3}{2r^3}+\epsilon_{kj2}\frac{r_jr_3}{r^2}\frac{5(\frac{a}{L})^3}{2r^3}\Big)\Big]$$

$$+\frac{4}{3}\frac{L}{U_0}\epsilon_{il1}\Omega_1\Bigg\}.$$

and the particle velocity is

$$N^{2/3}U_p=\sum_{q=1}^{N}\Bigg[\Big(\frac{\delta_{i1}}{r}+\frac{r_ir_1}{r^3}\Big)+\frac{2}{3}\frac{a^2}{L^2}\Big(\frac{\delta_{i1}}{r_{ij}}-\frac{3r_ir_1}{r^5}\Big)\Bigg] \tag{3.29}$$

$$-\int\Big(\frac{\delta_{i1}}{r}+\frac{r_ir_1}{r^3}\Big)dr+\frac{4}{3}\frac{L}{a}ce_1+\frac{4}{3}\frac{\gamma L}{\frac{a}{L}U_0}r_3e_2$$

$$+\frac{4}{3}\frac{E_{23}L}{\frac{a}{L}U_0}\sum_{q=1}^{N}\Bigg[\frac{8}{3}\frac{a^5}{L^5}\frac{\big(\delta_{i2}r_3+\delta_{i3}r_2\big)}{r^5}+\frac{r_ir_2r_3}{r^2}\Big(\frac{-5a^3}{L^3}\frac{1}{r^3}+\frac{40}{3}\frac{a^5}{L^5}\frac{1}{r^5}\Big)\Bigg].$$

The treatment of the cluster of particles using the hybrid method is unchanged except that the velocities and velocity gradient needed are given by (3.27) and (3.28) instead.

The characteristic time $\frac{4}{3}\frac{L^2}{aU_sN^{\frac{2}{3}}}$ is appropriate when sedimentation is dominant, but when the suspension is sheared vigorously, we choose $\frac{2}{\gamma}$ (denoted by τ_h) as the characteristic time. Scaling time this way leads to

$$u_{if}(x_0)=\frac{3}{2}\frac{U_s}{\gamma L}\frac{a}{L}e_1\sum_{q=1}^{N}\Bigg[\Big(\frac{\delta_{i1}}{r}+\frac{r_ir_1}{r^3}\Big)+\frac{(\frac{a}{L})^2}{3}\Big(\frac{\delta_{i1}}{r^3}-\frac{3r_ir_1}{r^5}\Big)\Bigg] \tag{3.30}$$

$$-\frac{3}{2}\frac{U_s}{\gamma L}\frac{a}{L}e_1\int\Bigg[\Big(\frac{\delta_{i1}}{r}+\frac{r_ir_1}{r^3}\Big)\Bigg]dr$$

$$+2R_3e_2+\frac{a^5}{L^5}\sum_{q=1}^{N}E_{ij}r_j\Bigg[-\frac{\delta_{ik}}{r^5}+\frac{r_ir_k}{r^2}\Big(\frac{-5(\frac{L}{a})^2}{2r^3}+\frac{5}{2r^5}\Big)\Bigg]$$

for the velocity

$$\nabla u_f \sim \Bigg\{ \frac{3}{2}\frac{U_s}{\gamma L}\frac{a}{L}\sum_{q=1}^{N}\Bigg[\Big(\frac{\delta_{il}r_1}{r^3}-\frac{3r_ir_lr_1}{r^5}\Big) + \frac{1}{3}\frac{a^2}{L^2}\Big(\frac{-3r_l\delta_{il}+r_1\delta_{il}+r_i\delta_{l1}}{r^5}+\frac{15r_ir_lr_1}{r^7}\Big)\Bigg] + 2\Big(\frac{a}{L}\Big)^5\sum_{q=1}^{N}\Bigg[\Big(\frac{r_ir_2\delta_{l3}+r_lr_2\delta_{i3}}{r^2}-\frac{2}{3}\delta_{il}\frac{r_2r_3}{r^2}\Big)\Big(-\frac{5}{2}\frac{(\frac{L}{a})^2}{r^3}+\frac{5}{r^5}\Big) + \Big(\frac{r_2r_3}{r^2}\Big)\Big(\frac{r_ir_3}{r^2}-\frac{\delta_{il}}{3}\Big)\Big(\frac{25(\frac{L}{a})^2}{2r^3}-\frac{35}{2}\frac{1}{r^5}\Big)\Bigg] + \big(\delta_{i2}\delta_{l3}+\delta_{i3}\delta_{l2}\big)\Bigg\} + \Bigg\{\epsilon_{i3l}\frac{3}{2}\frac{U_s}{\gamma L}\frac{a}{L}\sum_{q=1}^{N}\frac{r_l}{r^3}+\epsilon_{ikl}\Big(\frac{a}{L}\Big)^3\sum_{q=1}^{N}\Bigg[\Big(\epsilon_{kj3}\frac{r_jr_2}{r^2}\frac{5(\frac{L}{a})^2}{2r^3}+\epsilon_{kj2}\frac{r_jr_3}{r^2}\frac{5}{2r^3}\Big)\Bigg] + \epsilon_{i1l}\Omega_1\Bigg\} \tag{3.31}$$

for the velocity gradient, and

$$U_p = \frac{3}{2}\frac{U_s}{\gamma L}U_se_1\sum_{q=1}^{N}\Bigg[\Big(\frac{\delta_{i1}}{r}+\frac{r_ir_1}{r^3}\Big)+\frac{2}{3}\frac{a^2}{L^2}\Big(\frac{\delta_{i1}}{r_{ij}}-\frac{3r_ir_1}{r^5}\Big)\Bigg] - \frac{3}{2}\frac{U_s}{\gamma L}U_se_1\int\Big(\frac{\delta_{i1}}{r}+\frac{r_ir_1}{r^3}\Big)dr+\frac{2U_s}{\gamma L}ce_1+2R_3e_2 - \Big(\frac{a}{L}\Big)^5\sum_{q=1}^{N}\Bigg[\frac{8}{3}\frac{(\delta_{i2}r_3+\delta_{i3}r_2)}{r^5}-\frac{r_ir_2r_3}{r^2}\Big(\frac{-5L^2}{a^2}\frac{1}{r^3}+\frac{40}{3}\frac{1}{r^5}\Big)\Bigg] \tag{3.32}$$

for the particle velocity.

The toroidal boundary conditions allow us to model the unbounded homogeneous supension by a rectangular cell containing N particles. Using the methods described in section 3.1 and equations (3.22) through (3.32), the velocities of these N particles can be determined. These velocities must now be integrated to determine the new positions of the particles. The two integration methods we have used

are the first-order Euler method, and a fourth order predictor-corrector scheme, with Adam-Bashforth as the predictor, and Adam-Moulton as the corrector. The reason for using two integrators is to guard against the possibility that the results obtained are due to the numerical technique rather than the physics of the problem.

With the integrator chosen, we must next choose the step size. The step size must be sufficiently small so that all the important details can be captured. Lynch (1985) identified three important time scales associated with the sedimentation problem. They are the time needed for well spaced particles to move relative to each other a distance $(\frac{4}{3}\pi)^{\frac{1}{3}}ac^{-\frac{1}{3}}$ (i.e., τ_l), the time for a cluster of two particles to move a distance comparable to their separation in the straining flow cause by the other particles (also equal to τ_l), and the time for a pair of particles to settle relative to the other particles a distance $(\frac{4}{3}\pi)^{\frac{1}{3}}ac^{-\frac{1}{3}}$. For the latter, the velocity of a pair of particles is approximately twice U_s, and therefore this time is $\frac{(\frac{4}{3}\pi)^{\frac{1}{3}}ac^{-\frac{1}{3}}}{U_s}$. It is the smallest of the three time scales. We typically use time steps which are $\frac{1}{40}$ of this time scale when sedimentation is the dominant motion. When shear is imposed on the suspension the time it takes for the shear flow to separate two close particles is also important. The smallest is the time required by the shear flow to move a pair of nearly touching spheres relative to each other a distance comparable to their gap width. The velocity along the line connecting the centers of the particles is approximately given by $4.0\frac{\delta}{a}\mathbf{E}a$, where δ is the gap width between the two particles (Batchelor and Green (1972)). The time it takes to move along the line of center a distance δ is therefore given by,

$$\tau_1 = \frac{1}{4.0E_{23}}. \tag{3.33}$$

The velocity perpendicular to the line of center is given by $(1.6 - \frac{.78}{log(\delta)})E_{23}a$. The time it takes to move a distance l is,

$$\tau_2 = \frac{\frac{l}{a}}{1.6E_{23}}. \tag{3.34}$$

We choose l to be a and therefore τ_2 is $\frac{1}{1.6E}$. We typically use a step size that is $\frac{1}{5}$ of τ_1.

Finally we will mention two *ad hoc* procedures which we have found convenient. Due to the inaccuracy in the velocities and the integration routine, the particles sometimes overlap. When this occurs, we pull them apart along their line of center by a small amount. The second *ad hoc* procedure involves inversion of the resistance matrix. When particles in a large cluster are all nearly touching each other, the resistance matrix, though it remains positive definite, can become ill-conditioned and the inversion routine we use does not permit the inversion of such a matrix. To avoid this problem, we do not allow particles to come within $(2+\epsilon)a$ of each other. When ϵ is chosen to be 10^{-6} we have experienced no problems with the matrix becoming ill-conditioned.

3.5 Statistics

The results of a simulation run is summarized using eight statistics. They are the average particle velocity, the variance of the particle velocity, the particle diffusion coefficient, the particle radial and angular distribution functions, the particle-correlation time, and the velocity and variance autocorrelation times.

The average particle velocity is obtained by first number-averaging the particles' velocity at an instant in time and then time-averaging these means. We employ both averages because the number of particles used in our simulator is small, and significant fluctuations in this statistic will occur if we do not also perform the time average. We report the sedimentation velocity in terms of the deviation from Stokes's velocity, $\frac{U_s - <U_p>}{U_s}$.

The variance of the particle velocity is given by

$$V = \left\langle \frac{\sum_{i=1}^{N} (U_{pi} - \overline{U}_p^2)^2}{N} \right\rangle_T , \tag{3.35}$$

Again time-averaging is employed to smooth the fluctuation in this statistic. The variance is given in units of U_s^2 for the quiescent suspension, and both U_s^2 and $(Ea)^2$ for the sheared suspension, the latter being more appropriate at high shear rates. In chapter 2 we have shown that the variance is small for suspensions whose

instantaneous distributions are homogeneous. This statistic therefore can be used to measure the degree of homogeneity of the suspension in the simulator.

The diffusion coefficient is given by

$$\mathcal{D}_i(t) = \lim_{t \to \infty} \frac{1}{t}\left[\frac{\sum_{i=1}^{N}\left(x_i^k(t) - \overline{x}_i^k(t)\right)^2}{N}\right], \tag{3.36}$$

where $x_i^k(t)$ is the distance particle k would have travel in the i^{th} direction, $\overline{x}_i^k(t)$ is the distance travelled by particle k in the i^{th} direction if this particle had moved with the average particle velocity (instantaneous number average), and t is the elapsed time. Subtracting $\overline{x}_i^k(t)$ from $x_i^k(t)$ removes the displacement due to the convective motion of the particles. In practice we cannot perform the simulation for a very long time. Instead we perform the simulation sufficiently long so that $\mathcal{D}_i$ reaches a constant value. This usually occurs within 100 τ_l for quiescent sedimenting suspension, and 1000 τ_h for the sheared sedimenting suspension.

Since we are using a small number of particles, and a short t, the values of the diffusion coefficients vary between runs with different initial positions. To overcome this problem, we can make many runs with different initial positions and average the resulting diffusion coefficients. Alternatively, we can from a single run extract multiple sets of diffusion coefficients. At time zero we begin to follow the time evolution of one set of $\mathcal{D}_{ij}(t)$. At some later time we treat this new time as time zero and begin a second set of $\mathcal{D}_{ij}(t)$. This process is repeated many times over the course of a single simulation run. If the period between starting a new set of $\mathcal{D}_{ij}(t)$ (τ) is sufficiently long so that the initial particle positions for each set of $\mathcal{D}_{ij}(t)$ are different, then effectively we have $\mathcal{D}_{ij}(t)$ for many runs with different initial conditions. We applied both methods. The diffusion coefficients are given in units of $U_s a$.

The diffusion coefficient can also be determined from

$$D_l = \frac{1}{N}\sum_{i}^{N}\int (U_l^i(t+\tau) - < U_l >)(U_l^i(t) - < U_l >)d\tau, \tag{3.37}$$

where U_l^i is the velocity of particle i in the l^{th} direction, and $< U_l >$ is the average particle velocity. If the velocity becomes uncorrelated after a time τ_0, this expression can be rewritten as,

$$D_l \sim \tau_0 \frac{1}{N} \sum_i^N (U_l^i(t) - < U_l >)^2, \tag{3.38}$$

where τ_0 is the correlation time, and the sum is the velocity variance. Equation (3.38) relates the diffusion coefficient with the correlation time and the velocity variance, two quantities which we can measure independently. Thus we have an independent check on the diffusion coefficient.

The radial distribution function is found by dividing the space about each particle into concentric spherical shells. The number of particles in each shell is determined and is then normalized by the number of particles that would have been there if the suspension was uniform. After averaging over all the particles and time averaging these means, the radial distribution is obtained. We typically use shells which are 0.1 particle radius thick.

The phi and theta angular distributions are found by taking the set of shells used in determining the radial distribution and further subdividing them in the ϕ and θ directions to form smaller volumes bounded by constant ϕ, θ, and r surfaces. Counting all the particles in the volumes with the same value of θ and r, and normalizing with the number of particles that would have been there if the suspension was uniform, gives the theta distribution at a fixed r. Similarly counting all the particles in the volumes with the same values of ϕ and r, and normalizing gives the phi distribution at a fixed r. The reason for determining phi and theta distributions at a fixed r is that if any angular dependence develops, it is expected to appear at small values of r. If these phi and theta distributions are averaged over all r, the uniformity of the suspension at large r will mask out any angular dependence that may exist in the inner shells. In the simulator, we divide the θ and ϕ directions into ten slices. The coordinate system is shown in figure 3.3.

The particle correlation time measures the average time a pair of particles remains together. Suppose there are $A_i(t)$ particles at a distance between r and

$r + dr$ from particle i at time t. To determine the correlation time, we first obtain the autocorrelation function for $A_i(t)$ using,

$$A_i(\tau) = \frac{\int (A_i(t) - < A >)(A_i(t+\tau) - < A >)dt}{\int (A_i(t) - < A >)^2 dt}, \tag{3.39}$$

where $< A >$ is the average number of particles (averaged over the entire simulation) in the shell. Since there are only a small number of particles used in the simulator, $A_i(\tau)$ differs from particle to particle. To obtain a better estimate of the true autocorrelation function, one can determine $A_i(\tau)$ for each of the particles and then average them. This is the correct procedure for determining the average autocorrelation function, and it will be denoted by the subscript *pd*. However, because each $A_i(t)$ requires a substantial amount of memory, we determine the autocorrelation function for three particles only. Three particles may not be enough to determine the average autocorrelation function. Another approach is to average $A_i(t)$ over all the particles first and then determine the autocorrelation function of the average $A_i(t)$. This procedure will be denoted by the subscript $< pd >$. After the autocorrelation function is obtained, the correlation time is determined by finding the time at which the correlation function becomes zero (denoted by the superscript z). Sometimes the correlation curve never falls to zero or the slope of the curve decreases abruptly before the function becomes zero. To accommodate these cases, we obtain another estimate of the correlation time by drawing a tangent to the initial portion of the curve and determining the time at which this tangent reaches the value of zero correlation. This method will be denoted by the superscript i. For each simulation we extract a total of four correlation times, τ^i_{pd}, τ^z_{pd}, $\tau^i_{<pd>}$, and $\tau^z_{<pd>}$.

The autocorrelation functions $A(\tau)_{pd}$ and $A(\tau)_{<pd>}$ are not necessarily the same. The former is defined as

$$A(\tau)_{pd} = \frac{\sum_i \int (A_i(t) - < A >)(A_i(t+\tau) - < A >)dt}{\sum_i \int (A_i(t) - < A >)^2 dt}, \tag{3.40}$$

while the latter is defined by

$$A(\tau)_{<pd>} = \frac{\int (\frac{1}{N}\sum_i A_i(t) - < A >)(\frac{1}{N}\sum_i A_i(t+\tau) - < A >)dt}{\sum_i \int (\frac{1}{N}\sum_i A_i(t) - < A >)^2 dt}. \tag{3.41}$$

The difference is given by

$$A(\tau)_{pd} - A(\tau)_{<pd>} = \tag{3.42a}$$
$$\frac{(1-\lambda_1)}{\lambda_2}\sum_i \int (A_i(t) - < A >)(A_i(t+\tau) - < A >)dt$$
$$- \frac{\lambda_1}{\lambda_2 N^2}\sum_i \sum_{\substack{j \\ j\neq i}} \int (A_i(t) - < A >)(A_j(t+\tau) - < A >)dt,$$

where,

$$\lambda_1 = \frac{\sum_i \int (A_i(t) - < A >)^2 dt}{\int (\frac{1}{N}\sum_i A_i(t) - < A >)^2 dt}, \tag{3.42b}$$

$$\lambda_2 = \sum_i \int (A_i(t) - < A >)^2 dt. \tag{3.39c}$$

The difference is in the cross term (the second integral in (3.42a)). If the cross term has the same correlation time as the autocorrelation function (the first integral in (3.42a)) or if $A_i(t)$ and $A_j(t)$ are not correlated, then $A(\tau)_{<pd>}$ will have the same correlation time as $A(\tau)_{pd}$. We shall see from the simulations that in fact these correlation times are the same.

In determining the correlation time we need to choose the shell with which to determine $A_i(t)$ since the correlation time will depend on the particlular choice. Since we wish this correlation time to be related to the time particles in a cluster remain together, we should choose a shell which is less than the average particle spacing ($ac^{-\frac{1}{3}}$). We have chosen a shell between $2a$ and $3a$.

The velocity and variance correlation times are obtained by taking the auto-correlations of the average velocity and the average variance,

$$U(\tau)_{<pd>} = \frac{\int (\frac{1}{N}\sum_i U_i(t) - < U >)(\frac{1}{N}\sum_i U_i(t+\tau) - < U >)dt}{\sum_i \int (\frac{1}{N}\sum_i U_i(t) - < U >)^2 dt}, \tag{3.43}$$

$$V(\tau)_{<pd>} = \frac{\int (\frac{1}{N}\sum_i V_i(t) - < V >)(\frac{1}{N}\sum_i V_i(t+\tau) - < V >)dt}{\sum_i \int (\frac{1}{N}\sum_i V_i(t) - < V >)^2 dt}, \tag{3.44}$$

where $< U >$ and $< V >$ are the velocity and variance averaged over all time. For each $U(\tau)$ and $V(\tau)$ we again obtain two estimates of the correlation time. These

correlation times are useful information because they represent the minimum time it takes for the memory of the initial conditions to be forgotten. The simulation should be performed longer than these times.

Method 1 FT Method
Method 2 Hybrid Method
Method 3 PAV

particle #	coordinate
1	(0,0,0)
2	(4.0,0,0)
3	(0,4.0,0)
4	(0,0,4.0)
5	(4.0,0,4.0)
6	(4.0,4.0,4.0)

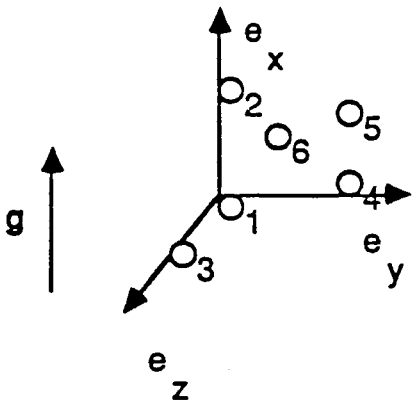

$\frac{\gamma a}{u_s} = 0.0$

X Velocity Us

Particle # / Method	1	2	3	4	5	6
1	2.08	2.06	1.86	2.06	2.08	1.86
2	2.09	2.08	1.87	2.08	2.09	1.87
3	2.09	2.08	1.87	2.08	2.09	1.87

Y Velocity Us

Particle # / Method	1	2	3	4	5	6
1	.033	-.062	-.094	.062	-.033	.094
2	.034	-.062	-.097	.062	-.034	.097
3	.034	-.062	-.097	.062	-.034	.097

Z Velocity Us

Particle # / Method	1	2	3	4	5	6
1	.094	-.060	.096	-.060	.094	.096
2	.097	-.062	.097	-.062	.097	.097
3	.097	-.062	.097	-.062	.097	.097

Table 3.1 Comparison between the three different methods (1). All the particles are well spaced. No shear flow is imposed.

Method 1 FT Method
Method 2 Hybrid Method
Method 3 PAV

particle #	coordinate
1	(0,0,0)
2	(2.01,0,0)
3	(0,2.01,0)
4	(0,0,2.01)
5	(4.02,4.02,0)
6	(4.02,0,4.02)

$\frac{\gamma a}{Us} = 0.0$

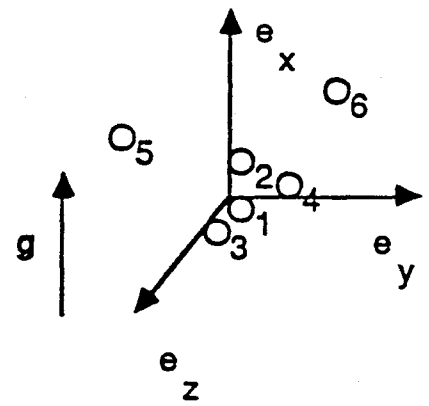

X Velocity Us

Particle #	1	2	3	4	5	6
Method						
1	2.56	2.55	2.40	2.40	1.93	1.98
2	2.59	2.59	2.42	2.42	2.00	2.00
3	2.88	2.58	2.58	2.58	2.00	2.00

Y Velocity Us

Particle #	1	2	3	4	5	6
Method						
1	.026	-.010	.018	.053	0.22	-.018
2	.026	-.017	.022	.052	0.23	-.026
3	.062	-.039	-.065	.052	0.23	-.026

Z Velocity Us

Particle #	1	2	3	4	5	6
Method						
1	.026	-.010	.053	.018	-.018	0.22
2	.026	-.017	.052	.022	-.026	0.23
3	.062	-.039	.052	-.065	-.026	0.23

Table 3.2 Comparison between the three different methods (2). Four particles are in a cluster surrounded by two other particles far away. No shear flow is imposed.

Method 1 FT Method
Method 2 Hybrid Method
Method 3 PAV

particle #	coordinate
1	(0,0,0)
2	(1.01,1.74,0)
3	(2.02,0,0)
4	(6.01,0,0)
5	(7.02,0,1.74)
6	(8.03,0,0)

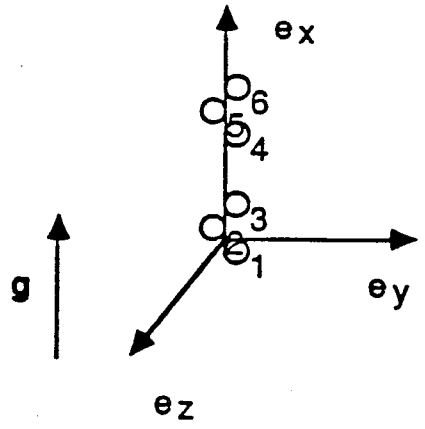

$\frac{\gamma a}{u_s} = 0.0$

X Velocity Us

Particle # / Method	1	2	3	4	5	6
1	2.43	2.40	2.45	2.45	2.40	2.43
2	2.61	2.54	2.59	2.59	2.54	2.61
3	2.73	2.64	2.97	2.97	2.64	2.73

Y Velocity Us

Particle # 1 / Method		2	3	4	5	6
1	-.022	-.014	.007	-.025	-.020	-.021
2	-.034	-.010	-.005	-.035	-.029	-.028
3	.082	-.090	-.008	-.040	-.027	-.023

Z Velocity Us

Particle # / Method	1	2	3	4	5	6
1	.020	.021	.025	-.007	.014	.022
2	.028	.029	.035	.005	.010	.034
3	.023	.027	.041	.082	.090	-.082

Table 3.3 Comparison between the three different methods (3). The six particles are divided into two groups of three particles. No shear flow is imposed.

Method 1 FTS Method
Method 2 Hybrid Method
Method 3 PAV

particle #	coordinate
1	(0,0,0)
2	(4.0,0,0)
3	(0,4.0,0)
4	(0,0,4.0)
5	(4.0,0,4.0)
6	(4.0,4.0,4.0)

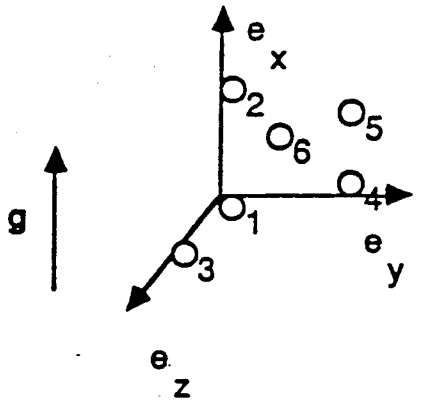

$\frac{\gamma a}{u_s} = 13.6$

X Velocity Us

Particle # / Method	1	2	3	4	5	6
1	2.18	2.06	1.74	2.06	2.18	1.74
2	2.22	2.09	1.74	2.09	2.22	1.75
3	2.22	2.09	1.74	2.09	2.22	1.74

Y Velocity Us

Particle # / Method	1	2	3	4	5	6
1	0.24	0.37	0.40	53.0	53.1	52.9
2	0.25	0.37	0.40	53.0	53.1	52.9
3	0.25	0.37	0.40	53.0	53.1	52.9

Z Velocity Us

Particle # / Method	1	2	3	4	5	6
1	0.28	0.31	-0.46	0.31	0.28	-0.46
2	0.30	0.30	-0.47	0.30	0.30	-0.47
3	0.30	0.30	-0.47	0.30	0.30	-0.47

Table 3.4 Comparison between the three different methods (4). All the particles are well spaced. The dimensionless shear rate is 13.

Method 1 FTS Method
Method 2 Hybrid Method
Method 3 PAV

particle #	coordinate
1	(0,0,0)
2	(2.01,0,0)
3	(0,2.01,0)
4	(0,0,2.01)
5	(4.02,4.02,0)
6	(4.02,0,4.02)

$\frac{\gamma a}{u_s} = 13.36$

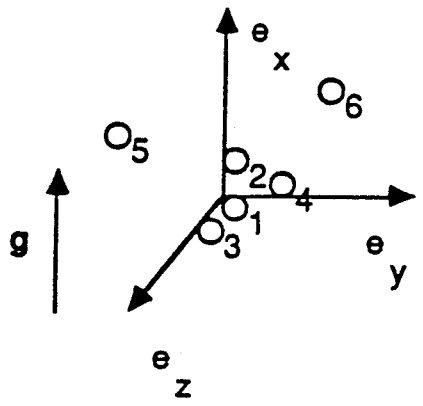

X Velocity Us

Particle # / Method	1	2	3	4	5	6
1	2.54	2.53	2.37	2.37	2.07	2.07
2	2.55	2.55	2.37	2.37	2.13	2.13
3	2.88	2.80	2.45	2.45	2.13	2.13

Y Velocity Us

Particle # / Method	1	2	3	4	5	6
1	1.73	0.50	1.72	23.5	0.69	53.2
2	1.72	0.50	1.78	23.5	0.71	53.2
3	1.16	0.19	1.18	24.3	0.71	53.2

Z Velocity Us

Particle # / Method	1	2	3	4	5	6
1	1.73	0.50	-3.35	1.72	-0.52	0.69
2	1.72	0.50	-3.39	1.78	-0.52	0.71
3	1.16	0.19	-2.52	1.18	-0.52	0.71

Table 3.5 Comparison between the three different methods (5). Four particles are in a cluster surrounded by two other particles far away. The dimensionless shear rate is 13.

Method 1 FTS Method
Method 2 Hybrid Method
Method 3 PAV

particle #	coordinate
1	(0,0,0)
2	(1.01,1.74,0)
3	(2.02,0,0)
4	(6.01,0,0)
5	(7.02,0,1.74)
6	(8.03,0,0)

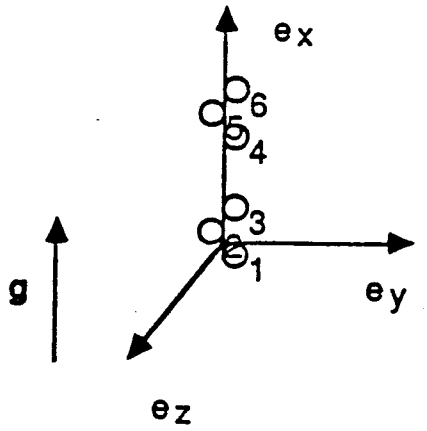

$\frac{\gamma a}{u_s} = 13.36$

X Velocity Us

Particle # / Method	1	2	3	4	5	6
1	2.56	2.45	2.58	2.59	2.56	2.57
2	2.65	2.53	2.64	2.64	2.63	2.65
3	2.73	2.59	2.97	2.97	2.68	2.73

Y Velocity Us

Particle # / Method	1	2	3	4	5	6
1	-.033	.001	.047	1.21	20.7	1.22
2	-.038	.008	.010	1.21	20.7	1.22
3	.083	-.074	-.074	0.90	21.3	0.92

Z Velocity Us

Particle # / Method	1	2	3	4	5	6
1	1.27	-2.47	1.27	.028	.037	.036
2	1.27	-2.47	1.28	.005	.026	.041
3	0.96	-1.88	0.98	.089	.108	-.080

Table 3.6 Comparison between the three different methods (6). The six particles are divided into two groups of three particles. The dimensionless shear rate is 13.

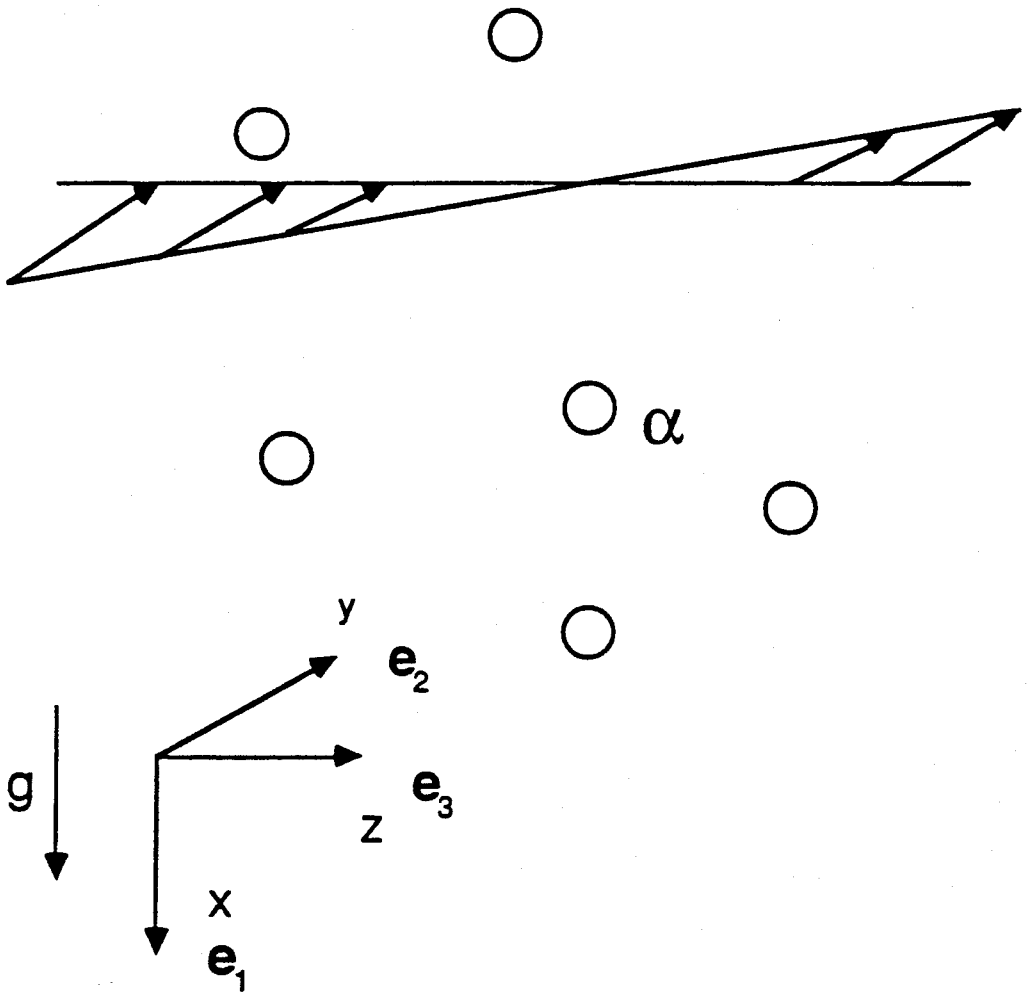

Figure 3.1 Problem description.

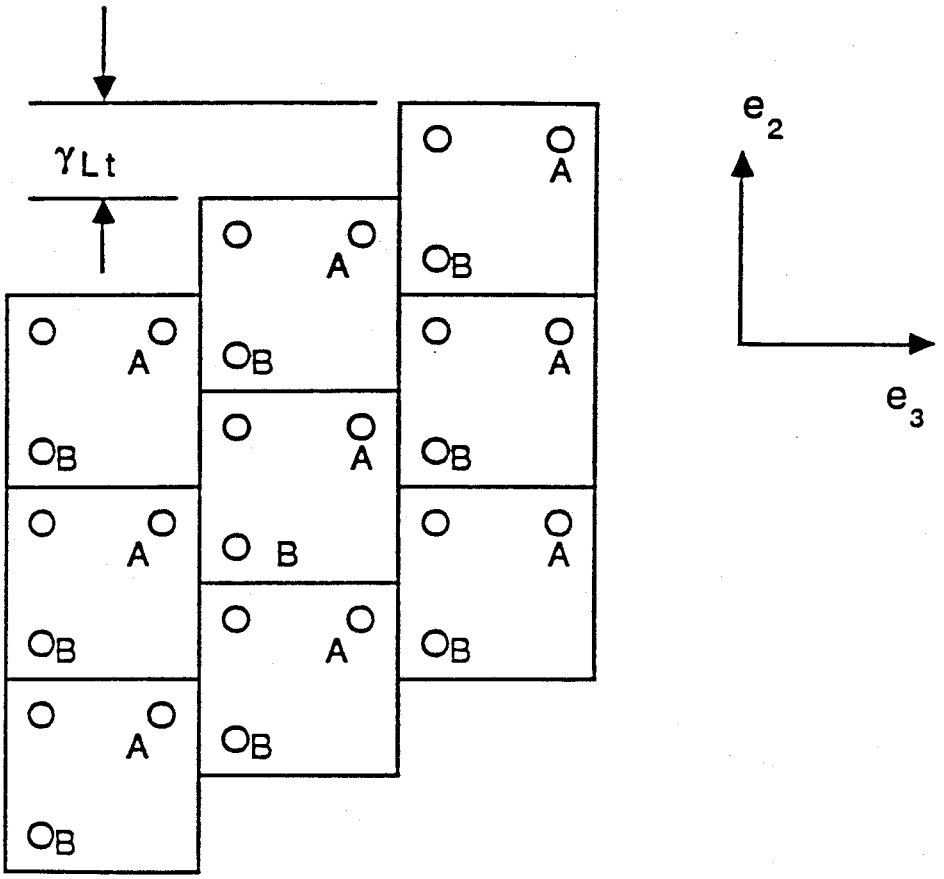

Figure 3.2 Toroidal boundary conditions. γ is the shear rate, t is the elapsed time, and the velocity field is $v = \gamma z e_2$.

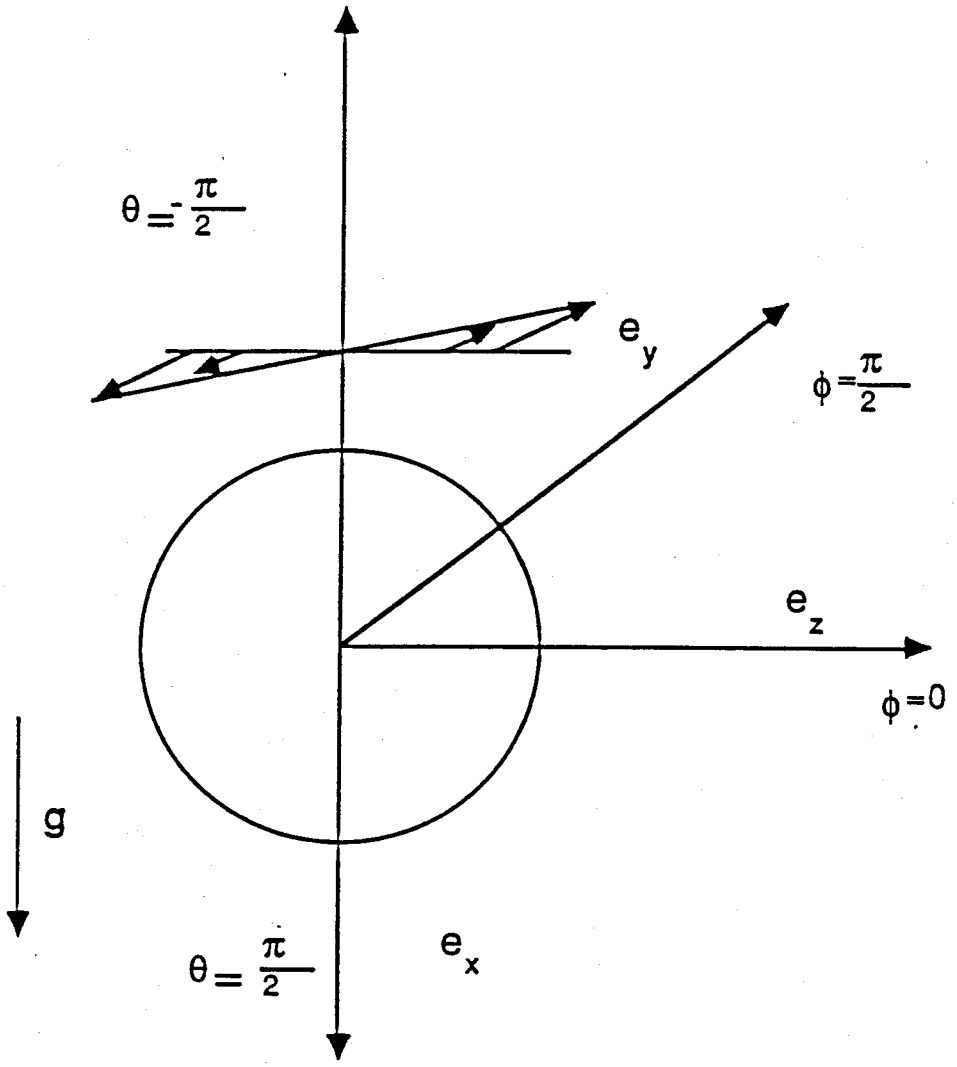

Figure 3.3 Coordinate system for determining the angular distributions.

4 Results and Discussion

4.1 Introduction

The simulator described in the previous chapter has been used to investigate the effects of concentration and shear rate on the settling behavior of particles in a suspension. We have modelled suspensions in which the volume fraction of particles ranged from 0.0025 to 0.05 and for imposed dimensionless shear rate (defined as $\frac{\gamma a}{U_s}$) ranging from 0 to 20.0. Of course, before the simulations could be performed, an integration method, an integration step size, the number of particles to be used in the simulator, and the method of determining the particles' velocities had to be chosen. We shall begin by investigating how different choices of these parameters affect the suspension statistics, and then present the results for the full range of concentrations and shear rates.

4.2 Effects of Integration Methods and Simulation Parameters on the Suspension Statistics

We start by comparing the results obtained using the Euler integration method and the fourth order predictor-corrector integration routine with Adam-Bashforth as the predictor and Adam-Moulton as the corrector for a broad range of integration step sizes. Although the predictor-corrector takes twice as much computer time for a given time step, one would normally expect that the much greater accuracy and stability of this method would allow a significantly larger time step and hence an improvement in efficiency. It is not clear whether this savings can be realized in the present problem however, since the method of calculating the particle velocities introduces artificial jumps when clusters of particles are formed. Hence, one might expect that even with a high order integration method, a very small time step might be needed in order to prevent particles from coming artificially close to each other. Furthermore, this effect should be more important at higher concentrations.

The results for a quiescent suspension with volume fraction of solids of 0.01 are given in tables 4.1a and 4.1b for the Euler and predictor-corrector methods, respectively. The time step is made dimensionless with τ_l, and all runs had the

same initial particle positions. With the Euler method the sedimentation velocity, variance and the diffusion coefficient all increase with increasing step size, with a dramatic change between step sizes of 0.01 and 0.1. The deviation from Stokes's velocity changes from 0.058 to -0.095, while the variance and the diffusion coefficient double. The corresponding radial distributions (shown in figure 4.1) show little change except for the largest time step for which the excess of particles extending to $r = 8a$. It thus appears that increasing the step size causes particles to form large clusters. The corresponding results for the predictor-corrector method (table 4.1b and figure 4.2) show no change except at the largest time step and agree with the small time step Euler results. We repeated these tests using a suspension with $c = 0.03$. The same general trend is again observed (table 4.2a, figure 4.3) with significant changes in the statistics occurring between the step sizes of 0.02 and 0.1. At the higher concentration, however replacing the Euler integration scheme with the predictor-corrector method does not give any improvement for larger time steps (cf. table 4.2b and figure 4.4). For both 1% and 3% suspension, significant clustering occurs only at a step size between 0.01 and 0.1. The predictor-corrector performs better than the Euler scheme at 1%, but at 3%, the Euler method is better in determining the diffusion coefficient and the variance. From this series of tests, we have decided to perform most of the simulations of the quiescent sedimenting suspension using the Euler method with a step size of 0.005 τ_l.

A similar set of tests has been performed on a suspension with an imposed dimensionless shear rate of 20. The step size for these runs was made dimensionless with τ_h. The results in table 4.3 show no discernible step size effect for either integration method. No diffusion coefficient was obtained because the simulations were not carried out long enough (the final time equals 500 τ_h) for the traces of $\mathcal{D}(t)$ to asymptote to a constant. With the Euler method, however, the radial distribution function (cf. figure 4.5) has a narrow peak at a radius near $2a$ with the smallest time step, but a slight deficit near $2a$ for all larger step sizes. On the other hand, as shown in figure 4.8 the radial distributions of the predictor-corrector method retained a narrow peak near $2a$ for all time steps. This peak may not

be significant since neither the sedimentation velocity nor the variance differ much from the results using the Euler integration method where this peak is absent (table 4.3b). We also examined the influence of step size and integration scheme on the suspension statistics at a dimensionless shear rate of 0.5. The radial distributions showed a broader peak near the radius of $2a$ (figures 4.9 and 4.10) which did not change significantly with either step size or the integration method. Varying the step sizes between 0.02 to 0.1 made only a slight difference (table 4.4a) in the other statistics as well. From these tests we have chosen to use an Euler integration method with a step size of 0.05 τ_h in simulating sheared sedimenting suspensions.

We next examine whether changing N, the number of particles used in the simulation will influences the statistics. Using the Euler integration method and a step size of 0.005, a series of simulations of a quiescent sedimenting suspension were performed with 27, 64, and 125 particles, and at volume fractions of 0.005, 0.01, and 0.02. (We will refer to this set of simulations as set A). Figure 4.11 shows the sedimentation velocity as a function of N. Despite increasing N by a factor of five, no noticeable difference is observed. The sedimentation velocity of a sheared suspension is also independent of N. Using 135 particles or 192 particles makes no difference (cf., table 4.7, runs s3 through s11, and s20).

From the discussions in chapter 2, we expect that for the quiescent sedimenting suspension, the variance of the particle velocity depends on N since it is a nonconvergent quantity for a random suspension. The dependence on N of the x variance for a quiescent suspension is shown in figure 4.12. A least squares fit shows that the variance grows approximately as $N^{\frac{1}{2}}$. For the sheared suspensions, if the shear rate is sufficiently large, the variance in the x and z directions should be independent of N. This is because the dominant portion of the variance will be due to the shear flow and we have seen in chapter two that this contribution is convergent since the disturbance velocity field of a particle in a shear flow decays as $O((\frac{1}{r})^2)$ for large r. An examination of the variances of the particle velocity for runs s3 through s11, and s20 shown in table 4.11 reveals that when expressed in units of $(Ea)^2$, the variances in the z direction are independent of N, but the variances in the x direction are

not. This is because even at a dimensionless shear rate of 13, the variance due to the difference in the sedimentation velocity among the particles is still large. To obtain an estimate of the relative size of the contributions to the variance from the sedimentation and the shear portions of the problem, the following Monte-Carlo simulations were performed. N particles were randomly placed into a box which is three times longer in the y direction than in the other two (the same box which we use to perform our molecular-dynamics-type simulations). The only restriction on the placement of these particles was that no particle may come within $2a$ of the center of the box. Using (3.29) and keeping only the leading order terms (stokeslet and stresslet), we determined the velocity that a particle would have if it is located at the center of the box. The first two terms in (3.29) represent the contributions to the velocity from the sedimentation portion of the problem (which will be denoted by $\mathcal{U}_{sed}$), and the remaining terms are the contributions to the velocity from the shear portion of the problem (denoted by $\mathcal{U}_{shear}$). After generating many configurations by repeatedly placing N particles into the box, the variances were determined. From these Monte-Carlo simulations, we extracted three velocity variances,

$$V_{\text{sed}} = \frac{\sum_i (\mathcal{U}^i_{\text{sed}} - < \mathcal{U}_{\text{sed}} >)^2}{N}, \tag{4.1}$$

$$V_{\text{shear}} = \frac{\sum_i (\mathcal{U}^i_{\text{shear}} - < \mathcal{U}_{\text{shear}} >)^2}{N}, \tag{4.2}$$

and

$$V_{\text{total}} = \frac{\sum_i (\mathcal{U}^i_{\text{total}} - < \mathcal{U}_{\text{total}} >)^2}{N}, \tag{4.3}$$

where V_{sed} is the contribution to the total variance (V_{total}) from the sedimentation part of the problem, V_{shear} is the shear contribution to V_{total}, and the angle brackets represent the average over all configurations. The results for a suspension with a concentration of 0.01 and a shear rate of 13, using 81 and 192 particles, are shown in table 4.5. V_{sed} grows with the number of particles used while V_{shear} does not. Also notice that the V_{sed} in the x direction is twice as large as the corresponding V_{shear}, while V_{sed} in the y direction is only 5% of the corresponding V_{shear}. The

total x variance depends on N because V_{sed} in the x direction depends on N. We see that the critical shear rate at which the sedimentation portion of the problem can be neglected is much higher in the x direction than in the y direction.

Since the variance depends on N, the diffusion coefficient which is proportional to the variance is expected to depend on N also. From the results of set A, we find that this is indeed true. The dependence of the x diffusion coefficient on N for a quiescent suspension is shown in figure 4.13 for volume fraction of 0.005, 0.01 and 0.02. Suprisingly at 1% and 2%, the curves appear to be asymptoting to a constant value. The diffusion coefficient is equal to the variance multiplied by the correlation time, but since the variance grows steadily with increasing N for a 1% and 2% suspension, and since the correlation time shows no dependence on N (tables 4.12, 4.15 and 4.16, runs q46 through q49, q54 through q51, q62 and q63), the diffusion coefficient should not be asymptoting to a constant value. This decrease in the slope may be due to scatter in the diffusion coefficients.

From these tests we conclude that for 27 or more particles, the sedimentation velocity and the correlation time are independent of N, but the variance and the diffusion coefficient increase with increasing N. In chapter 2 it has been argued that on the order of ten thousand particles may be needed before the variance and thus also the diffusion coefficient become independent of N. Since too much computation time is needed for this many particles, we must accept the fact that the variance and the diffusion coefficient obtained from the simulator will be smaller than the true values. For performing the bulk of the simulations, we have chosen to use 64 particles for modelling the quiescent suspension and 192 particles for modelling the sheared suspensions.

Finally, to examine the effects that the method used to determine the particle velocities has on the statistics, we performed several simulations of quiescent sedimenting suspensions using the PAV approximation. Surprisingly, the variance and diffusion coefficient using the PAV approximation are similar to those obtained using the hybrid method (cf., tables 4.10 and 4.20 runs q21, q22, and q23). The sedimentation velocity, on the other hand, is higher, which is expected since for

the same configuration, the PAV approximation predicts a larger velocity than the hybrid method. We chose to continue using the hybrid method because it does not cost much more to use and it does reduce the occurence of particle overlap.

Before concluding this section, we wish to point out the sensitivity of the simulation to round off. As an example, in figures 4.14a, and b, two graphs of the instantaneous number average of the particle velocity versus time are shown. They were both performed using the same initial configuration, 64 particles, a step size of $0.01\tau_h$, and the predictor-corrector integration method. The only difference was that the run shown in figure 4.14a was performed on a Sun 3/160 without the floating point accelerator board while the other run shown in figure 4.14b was performed on the same computer but with a floating point accelerator board. The two curves are similar up to the time of $50\tau_h$, or 5000 iterations, and then the two curves diverge. Part of the reason for this behavior is the artificial jump in the velocity due to the hybrid method. In the hybrid method, when a cluster of particles are within the critical radius of each other, they are treated using the FTS method, and when they are not within this critical radius, they are treated using the PAV approximation. The two methods do not give identical results. Since the round off in the two runs is slightly different, at some point in time, in one run some of the particles will be close enough to be in a cluster while in the other run they are not. The difference in the PAV and the FTS methods will magnify the difference in the round off errors. Another reason for the behavior of these two runs is that the equations governing the positions of the particles are nonlinear, and nonlinear equations can give rise to chaotic behavior. If the equations are chaotic, a small perturbation in the particle positions will quickly grow to the point where the configurations in the two runs are totally different.

Though the two curves of the instantaneous average deviate by as much as $0.1U_s$ after the time of 50.0, the running averages shown in figures 4.15a, b differ by less than 0.01. In another words, though the configurations in the two given runs at any instance in time may be quite different, and therefore their statistics are also different, over a long period of time, the two runs will experience approximately the

same set of configurations, and the time average of their statistics will be the same. The time average therefore is a meaningful quantity.

4.3 Simulation Results

From the above sensitivity analysis we have decided to employ 64 particles, the Euler integration method, a step sizes of 0.005 τ_l, and the hybrid method to model the quiescent sedimenting suspensions. For a sheared sedimenting suspension, we will use 192 particles distributed in a simulation box which is three times longer in the y direction than in the x or z directions, the Euler integration method, the step size of 0.05 τ_h, and the hybrid method to model the sheared sedimenting suspension. We typically perform the simulation for a hundred τ_l for the quiescent sedimentation suspensions, and a thousand τ_h for the sheared suspensions. This is usually long enough for the diffusion coefficient to asymptote to a constant value. The results of these simulations will now be presented. Because we did not recognize the importance of some of the statistics at the beginning, some runs do not have all of them. (Since these runs are costly, we did not discard the runs which do not have all the statistics. A simulation run for a quiescent suspension of 1% volume fraction with a step size of 0.005 τ_l requires six hours on a Sun 3/160 mini computer, and for a sheared suspension with a step size of $0.05\tau_h$ requires three cpu days.)

In figure 4.16 we show the number average of the particle velocity against time for run q45. Since we are using only 64 particles, whenever a group of particles come together to form a cluster, the average velocity increases. At other times the particles are well separated and the average velocity decreases. This is why the curve in figure 4.16 contains many peaks and valleys. The curve of the running average, on the other hand, is smooth.

The time-averaged velocities for all the quiescent simulations are compiled in table 4.6 and those for the sheared suspension are listed in table 4.7. From these tables one sees that there is little difference between the sedimentation velocity in a sheared and a quiescent suspension. In figure 4.17, we show the concentration dependence of the sedimentation velocity obtained from our simulator, along with

the experimental data and Batchelor's theoretical predictions. The sedimentation velocity from the simulator for both the sheared and quiescent cases falls along the experimental curve for the sheared suspension, and furthermore in both cases the deviation from Stokes's velocity depended on c and not $c^{\frac{1}{3}}$. From this linear dependence on c we can infer that the length scale of the radial distribution is proportional to a and not $ac^{-\frac{1}{3}}$. Performing a linear regression analysis on the sedimentation velocity gives, for the quiescent sedimenting suspensions,

$$U_p = U_s(1.0 - 4.0c), \tag{4.4}$$

and for the sheared sedimenting suspension,

$$U_p = U_s(1.0 - 4.5c). \tag{4.5}$$

Next we will examine the radial distributions. The radial distributions for runs q45 (quiescent sedimenting suspension) and s62 (sheared sedimenting suspension) are shown in figures 4.18 and 4.19, respectively. The shear rate for run s62 is eight and the concentration is 0.01 for both runs. The radial distribution for run q45 exhibits a significant peak at the radius of $2a$. Table 4.8, which describes the radial distribution function for each of the quiescent simulations, shows that this is a common feature of the quiescent sedimenting suspensions and that this peak generally disappears by $r = 3.0a$. The radial distribution for run s62 shows a small peak at the radius $2a$ and a slight deficit from $2.5a$ to $3.5a$. Table 4.9, which describes the radial distribution for each of the sheared simulations, shows that this is ususally the case when a high shear rate is imposed or when the concentration is low. The reason again is because of the accumulation of error as discussed in section 3.4. Upon examining the brief descriptions of the radial distributions for the different runs in tables 4.8 and 4.9, we conclude that the microscale structure does not scale with $ac^{-\frac{1}{3}}$.

Besides testing the particle distributions for radial dependence, we have also tested it for angular dependence. The phi and theta distributions for run q45 are shown in figures 4.20 through 4.22, and those for run s62 are shown in figures 4.23

through 4.25. For both sheared and quiescent suspensions, the phi distributions averaged over all r are uniform. For the sheared suspension, between $r = 2a$ to $r = 4a$, the phi distributions show an excess along the axis perpendicular to the direction of shear ($\phi = 0, \pi$), and a deficit along the direction of shear ($\phi = \pm\frac{\pi}{2}$). The reason can be seen from figure 4.26, which shows the trajectories of two particles in a shear flow. The second particle moving toward particle A is deflected to one side before it can come close to $r = 2a$, and hence a deficit in the phi distribution near $\phi = \pm\frac{\pi}{2}$ and $r = 2a$. Furthermore notice that the trajectories are compressed at $\phi = 0$. This is why there is an excess of particles there. For quiescent sedimentation, because there is no preferred ϕ angle, the particle distribution is not expected to show any ϕ dependence. Figures 4.23 through 4.25 indeed show no phi dependence. The theta distributions for run q45 are shown in figures 27 through 29, and those for run s62 are shown in figures 30 through 32. The theta distributions averaged over all r for both sheared and quiescent suspension runs also show no structure. Between $r = 2a$ to $r = 4a$, the particle distributions for the sheared suspension show a dependence on the angle θ. The features are not as pronounced as the structure in the phi distribution. For quiescent sedimentation, similar features are observed but they are even less pronounced. This theta dependence may be just statistical fluctuations.

The time-averaged variances for the quiescent sedimenting suspensions are collected in table 4.10, and those for the sheared suspensions are in table 4.11. For the quiescent sedimenting suspensions, the variances in the x direction (the direction of sedimentation) are five times larger than those in either the y, or z directions. In a suspension, the variation in the particles' velocities arises because particles in a cluster tend to move faster than isolated particles. If one compares the velocity of isolated particles to the velocity of the particles in a cluster, one will find that the difference is larger in the x direction than in the other two, and hence the variance is also larger in the x direction. We can show this by estimating the variance for a simple type of particle configuration. A typical arrangement of particles in the simulator will consist of say n isolated particles and $\frac{m}{2}$ doublets. Triplets and larger

clusters do form, but at low concentration; only several percent of the particles are in these large groups, and we will neglect their contribution to the variance. To further simplify the analysis, we will assume that the doublets consist of two particles in contact with each other. For such a doublet, the x velocity on the average is $\frac{3}{2}U_s$ and the maximum y velocity is $\frac{3}{16}U_s$. The isolated particles will settle with U_s and will not move in the y direction. The average velocities for this arrangement of particles are

$$< u_x > = \frac{nU_s + m\frac{3}{2}U_s}{n+m}, \tag{4.6}$$

$$= U_s\left[1 + \frac{1}{2}\frac{m}{n+m}\right],$$

$$< u_y > \sim 0. \tag{4.7}$$

The x variance is given by

$$< V_x > = U_s^2 \frac{\sum_{single}(1-(1+\frac{1}{2}\frac{m}{n+m}))^2 + \sum_{double}(\frac{3}{2}-(1+\frac{1}{2}\frac{m}{n+m}))^2}{n+m}, \tag{4.8}$$

$$= \frac{U_s^2}{4}\left[(1-\phi_D)\phi_D^2 + \phi_D(1-\phi_D)^2\right],$$

where ϕ_D is equal to $\frac{m}{n+m}$, the fraction of the particles in a doublet. Similarly, the y variance is given by,

$$< V_y > = \frac{\sum_{double}(\frac{3}{16}U_s)^2}{n+m}, \tag{4.9}$$

$$= U_s^2(\frac{3}{16})^2\phi_D.$$

For a 1% suspension, typically 20 to 30% of the particles are in a doublet. If we let ϕ_D be 20% then the x variance is $0.04U_s^2$, the y variance is $0.007U_s^2$, and the ratio of the x variance to the y variance is 5.7.

The concentration dependence of the x variance for the quiescent sedimenting system is shown in figure 4.33. The log log plot of the variance versus concentration is linear which suggest that we can fit the variance to an equations of the form Ac^{α}. For 27 particles,

$$V_x = 0.21c^{0.30}, \tag{4.10}$$

and for 64 particles,

$$V_x = 0.41c^{0.34}, \tag{4.11}$$

and for 125 particles,

$$V_x = 0.63c^{0.36}. \tag{4.12}$$

The variance is a measure of the homogeneity in the suspension with the more homogeneous suspension having the smaller variance. To determine whether the suspension in our simulator is more homogeneous than random, we need to first determine the variance for a random suspension. To accomplish this, we used our molecular-dynamics simulator and performed the simulation exactly as before except that now at each iteration, the particle positions are randomly assigned rather than determined from integrating the particles' velocities. The results for 27, 64, and 125 particles, and for a volume fraction ranging from 0.0005 to 0.03 are shown in figure 4.34. On this log log plot, notice that for volume fractions less than 0.005 the slope is $\frac{2}{3}$, while at concentration over 0.01 the slope is approximately $\frac{1}{3}$. This behavior is consistent with the results of our Monte Carlo simulation discussed in chapter two. In figure 4.35, we compare the variances of the random suspension with those obtained from our molecular-dynamics-type simulations (i.e., table 4.10). The two sets of variances are identical and we conclude that the structure of the suspensions produced in our molecular-dynamics-type simulator, on the length scale of our simulator, is essentially random.

Figure 4.36 shows the concentration dependence of the variance when the suspension is sheared with a shear rate of 10. The best fit through these data is,

$$V_x = 4.17c^{0.57}. \tag{4.13}$$

In figure 4.37 the variance dependence on the shear rate is shown. These data are for a 1% suspension and are in units of $(Ea)^2$. At the shear rate of four, the z variance asymptotes to a constant value. The reason is that the z variance is composed of two parts. One part is due to two particles moving apart in the z direction as they pass each other, and this portion scales with $(Ea)^2$. The other

part is due to particles sedimenting, and it scales with Stokes's velocity. As the shear rate is increased, the former contribution dominates and the variance in units of $(Ea)^2$ asymptotes to a constant. In figure 4.38 the x variance's dependence on the shear rate is shown. Even with a shear rate of 13.3, the x variance in units of $(Ea)^2$ still depends on the shear rate. This implies that the sedimentation part of the problem still contributes significantly to the total x variance. The critical shear rate at which the sedimentation part of the problem can be neglected is larger than 13.0, especially since we are underestimating the variance because we are using a small number of particles. This agrees with our earlier finding. In figure 4.39, the x variance's dependence on shear rate is again shown, but the variance is now in units of U_s^2. In these units, the x variance first decreases and then increases with increasing shear rate. The reason why the x variance increases with shear rate is because the contribution from the shear portion is increasing with shear rate. However we are not certain why the variance decreases with increasing shear rate at low shear rate.

Figure 4.40 shows the time evolution of the x velocity variance for run q45. Earlier we noted that the valleys in the x velocity versus time curve for run q45 (figure 4.16) are due to the formation of clusters. If this is so then we will expect a corresponding peak in the x variance versus time curve because the variance is large when a cluster is present. Examination of figures 4.16 and 4.40 shows that this is indeed the case.

The radial distribution correlation times for the quiescent sedimenting suspensions are shown in table 4.12, and those for the sheared suspensions are shown in table 4.14. The autocorrelation times obtained from $A(\tau)_{pd}$ and $A(\tau)_{<pd>}$ give similar results, which implies that the cross terms in (3.39) are small. The values of T^i_{pd} and $T^i_{<pd>}$ are approximately 0.5 τ_l for the quiescent suspensions and 1.7 τ_h for the sheared suspensions. The values of T^z_{pd} and $T^z_{<pd>}$ are approximately 1.0 τ_l for the quiescent sedimenting suspensions and 4.75 τ_h for the sheared suspensions. These values appear to be independent of concentration. Since these correlation times are large compared to the integration step size used, our step size is sufficiently

small to capture the breakup and formation of clusters. Also this correlation time is small compared to the total time of the simulation, which implies that many cluster breakups and formations occur over the course of the run. In table 4.13, we have also expressed the correlation times for the sheared suspensions in units of τ_l to facilitate the comparison between the sheared and quiescent suspensions. Tables 4.12 and 4.13 show that the correlation time for a quiescent sedimenting suspension is larger. For instance, at the shear rate of 10.0, the correlation time for the quiescent suspensions is over 50 times larger. The difference in the correlation time is to be expected since the time for moving two nearly touching particles apart a distance l due to the shear flow is approximately given by $\frac{l}{\gamma a}$, and due to the sedimentation is $\frac{l}{U_s c^{\frac{2}{3}}}$. The ratio is $\frac{\gamma a}{U_s c^{\frac{2}{3}}}$ or $O(100)$. Since the diffusion coefficient is proportional to the correlation time, the diffusion coefficient should be larger for the quiescent sedimenting suspension. This will be shown to be true.

In tables 4.14 and 4.15, a summary of the velocity and variance correlation times for the quiescent sedimenting suspensions is shown. From these tables, it can be seen that the correlation times in the x direction are ten times larger than in the y or z directions. Since the diffusion coefficients are proportional to the correlation time, one expects that the diffusion coefficient to be greater in the x direction than in the other two. This will be shown to be true. Since the velocity and variance correlation times in the x direction ultimately depend on how long a cluster of particles stay together, we expect these correlation times to be approximately the same as the particle correlation time. Comparing the three correlation times shows this to be true. The velocity and variance correlation times in the other two directions depend not only on how long the particles remain together, but on also how long the orientation of the clusters remains the same. From the correlation time data, it appears that the latter is significantly shorter than the former.

In tables 4.16 and 4.17 the velocity and variance correlation times for the sheared suspensions are shown. These times are given in units of τ_l for comparing with the quiescent suspension cases. The effect of the shear flow is already significant even at a dimensionless shear rate of 0.125; the x correlation time has fallen to $\frac{1}{4}$

of its quiescent value. In the absence of a shear flow, a cluster of particles is broken up by the velocity gradient generated by the surrounding particles. This is a slow process because the velocity gradient is weak. When a shear flow is imposed upon the supension, the velocity gradient due to the shear flow is much larger, and the cluster dissociates faster. Table 4.16 also shows that at a dimensionless shear rate of 0.125, the y correlation time has quadrupled. The reason is that the mechanism which produces significant changes in the y velocity is different in the two cases. Consider the following example. Suppose we center the coordinate system at an isolated particle, and suppose further that a doublet is located in the positive x - positive y quadrant of this coordinate system. In this configuration, the three particles will as a group move in the negative y direction. However, since the doublet settles faster than the isolated particle, the doublet will quickly settle past this particle. Now the doublet is located in the positive x - negative y quadrant with respect to the isolated particle, and in this configuration, the three particles drift in the positive y direction. Now consider what occurs when a shear flow is applied. The y velocity is given approximately by $i_y \gamma z$. This is an approximation because the velocity in the y direction due to the arrangement of particles (i.e., the y velocity due to the mechanism just discussed) still exists, but it is small compared with the y velocity due to the shear flow. Now in order to change the y velocity significantly, the particles must migrate in the z direction. As we shall see, the migration in the z direction is slow and this is why there is an increase in the correlation time when a shear flow is applied.

Tables 4.18 and 4.19 show the velocity and variance correlation times in units of τ_h. Expressed in these units, the x and z correlation times are independent of shear rate. The y correlation time, however, increases with the shear rate, and this again is because the change in the y velocity depends on the migration of the particles in the z direction, and because the rate of migration in the z direction decreases with shear rate.

The diffusion coefficients proved to be the most difficult statistic to extract from the simulator, especially when the shear rate is large. It takes a long time

before $\mathcal{D}_{ij}$ asymptotes to a constant value. In many sheared suspension cases, $\mathcal{D}_{ij}$ never asymptotes even after a time of $1000\tau_h$. Figures 4.41 through 4.43, and figures 4.44 through 4.46, show the time evolution of the diffusion coefficients for runs q45 and s62. The constant values which these curves asymptote to are the diffusion coefficients. In the case of the y diffusion coefficient for run s62 (figure 4.45), the curve never asymptotes to a constant value and no diffusion coefficient was obtained. The diffusion coefficients for all the quiescent simulations are recorded in table 4.20, and the diffusion coefficients for the sheared suspension simulations are shown in table 4.21.

Figures 4.47 and 4.48 show the time evolution of the x diffusion coefficients with restart for runs q45 and s62, respectively. In obtaining the diffusion coefficients with restart, a new set of $\mathcal{D}_{ij}(t)$ was started at regular intervals of one τ_l for the quiescent cases, and $10\tau_h$ for the sheared suspension cases. We terminated this process midway into the run so that we could observe the variation between the different $\mathcal{D}_{ij}$. For instance, for figure 4.48, we kept track of 50 sets of $\mathcal{D}_{ij}$ each spaced $10\tau_h$ apart. From time 0 to time $500\tau_h$, the curve was obtained from averaging over all 50 sets of $\mathcal{D}_{ij}$. However after the time of $500\tau_h$, only a subset of these 50 $\mathcal{D}_{ij}$ was averaged to obtain the curve. For example, at time of 600 τ_h, only the 40 $\mathcal{D}_{ij}$ which began before the time of 400 τ_h, were used. Since the portion of the curve after the time of 500 is rising, we deduce that the $\mathcal{D}_{ij}$, which began during the early portion of the run, gave a significantly larger diffusion coefficient. We can also deduce that some of the $\mathcal{D}_{ij}$ have not asymptoted to a constant value by the time of $500\tau_h$ because the curve is still rising at that point. In this type of curve, since only the first half contains the average over all the $\mathcal{D}_{ij}$, the diffusion coefficient with restart is defined to be the asymptotic value at the middle of the run. These diffusion coefficients for the quiescent sedimenting suspensions are recorded in table 4.22, and those for the sheared sedimenting suspensions are shown in table 4.23. In principle the diffusion coefficients with restart are more accurate since they are averages over several runs. The disadvantage, however, is that they are determined from only half of the simulation run, and for runs, where the diffusion coefficients

have not asymptoted by the middle of the run, no diffusion coefficient with restart can be obtained. Comparing the diffusion coefficients with restart and those without shows good agreement for the quiescent suspensions. For the sheared suspensions, in many of the runs especially at the high shear rates, the diffusion coefficients with restart fail to asymptote to a constant value by the middle of the run. Those that did asymptote by then show good agreement with those determined without restart.

The concentration dependence of the diffusion coefficients for the quiescent sedimenting suspensions performed using 64 particles are shown in figure 4.49. The diffusion coefficients vary with $c^{-\frac{1}{4}}$. If the data point for the concentration of 0.25% is neglected, the diffusion coefficients vary with $c^{-\frac{1}{3}}$. (Because of the scatter in the data, and because of the limited number of data points, no attempt will be made to correlate the diffusion coefficients for the sheared suspensions or for quiescent suspension simulations performed using 27 and 125 particles.) The dependence on a negative power of concentration implies that the diffusion coefficient grows as the concentration decreases. One, however, should be cautious in extrapolating this correlation to zero volume fraction because the variance's dependence on concentration changes at small volume fraction. We have seen that the variances from the simulator are the same as those from the Monte Carlo simulations. The variance depends on $c^{\frac{2}{3}}$ for concentration less than 0.005. The diffusion coefficient is equal to the variance multiplied by the correlation time, and the latter appears to be independent of concentration when expressed in units of τ_l (i.e., $\frac{4}{3}(\frac{4}{3}\pi)^{\frac{2}{3}}c^{-\frac{2}{3}}\frac{a}{U_s}$). Therefore it is possible that at very low concentration, the diffusion coefficient may be independent of concentration.

From tables 4.20 and 4.21, notice that the x diffusion coefficients for the quiescent sedimenting suspensions are 20 times larger than the diffusion coefficients in the other two directions. The reason is that the variances and the correlation times are larger in the x direction than in the other two. The x diffusion coefficient is also larger than the z diffusion coefficient for the sheared suspension even though at high shear rates, the velocity correlation time is the same in these two directions and the variance is larger in the z direction. The relative size of the diffusion coefficient

is suprising since by (3.35), the diffusion coefficient is the product of the variance and the correlation time; the z diffusion coefficient therefore should be larger. The reason why the x diffusion coefficient is larger can be understood from considering the following. Suppose in the suspension, all the particles are well spaced except for two. Under the influence of the shear flow ($u_f = \gamma z e_y$), the particles in the clusters will move apart in the x and z directions as they move pass each other. This leads to a large variance. However after passing each other, their motion in the x and z directions is reversed so that the net displacements in the x and the z directions are zero. The shear flow leads to a large variance but does not cause the particles to drift away from their center of mass, and hence the diffusion coefficient is zero. This anti-correlation which occurs when two particles interact in a shear flow is not reflected in (3.35). In the x, direction when the two particles come close to each other, they will settle faster than the average particle so that they will drift downward relative to the center of mass of the system. When the two particles are finally separated, they now settle with the average particle velocity, and the downward displacement relative to the center of mass of the system is retained after the encounter. This is why the diffusion coefficient is larger in the x direction than in the z direction.

Comparing the x diffusion coefficient of the sheared and the quiescent sedimenting suspension reveals that the former is an order of magnitude smaller when the dimensionless shear rate is above eight. Physically the reason is that when the suspension is being sheared rapidly, before the particles can settle a significant distance, each particle will have sampled the average particle distribution. Since the average distribution is approximately the same for all the particles, all the particles will settle the same distance and the diffusion coefficient will be small. Figure 4.50 shows the diffusion coefficient's dependence on shear rate.

Using (3.35), we can determine a correlation time from the diffusion coefficient and the variance. The derived correlation times for the quiescent suspension simulations are shown in table 4.24, and those for the sheared suspension simulations are shown in table 4.25. These derived correlation times were obtained using the

diffusion coefficient with no restart since there are more of them than the diffusion coefficient with restart. We expect these derived correlation times to be of the same order of magnitude as the velocity correlation time. This is because (3.35) is an expression of the mean value theorem, where τ is the velocity correlation time, and the constant of proportionality multiplied by the variance is the mean value of the integrand of (3.34). The derived correlation time therefore is the product of the proportionality constant and the velocity correlation time. Since the proportionality constant is $O(1)$, the derived and the velocity correlation times should be the same order of magnitude. Comparison of these two times shows this to be true. The derived correlation times are about $\frac{1}{4}$ to $\frac{1}{2}$ of the the velocity and the variance correlation times and about the same size as the particle correlation times. The sheared suspensions showed similar behavior. The derived correlation times for the sheared suspensions fluctuate significantly because of the the scatter in the diffusion coefficients.

In order to compare the diffusion coefficients from different simulations, the number of particles used in each case should be the same. In this way, any differences will not be due to the effects of different N. However, we need to model the sheared sedimenting suspensions using 192 particles while we prefer to use only 64 particles in modelling the quiescent sedimenting suspensions to reduce the computational cost. Since the diffusion coefficient increases with the number of particles, after accounting for the larger number of particles used in modelling the sheared suspensions, the statement that the diffusion coefficient is smaller for sheared sedimenting suspensions is even more true.

4.4 Discussions and Conclusions

From all the statistics extracted from the simulator and discussed in the previous section, we have pieced together the following picture of a sedimenting suspension. For both a quiescent and sheared suspension, the microscale structure is proportional to a rather than $ac^{\frac{-1}{3}}$. Furthermore, the sedimentation velocities in both cases depend on c rather than $c^{\frac{1}{3}}$. This contradicts some of the quiescent

sedimentation experiments reported in the literature (e.g., Barnea and Mizhrahi 1973, Oliver 1961, Lynch 1985). The particles in the suspension do not all settle with a uniform velocity. Those with near neighbors tend to settle faster than those without. The distribution of particles changes with time so that during one period of time, a particle may be settling downward relative to the center of mass of the system, while during another period, the same particle may be moving upward with respect to the center of mass of the system. This leads to a diffusive type behavior. The diffusion coefficient is anisotropic and is the largest in the direction of sedimentation. The size of the diffusion coefficient generally depends on how long a cluster of particles stay together (correlation time) and the difference between the velocities of the particles in the cluster and the mean velocity (related to the velocity variance). When the suspension is sheared, the correlation time falls and so does the diffusion coefficient. At a shear rate of 10, the diffusion coefficient is less than a tenth of the corresponding quiescent case.

If this is an accurate description of the suspension, then the question still remains, why is there a discrepancy among the sedimentation data for the sheared and quiescent supensions, and the suspensions of small Brownian particles? From the simulations we find two important differences between the sheared and quiescent suspensions, their particle correlation times, and their diffusion coefficients in the x direction. We propose that these two differences may account for the differences in the sedimentation velocities

The sedimentation velocity is obtained experimentally by measuring the rate of fall of the interface. It is generally assumed that this is the same as the sedimentation velocity in the bulk of the suspension, but this may not be true. For instance, at the interface, particles that have near neighbors settle faster and will leave the isolated particles behind. The particles at the interface are biased toward a distribution where particles are well spaced, and they will tend to settle slower than those in the bulk of the suspension. If the time it takes for the particles to rearrange themselves is short relative to the time for the interface to settle a significant distance, the particles at the interface can quickly reform close pairs and

the particle distribution will not be significantly biased. However, if the time for particle rearrangement is long, then there will be a strong bias at the interface. To compare these two times, we introduce the peclet number $\frac{\tau}{\frac{l}{U_s}}$. It is the ratio of the time for two particles to dissociate to the time for the interface to settle a distance l. For the quiescent sedimenting suspension of large particles, τ is $\frac{4}{3}(\frac{4}{3}\pi)^{\frac{2}{3}}c^{\frac{-2}{3}}\frac{a}{U_s}$, and for the sheared suspension, it is $\frac{6}{\gamma}$. (Both values are from the simulations.) For Lynch's (1985) experiments, where a is 50 μm, and U_s is 1 mm/min, and the concentration is 5.0%, the peclet number is $\frac{1.3\text{mm}}{l}$. When the same suspension is sheared ($\frac{\gamma a}{U_s} = 10.0$), the peclet number is $\frac{.03\text{mm}}{l}$. In the case of a suspension of Brownian particles, τ is $\frac{a^2c^{-\frac{2}{3}}}{\mathcal{D}_B}$, $\mathcal{D}_B$ is the Brownian diffusion coefficient. For the experiments of Buscall *et al.* (1982) (they reported a sedimentation velocity which depends on c.) where the particles were 1.55 μm in radius, U_s was 0.02 mm/min, and $\mathcal{D}_B$ was 0.0084 mm^2/min, the peclet number is $\frac{.04\text{mm}}{l}$. We see that the peclet numbers show the correct trend.

The difference in the diffusion coefficients can also cause the interface to settle slower than the sedimentation velocity in the bulk of the suspension. This diffusive behavior causes a concentration gradient to develop at the top of the suspension, and hence, smears the apparent boundary between the suspension and the pure fluid above. During an experiment, the eye chooses as the interface the point in this transition region where the suspension becomes opaque. As the experiment progresses, this transition zone continues to spread so the measured velocity of the interface is equal to the sedimentation velocity minus the velocity due to the spreading of the boundary region. When diffusion is large, the velocity of the interface can deviate substantially from the true sedimentation velocity. In the next chapter we will examine this problem further.

Run	Step Size	Deviation from U_s	Dxx $(U_s a)$	Vxx (U_s^2)
q28	0.001	0.058	5.0	0.077
q60	0.005	0.037	6.7	0.098
q26	0.01	0.025	7.6	0.106
q27	0.1	-0.095	14.0	0.196

Table 4.1a The effects of step size on the simulation of a quiescent 1% suspension using the Euler integrator. N is 64. D_{xx} is the x diffusion coefficient, and V_{xx} is the x variance.

Run	Step Size	Deviation from U_s	Dxx $(U_s a)$	Vxx (U_s^2)
q29	0.001	0.05	6.0	0.087
q30	0.002	0.05	6.0	0.089
q31	0.01	0.05	6.0	0.092
q32	0.1	-0.265	49.0	0.35

Table 4.1b The effects of step size on the simulation of a quiescent 1% suspension using a predictor-corrector integrator N is 64. D_{xx} is the x diffusion coefficient, and V_{xx} is the x variance.

Run	Step Size	Deviation from U_s	Dxx $(U_s a)$	Vxx (U_s^2)
q35	0.002	0.145	4.5	0.13
q61	0.005	0.128	4.7	0.14
q33	0.01	0.125	5.2	0.15
q37	0.02	0.13	4.5	0.13
q39	0.1	0.065	7.0	0.18

Table 4.2a The effects of step size on the simulation of a quiescent 3% suspension using the Euler integrator. N is 64. D_{xx} is the x diffusion coefficient, and V_{xx} is the x variance.

Run	Step Size	Deviation from U_s	Dxx $(U_s a)$	Vxx (U_s^2)
q40	0.002	0.135	6.0	0.13
q34	0.01	0.145	3.2	0.12
q36	0.02	0.105	10.0	0.17
q38	0.1	-0.645	80.0	0.96

Table 4.2b The effects of step size on the simulation of a quiescent 3% suspension using a predictor-corrector. N is 64. D_{xx} is the x diffusion coefficient, and V_{xx} is the x variance.

Run	Step Size	Deviation from U_s	Dxx $(U_s a)$	Vxx (U_s^2)
s36	0.01	0.055	-	0.54
s35	0.02	0.072	-	0.48
s32	0.05	0.061	-	0.51
s31	0.1	0.075	-	0.47
s37	0.2	0.067	-	0.48
s39	0.5	0.059	-	0.55

Table 4.3a The effects of step size on the simulation of a quiescent 1% suspension subjected to a shear rate of 20.0 and performed using the Euler integrator. N is 192. D_{xx} is the x diffusion coefficient, and V_{xx} is the x variance.

Run	Step Size	Deviation from U_s	Dxx $(U_s a)$	Vxx (U_s^2)
s34	0.02	0.058	-	0.55
s33	0.05	0.054	-	0.57
s30	0.1	0.063	-	0.54
s38	0.2	0.059	-	0.55
s40	0.5	0.054	-	0.53

Table 4.3b The effects of step size on the simulation of a quiescent 1% suspension subjected to a shear rate of 20.0 and performed using a predictor-corrector integrator. N is 192. D_{xx} is the x diffusion coefficient, and V_{xx} is the x variance.

Run	Step Size	Deviation from U_s	Dxx $(U_s a)$	Vxx (U_s^2)
s42	0.02	0.048	4.5	0.22
s45	0.05	0.054	-	0.19
s46	0.1	0.049	4.2	0.22

Table 4.4a The effects of step size on the simulation of a quiescent 1% suspension subjected to a shear rate of 0.5 and performed using the Euler integrator. N is 192. D_{xx} is the x diffusion coefficient, and V_{xx} is the x variance.

Run	Step Size	Deviation from U_s	Dxx $(U_s a)$	Vxx (U_s^2)
s41	0.02	0.042	3.0	0.23
s43	0.05	0.046	-	0.22
s44	0.1	0.047	-	0.22

Table 4.4b The effects of step size on the simulation of a quiescent 1% suspension subjected to a shear rate of 0.5 and performed using a predictor-corrector integrator. N is 192. D_{xx} is the x diffusion coefficient, and V_{xx} is the x variance.

X Variance

number of particles	sedimentation contribution	shear contribution	total
81	3.736e-3	3.08e-3	6.73e-3
192	5.60e-3	3.11e-3	8.52e-3

Y Variance

number of particles	sedimentation contribution	shear contribution	total
81	2.99e-4	9.36e-3	9.66e-3
192	4.63e-4	9.66e-3	1.03e-2

Table 4.5 The relative importance of sedimentation and shear to the variance of a sedimenting suspension subjected to a shear rate of 13.3. The variances are in units of $(Ea)^2$. The data are from performing a Monte-Carlo simulation using a 1% suspension.

Run	C	N	Method	dt	T	Deviation from U_s
q6	.01	64	Euler	.0005	0-100	.068
q7	.01	64	Euler	.0005	0-100	.063
q3	.01	64	Euler	.001	0-100	.061
q4	.01	64	Euler	.001	0-100	.054
q5	.01	64	Euler	.002	0-400	.057
q43	.01	64	Euler	.005	0-100	.044
q44	.01	64	Euler	.005	0-100	.057
q45	.01	64	Euler	.005	0-100	.04
q60	.01	64	Euler	.005	0-100	.037
q10	.01	64	PC	.001	0-100	.043
q11	.01	64	PC	.001	0-100	.037
q29	.01	64	PC	.001	0-100	.049
q30	.01	64	PC	.001	0-100	.052
q8†	.01	64	Euler	.001	0-100	.058
q9†	.01	64	Euler	.001	0-200	.065
q1	.01	27	Euler	.001	0-100	.058
q2	.01	27	Euler	.001	0-100	.051
q12	.01	125	Euler	.001	0-50	.055
q13	.01	125	Euler	.001	0-50	.055
q14	.01	125	Euler	.001	0-50	.059
q16	.01	125	PC	.001	0-50	.055
q15†	.01	125	Euler	.001	0-50	.076
q21‡	.01	64	Euler	.001	0-52	.033
q22‡	.01	64	Euler	.001	0-50	.045
q23‡	.01	125	Euler	.001	0-100	.046

Table 4.6 The sedimentation velocities of the quiescent sedimenting suspensions. C is the concentration, N is the number of particles used, dt is the step size, T is the length of the run, and pc is the predictor-corrector method.
† runs performed with an initial configuration which has a deficit of close pairs.
‡ runs performed using the PAV method.

Run	C	N	Method	dt	T	Deviation from U_s
q50	.0025	64	Euler	.005	0-100	.007
q51	.0025	64	Euler	.005	0-100	.003
q17	.005	64	Euler	.001	0-100	.031
q18	.005	64	Euler	.001	0-100	.018
q19	.005	64	Euler	.001	0-100	.031
q48	.005	64	Euler	.005	0-100	.029
q49	.005	64	Euler	.005	0-100	.022
q20†	.005	64	Euler	.001	0-200	.018
q62	.005	27	Euler	.005	0-200	.018
q63	.005	27	Euler	.005	0-200	.02
q56	.005	125	Euler	.005	0-100	.018
q57	.005	125	Euler	.005	0-100	.021
q64	.02	27	Euler	.005	0-200	.09
q65	.02	27	Euler	.005	0-200	.09
q46	.02	64	Euler	.005	0-100	.12
q47	.02	64	Euler	.005	0-100	.10
q54	.02	125	Euler	.005	0-100	.10
q55	.02	125	Euler	.005	0-100	.09
q42	.03	64	Euler	.005	0-100	.14
q52	.03	64	Euler	.005	0-100	.12
q53	.03	64	Euler	.005	0-100	.12
q61	.03	64	Euler	.005	0-100	.128
q35	.03	64	Euler	.002	0-100	.13
q40	.03	64	PC	.002	0-100	.13
q41	.03	64	PC	.01	0-100	.14
q34	.03	64	PC	.01	0-100	.14
q37	.03	64	Euler	.01	0-100	.14
q58	.05	64	Euler	.005	0-100	.185
q59	.05	64	Euler	.005	0-100	.215

Table 4.6 continued.

Run	C	γ	N	Method	dt	T	Deviation from U_s
s23	.01	.125	192/3	Euler	.01	0-200	.040
s24	.01	.25	192/3	Euler	.01	0-200	.048
s25	.01	.25	192/3	Euler	.01	0-200	.035
s26	.01	.5	192/3	Euler	.01	0-200	.044
s27	.01	.5	192/3	Euler	.01	0-200	.045
s42	.01	.5	192/3	Euler	.02	0-200	.048
s45	.01	.5	192/3	Euler	.05	0-200	.054
s46	.01	.5	192/3	Euler	.1	0-200	.049
s51	.01	.5	192/3	Euler	.05	0-1000	.040
s53	.01	.5	192/3	Euler	.05	0-1000	.038
s41	.01	.5	192/3	PC	.02	0-200	.042
s43	.01	.5	192/3	PC	.05	0-200	.046
s44	.01	.5	192/3	PC	.1	0-200	.047
s54	.01	1.0	192/3	Euler	.05	0-1000	.045
s60	.01	1.0	192/3	Euler	.05	0-1000	.047
s21	.01	1.25	192/3	Euler	.02	0-400	.041
s28	.01	1.25	192/3	Euler	.01	0-200	.056
s61	.01	2.0	192/3	Euler	.05	0-1000	.055
s29	.01	2.5	192/3	Euler	.01	0-200	.060
s17	.01	2.5	192/3	Euler	.1	0-800	.060
s52	.01	4.0	192/3	Euler	.05	0-1000	.065
s16	.01	5.	192/3	Euler	.1	0-800	.042

Table 4.7 The sedimentation velocities of the sheared sedimenting suspensions. C is the concentration, γ is the dimensionless shear rate, N is the number of particles used, dt is the step size, T is the length of the run, and pc is the predictor-corrector method.

Run	C	γ	N	Method	dt	T	Deviation from U_s
s62	.01	8.0	192/3	Euler	.05	0-1000	.057
s56	.01	10.0	192/3	PC	.05	0-1000	.031
s63	.01	10	192/3	Euler	.05	0-1000	.056
s7	.01	13.3	192/3	Euler	.1	0-300	.041
s8	.01	13.3	192/3	Euler	.1	0-800	.060
s9	.01	13.3	192/3	Euler	.05	0-800	.065
s10	.01	13.3	192/3	Euler	.1	0-800	.060
s11	.01	13.3	192/3	Euler	.1	0-800	.058
s20	.01	13.3	192/3	Euler	.1	0-800	.060
s3	.01	17.8	135/3	Euler	.1	0-800	.060
s4	.01	17.8	135/3	Euler	.1	0-800	.058
s5	.01	17.8	135/3	Euler	.1	0-1600	.062
s6	.01	17.8	135/3	Euler	.05	0-800	.062
s14	.005	10.6	192/3	Euler	.1	0-800	.044
s15	.005	10.6	192/3	Euler	.1	0-800	.0
s57	.005	10.0	192/3	Euler	.05	0-1000	.017
s18	.02	16.8	192/3	Euler	.1	0-800	.072
s19	.02	16.8	192/3	Euler	.1	0-800	.082
s65	.03	.5	192/3	Euler	.05	0-1000	.114
s64	.03	1.	192/3	Euler	.05	0-1000	.117
s55	.03	10.	192/3	Euler	.05	0-1000	.142

Table 4.7 continued.

Run	C	N	Method	dt	T	Discription of g(r)
q50	.0025	64	Euler	.005	0-100	excess extends to 4a
q51	.0025	64	Euler	.005	0-100	excess extends to 4a
q48	.005	64	Euler	.005	0-100	excess extends to 2.5a
q49	.005	64	Euler	.005	0-100	excess extends to 2.5a
q62	.005	27	Euler	.005	0-200	excess extends to 3.0a
q63	.005	27	Euler	.005	0-200	excess extends to 2.6a
q56	.005	125	Euler	.005	0-100	excess extends to 3.0a
q57	.005	125	Euler	.005	0-100	excess extends to 3.0a
q43	.01	64	Euler	.005	0-100	excess extends to 2.75a
q44	.01	64	Euler	.005	0-100	excess extends to 3a
q45	.01	64	Euler	.005	0-100	excess extends to 3.0a
q60	.01	64	Euler	.005	0-100	excess extends to 3.0a
q30	.01	64	PC	.001	0-100	excess extends to 3.0 a
q64	.02	27	Euler	.005	0-200	excess extends to 2.5a
q65	.02	27	Euler	.005	0-200	excess extends to 2.5a slight deficit from 2.5a to 5.5a
q46	.02	64	Euler	.005	0-100	excess extends to 2.5a slight deficit from 2.5a to 4.5a
q47	.02	64	Euler	.005	0-100	excess extends to 2.5a
q54	.02	125	Euler	.005	0-100	excess extends to 3.0a
q55	.02	125	Euler	.005	0-100	excess extends to 3.0a
q42	.03	64	Euler	.005	0-100	excess extends to 3.0a
q52	.03	64	Euler	.005	0-100	excess extends to 3.0a
q53	.03	64	Euler	.005	0-100	excess extends to 2.5a
q61	.03	64	Euler	.005	0-100	excess extends to 3.0a
q35	.03	64	Euler	.002	0-100	excess extends to 2.75a
q40	.03	64	PC	.002	0-100	excess extends to 3.0a
q41	.03	64	PC	.01	0-100	excess extends to 2.5a
q34	.03	64	PC	.01	0-100	excess extends to 2.5a
q37	.03	64	Euler	.01	0-100	excess extends to 3.0a
q58	.05	64	Euler	.005	0-100	excess extends to 3.0a
q59	.05	64	Euler	.005	0-100	excess extends to 2.5a

Table 4.8 The radial distributions of the quiescent sedimenting suspensions. C is the concentration, N is the number of particles used, dt is the step size, T is the length of the run, and pc is the predictor-corrector method.

Run	C	γ	N	Method	dt	T	Discription of g(r)
s57	.005	10.0	192/3	Euler	.05	0-1000	slight peak ending at 2.5a
s23	.01	.125	192/3	Euler	.01	0-200	excess extends to 2.5a
s24	.01	.25	192/3	Euler	.01	0-200	excess extends to 3.0a
s25	.01	.25	192/3	Euler	.01	0-200	excess extends to 3.0a
s26	.01	.5	192/3	Euler	.01	0-200	excess extends to 2.5a
s27	.01	.5	192/3	Euler	.01	0-200	excess extends to 3.0a
s42	.01	.5	192/3	Euler	.02	0-200	excess extends to 2.5a
s45	.01	.5	192/3	Euler	.05	0-200	excess extends to 2.5a
s46	.01	.5	192/3	Euler	.1	0-200	excess extends to 2.5a
s51	.01	.5	192/3	Euler	.05	0-1000	excess extends to 3.0a
s53	.01	.5	192/3	Euler	.05	0-1000	excess extends to 2.5a
s41	.01	.5	192/3	PC	.02	0-200	excess extends to 3.0a
s43	.01	.5	192/3	PC	.05	0-200	excess extends to 2.5a
s44	.01	.5	192/3	PC	.1	0-200	excess extends to 3.0a
s54	.01	1.0	192/3	Euler	.05	0-1000	excess extends to 2.5a
s60	.01	1.0	192/3	Euler	.05	0-1000	excess extends to 2.5a
s21	.01	1.25	192/3	Euler	.02	0-400	excess extends to 2.5a
s28	.01	1.25	192/3	Euler	.01	0-200	excess extends to 2.5a
s61	.01	2.0	192/3	Euler	.05	0-1000	excess extends to 2.4a
s29	.01	2.5	192/3	Euler	.01	0-200	excess extends to 2.5a
s62	.01	8.0	192/3	Euler	.05	0-1000	excess ends at 2.4a then deficit to 3.5a
s56	.01	10.0	192/3	PC	.05	0-1000	excess extends to 5.2a
s63	.01	10	192/3	Euler	.05	0-1000	slight deficit to 3.2a
s65	.03	.5	192/3	Euler	.05	0-1000	excess extends to 3.0a
s64	.03	1.	192/3	Euler	.05	0-1000	excess extends to 2.5a
s55	.03	10.	192/3	Euler	.05	0-1000	excess extends to 2.5a

Table 4.9 The radial distributions of the sheared sedimenting suspensions. C is the concentration, γ is the dimensionless shear rate, N is the number of particles used, dt is the step size, T is the length of the run, and pc is the predictor-corrector method.

Run	C	N	Method	dt	T	$\frac{V_{xx}}{U_s^2}$	$\frac{V_{yy}}{U_s^2}$	$\frac{V_{zz}}{U_s^2}$
q6	.01	64	Euler	.0005	0-100	.076	.015	.015
q7	.01	64	Euler	.0005	0-100	.079	.016	.016
q3	.01	64	Euler	.001	0-100	.079	.015	.015
q4	.01	64	Euler	.001	0-100	.084	.016	.016
q5	.01	64	Euler	.002	0-400	.083	.015	.015
q43	.01	64	Euler	.005	0-100	.09	.016	.016
q44	.01	64	Euler	.005	0-100	.089	.015	.015
q45	.01	64	Euler	.005	0-100	.092	.016	.016
q60	.01	64	Euler	.005	0-100	.095	.016	.016
q10	.01	64	PC	.001	0-100	.043	.015	.016
q11	.01	64	PC	.001	0-100	.037	.016	.016
q29	.01	64	PC	.001	0-100	.049	.016	.016
q30	.01	64	PC	.001	0-100	.052	.016	.016
q8†	.01	64	Euler	.001	0-100	.08	.015	.016
q9†	.01	64	Euler	.001	0-200	.079	.014	.014
q1	.01	27	Euler	.001	0-100	.051	.01	.01
q2	.01	27	Euler	.001	0-100	.055	.01	.01
q12	.01	125	Euler	.001	0-50	.11	.022	.022
q13	.01	125	Euler	.001	0-50	.12	.02	.02
q14	.01	125	Euler	.001	0-50	.11	.02	.02
q16	.01	125	PC	.001	0-50	.11	.02	.02
q15†	.01	125	Euler	.001	0-50	.095	.02	.02
q21‡	.01	64	Euler	.001	0-52	.11	.02	.02
q22‡	.01	64	Euler	.001	0-50	.1	.02	.02
q23‡	.01	125	Euler	.001	0-100	.09	.02	.02

Table 4.10 The variances of the quiescent sedimenting suspensions. C is the concentration, N is the number of particles used, dt is the step size, T is the length of the run, V_{xx}, V_{yy}, and V_{zz} are the velocity variances in the x, y, and z directions, respectively, and pc is the predictor-corrector method.
† runs performed with an initial configuration which has a deficit of close pairs.
‡ runs performed using the PAV method.

Run	C	N	Method	dt	T	$\frac{V_{xx}}{U_s^2}$	$\frac{V_{yy}}{U_s^2}$	$\frac{V_{zz}}{U_s^2}$
q50	.0025	64	Euler	.005	0-100	.048	.007	.007
q51	.0025	64	Euler	.005	0-100	.053	.007	.007
q17	.005	64	Euler	.001	0-100	.06	.01	.009
q18	.005	64	Euler	.001	0-100	.09	.01	.01
q19	.005	64	Euler	.001	0-100	.07	.01	.01
q48	.005	64	Euler	.005	0-100	.064	.01	.01
q49	.005	64	Euler	.005	0-100	.07	.01	.01
q20†	.005	64	Euler	.001	0-200	.07	.01	.01
q62	.005	27	Euler	.005	0-200	.044	.007	.0069
q63	.005	27	Euler	.005	0-200	.043	.007	.0069
q56	.005	125	Euler	.005	0-100	.096	.014	.014
q57	.005	125	Euler	.005	0-100	.097	.014	.014
q46	.02	64	Euler	.005	0-100	.095	.02	.02
q47	.02	64	Euler	.005	0-100	.11	.02	.02
q64	.02	27	Euler	.005	0-200	.065	.014	.014
q65	.02	27	Euler	.005	0-200	.067	.014	.014
q54	.02	125	Euler	.005	0-100	.16	.031	.031
q55	.02	125	Euler	.005	0-100	.16	.031	.032
q42	.03	64	Euler	.005	0-100	.14	.027	.028
q52	.03	64	Euler	.005	0-100	.14	.027	.03
q53	.03	64	Euler	.005	0-100	.15	.03	.03
q61	.03	64	Euler	.005	0-100	.14	.027	.028
q35	.03	64	Euler	.002	0-100	.13	.028	.027
q40	.03	64	PC	.002	0-100	.13	.028	.028
q41	.03	64	PC	.01	0-100	.12	.027	.028
q34	.03	64	PC	.01	0-100	.12	.026	.03
q37	.03	64	Euler	.01	0-100	.13	.029	.029
q58	.05	64	Euler	.005	0-100	.15	.039	.035
q59	.05	64	Euler	.005	0-100	.126	.034	.036

Table 4.10 continued.

Run	C	γ	N	Method	dt	T	V_{xx}/U_s^2	V_{yy}/U_s^2	V_{zz}/U_s^2	$V_{xx}/(Ea)^2$	$V_{yy}/(Ea)^2$	$V_{zz}/(Ea)^2$
s23	.01	.125	192/3	Euler	.01	0-200	.24	1.13	.017	61.4	289.	4.34
s24	.01	.25	192/3	Euler	.01	0-200	.22	4.9	.017	14.1	312.	1.1
s25	.01	.25	192/3	Euler	.01	0-200	.25	4.7	.017	16.	301.	1.1
s26	.01	.5	192/3	Euler	.01	0-200	.23	18.4	.018	3.6	294.	.288
s27	.01	.5	192/3	Euler	.01	0-200	.21	17.7	.018	3.36	283.	.288
s41	.01	.5	192/3	PC	.02	0-200	.23	18.3	.019	3.68	293.	.304
s42	.01	.5	192/3	Euler	.02	0-200	.22	19.2	.017	3.52	307.	.272
s43	.01	.5	192/3	PC	.05	0-200	.22	19.5	.017	3.52	312.	.272
s44	.01	.5	192/3	PC	.1	0-200	.22	18.4	.017	3.52	294.	.272
s45	.01	.5	192/3	Euler	.05	0-200	.19	19.7	.019	3.0	315.	.300
s46	.01	.5	192/3	Euler	.1	0-200	.22	18	.017	3.52	288.	.272
s51	.01	.5	192/3	Euler	.05	0-1000	.21	18.9	.018	3.0	315.	.301
s53	.01	.5	192/3	Euler	.05	0-1000	.22	19.6	.017	3.52	313	.272
s54	.01	1.0	192/3	Euler	.05	0-1000	.218	75	.0197	.87	148.	.075
s60	.01	1.0	192/3	Euler	.05	0-1000	.21	72.6	.019	.84	290	.076
s21	.01	1.25	192/3	Euler	.02	0-400	.22	115	.022	.564	294.	.056
s28	.01	1.25	192/3	Euler	.01	0-200	.21	117	.02	.536	.436	.013
s61	.01	2.0	192/3	Euler	.05	0-1000	.2	2.96e2	.028	.2	296.	.028
s29	.01	2.5	192/3	Euler	.01	0-200	.21	476.	.041	.134	301.	.027
s17	.01	2.5	192/3	Euler	.1	0-800	.20	450.	.03	.128	288.	.0192
s16	.01	5.	192/3	Euler	.1	0-800	.24	1.7e3	.09	.038	272.	.0144

Table 4.11 The variances of the sheared sedimenting suspensions. C is the concentration, γ is the dimensionless shear rate, N is the number of particles used, dt is the step size, T is the length of the run, V_{xx}, V_{yy}, and V_{zz} are the velocity variances in the x, y, and z directions, respectively, and pc is the predictor-corrector method.

Run	C	γ	N	Method	dt	T	$\frac{V_{xx}}{U_*^2}$	$\frac{V_{yy}}{U_*^2}$	$\frac{V_{zz}}{U_*^2}$	$\frac{V_{xx}}{(Ea)^2}$	$\frac{V_{yy}}{(Ea)^2}$	$\frac{V_{zz}}{(Ea)^2}$
s62	.01	8.0	192/3	Euler	.05	0-1000	.25	4.8e3	.226	.016	303.	.0141
s56	.01	10.0	192/3	PC	.05	0-1000	.32	7.83e3	.46	.0128	315	.0184
s63	.01	10	192/3	Euler	.05	0-1000	.274	7.66e3	.34	.01	306	.013
s7	.01	13.3	192/3	Euler	.1	0-300	.35	1.2e4	.56	7.9e-3	271	.0126
s8	.01	13.3	192/3	Euler	.1	0-800	.25	1.3e4	.56	7.2e-3	298.	.0127
s9	.01	13.3	192/3	Euler	.05	0-800	.32	1.3e4	.56	7.2e-3	294.	.0123
s10	.01	13.3	192/3	Euler	.1	0-800	.33	1.4e4	.55	7.5e-3	316.	.0124
s11	.01	13.3	192/3	Euler	.1	0-800	.34	1.4e4	.57	7.7e-3	316.	.013
s20	.01	13.3	192/3	Euler	.1	0-800	.34	1.4e4	.56	.008	316.	.0128
s3	.01	17.8	135/3	Euler	.1	0-800	.43	1.3e4	.97	5.4e-3	164	.012
s4	.01	17.8	135/3	Euler	.1	0-800	.42	1.4e4	.98	5.3e3	177	.012
s5	.01	17.8	135/3	Euler	.1	0-1600	.41	1.3e4	.96	5.3e-3	177	.012
s6	.01	17.8	135/3	Euler	.05	0-800	.41	1.3e4	.96	5.3e-3	177.	.013
s14	.005	10.6	192/3	Euler	.1	0-800	.17	1.28e4	.174	.061	456.	.006
s15	.005	10.6	192/3	Euler	.1	0-800	.22	1.1e4	.197	.077	392.	.007
s57	.005	10.0	192/3	Euler	.05	0-1000	.19	1.1e4	.183	.008	440	.007
s18	.02	16.8	192/3	Euler	.1	0-800	.69	1.4e4	1.72	.01	198.	.024
s19	.02	16.8	192/3	Euler	.1	0-800	.66	1.4e4	1.7	.01	198	.024
s65	.03	.5	192/3	Euler	.05	0-1000	.37	9.1	.032	5.92	146.	.512
s64	.03	1.	192/3	Euler	.05	0-1000	.346	36.2	.038	1.38	145	.152
s55	.03	10.	192/3	Euler	.05	0-1000	.54	3.7e3	.94	.02	148	.038

Table 4.11 continued.

Run	C	N	Method	dt	T	T_{pd}	$T_{<pd>}$
q50	.0025	64	Euler	.005	0-100	.4(1.2)	.5(1.)
q51	.0025	64	Euler	.005	0-100	.3(1.2)	.4(1.)
q62	.005	27	Euler	.005	0-200	.6(1.0)	.4(1.8)
q63	.005	27	Euler	.005	0-200	.3(1.5)	.4(1.0)
q48	.005	64	Euler	.005	0-100	.5(.8)	.5(5)
q49	.005	64	Euler	.005	0-100	.4(1.)	.5(1.2)
q56	.005	125	Euler	.005	0-100	.5(1.)	.5(1.8)
q57	.005	125	Euler	.005	0-100	.4(.9)	.4(1.)
q43	.01	64	Euler	.005	0-100	.6(1.6)	.4(1.1)
q44	.01	64	Euler	.005	0-100	.6(1.0)	.5(.8)
q45	.01	64	Euler	.005	0-100	.6(1.1)	.7(2)
q60	.01	64	Euler	.005	0-100	.4(1.6)	.4(2.4)
q64	.02	27	Euler	.005	0-200	.4(.82)	.4(2.4)
q65	.02	27	Euler	.005	0-200	.6(1.6)	.6(1.6)
q46	.02	64	Euler	.005	0-100	.5(1.0)	.5(1.1)
q47	.02	64	Euler	.005	0-100	.4(.7)	.5(1.8)
q54	.02	125	Euler	.005	0-100	.4(1.)	.5(-)
q55	.02	125	Euler	.005	0-100	.4(1.)	.5(2.)
q42	.03	64	Euler	.005	0-100	.6(3.2)	-
q52	.03	64	Euler	.005	0-100	.5(1.7)	.6(1.1)
q53	.03	64	Euler	.005	0-100	.5(.9)	.6(2.3)
q61	.03	64	Euler	.005	0-100	.5(1.3)	.4(3.3)
q41	.03	64	PC	.01	0-100	.9	.9
q58	.05	64	Euler	.005	0-100	.4(2.7)	.8(2.6)
q59	.05	64	Euler	.005	0-100	.3(1.3)	.6(2.0)

Table 4.12 The radial distribution correlation times of the quiescent sedimenting suspensions. The values in the parentheses are T^z and the values not enclosed by the parentheses are T^i. The correlation times are in units of τ_l. C is the concentration, N is the number of particles used, dt is the step size, T is the length of the run, and pc is the predictor-corrector method.

Run	C	γ	N	Method	dt	T	T'_{pd}	$T'_{<pd>}$	T_{pd}	$T_{<pd>}$
s23	.01	.125	192/3	Euler	.01	0-200	1.0(3.4)	-	.214(.73)	-
s24	.01	.25	192/3	Euler	.01	0-200	1.6(2.8)	-	.17(.3)	-
s25	.01	.25	192/3	Euler	.01	0-200	1.7(3.1)	-	.18(.3)	-
s26	.01	.5	192/3	Euler	.01	0-200	1.8(4.3)	-	.10(.23)	-
s27	.01	.5	192/3	Euler	.01	0-200	2.0(5.3)	-	.11(.28)	-
s41	.01	.5	192/3	PC	.02	0-200	1.3(2.7)	-	.07(.14)	-
s42	.01	.5	192/3	Euler	.02	0-200	1.3(3.8)	-	.07(.14)	-
s43	.01	.5	192/3	PC	.05	0-200	1.7(3.2)	-	.091(.17)	-
s44	.01	.5	192/3	PC	.1	0-200	2.7(-)	-	.145(-)	-
s45	.01	.5	192/3	Euler	.05	0-200	1.1(2.9)	-	.06(.16)	-
s46	.01	.5	192/3	Euler	.1	0-200	1.1(3.7)	-	.06(.20)	-
s51	.01	.5	192/3	Euler	.05	0-1000	1.7(8.2)	1.5(-)	.09(.4)	.1(-)
s53	.01	.5	192/3	Euler	.05	0-1000	1.7(7.3)	1.8(-)	.09(.39)	.10(-)
s54	.01	1.0	192/3	Euler	.05	0-1000	2(11)	1.2(6.0)	.05(.3)	.03(.16)
s60	.01	1.0	192/3	Euler	.05	0-1000	2.1(9)	1.9(9.0)	.06(.24)	.05(.24)
s21	.01	1.25	192/3	Euler	.02	0-400	.6(1.7)	-	.013(.036)	-
s28	.01	1.25	192/3	Euler	.01	0-200	2.3(3.6)	-	.049(.077)	-
s61	.01	2.0	192/3	Euler	.05	0-1000	1.6(8.1)	2.5(5.4)	.02(.11)	.033(.07)
s29	.01	2.5	192/3	Euler	.01	0-200	1.3(2.4)	-	.014(.03)	-
s52	.01	4.0	192/3	Euler	.05	0-1000	2.0(3.0)	2.5(-)	.013(.02)	.02(-)
s62	.01	8.0	192/3	Euler	.05	0-1000	1.7(5.3)	2.5(8.5)	.006(.018)	.008(.03)
s56	.01	10.0	192/3	PC	.05	0-1000	1.4(3.6)	4.(-)	.004(.01)	.011(-)
s63	.01	10	192/3	Euler	.05	0-1000	2.0(3.3)	2.0(3.6)	.005(.009)	.005(.01)
s57	.005	10.0	192/3	Euler	.05	0-1000	1.6(3.6)	1.5(5.5)	.003(.006)	.002(.009)
s65	.03	.5	192/3	Euler	.05	0-1000	2.0(9.1)	2.0(11.)	.22(1.0)	.22(1.2)
s64	.03	1.	192/3	Euler	.05	0-1000	1.6(5.7)	-	.089(.32)	-
s55	.03	10.	192/3	Euler	.05	0-1000	1.8(3.0)	1.5(5.5)	.01(.017)	.008(.03)

Table 4.13 The radial distribution correlation times of the sheared sedimenting suspensions. The values in the parentheses are T^s and the values not enclosed by the parentheses are T^i. T_{pd} and $T_{<pd>}$ are in units of τ_l, while T'_{pd} and $T'_{<pd>}$ are in units of τ_h. C is the concentration, γ is the dimensionless shear rate, N is the number of particles used, dt is the step size, T is the length of the run, and pc is the predictor-corrector method.

Run	C	N	Method	dt	T	T^{xx}_{var}	T^{yy}_{var}	T^{zz}_{var}	T^{xx}_{vel}	T^{yy}_{vel}	T^{zz}_{vel}
q50	.0025	64	Euler	.005	0-100	1.8	.2	.2	2.	.2	.2
q51	.0025	64	Euler	.005	0-100	1.4	.1	.2	1.6	.2	.2
q62	.005	27	Euler	.005	0-200	2.	0.	0.	2.0	0.	0.
q63	.005	27	Euler	.005	0-200	1.5	0.	0.	.5	0.	0.
q48	.005	64	Euler	.005	0-100	1.8	.4	.4	3.8	.2	.2
q49	.005	64	Euler	.005	0-100	1.8	.4	.2	1.8	.2	.2
q56	.005	125	Euler	.005	0-100	2.8	.2	.2	3.	.2	.2
q57	.005	125	Euler	.005	0-100	1.4	.2	.3	2.	.2	.2
q43	.01	64	Euler	.005	0-100	1.2	.4	.4	1.7	.3	.2
q44	.01	64	Euler	.005	0-100	2.	.4	.4	2.	.2	.3
q45	.01	64	Euler	.005	0-100	1.4	.2	.4	1.75	.2	.2
q60	.01	64	Euler	.005	0-100	1.	0	0	1.5	0	0
q64	.02	27	Euler	.005	0-200	2.	0.	0.	.8	0.	0.
q65	.02	27	Euler	.005	0-200	4.2	0.	0.	2.	0.	0.
q46	.02	64	Euler	.005	0-100	1.1	.4	.4	1.2	.2	.2
q47	.02	64	Euler	.005	0-100	2.4	.3	.2	6.	.2	.3
q54	.02	125	Euler	.005	0-100	1.8	.8	.4	1.8	.2	.2
q55	.02	125	Euler	.005	0-100	1.4	.2	.4	1.8	.2	.2
q42	.03	64	Euler	.005	0-100	5	.5	.6	7	.6	.6
q52	.03	64	Euler	.005	0-100	2.2	.2	.2	2.	.2	.3
q53	.03	64	Euler	.005	0-100	1.4	1.	.3	2.5	.3	.2
q61	.03	64	Euler	.005	0-100	.2	0.	0.	1.5	0.	0.
q41	.03	64	PC	.01	0-100	3.8	.6	.4	4.	.2	.2
q58	.05	64	Euler	.005	0-100	1.	0.	.4	1.	.5	0.
q59	.05	64	Euler	.005	0-100	3.	0.	0.	2.5	.5	.5

Table 4.14 The velocity and variance correlation times (T^i) of the quiescent sedimenting suspensions. The correlation times are in units of τ_l. C is the concentration, N is the number of particles used, dt is the step size, T is the length of the run, and pc is the predictor-corrector method.

Run	C	N	Method	dt	T	T^{xx}_{var}	T^{yy}_{var}	T^{zz}_{var}	T^{xx}_{vel}	T^{yy}_{vel}	T^{zz}_{vel}
q50	.0025	64	Euler	.005	0-100	2.2	.2	.2	4	.2	.2
q51	.0025	64	Euler	.005	0-100	3.	.1	.2	3.4	.2	.2
q62	.005	27	Euler	.005	0-200	3.	1.5	1.5	3.5	.5	0
q63	.005	27	Euler	.005	0-200	4.5	.3	1.1	5.5	.5	.2
q48	.005	64	Euler	.005	0-100	3.2	.4	.4	3.8	.2	.6
q49	.005	64	Euler	.005	0-100	3.8	.4	.2	3.4	.2	.2
q56	.005	125	Euler	.005	0-100	2.8	.2	.2	3.	.2	.2
q57	.005	125	Euler	.005	0-100	4.	.2	.3	4.2	.2	.2
q43	.01	64	Euler	.005	0-100	2.6	.4	.4	4.	.3	.2
q44	.01	64	Euler	.005	0-100	9.	.4	.4	4.	.2	.3
q45	.01	64	Euler	.005	0-100	1.4	.6	1.	3.	.2	.2
q60	.01	64	Euler	.005	0-100	8.5	1.	1.	5	0.	.5
q64	.02	27	Euler	.005	0-200	7.5	.4	1.	11.	.2	0.
q65	.02	27	Euler	.005	0-200	5.0	2.0	1.0	5.5	.2	.4
q46	.02	64	Euler	.005	0-100	2.	1.4	1.2	2.	.2	.2
q47	.02	64	Euler	.005	0-100	5.0	.3	.2	6.	.2	.3
q54	.02	125	Euler	.005	0-100	3.	.8	.4	3.8	.2	.2
q55	.02	125	Euler	.005	0-100	3.	.2	.4	3.2	.2	.2
q42	.03	64	Euler	.005	0-100	5.	.5	.6	7.	.6	.6
q52	.03	64	Euler	.005	0-100	-	1.1	1.	4.	.2	.3
q53	.03	64	Euler	.005	0-100	8.2	1.	.3	-	.3	.2
q61	.03	64	Euler	.005	0-100	-	.5	.4	-	.5	0.
q41	.03	64	PC	.01	0-100	3.8	.6	.4	7.	.2	.6
q58	.05	64	Euler	.005	0-100	2.	.5	.5	6.	1.5	.4
q59	.05	64	Euler	.005	0-100	4.	1.	2.5	4.	.5	2.4

Table 4.15 The velocity and variance correlation times (T^z) of the quiescent sedimenting suspensions. The correlation times are in units of τ_l. C is the concentration, N is the number of particles used, dt is the step size, T is the length of the run, and pc is the predictor-corrector method.

Run	C	γ	N	Method	dt	T	T^{xx}_{vel}	T^{zz}_{vel}	T^{xz}_{vel}	T^{xz}_{var}	T^{zz}_{var}	T^{xz}_{var}
s23	.01	.125	192/3	Euler	.01	0-200	7.0	48	1.0	7.0	10	3.0
s24	.01	.25	192/3	Euler	.01	0-200	-	1.0	1.6	3.0	16	6.0
s25	.01	.25	192/3	Euler	.01	0-200	6.0	64	2.0	2.5	32	1.5
s26	.01	.5	192/3	Euler	.01	0-200	3.0	36	9	2.0	24	3.8
s27	.01	.5	192/3	Euler	.01	0-200	5.0	40	4.0	3.5	24	7.8
s41	.01	.5	192/3	PC	.02	0-200	13.	40	2.0	3.8	56	5.8
s42	.01	.5	192/3	Euler	.02	0-200	7.5	36	2.0	5.0	30	8.8
s43	.01	.5	192/3	PC	.05	0-200	3.5	16	7.5	3.6	14	14
s44	.01	.5	192/3	PC	.1	0-200	9.5	90	4.5	6.4	5.2	7.6
s45	.01	.5	192/3	Euler	.05	0-200	12	16	5.5	7	55	10
s46	.01	.5	192/3	Euler	.1	0-200	7.5	85	5.4	7.5	75	15.5
s51	.01	.5	192/3	Euler	.05	0-1000	6.5	270	9.5	3.0	105	8.0
s53	.01	.5	192/3	Euler	.05	0-1000	-	3.8	4.5	13.	170	6.5
s54	.01	1.0	192/3	Euler	.05	0-1000	14.	135.	11	3.0	300	25
s60	.01	1.0	192/3	Euler	.05	0-1000	7.	115	11	1.5	250	12
s21	.01	1.25	192/3	Euler	.02	0-400	5.0	70.	13.	4.0	40.	-
s28	.01	1.25	192/3	Euler	.01	0-200	3.0	68.	18	4.0	44.	17
s61	.01	2.0	192/3	Euler	.05	0-1000	5.6	115	-	3.0	150	-
s29	.01	2.5	192/3	Euler	.01	0-200	3.5	30.	2.0	2.0	28	3.5
s62	.01	8.0	192/3	Euler	.05	0-1000	4.5	260.	1.6	2.5	150	3.0
s56	.01	10.0	192/3	PC	.05	0-1000	7.	160.	3.0	3.0	190.	6.8
s63	.01	10	192/3	Euler	.05	0-1000	4.5	-	-	2.0	195	1.5
s57	.005	10.0	192/3	Euler	.05	0-1000	5.5	50.	17.	2.9	-	6.5
s65	.03	.5	192/3	Euler	.05	0-1000	16.	112.	4.0	2.5	52	5.6
s64	.03	1.	192/3	Euler	.05	0-1000	5.5	50.	17.0	2.9	-	6.5
s55	.03	10.	192/3	Euler	.05	0-1000	7.8	40	1.6	2.5	-	1.2

Table 4.16 The velocity and variance correlation times (T^{*}) of the sheared sedimenting suspensions. The correlation times are in units of τ_h. C is the concentration, γ is the dimensionless shear rate, N is the number of particles used, dt is the step size, T is the length of the run, and pc is the predictor-corrector method.

Run	C	γ	N	Method	dt	T	T^{xx}_{vel}	T^{zz}_{vel}	T^{xx}_{var}	T^{xx}_{var}	T^{zz}_{var}	T^{xx}_{var}
s23	.01	.125	192/3	Euler	.01	0-200	2.5	4	1.0	1.5	2.0	1.5
s24	.01	.25	192/3	Euler	.01	0-200	3.0	10	1.5	1.4	16	4.0
s25	.01	.25	192/3	Euler	.01	0-200	2.5	10	1.5	2.0	24	1.5
s26	.01	.5	192/3	Euler	.01	0-200	3.0	24	1.5	1.5	4	2.5
s27	.01	.5	192/3	Euler	.01	0-200	3.0	16	2.0	2.0	12	4.0
s41	.01	.5	192/3	PC	.02	0-200	3.2	20	1.0	1.0	22	1.2
s42	.01	.5	192/3	Euler	.02	0-200	3.0	8	1.0	1.0	22	1.2
s43	.01	.5	192/3	PC	.05	0-200	2.5	6	.8	.6	4	1.2
s44	.01	.5	192/3	PC	.1	0-200	2.5	20	2.9	2.5	1.5	2.8
s45	.01	.5	192/3	Euler	.05	0-200	3.3	8	1.2	5.0	55	5.1
s46	.01	.5	192/3	Euler	.1	0-200	3.0	35	2	2.5	75	2.5
s51	.01	.5	192/3	Euler	.05	0-1000	3.0	2.5	2.5	2	90	5.5
s53	.01	.5	192/3	Euler	.05	0-1000	4.0	1.5	2.2	2.5	150	3.5
s54	.01	1.0	192/3	Euler	.05	0-1000	3.5	30	.2	2.	300	9
s21	.01	1.25	192/3	Euler	.02	0-400	3.0	20	2.0	2.0	23	4.0
s28	.01	1.25	192/3	Euler	.01	0-200	3.0	22	2.0	2.5	44	2.0
s60	.01	1.0	192/3	Euler	.05	0-1000	1.9	18	2.1	1.5	250	8.2
s61	.01	2.0	192/3	Euler	.05	0-1000	2.5	25	2.0	1.9	110	3.5
s29	.01	2.5	192/3	Euler	.01	0-200	3.5	16	1.5	2.0	28	1.5
s62	.01	8.0	192/3	Euler	.05	0-1000	2	80	1.6	2.2	150	1.5
s56	.01	10.0	192/3	PC	.05	0-1000	2.2	155	3.0	2.9	230	2.9
s63	.01	10	192/3	Euler	.05	0-1000	2.0	50.	2.5	1.5	320	1.5
s57	.005	10.0	192/3	Euler	.05	0-1000	3.5	300	2.7	2.5	350	2.0
s65	.03	.5	192/3	Euler	.05	0-1000	2.9	11.	2.5	2.0	20.	3.1
s64	.03	1.	192/3	Euler	.05	0-1000	3.0	5.	3.2	2.	130.	6.5
s55	.03	10.	192/3	Euler	.05	0-1000	2.5	25	1.6	2.	320	1.2

Table 4.17 The velocity and variance correlation times (T^{α}) of the sheared sedimenting suspensions. The correlation times are in units of τ_h. C is the concentration, γ is the dimensionless shear rate, N is the number of particles used, dt is the step size, T is the length of the run, and pc is the predictor-corrector method.

Run	C	γ	N	Method	dt	T	T^{zz}_{vel}	T^{yy}_{vel}	T^{zz}_{vel}	T^{zz}_{var}	T^{yy}_{var}	T^{zz}_{var}
23	.01	.125	192/3	Euler	.01	0-200	.54	.86	.214	.32	.428	.32
24	.01	.25	192/3	Euler	.01	0-200	.32	1.07	.161	.15	1.7	.43
25	.01	.25	192/3	Euler	.01	0-200	.27	1.07	.161	.21	2.57	.16
26	.01	.5	192/3	Euler	.01	0-200	.161	1.29	.08	.08	.21	.13
27	.01	.5	192/3	Euler	.01	0-200	.161	.86	.107	.107	.64	.21
41	.01	.5	192/3	PC	.02	0-200	.17	1.07	.05	.05	1.18	.06
42	.01	.5	192/3	Euler	.02	0-200	.17	.43	.05	.05	1.18	.06
43	.01	.5	192/3	PC	.05	0-200	.13	.32	.04	.03	.21	.06
44	.01	.5	192/3	PC	.1	0-200	.13	1.07	.155	.134	.08	.15
45	.01	.5	192/3	Euler	.05	0-200	.18	.43	.011	.27	2.95	.273
46	.01	.5	192/3	Euler	.1	0-200	.16	1.87	.107	.13	4.	.134
51	.01	.5	192/3	Euler	.05	0-1000	.16	1.3	.13	.11	4.8	.29
53	.01	.5	192/3	Euler	.05	0-1000	.21	.78	.12	.13	8.	.187
54	.01	1.0	192/3	Euler	.05	0-1000	.094	.80	.005	.054	8.	.24
60	.01	1.0	192/3	Euler	.05	0-1000	.051	.48	.056	.04	6.69	.22
21	.01	1.25	192/3	Euler	.02	0-400	.064	.43	.043	.043	.49	.49
28	.01	1.25	192/3	Euler	.01	0-200	.064	.47	.043	.054	.94	.043
61	.01	2.0	192/3	Euler	.05	0-1000	.033	.33	.027	.025	1.47	.047
29	.01	2.5	192/3	Euler	.01	0-200	.038	.17	.016	.02	.3	.016
62	.01	8.0	192/3	Euler	.05	0-1000	.007	.27	.005	.007	.5	.005
56	.01	10.0	192/3	PC	.05	0-1000	.006	.42	.008	.008	.62	.008
63	.01	10	192/3	Euler	.05	0-1000	.005	.13	.007	.004	.85	.004
57	.005	10.0	192/3	Euler	.05	0-1000	.006	.51	.0046	.004	.85	.004
65	.03	.5	192/3	Euler	.05	0-1000	..323	1.2	.28	.22	2.2	.34
64	.03	1.	192/3	Euler	.05	0-1000	.167	.28	.18	.11	7.2	.36
55	.03	10.	192/3	Euler	.05	0-1000	.014	.139	.009	.01	1.78	.007

Table 4.18 The velocity and variance correlation times (T^i) of the sheared sedimenting suspensions. The correlation times are in units of τ_l. C is the concentration, γ is the dimensionless shear rate, N is the number of particles used, dt is the step size, T is the length of the run, and pc is the predictor-corrector method.

Run	C	γ	N	Method	dt	T	T^{xx}_{vel}	T^{yy}_{vel}	T^{zz}_{vel}	T^{xx}_{var}	T^{yy}_{var}	T^{zz}_{var}
s62	.01	8.0	192/3	Euler	.05	0-1000	.007	.27	.005	.007	.5	.005
s56	.01	10.0	192/3	PC	.05	0-1000	.006	.42	.008	.008	.62	.008
s63	.01	10	192/3	Euler	.05	0-1000	.005	.13	.007	.004	.85	.004
s57	.005	10.0	192/3	Euler	.05	0-1000	.006	.51	.0046	.004	.85	.004
s65	.03	.5	192/3	Euler	.05	0-1000	.323	1.2	.28	.22	2.2	.34
s64	.03	1.	192/3	Euler	.05	0-1000	.167	.28	.18	.11	7.2	.36
s55	.03	10.	192/3	Euler	.05	0-1000	.014	.139	.009	.01	1.78	.007

Table 4.18 continued

Run	C	γ	N	Method	dt	T	T^{xx}_{vel}	T^{yy}_{vel}	T^{zz}_{vel}	T^{xx}_{var}	T^{yy}_{var}	T^{zz}_{var}
s23	.01	.125	192/3	Euler	.01	0-200	1.5	10.3	.214	1.5	2.14	.64
s24	.01	.25	192/3	Euler	.01	0-200	-	1.07	.17	.32	1.7	.64
s25	.01	.25	192/3	Euler	.01	0-200	.64	6.8	.21	.27	3.4	.16
s26	.01	.5	192/3	Euler	.01	0-200	.64	7.7	1.93	.43	5.1	.81
s27	.01	.5	192/3	Euler	.01	0-200	1.07	8.57	.857	.75	5.1	1.67
s41	.01	.5	192/3	PC	.02	0-200	2.78	8.57	.43	.81	12.	1.24
s42	.01	.5	192/3	Euler	.02	0-200	1.6	7.7	.43	1.07	6.4	1.88
s43	.01	.5	192/3	PC	.05	0-200	.75	3.43	1.61	.77	3.	3.
s44	.01	.5	192/3	PC	.1	0-200	2.03	19.3	.96	1.37	1.11	1.63
s45	.01	.5	192/3	Euler	.05	0-200	2.6	3.43	1.18	1.5	11.8	2.14
s46	.01	.5	192/3	Euler	.1	0-200	1.6	18.	1.16	1.61	16.1	3.3
s51	.01	.5	192/3	Euler	.05	0-1000	1.4	57.9	2.04	.64	22.5	1.7
s53	.01	.5	192/3	Euler	.05	0-1000	-	.81	.96	2.76	36.4	1.4
s54	.01	1.0	192/3	Euler	.05	0-1000	.375	3.6	.29	.08	8.0	.67
s60	.01	1.0	192/3	Euler	.05	0-1000	.187	3.08	.29	.04	6.7	.32
s21	.01	1.25	192/3	Euler	.02	0-400	.107	1.5	.278	.086	.86	-
s28	.01	1.25	192/3	Euler	.01	0-200	.064	1.46	.386	.086	.94	.36
s61	.01	2.0	192/3	Euler	.05	0-1000	.075	1.54	.04	2	-	-
s29	.01	2.5	192/3	Euler	.01	0-200	.0187	.161	.011	.011	.15	.0187

Table 4.19 The velocity and variance correlation times (T^z) of the sheared sedimenting suspensions. The correlation times are in units of τ_l. C is the concentration, γ is the dimensionless shear rate, N is the number of particles used, dt is the step size, T is the length of the run, and pc is the predictor-corrector method.

Run	C	γ	N	Method	dt	T	T^{xx}_{vel}	T^{yy}_{vel}	T^{zz}_{vel}	T^{xx}_{var}	T^{yy}_{var}	T^{zz}_{var}
s62	.01	8.0	192/3	Euler	.05	0-1000	.015	.87	.005	.008	.50	.01
s56	.01	10.0	192/3	PC	.05	0-1000	.019	.429	.008	.008	.51	.018
s63	.01	10	192/3	Euler	.05	0-1000	.012	-	-.005	.522	.004	
s57	.005	10.0	192/3	Euler	.05	0-1000	.009	.084	.029	.005	-	.011
s65	.03	.5	192/3	Euler	.05	0-1000	1.78	12.5	.44	.28	5.8	.62
s64	.03	1.	192/3	Euler	.05	0-1000	.306	2.78	.947	.16	.36	-
s55	.03	10.	192/3	Euler	.05	0-1000	.043	.22	.009	.01	1.78	.007

Table 4.19 continued

Run	C	N	Method	dt	T	D_{xx} $U_s a$	D_{yy} $U_s a$	D_{zz} $U_s a$
q6	.01	64	Euler	.0005	0-100	5.7	.24	.44
q7	.01	64	Euler	.0005	0-100	5.4	.18	.14
q3	.01	64	Euler	.001	0-100	5.1	.18	.24
q4	.01	64	Euler	.001	0-100	6.0	.18	.24
q5	.01	64	Euler	.002	0-400	5.4	.13	.13
q43	.01	64	Euler	.005	0-100	4.5	.12	.16
q44	.01	64	Euler	.005	0-100	6.2	.15	.16
q45	.01	64	Euler	.005	0-100	7.7	.16	.13
q60	.01	64	Euler	.005	0-100	6.7	.15	.16
q10	.01	64	PC	.001	0-100	5.4	.16	.16
q11	.01	64	PC	.001	0-100	9.6	.17	.18
q29	.01	64	PC	.001	0-100	6.0	.16	.17
q30	.01	64	PC	.001	0-100	6.0	.14	.12
q8†	.01	64	Euler	.001	0-100	4.8	.15	.016
q9†	.01	64	Euler	.001	0-200	4.5	.15	.12
q1	.01	27	Euler	.001	0-100	4.4	.08	.1
q2	.01	27	Euler	.001	0-100	3.55	.08	.08
q12	.01	125	Euler	.001	0-50	5.9	.27	.22
q13	.01	125	Euler	.001	0-50	6.6	.27	.18
q14	.01	125	Euler	.001	0-50	6.2	.26	.22
q16	.01	125	PC	.001	0-50	6.9	.26	.18
q15†	.01	125	Euler	.001	0-50	5.0	.25	.22
q21‡	.01	64	Euler	.001	0-52	7.8	.14	.17
q22‡	.01	64	Euler	.001	0-50	4.8	.13	.10
q23‡	.01	125	Euler	.001	0-100	5.4	.17	.17

Table 4.20 The diffusion coefficent for the quiescent sedimenting suspensions. C is the concentration, N is the number of particles used, dt is the step size, T is the length of the run, D_{xx}, D_{yy}, and D_{zz} are the diffusion coefficients in the x, y, and z directions, respectively, and pc is the predictor-corrector method.
† runs performed with an initial configuration which has a deficit of close pairs.
‡ runs performed using the PAV method.

Run	C	N	Method	dt	T	D_{xx} U_*a	D_{yy} U_*a	D_{zz} U_*a
q50	.0025	64	Euler	.005	0-100	7.3	.17	.21
q51	.0025	64	Euler	.005	0-100	8.0	.15	.24
q17	.005	64	Euler	.001	0-100	6.6	-	-
q18	.005	64	Euler	.001	0-100	7.8	.12	.13
q19	.005	64	Euler	.001	0-100	8.4	.2	.16
q48	.005	64	Euler	.005	0-100	7.6	.12	.23
q49	.005	64	Euler	.005	0-100	11.0	.15	.14
q20†	.005	64	Euler	.001	0-200	11.5	.13	.16
q62	.005	27	Euler	.005	0-200	4.1	.11	.075
q63	.005	27	Euler	.005	0-200	3.2	.1	.07
q56	.005	125	Euler	.005	0-100	14.0	.21	.18
q57	.005	125	Euler	.005	0-100	14.0	.19	.21
q46	.02	64	Euler	.005	0-100	3.9	.12	.12
q47	.02	64	Euler	.005	0-100	5.9	.16	.17
q64	.02	27	Euler	.005	0-200	2.5	.14	.13
q65	.02	27	Euler	.005	0-200	3.1	.11	.13
q54	.02	125	Euler	.005	0-100	6.2	.19	.21
q55	.02	125	Euler	.005	0-100	6.9	.22	.23
q42	.03	64	Euler	.005	0-100	4.0	.13	.13
q52	.03	64	Euler	.005	0-100	5.7	.13	.15
q53	.03	64	Euler	.005	0-100	6.0	.13	.16
q61	.03	64	Euler	.005	0-100	4.7	.14	.12
q35	.03	64	Euler	.002	0-100	4.5	.11	.13
q40	.03	64	PC	.002	0-100	5.0	.14	.17
q41	.03	64	PC	.01	0-100	4.5	.2	.2
q34	.03	64	PC	.01	0-100	3.5	.15	.17
q37	.03	64	Euler	.01	0-100	4.4	.18	.12
q58	.05	64	Euler	.005	0-100	4.5	.12	.15
q59	.05	64	Euler	.005	0-100	2.9	.09	.09

Table 4.20 continued.

Run	C	γ	N	Method	dt	T	$\frac{D_{xx}}{U_s a}$	$\frac{D_{yy}}{U_s a}$	$\frac{D_{zz}}{U_s a}$
s23	.01	.125	192/3	Euler	.01	0-200	7.7	110	.12
s24	.01	.25	192/3	Euler	.01	0-200	3.5	800	.1
s25	.01	.25	192/3	Euler	.01	0-200	4.25	-	.09
s26	.01	.5	192/3	Euler	.01	0-200	2.3	-	.065
s27	.01	.5	192/3	Euler	.01	0-200	2.6	2200	.07
s41	.01	.5	192/3	PC	.02	0-200	2.4	-	.07
s42	.01	.5	192/3	Euler	.02	0-200	4.5	-	.07
s43	.01	.5	192/3	PC	.05	0-200	-	-	.063
s44	.01	.5	192/3	PC	.1	0-200	-	-	.065
s45	.01	.5	192/3	Euler	.05	0-200	-	-	.072
s46	.01	.5	192/3	Euler	.1	0-200	-	-	.08
s51	.01	.5	192/3	Euler	.05	0-1000	3.0	3600	.076
s53	.01	.5	192/3	Euler	.05	0-1000	6.0	3900	.07
s54	.01	1.0	192/3	Euler	.05	0-1000	3.0	1.8e4	.06
s60	.01	1.0	192/3	Euler	.05	0-1000	2.3	1.7e4	.04
s21	.01	1.25	192/3	Euler	.02	0-400	2.43	-	.056
s28	.01	1.25	192/3	Euler	.01	0-200	-	-	.04
s61	.01	2.0	192/3	Euler	.05	0-1000	1.3	-	.049
s29	.01	2.5	192/3	Euler	.01	0-200	.38	-	.048
s17	.01	2.5	192/3	Euler	.1	0-800	.58	-	.007
s16	.01	5.	192/3	Euler	.1	0-800	-	-	-

Table 4.21 The diffusion coefficients for the sheared sedimenting suspensions. C is the concentration, γ is the dimensionless shear rate, N is the number of particles used, dt is the step size, T is the length of the run, D_{xx}, D_{yy}, and D_{zz} are the diffusion coefficients in the x, y, and z directions, respectively, and pc is the predictor-corrector method.

Run	C	γ	N	Method	dt	T	$\frac{D_{xx}}{U_s a}$	$\frac{D_{yy}}{U_s a}$	$\frac{D_{zz}}{U_s a}$
s62	.01	8.0	192/3	Euler	.05	0-1000	.24	-	-
s56	.01	10.0	192/3	PC	.05	0-1000	-	-	.07
s63	.01	10	192/3	Euler	.05	0-1000	.2	-	.029
s7	.01	13.3	192/3	Euler	.1	0-300	-	-	-
s8	.01	13.3	192/3	Euler	.1	0-800	.42	-	.06
s9	.01	13.3	192/3	Euler	.05	0-800	.62	-	.025
s10	.01	13.3	192/3	Euler	.1	0-800	-	-	.06
s11	.01	13.3	192/3	Euler	.1	0-800	-	-	-
s20	.01	13.3	192/3	Euler	.1	0-800	-	-	-
s3	.01	17.8	135/3	Euler	.1	0-800	.2	-	.056
s4	.01	17.8	135/3	Euler	.1	0-800	.36	-	.03
s5	.01	17.8	135/3	Euler	.1	0-1600	.25	-	.03
s6	.01	17.8	135/3	Euler	.05	0-800	.35	-	.026
s14	.005	10.6	192/3	Euler	.1	0-800	.12	-	.01
s15	.005	10.6	192/3	Euler	.1	0-800	-	-	-
s57	.005	10.0	192/3	Euler	.05	0-1000	.80	-	.08
s18	.02	16.8	192/3	Euler	.1	0-800	.81	-	.06
s19	.02	16.8	192/3	Euler	.1	0-800	.43	-	.05
s65	.03	.5	192/3	Euler	.05	0-1000	3.5	600	.092
s64	.03	1.	192/3	Euler	.05	0-1000	2.1	3.4e3	.068
s55	.03	10.	192/3	Euler	.05	0-1000	.46	-	.024

Table 4.21 continued.

Run	C	N	Method	dt	T	$\mathcal{D}_x$ U,a	$\mathcal{D}_y$ U,a	$\mathcal{D}_z$ U,a
q43	.01	64	Euler	.005	0-100	4.7	.15	.15
q45	.01	64	Euler	.005	0-100	7.5	.17	.13
q60	.01	64	Euler	.005	0-100	8.5	.18	.17
q50	.0025	64	Euler	.005	0-100	7.5	.18	.19
q51	.0025	64	Euler	.005	0-100	7.8	.14	.22
q48	.005	64	Euler	.005	0-100	7.5	.12	.26
q49	.005	64	Euler	.005	0-100	12.	.14	.14
q62	.005	27	Euler	.005	0-200	-	-	.09
q63	.005	27	Euler	.005	0-200	3.6	.1	.08
q56	.005	125	Euler	.005	0-100	12.	.22	.18
q57	.005	125	Euler	.005	0-100	13.	.21	.22
q46	.02	64	Euler	.005	0-100	3.2	.11	.14
q47	.02	64	Euler	.005	0-100	5.5	.15	.2
q64	.02	27	Euler	.005	0-200	3.0	.14	.11
q65	.02	27	Euler	.005	0-200	3.0	.10	.14
q54	.02	125	Euler	.005	0-100	7.9	.19	.21
q55	.02	125	Euler	.005	0-100	6.7	.2	.22
q52	.03	64	Euler	.005	0-100	5.8	.15	.15
q53	.03	64	Euler	.005	0-100	5.	.14	.14
q61	.03	64	Euler	.005	0-100	-	.14	.12
q58	.05	64	Euler	.005	0-100	5.2	-	.15
q59	.05	64	Euler	.005	0-100	3.9	-	.12

Table 4.22 The diffusion coefficent with restart for the quiescent sedimenting suspensions. C is the concentration, N is the number of particles used, dt is the step size, T is the length of the run, D_{xx}, D_{yy}, and D_{zz} are the diffusion coefficients in the x, y, and z directions, respectively, and pc is the predictor-corrector method.
† runs performed with an initial configuration which has a deficit of close pairs.
‡ runs performed using the PAV method.

Run	C	γ	N	Method	dt	T	$\mathcal{D}_x$ U,a	$\mathcal{D}_y$ U,a	$\mathcal{D}_z$ U,a
s51	.01	.5	192/3	Euler	.05	0-1000	3.25	-	.08
s53	.01	.5	192/3	Euler	.05	0-1000	3.6	-	.07
s54	.01	1.0	192/3	Euler	.05	0-1000	2.1	-	.05
s60	.01	1.0	192/3	Euler	.05	0-1000	-	-	.04
s61	.01	2.0	192/3	Euler	.05	0-1000	1.2	-	.04
s62	.01	8.0	192/3	Euler	.05	0-1000	-	-	-
s56	.01	10.0	192/3	PC	.05	0-1000	-	-	.11
s63	.01	10	192/3	Euler	.05	0-1000	-	-	-
s57	.005	10.0	192/3	Euler	.05	0-1000	-	-	.13
s65	.03	.5	192/3	Euler	.05	0-1000	3.6	590	.09
s64	.03	1.	192/3	Euler	.05	0-1000	-	-	-
s55	.03	10.	192/3	Euler	.05	0-1000	.27	-	.02

Table 4.23 The diffusion coefficent with restart for the sheared sedimenting suspensions. C is the concentration, γ is the dimensionless shear rate, N is the number of particles used, dt is the step size, T is the length of the run, D_{xx}, D_{yy}, and D_{zz} are the diffusion coefficients in the x, y, and z directions, respectively, and pc is the predictor-corrector method.

Run	C	N	Method	dt	T	τ_x	τ_y	τ_z
q6	.01	64	Euler	.0005	0-100	1.0	.178	.39
q7	.01	64	Euler	.0005	0-100	.91	.15	.12
q3	.01	64	Euler	.001	0-100	.86	.16	.21
q4	.01	64	Euler	.001	0-100	.96	.15	.20
q5	.01	64	Euler	.002	0-400	.87	.116	.116
q43	.01	64	Euler	.005	0-100	.67	.10	.134
q44	.01	64	Euler	.005	0-100	.93	.13	.14
q45	.01	64	Euler	.005	0-100	1.12	.13	.11
q60	.01	64	Euler	.005	0-100	.94	.12	.13
q10	.01	64	PC	.001	0-100	1.68	.14	.13
q11	.01	64	PC	.001	0-100	3.47	.14	.15
q29	.01	64	PC	.001	0-100	1.64	.13	.14
q30	.01	64	PC	.001	0-100	1.54	.12	.1
q8†	.01	64	Euler	.001	0-100	.8	.13	.13
q9†	.01	64	Euler	.001	0-200	.76	.14	.11
q1	.01	27	Euler	.001	0-100	1.16	.11	.13
q2	.01	27	Euler	.001	0-100	.86	.11	.11
q12	.01	125	Euler	.001	0-50	.72	.16	.13
q13	.01	125	Euler	.001	0-50	.74	.18	.12
q14	.01	125	Euler	.001	0-50	.76	.17	.15
q16	.01	125	PC	.001	0-50	.97	.18	.12
q15†	.01	125	Euler	.001	0-50	.71	.167	.15
q21‡	.01	64	Euler	.001	0-52	.95	.09	.11
q22‡	.01	64	Euler	.001	0-50	.64	.087	.07
q23‡	.01	125	Euler	.001	0-100	.8	.11	.11

Table 4.24 The correlation times derived from the diffusion coefficients and the variances for the quiescent sedimenting suspensions in units of τ_l. C is the concentration, N is the number of particles used, dt is the step size, T is the length of the run, and pc is the predictor-corrector method.

Run	C	N	Method	dt	T	τ_x	τ_y	τ_z
q50	.0025	64	Euler	.005	0-100	.81	.13	.16
q51	.0025	64	Euler	.005	0-100	.8	.11	.18
q17	.005	64	Euler	.001	0-100	.93	-	-
q18	.005	64	Euler	.001	0-100	.73	.1	.11
q19	.005	64	Euler	.001	0-100	1.01	.169	.135
q48	.005	64	Euler	.005	0-100	.92	.10	.194
q49	.005	64	Euler	.005	0-100	1.32	.13	.12
q20†	.005	64	Euler	.001	0-200	1.39	.11	.14
q62	.005	27	Euler	.005	0-200	.79	.13	.092
q63	.005	27	Euler	.005	0-200	.63	.12	.086
q56	.005	125	Euler	.005	0-100	1.23	.126	.11
q57	.005	125	Euler	.005	0-100	1.22	.11	.127
q46	.02	64	Euler	.005	0-100	.87	.128	.128
q47	.02	64	Euler	.005	0-100	1.14	.17	.181
q64	.02	27	Euler	.005	0-200	.82	.21	.2
q65	.02	27	Euler	.005	0-200	.98	.167	.2
q54	.02	125	Euler	.005	0-100	.82	.13	.14
q55	.02	125	Euler	.005	0-100	.92	.15	.15
q42	.03	64	Euler	.005	0-100	.8	.13	.13
q52	.03	64	Euler	.005	0-100	1.13	.13	.14
q53	.03	64	Euler	.005	0-100	1.11	.13	.15
q61	.03	64	Euler	.005	0-100	.94	.14	.12
q35	.03	64	Euler	.002	0-100	.96	.11	.13
q40	.03	64	PC	.002	0-100	1.07	.14	.169
q41	.03	64	PC	.01	0-100	1.04	.21	.2
q34	.03	64	PC	.01	0-100	.81	.16	.16
q37	.03	64	Euler	.01	0-100	.94	.17	.12
q58	.05	64	Euler	.005	0-100	1.18	.12	.168
q59	.05	64	Euler	.005	0-100	.9	.1	.1

Table 4.24 continued.

Run	C	γ	N	Method	dt	T	τ_x	τ_y	τ_z	τ'_x	τ'_y	τ'_z
s23	.01	.125	192/3	Euler	.01	0-200	.43	1.3	.094	2.0	6.1	.44
s24	.01	.25	192/3	Euler	.01	0-200	.21	2.2	.08	1.96	20.	.75
s25	.01	.25	192/3	Euler	.01	0-200	.22	-	.07	2.0	-	.65
s26	.01	.5	192/3	Euler	.01	0-200	.14	-	.05	2.6	-	.93
s27	.01	.5	192/3	Euler	.01	0-200	.16	1.66	.05	3.0	31	.93
s41	.01	.5	192/3	PC	.02	0-200	.14	-	.05	2.6	-	.93
s42	.01	.5	192/3	Euler	.02	0-200	.27	-	.06	5.0	-	1.1
s51	.01	.5	192/3	Euler	.05	0-1000	.19	2.55	.06	3.5	-	1.1
s53	.01	.5	192/3	Euler	.05	0-1000	.14	2.67	.055	2.6	4.98	1.0
s54	.01	1.0	192/3	Euler	.05	0-1000	.184	3.2	.041	6.9	119	1.53
s60	.01	1.0	192/3	Euler	.05	0-1000	.15	3.13	.028	5.6	117.	1.04
s21	.01	1.25	192/3	Euler	.02	0-400	.15	-	.034	7.0	-	1.6
s61	.01	2.0	192/3	Euler	.05	0-1000	.09	-	.027	6.7	-	2.01
s29	.01	2.5	192/3	Euler	.01	0-200	.024	-	.016	2.2	-	1.5
s17	.01	2.5	192/3	Euler	.1	0-800	.04	-	.003	3.7	-	.28
s62	.01	8.0	192/3	Euler	.05	0-1000	.01	-	-	3.0	-	-
s63	.01	10	192/3	Euler	.05	0-1000	.01	-	.001	3.7	-	.37
s8	.01	13.3	192/3	Euler	.1	0-800	.02	-	.001	9.9	-	.73
s9	.01	13.3	192/3	Euler	.05	0-800	.026	-	0.0	12.9	-	.25
s3	.01	17.8	135/3	Euler	.1	0-800	.006	-	.001	4.0	-	.66
s4	.01	17.8	135/3	Euler	.1	0-800	.01	-	0.0	6.6	-	.26
s5	.01	17.8	135/3	Euler	.1	0-1600	.008	-	0.0	5.3	-	.26
s6	.01	17.8	135/3	Euler	.05	0-800	.011	-	0.0	7.3	-	.24
s14	.005	10.6	192/3	Euler	.1	0-800	.006	-	0.0	3.6	-	.31
s57	.005	10.0	192/3	Euler	.05	0-1000	.035	-	.007	2.1	-	3.9
s18	.02	16.8	192/3	Euler	.1	0-800	.025	-	.001	9.9	-	.4
s19	.02	16.8	192/3	Euler	.1	0-800	.014	-	.001	5.5	-	.4
s65	.03	.5	192/3	Euler	.05	0-1000	.26	1.84	.08	2.33	16.5	.72
s64	.03	1.	192/3	Euler	.05	0-1000	.17	2.62	.002	3.1	47.	.04
s55	.03	10.	192/3	Euler	.05	0-1000	.02	-	.001	3.6	-	.18

Table 4.25 The correlation times derived from the diffusion coefficients and the variances for the sheared sedimenting suspensions in units of τ_h. C is the concentration, γ is the dimensionless shear rate, N is the number of particles used, dt is the step size, T is the length of the run.

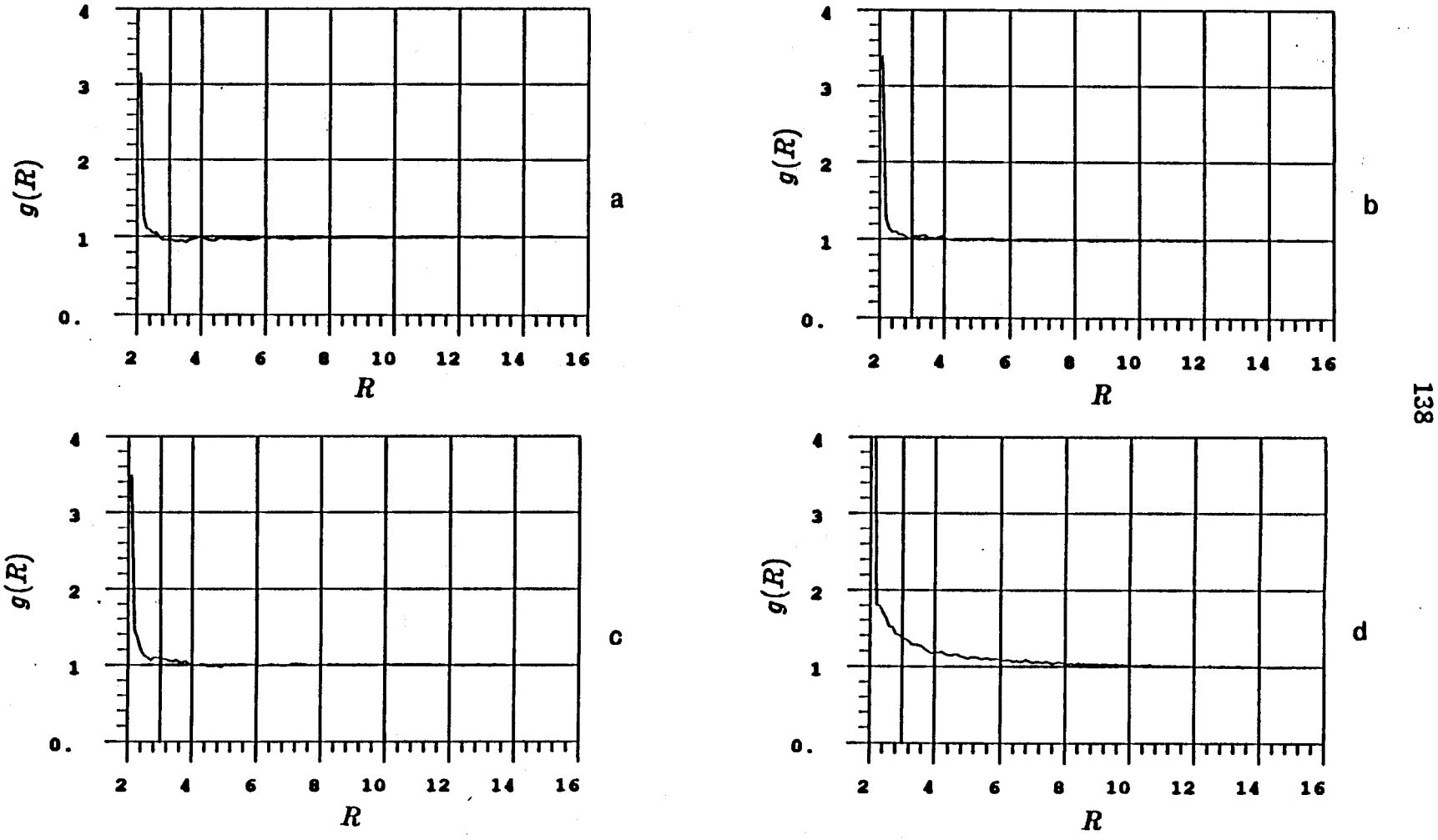

Figure 4.1 The effect of step size on the radial distribution for a 1% quiescent sedimenting suspension using the Euler integration scheme. (a) is step size of 0.001, (b) is step size of 0.005, (c) is step size of 0.01, and (d) is step size of 0.1.

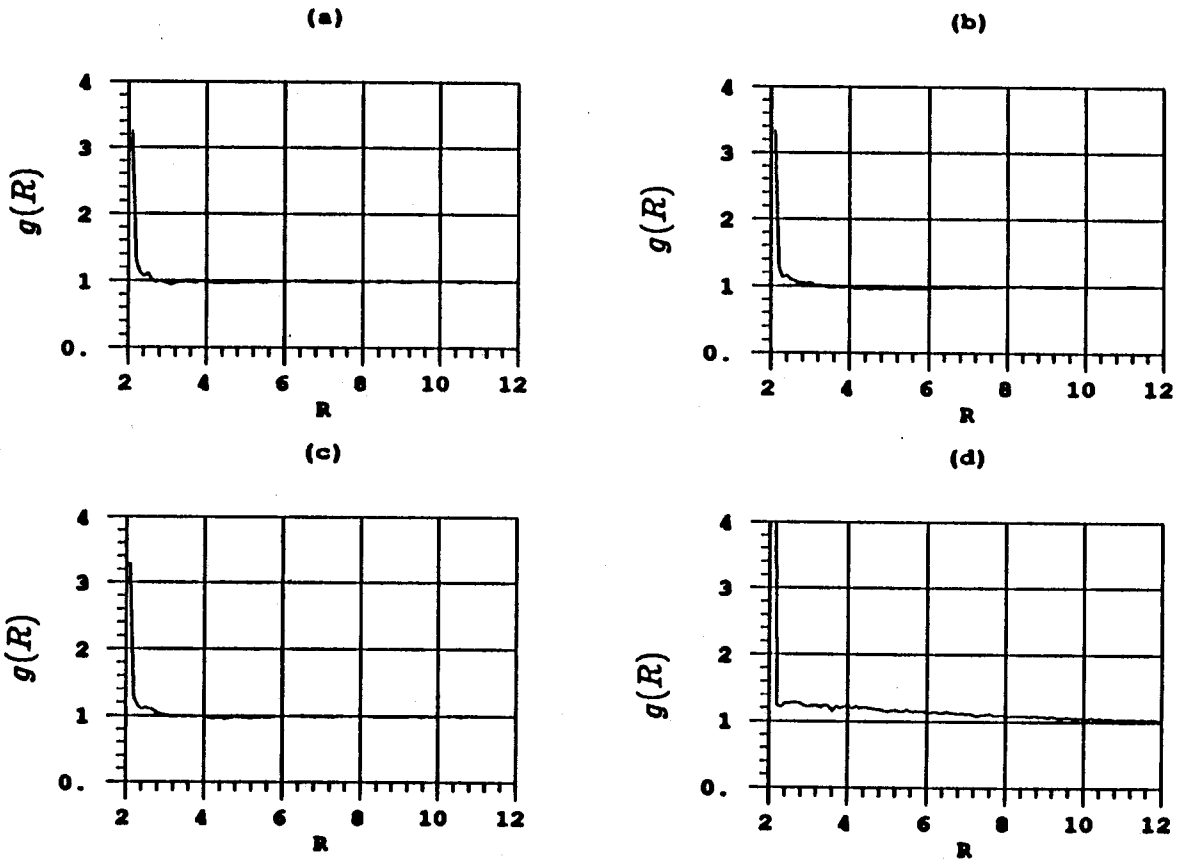

Figure 4.2 The effect of step size on the radial distribution for a 1% quiescent sedimenting suspension using a predictor-corrector integration scheme. (a) is step size of 0.001, (b) is step size of 0.005, (c) is step size of 0.01, and (d) is step size of 0.1.

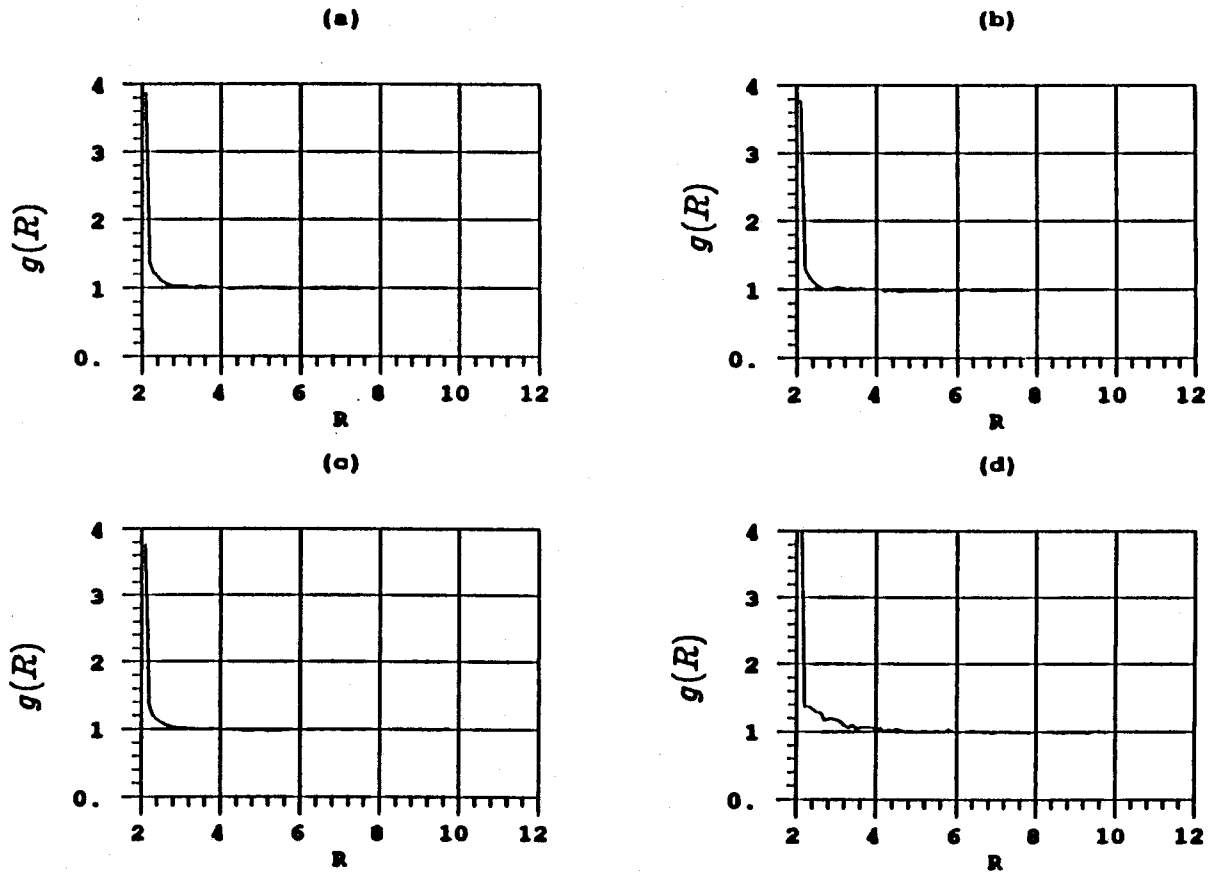

Figure 4.3 The effect of step size on the radial distribution for a 3% quiescent sedimenting suspension using the Euler integration scheme. (a) is step size of 0.002, (b) is step size of 0.01, (c) is step size of 0.02, and (d) is step size of 0.1.

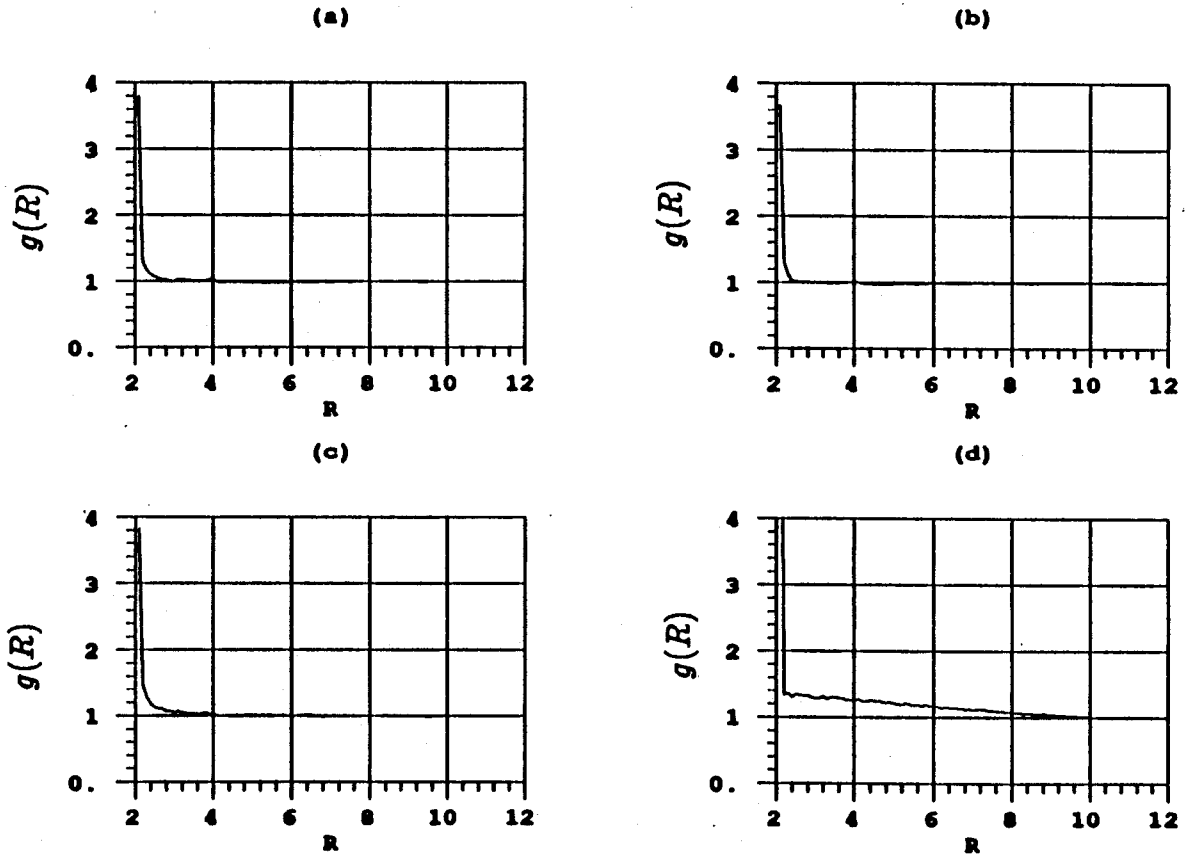

Figure 4.4 The effect of step size on the radial distribution for a 3% quiescent sedimenting suspension using a predictor-corrector integration scheme. (a) is step size of 0.002, (b) is step size of 0.01, (c) is step size of 0.02, and (d) is step size of 0.1.

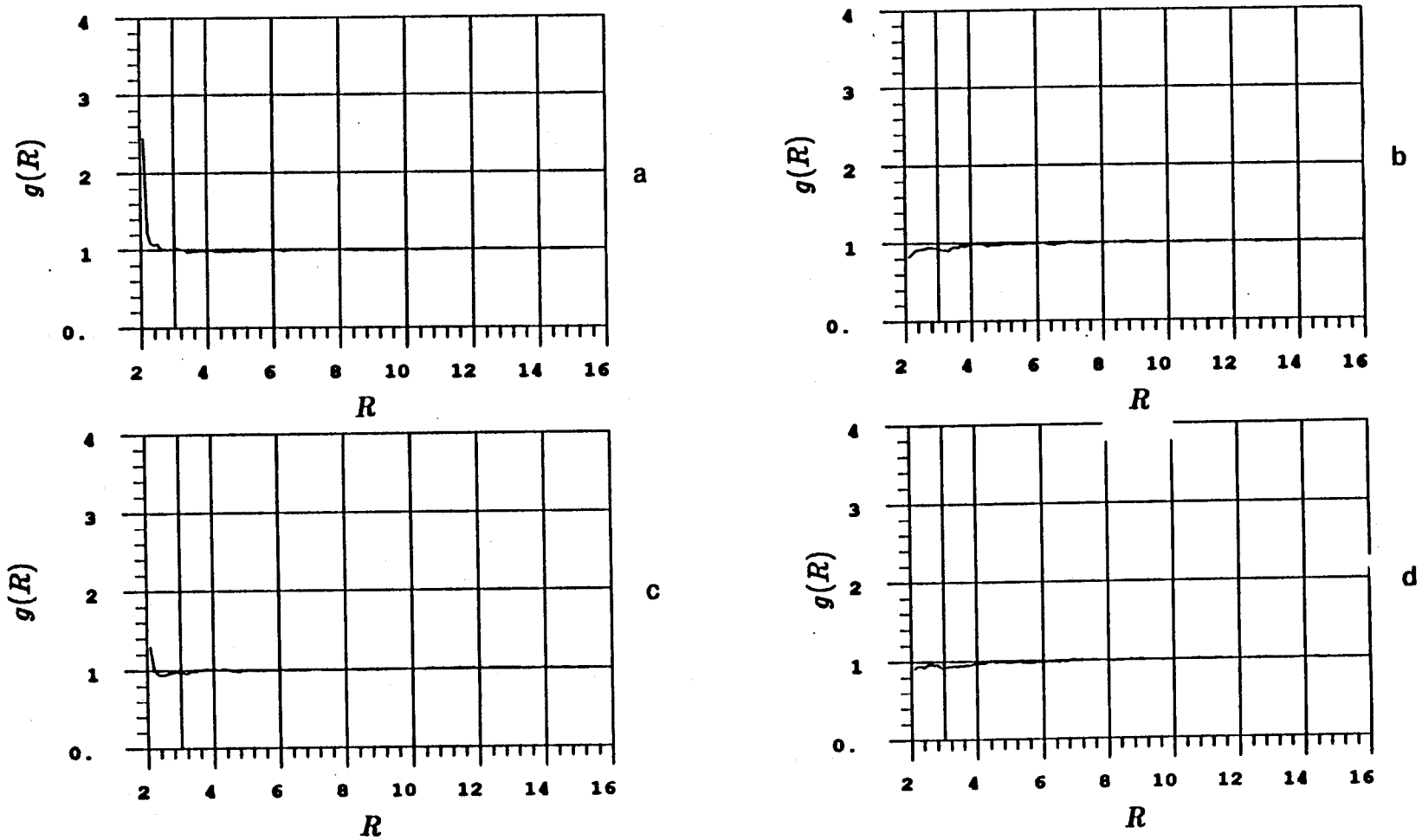

Figure 4.5 The effect of step size on the radial distribution for a 1% sheared sedimenting suspension subjected to a shear rate of 20 and performed using an euler integration scheme. (a) is step size of 0.01, (b) is step size of 0.02, (c) is step size of 0.05, and (d) is step size of 0.1.

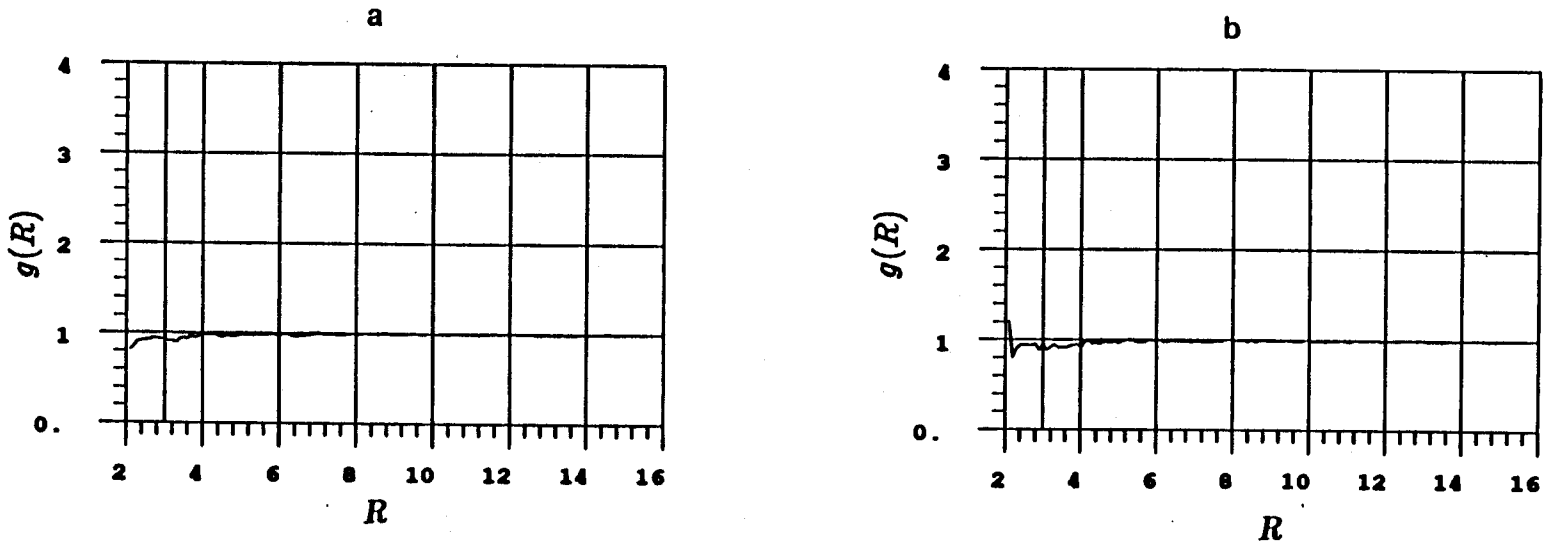

Figure 4.6 The effect of step size on the radial distribution for a 1% sheared sedimenting suspension subjected to a shear rate of 20.0 and performed using a predictor-corrector integration scheme. (a) is step size of 0.2, and (b) is step size of 0.5.

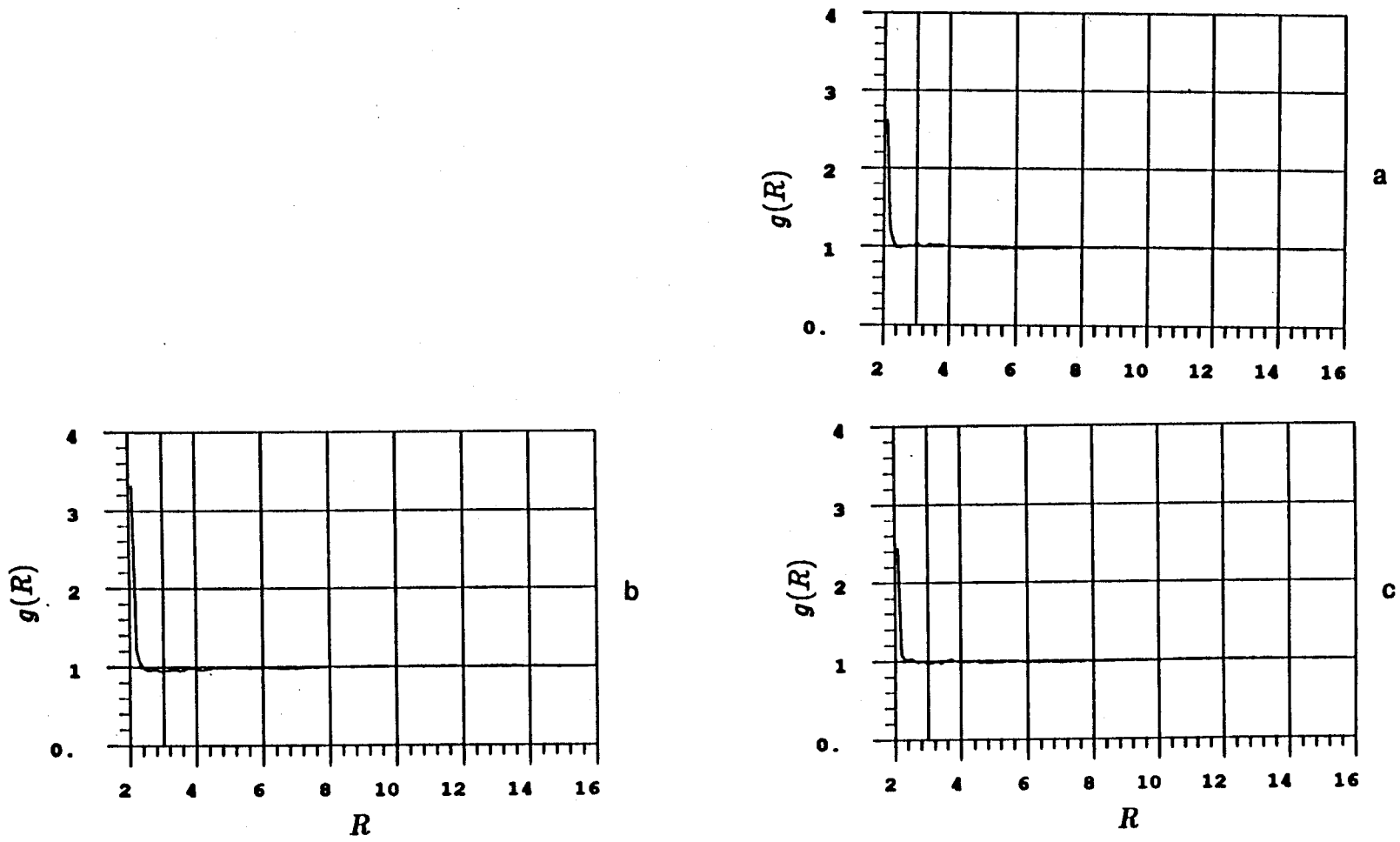

Figure 4.7 The effect of step size on the radial distribution for a 1% quiescent sedimenting suspension subjected to a shear rate of 20.0 and performed using a predictor-corrector integration scheme. (a) is step size of 0.02, (b) is step size of 0.05, and (c) is step size of 0.1.

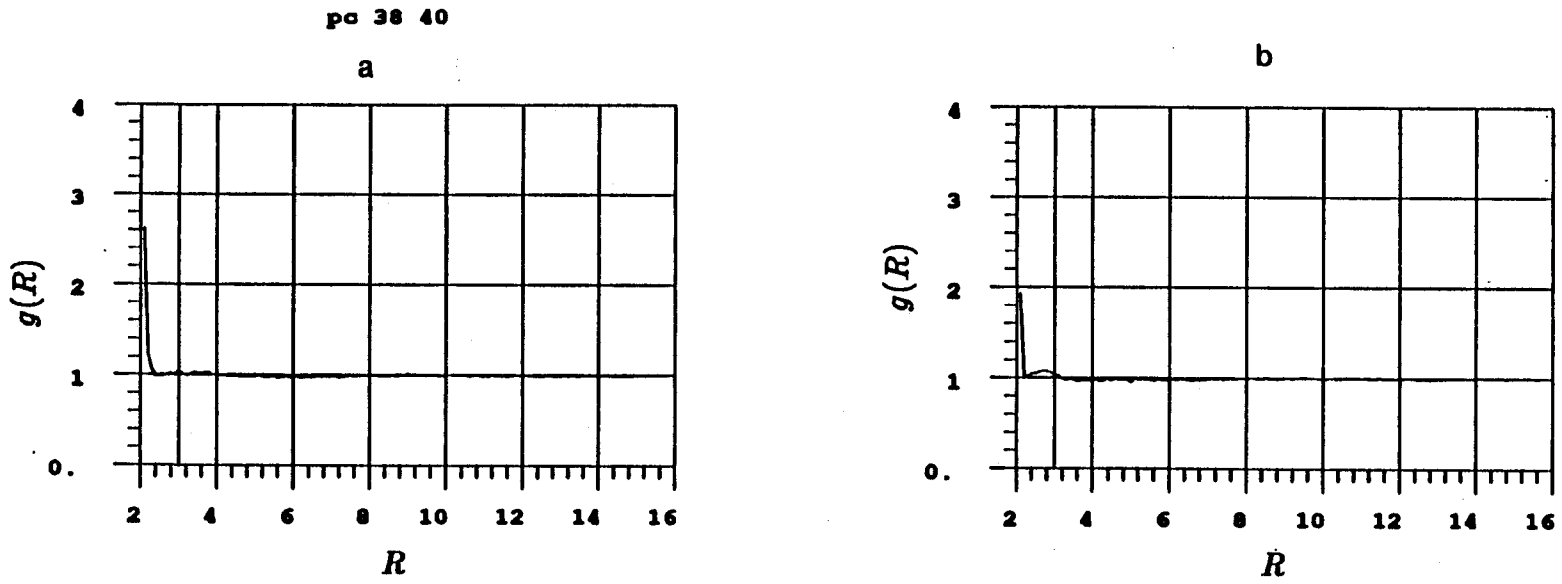

Figure 4.8 The effect of step size on the radial distribution for a 1% quiescent sedimenting suspension subjected to a shear rate of 20.0 and performed using a predictor-corrector integration scheme. (a) is step size of 0.2, and (b) is step size of 0.5.

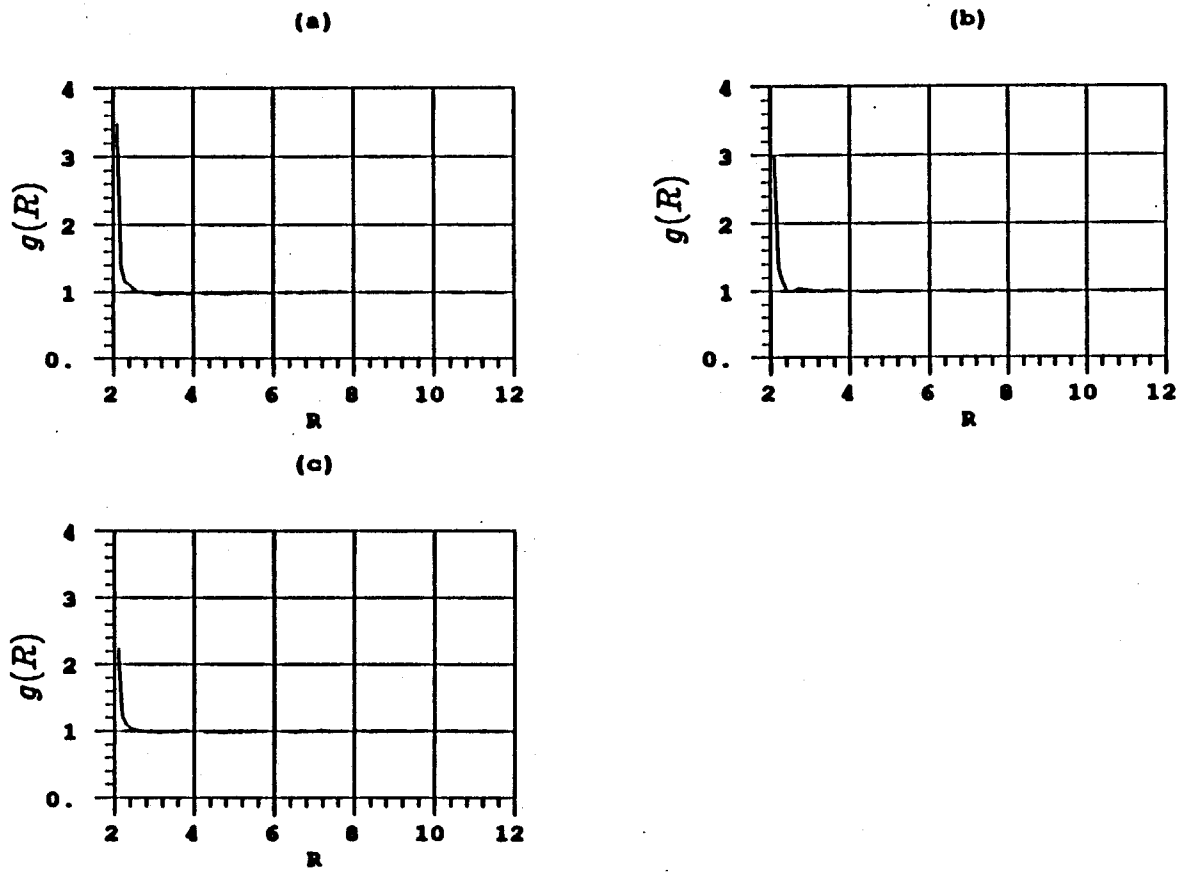

Figure 4.9 The effect of step size on the radial distribution for a 1% quiescent sedimenting suspension subjected to a shear rate of 0.5 and performed using the Euler integration scheme. (a) is step size of 0.02, (b) is step size of 0.05, and (c) is step size of 0.1.

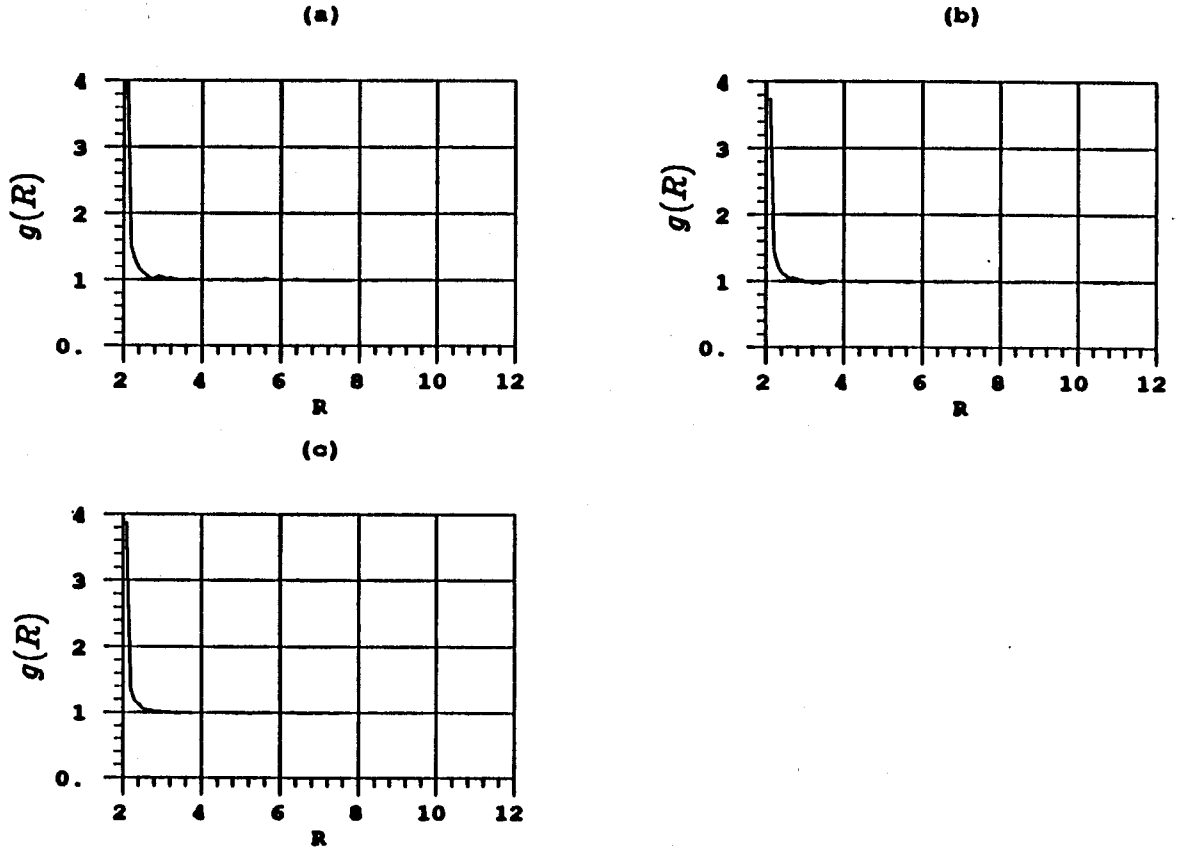

Figure 4.10 The effect of step size on the radial distribution for a 1% quiescent sedimenting suspension subjected to a shear rate of 0.5 and performed using a predictor-corrector integration scheme. (a) is step size of 0.02, (b) is step size of 0.05, and (c) is step size of 0.1.

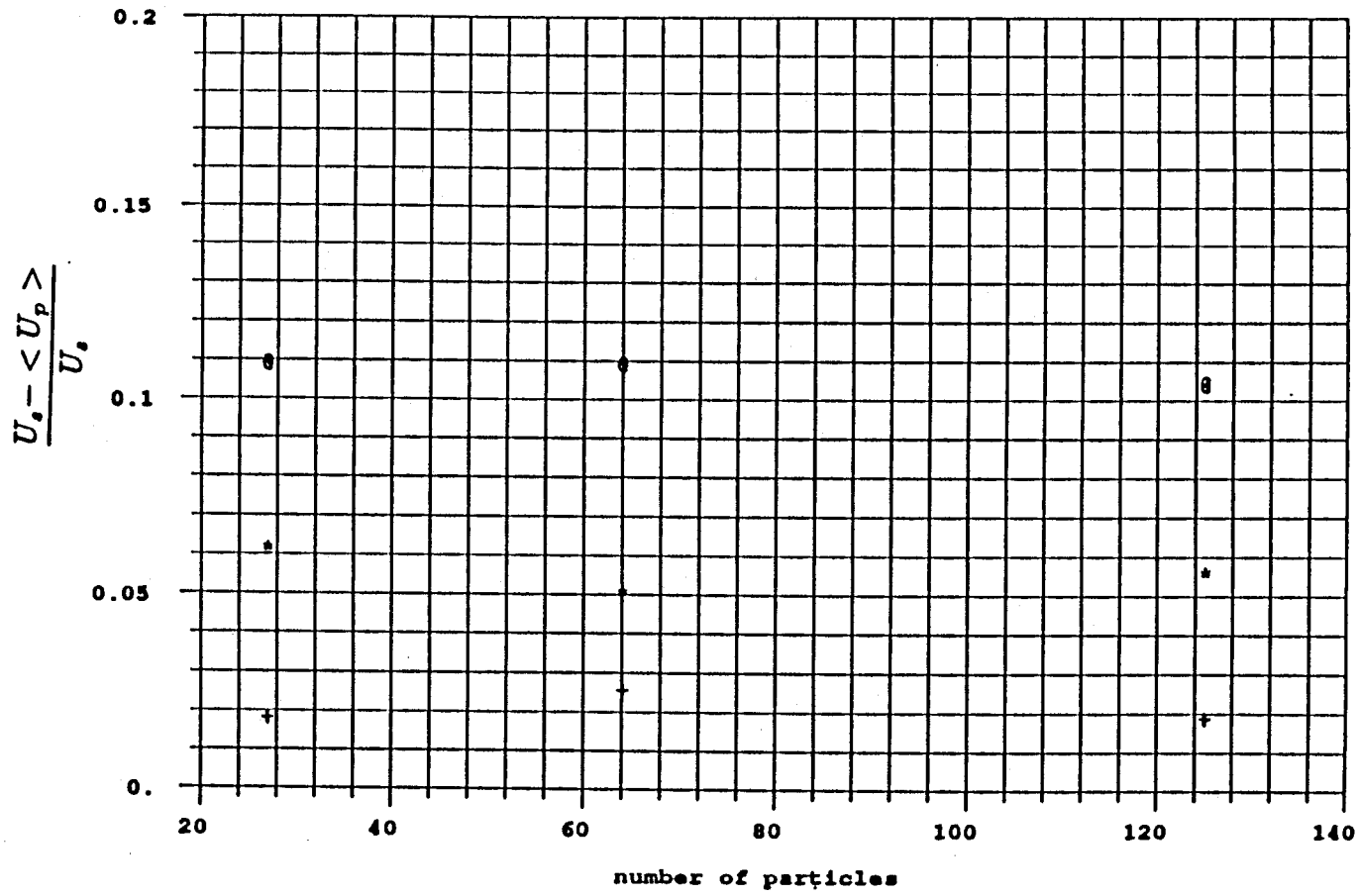

Figure 4.11 Sedimentation velocity's dependence on the number of particles used in the simulator. The simulations are performed using the Euler integration scheme and a step size of 0.005. The symbols *, x, and @ are for a suspension of 0.5%, 1.0%, and 2.0%, respectively.

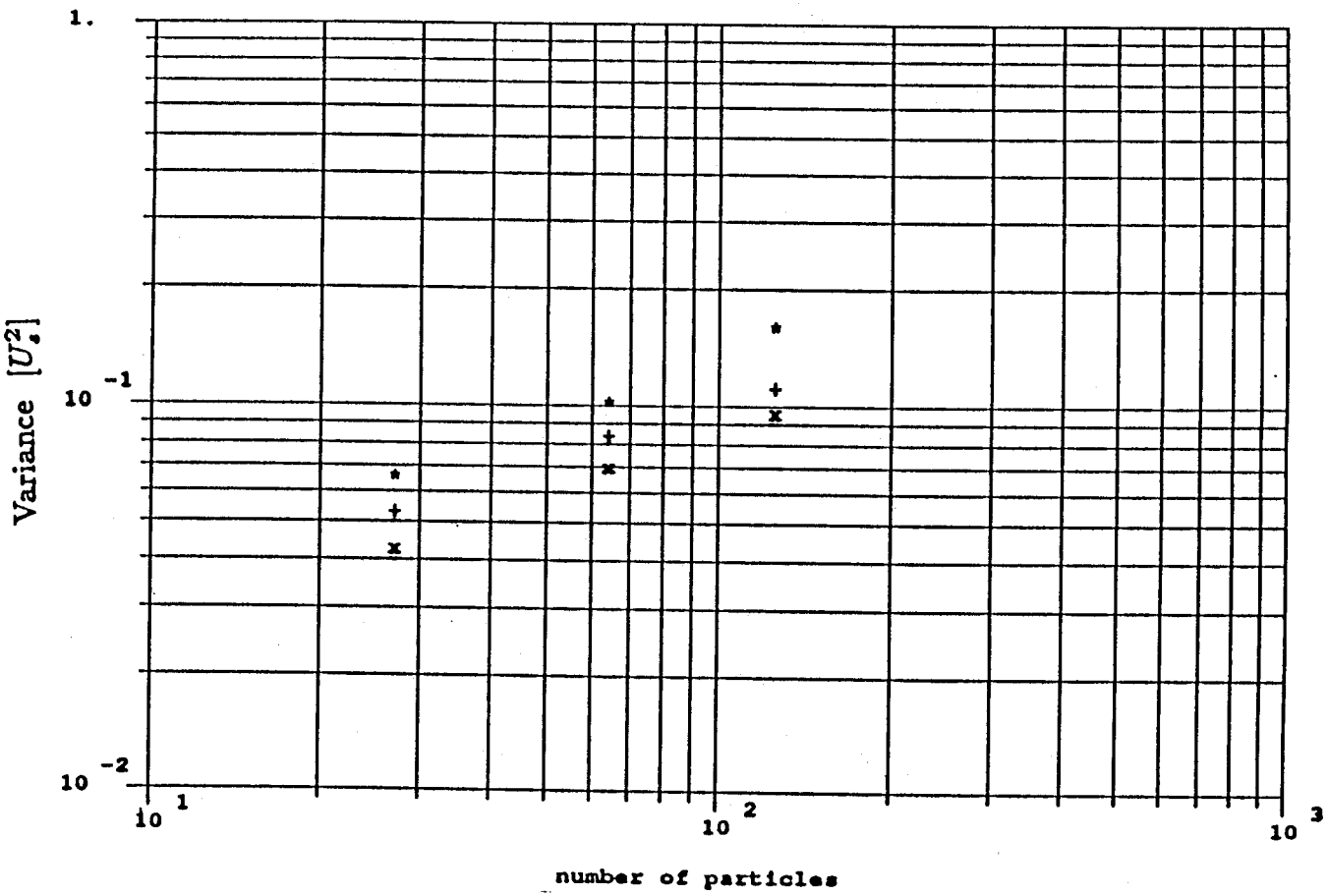

Figure 4.12 The dependence of the x variance on the number of particles used in the simulator. The simulations are performed using the Euler integration scheme and a step size of 0.005. The symbols x, +, and * are for a suspension of 0.5%, 1.0%, and 2.0%, respectively.

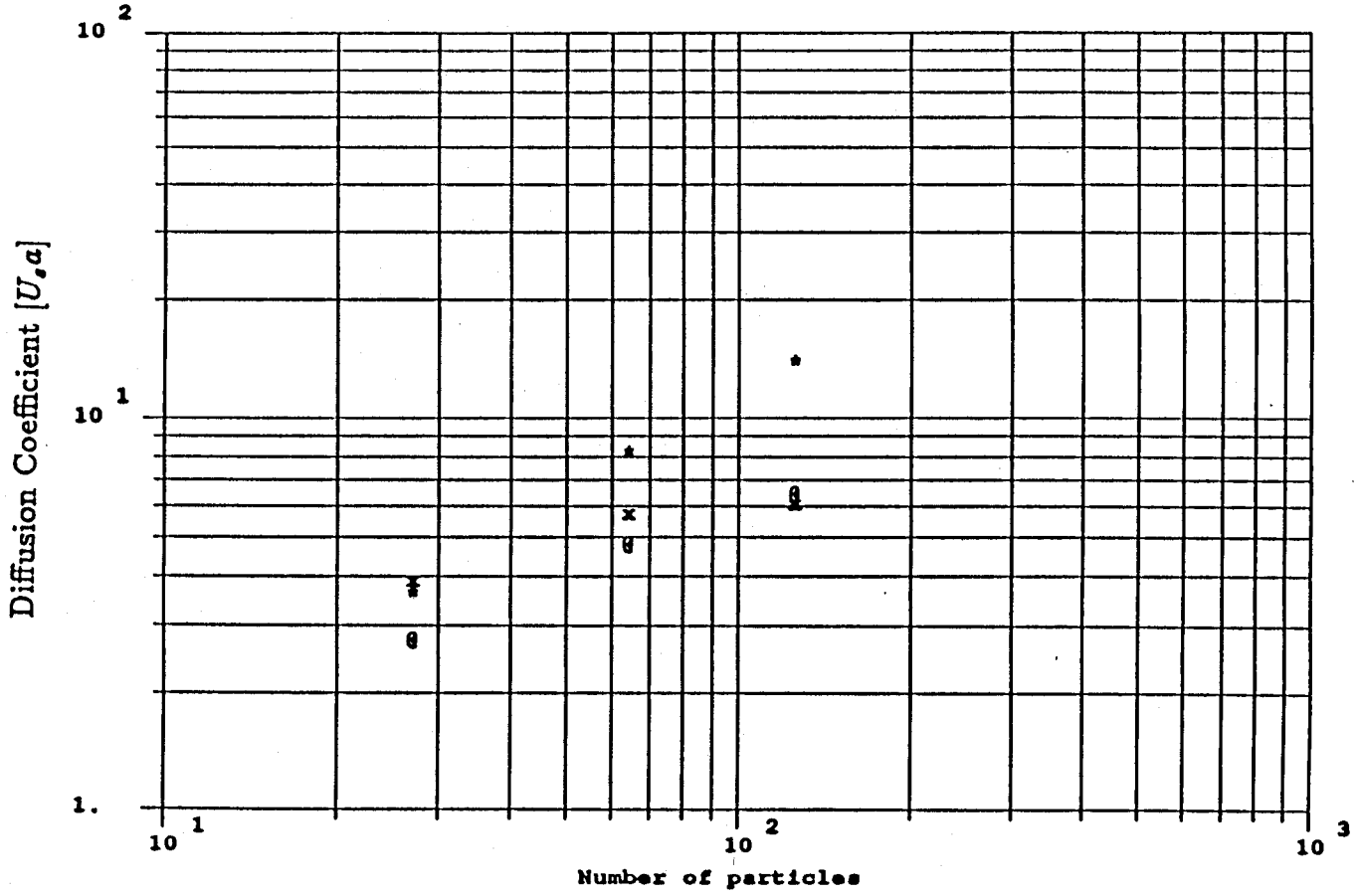

Figure 4.13 The dependence of the x diffusion coefficient on the number of particles used in the simulator. The simulations are performed using the Euler integration scheme and a step size of 0.005. The symbols *, x, and @ are for a suspension of 0.5%, 1.0%, and 2.0%, respectively.

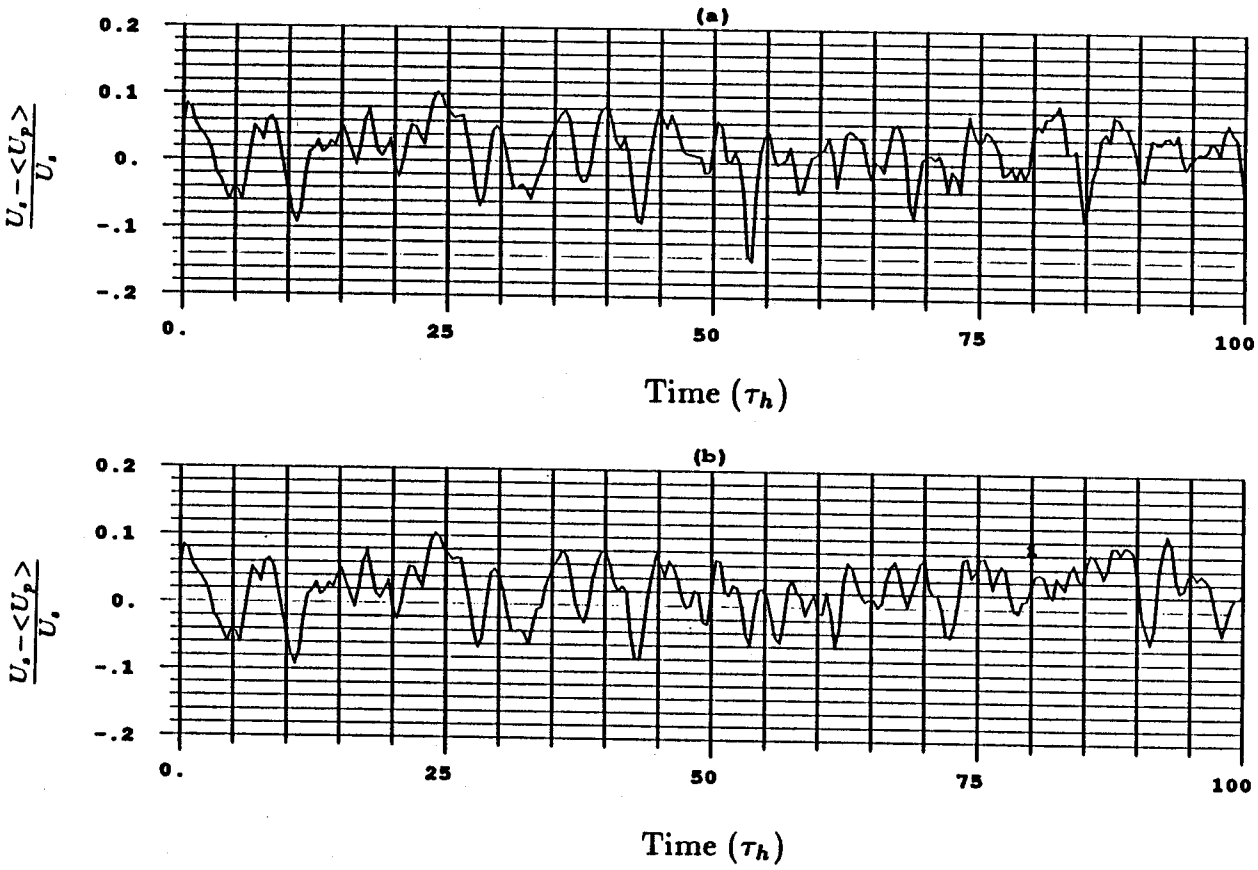

Figure 4.14 The chaotic behavior of the simulator. Both runs were performed using the same initial configuration, 192 particles, step size of 0.01 τ_h and the predictor-corrector integrator. (a) did not use the floating point accelerator. (b) used the floating point accelerator.

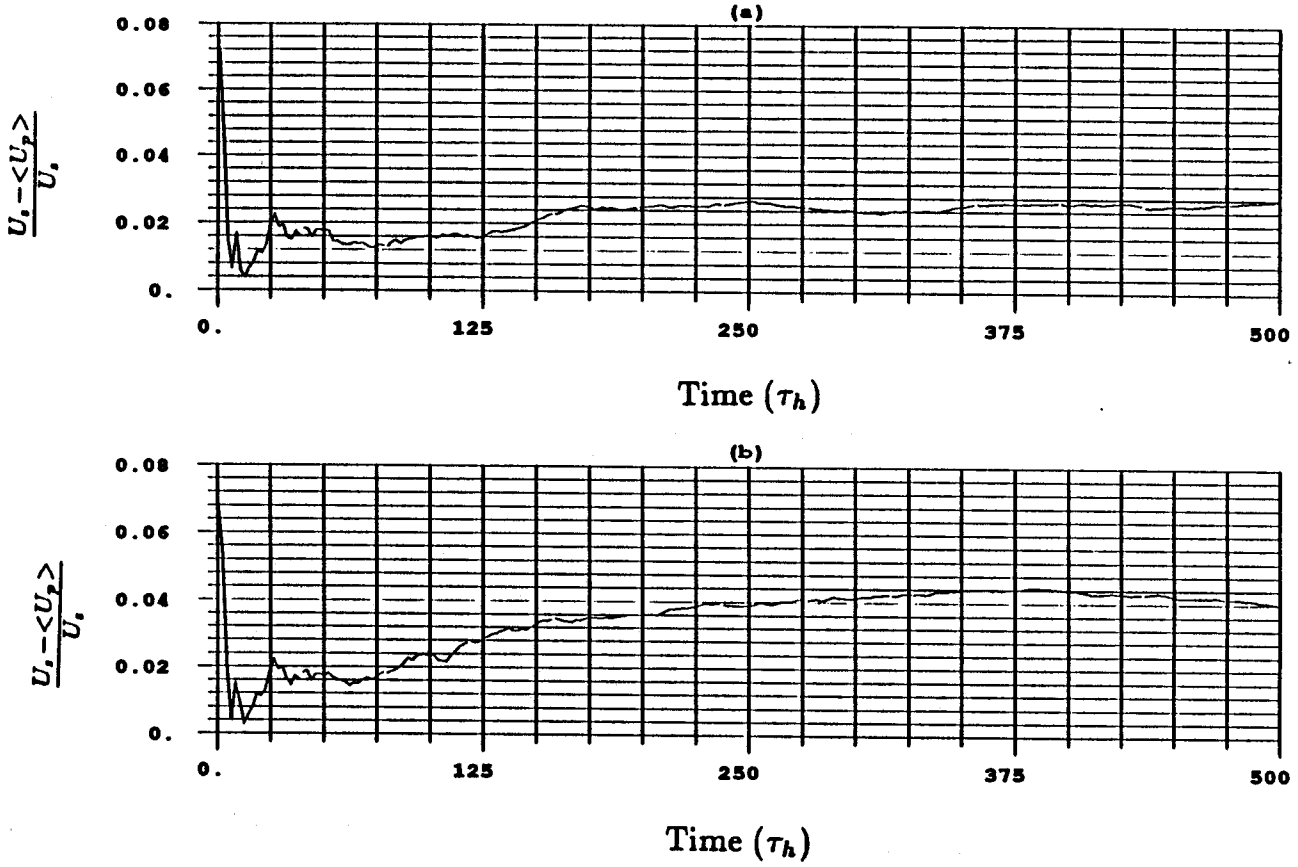

Figure 4.15 The running average of the x velocity. Both runs were performed using the same initial configuration, 192 particles, step size of 0.01 τ_{h_f} and the predictor-corrector integrator. (a) did not use the floating point accelerator. (b) used the floating point accelerator.

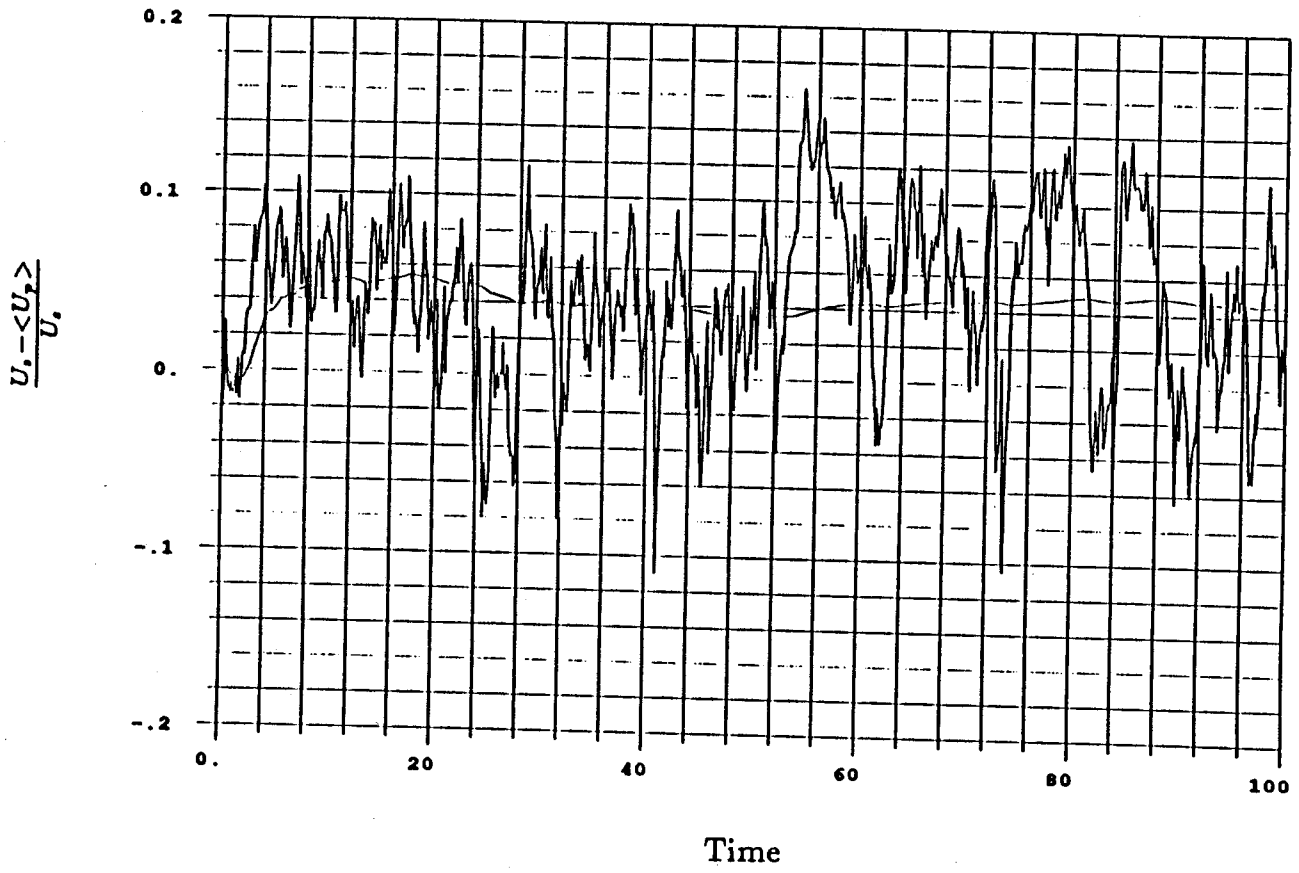

Figure 4.16 The time evolution of the x velocity for run q45. See table 4.6 for the simulation parameters. The smooth line is the running average of the x velocity.

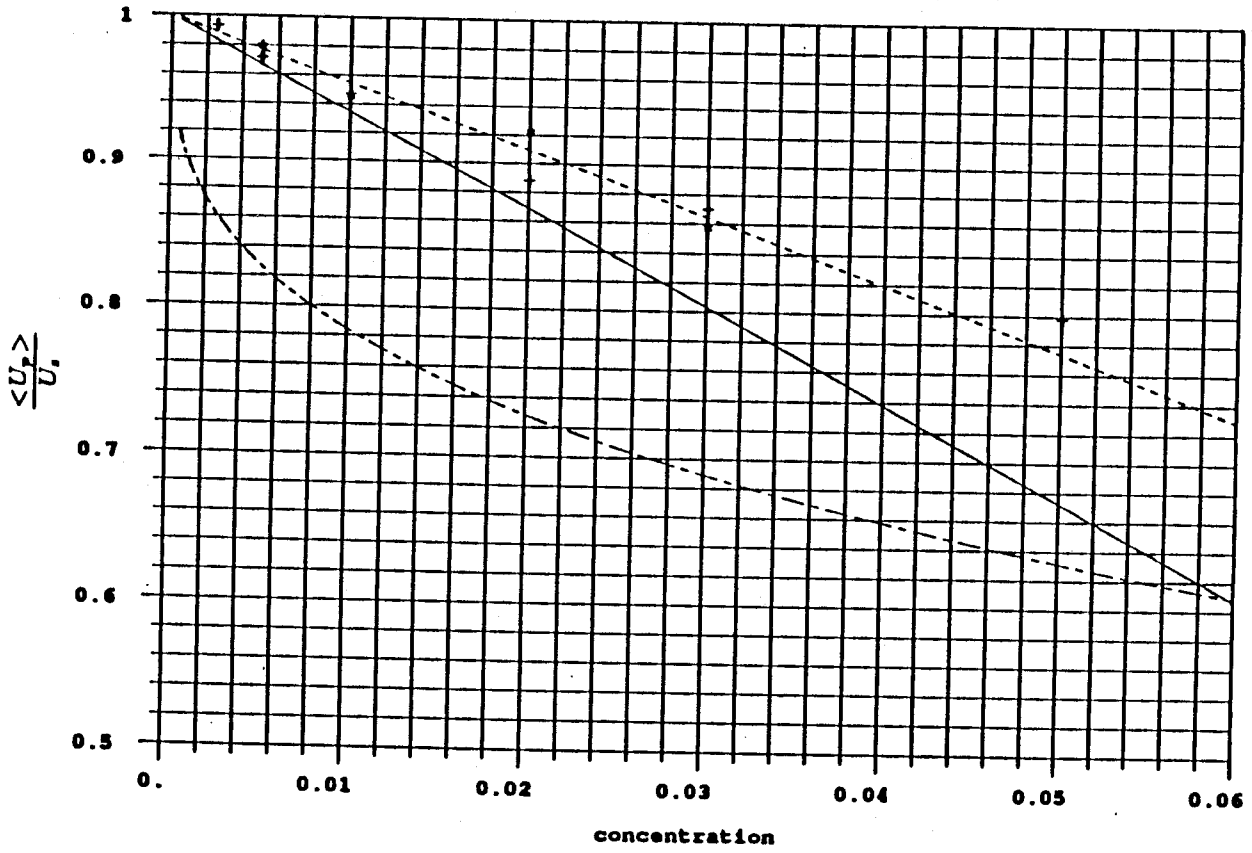

Figure 4.17 The sedimentation velocity's dependence on concentration. The dot-dash line is the experimental correlation, $U_s(1.0 - c^{\frac{1}{3}})$. The solid line is Batchelor's theoretical prediction, $U_s(1.0 - 6.55c^{\frac{1}{3}})$. The dotted line is the experimental correlation for a sheared suspension, $U_s(1.0 - 4.52c^{\frac{1}{3}})$. The symbol x is the simulation results for a quiescent suspension, while the symbol * is the simulation results for a sheared suspension.

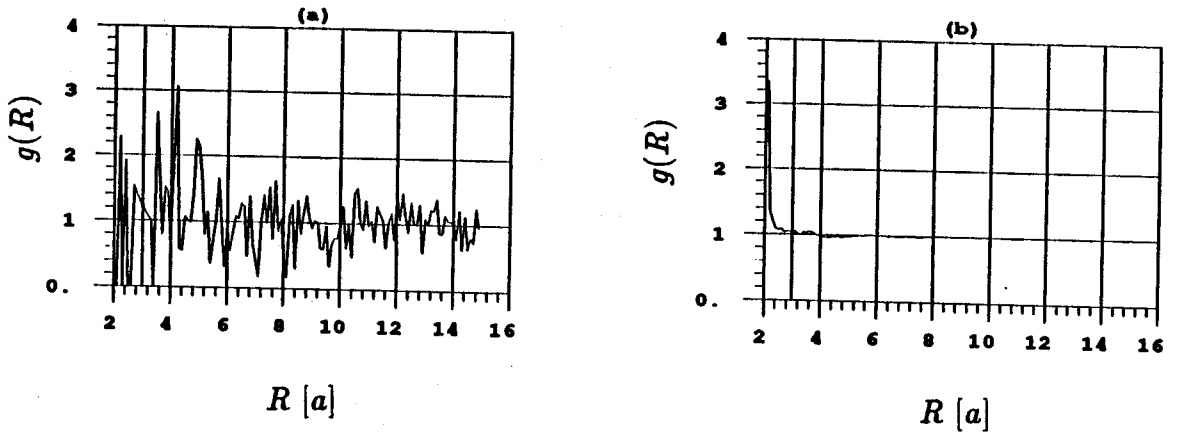

Figure 4.18 The radial distribution for run q45. See table 4.6 for the simulation parameters. (a) is the initial distribution, and (b) is the distribution averaged over the entire run.

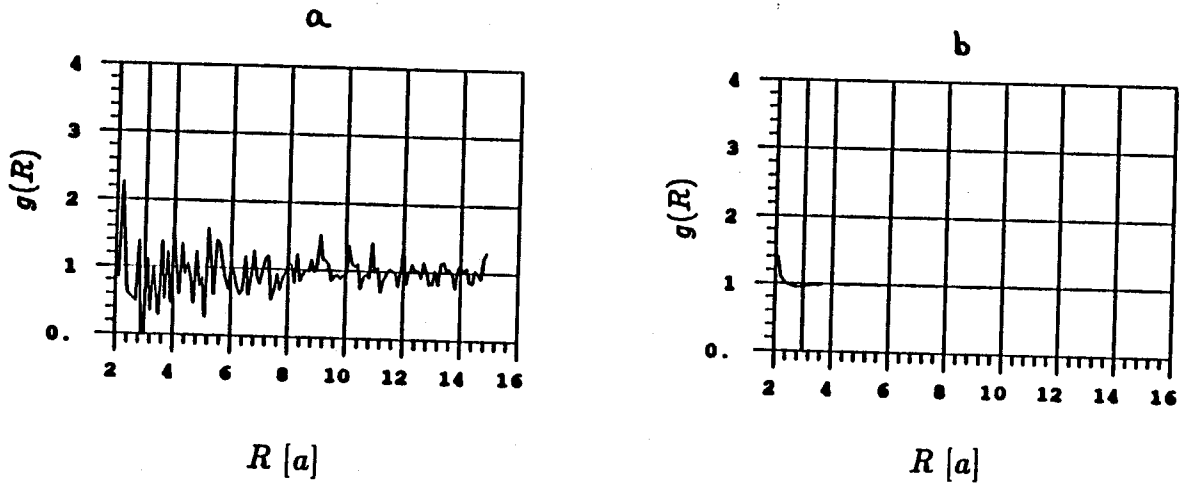

Figure 4.19 The radial distribution for run s62. See table 4.7 for the simulation parameters. (a) is the initial distribution, and (b) is the distribution averaged over the entire run.

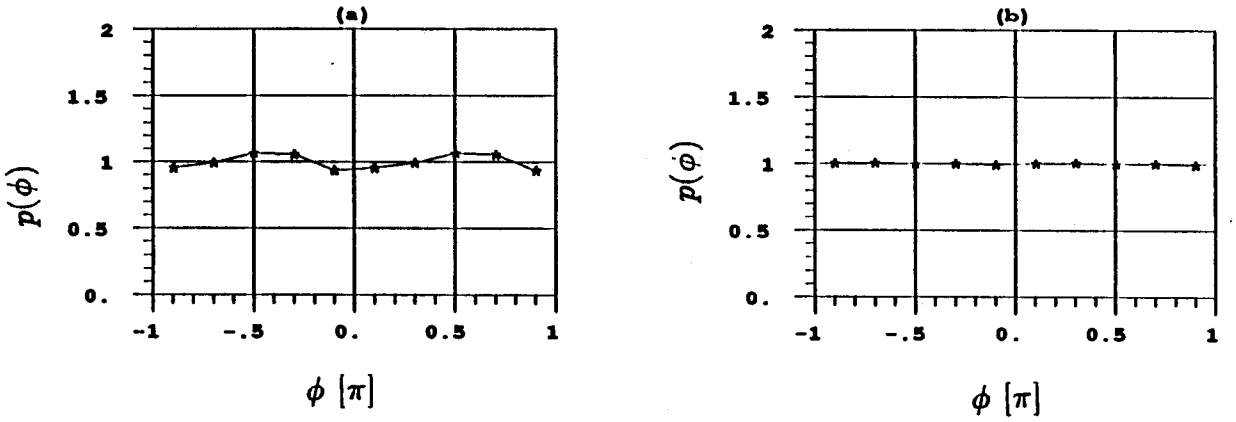

Figure 4.20 The phi distribution averaged over all r for run q45. See table 4.6 for the simulation parameters. (a) is the initial distribution, and (b) is the distribution averaged over the entire run.

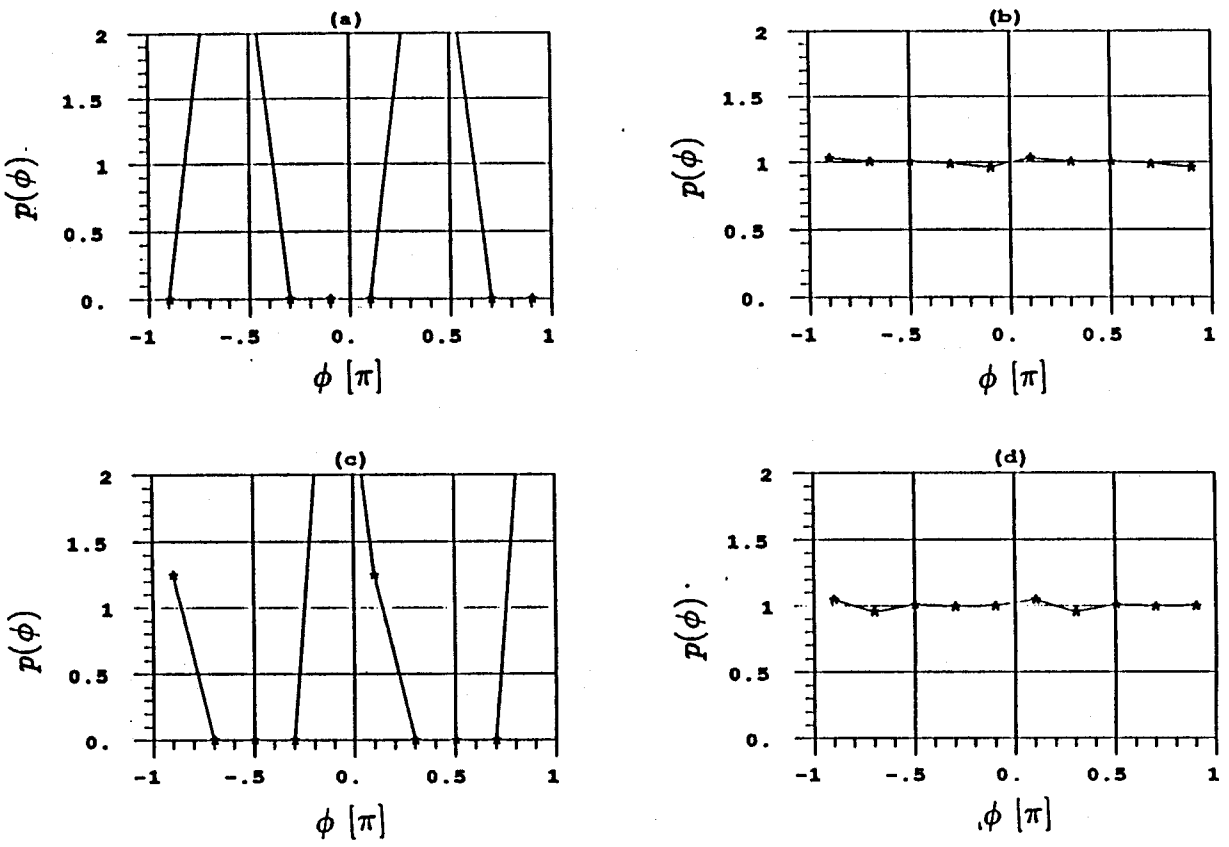

Figure 4.21 The phi distribution for run q45. See table 4.6 for the simulation parameters. (a) is the initial distribution, and (b) is the distribution averaged over the entire run for $r = 2.0a$ to $r = 2.5a$. (c) is the initial distribution, and (d) is the distribution averaged over the entire run for $r = 2.5a$ to $r = 3.0a$.

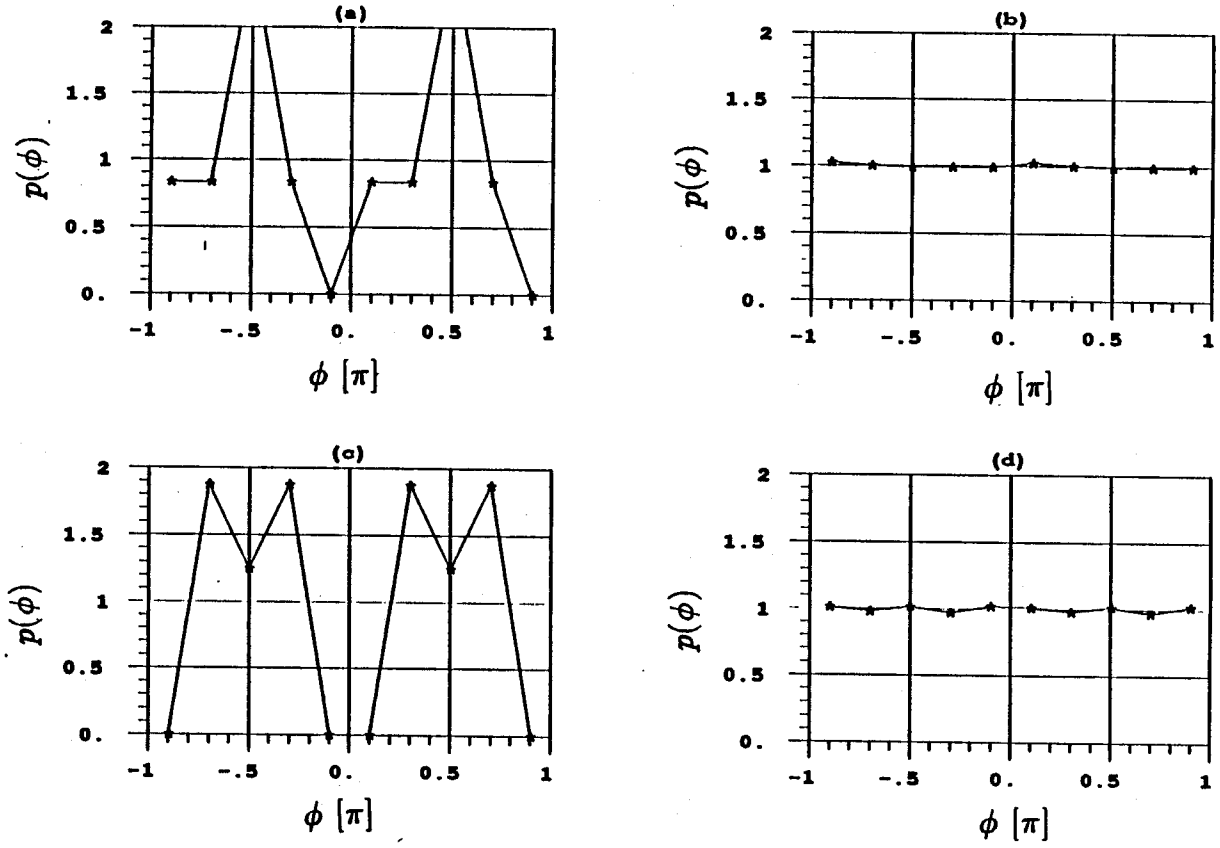

Figure 4.22 The phi distribution for run q45. See table 4.6 for the simulation parameters. (a) is the initial distribution, and (b) is the distribution averaged over the entire run for $r = 3.0a$ to $r = 3.5a$. (c) is the initial distribution, and (d) is the distribution averaged over the entire run for $r = 3.5a$ to $r = 4.0a$.

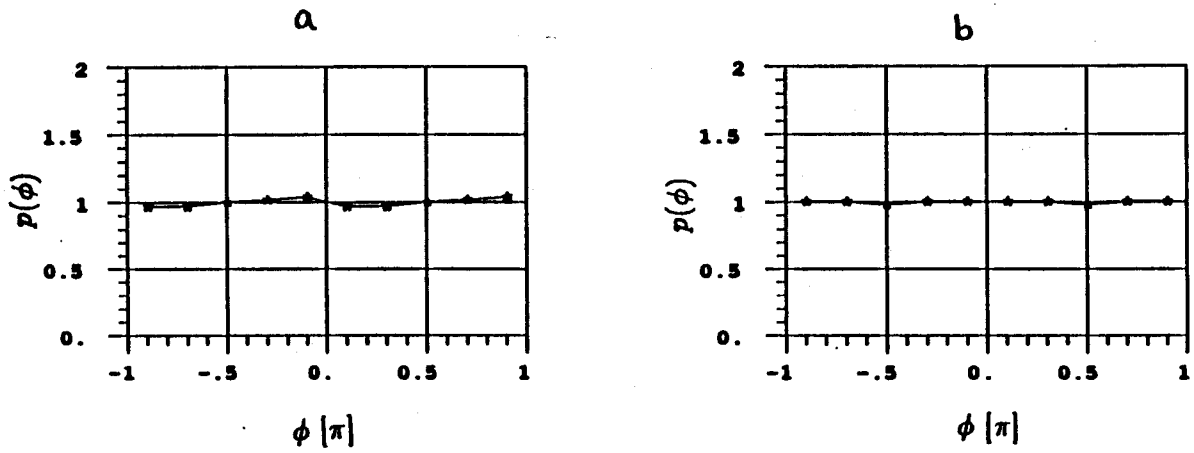

Figure 4.23 The phi distribution averaged over all r for run s62. See table 4.7 for the simulation parameters. (a) is the initial distribution, and (b) is the distribution averaged over the entire run.

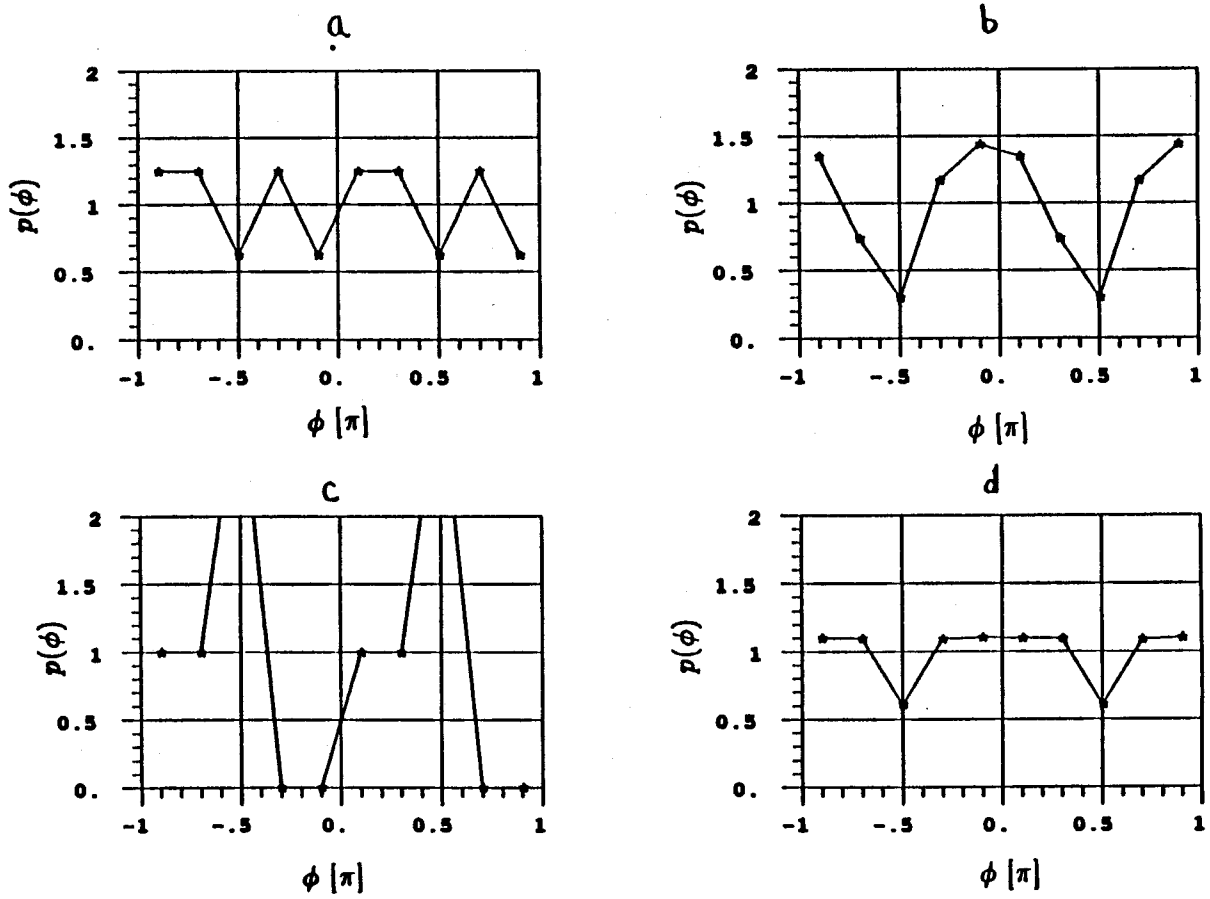

Figure 4.24 The phi distribution for run s62. See table 4.7 for the simulation parameters. (a) is the initial distribution, and (b) is the distribution averaged over the entire run for $r = 2.0a$ to $r = 2.5a$. (c) is the initial distribution, and (d) is the distribution averaged over the entire run for $r = 2.5a$ to $r = 3.0a$.

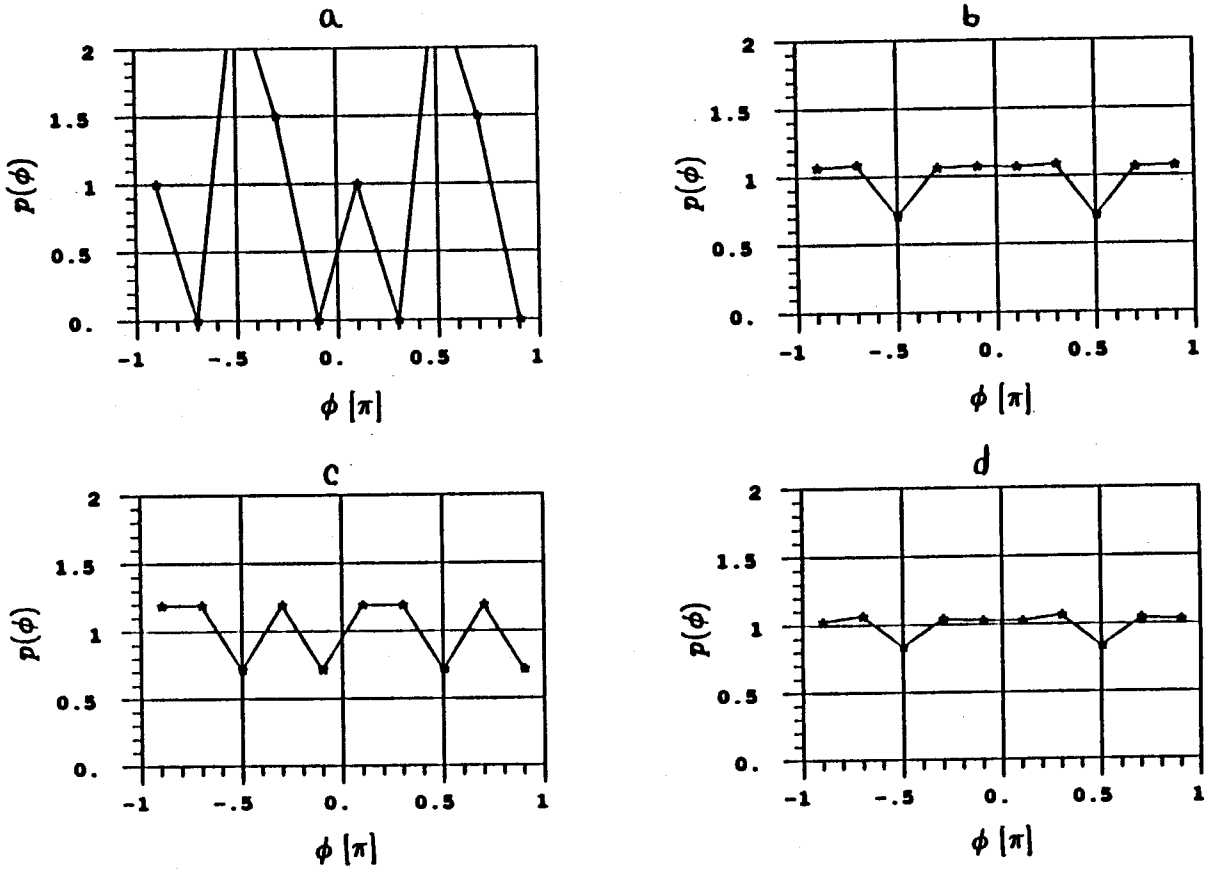

Figure 4.25 The phi distribution for run s62. See table 4.7 for the simulation parameters. (a) is the initial distribution, and (b) is the distribution averaged over the entire run for $r = 3.0a$ to $r = 3.5a$. (c) is the initial distribution, and (d) is the distribution averaged over the entire run for $r = 3.5a$ to $r = 4.0a$.

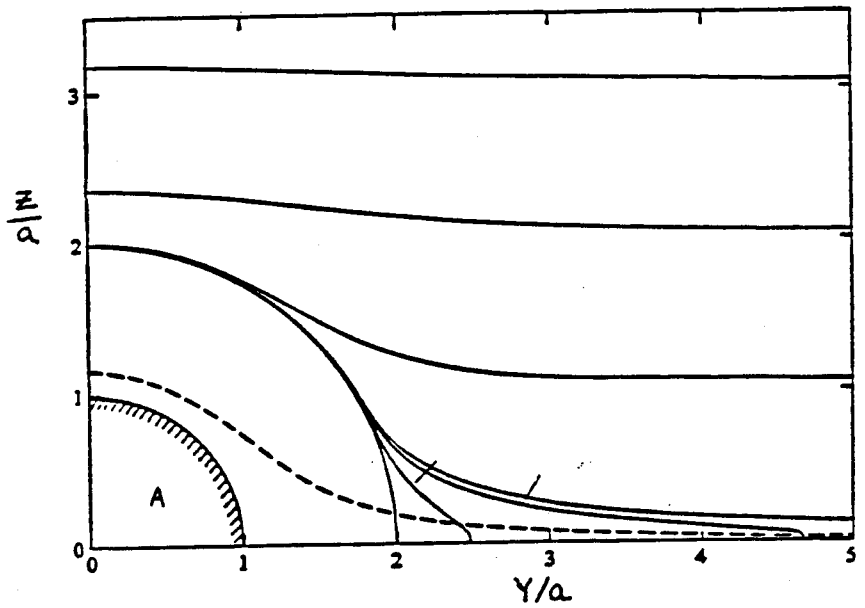

Figure 4.26 Trajectory of two particles in a shear flow. From Batchelor and Green (1972).

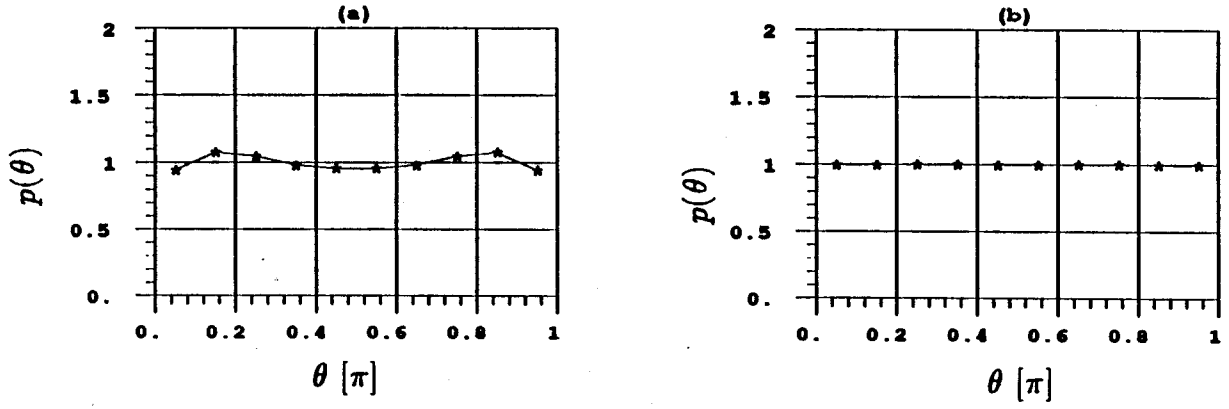

Figure 4.27 The theta distribution averaged over all r for run q45. See table 4.6 for the simulation parameters. (a) is the initial distribution, and (b) is the distribution averaged over the entire run.

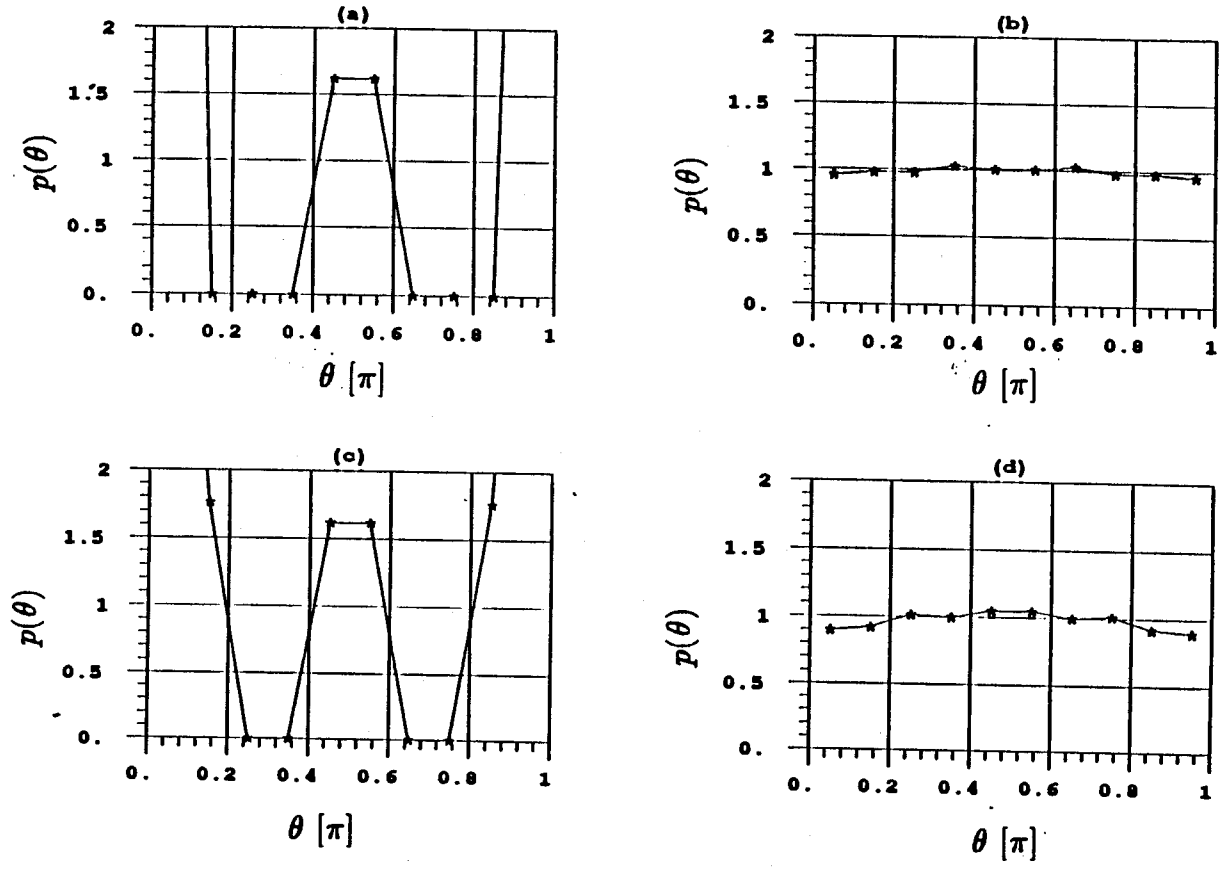

Figure 4.28 The theta distribution for run q45. See table 4.6 for the simulation parameters. (a) is the initial distribution, and (b) is the distribution averaged over the entire run for $r = 2.0a$ to $r = 2.5a$. (c) is the initial distribution, and (d) is the distribution averaged over the entire run for $r = 2.5a$ to $r = 3.0a$.

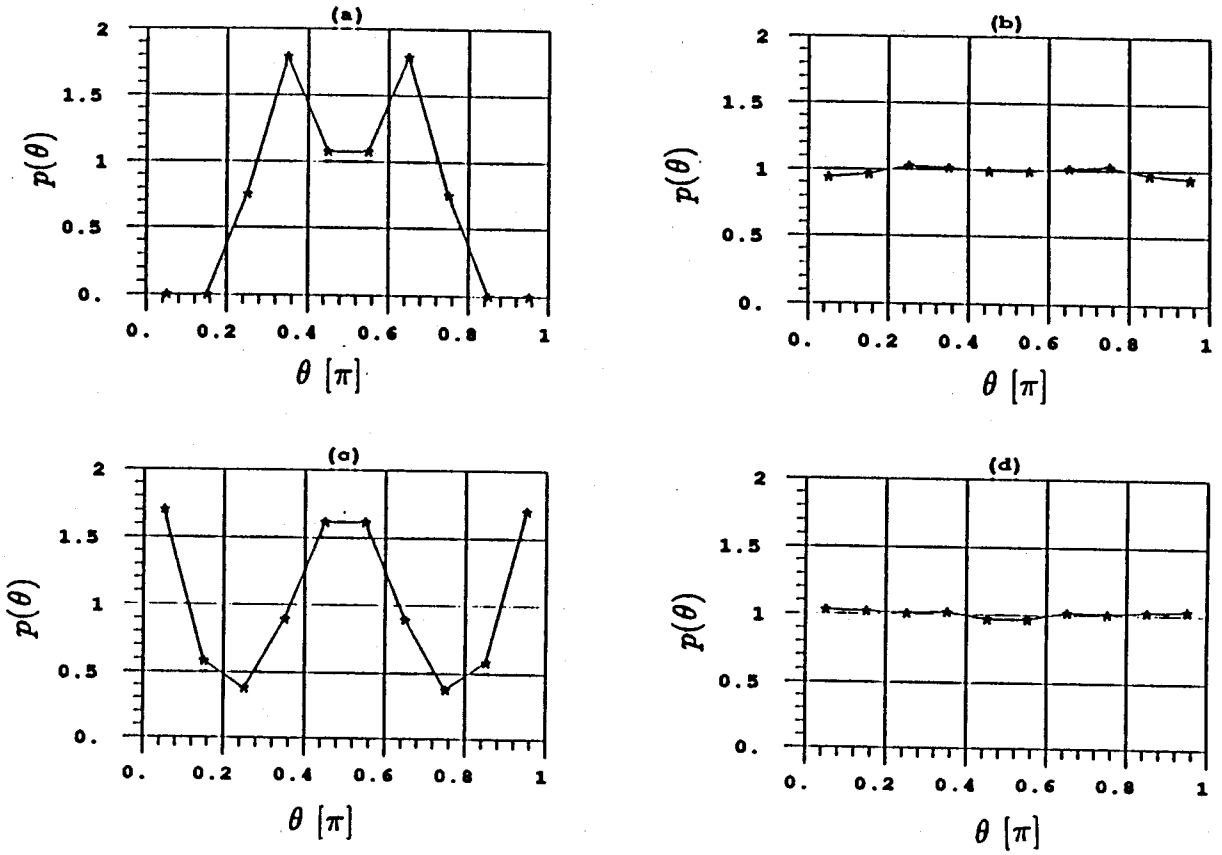

Figure 4.29 The theta distribution for run q45. See table 4.6 for the simulation parameters. (a) is the initial distribution, and (b) is the distribution averaged over the entire run for $r = 3.0a$ to $r = 3.5a$. (c) is the initial distribution, and (d) is the distribution averaged over the entire run for $r = 3.5a$ to $r = 4.0a$.

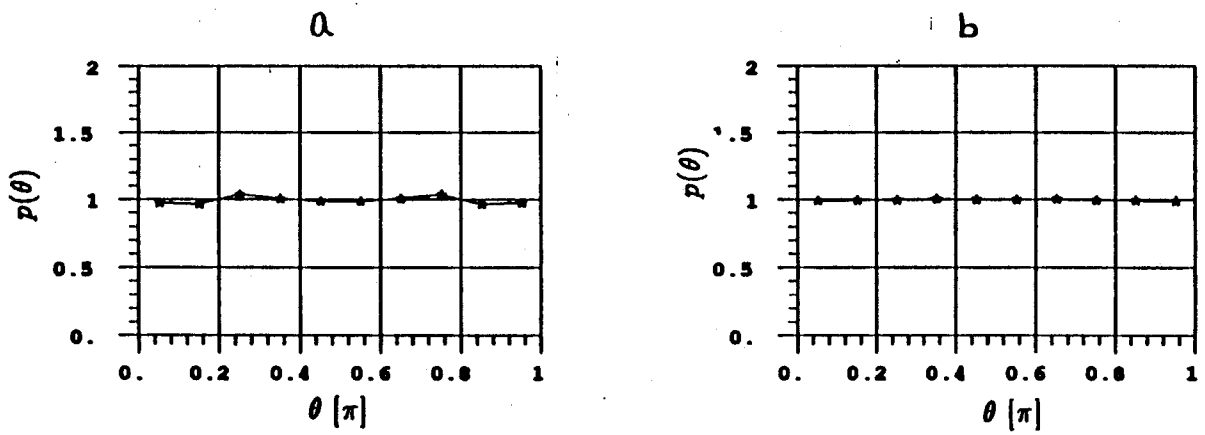

Figure 4.30 The theta distribution averaged over all r for run s62. See table 4.7 for the simulation parameters. (a) is the initial distribution, and (b) is the distribution averaged over the entire run.

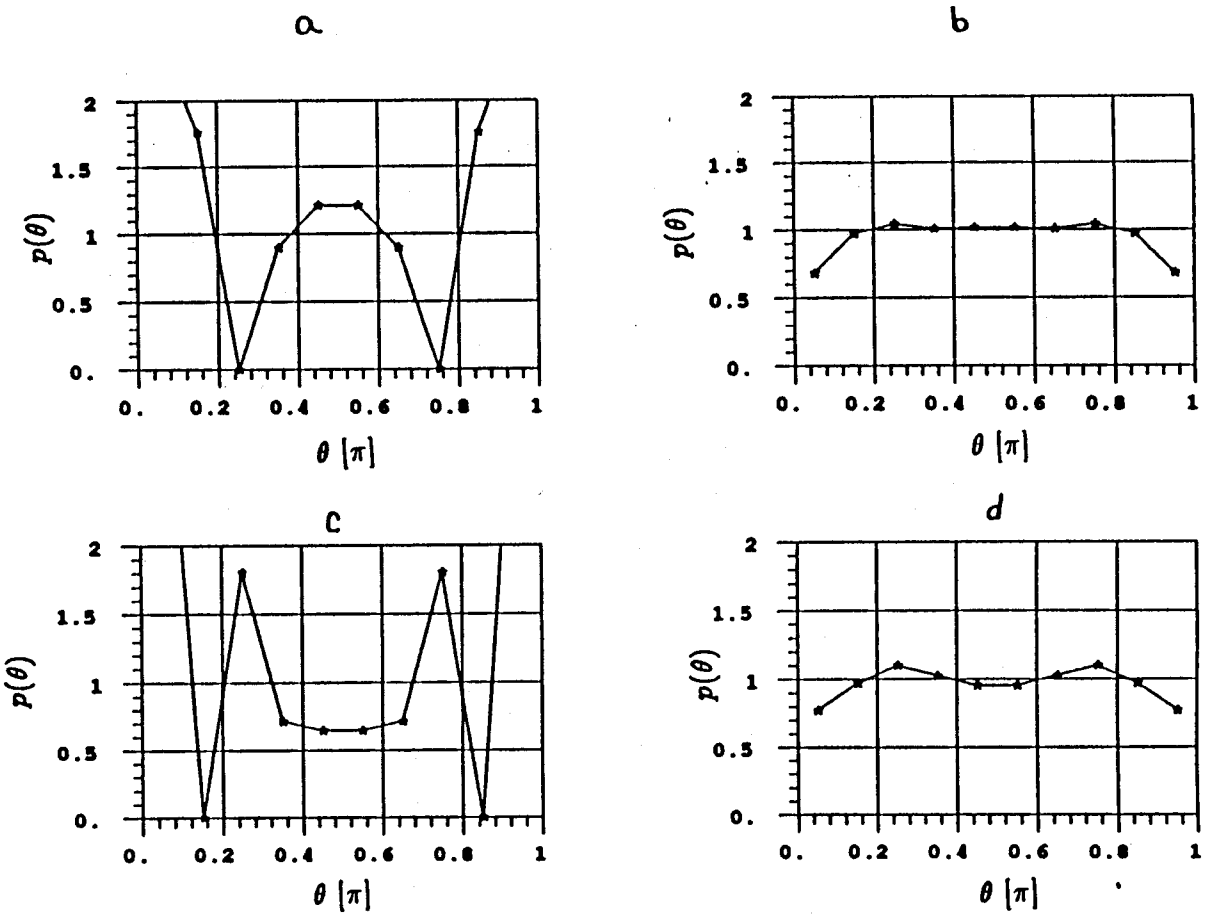

Figure 4.31 The theta distribution for run s62. See table 4.7 for the simulation parameters. (a) is the initial distribution, and (b) is the distribution averaged over the entire run for $r = 2.0a$ to $r = 2.5a$. (c) is the initial distribution, and (d) is the distribution averaged over the entire run for $r = 2.5a$ to $r = 3.0a$.

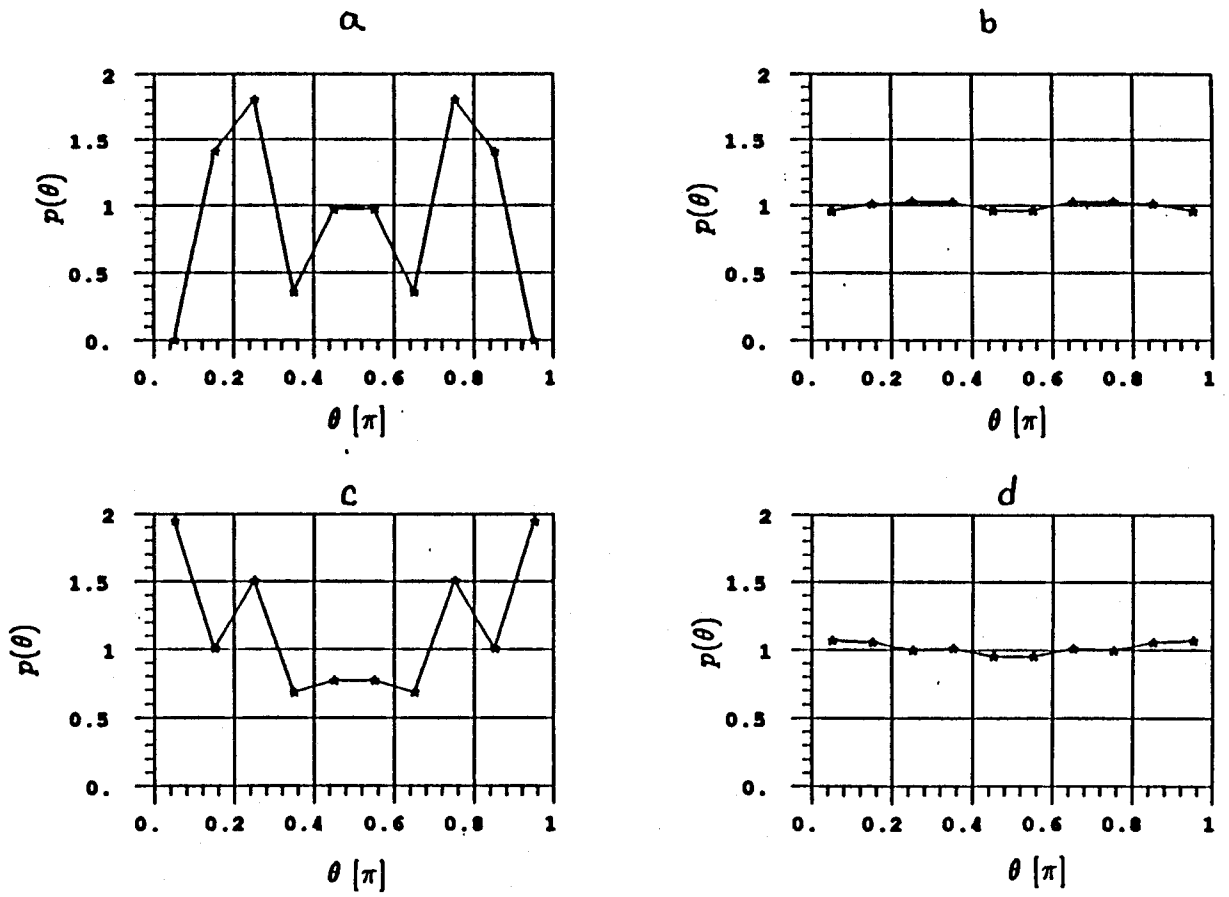

Figure 4.32 The theta distribution for run s62. See table 4.7 for the simulation parameters. (a) is the initial distribution, and (b) is the distribution averaged over the entire run for $r = 3.0a$ to $r = 3.5a$. (c) is the initial distribution, and (d) is the distribution averaged over the entire run for $r = 3.5a$ to $r = 4.0a$.

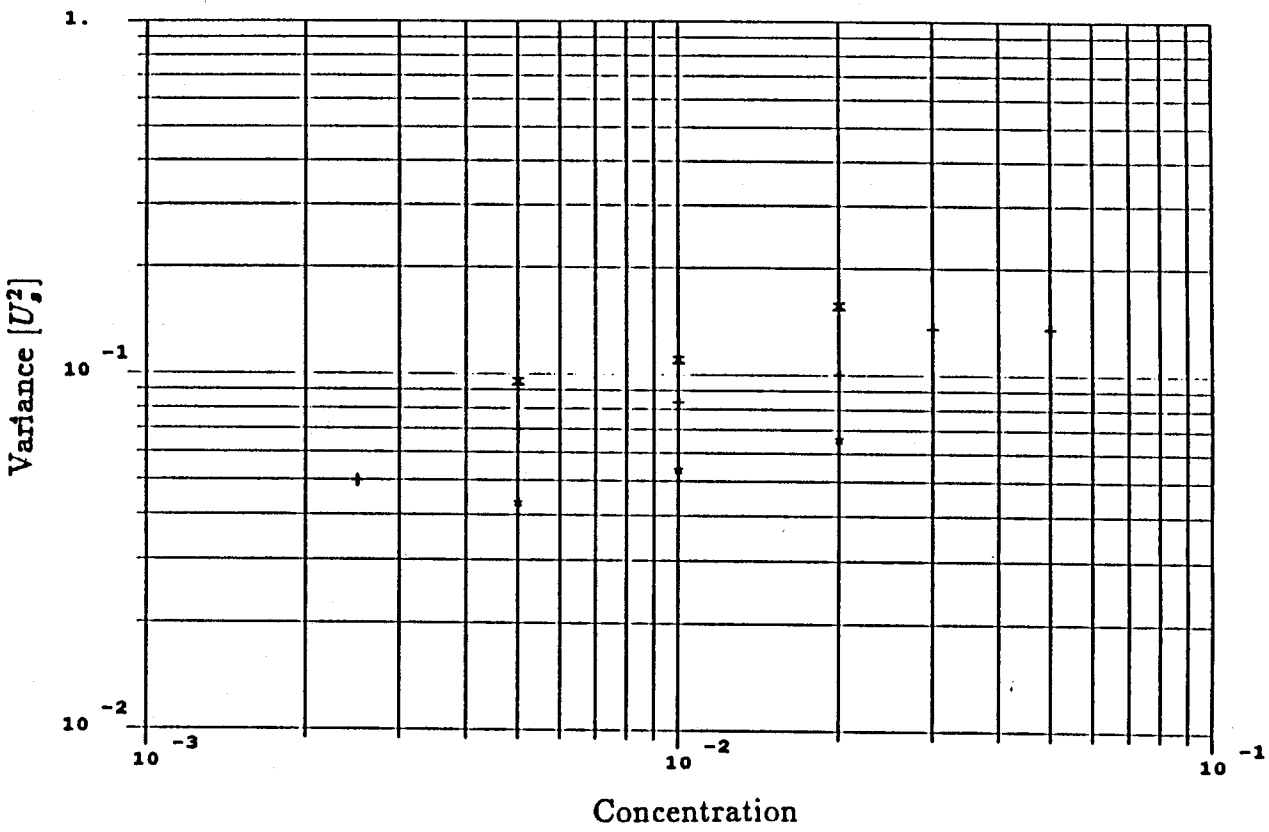

Figure 4.33 The dependence of the x variance on concentration for a quiescent sedimenting suspension. The data are from runs using an euler integration scheme. The symbols *, +, and x are for N equal to 27, 64, and 125 particles respectively.

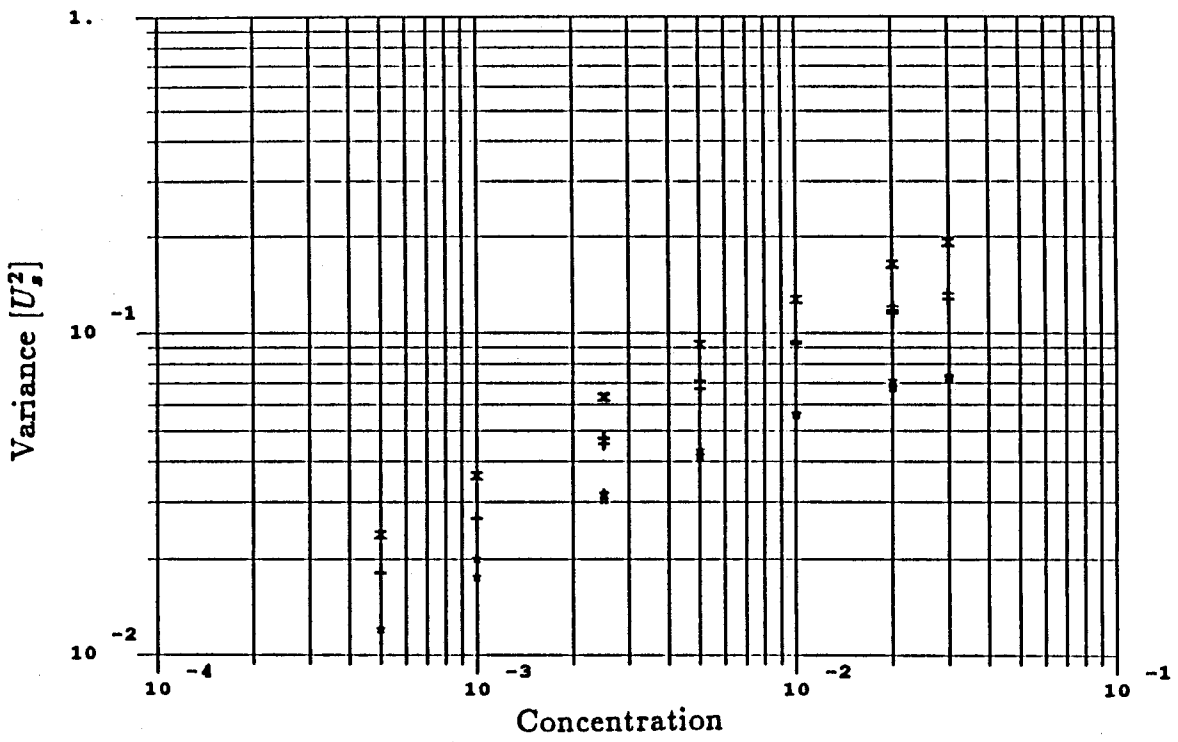

Figure 4.34 The dependence of variance on concentration for a random suspension. $*$ is for 27 particles, $+$ is for 64 particles, and x is for 125 particles.

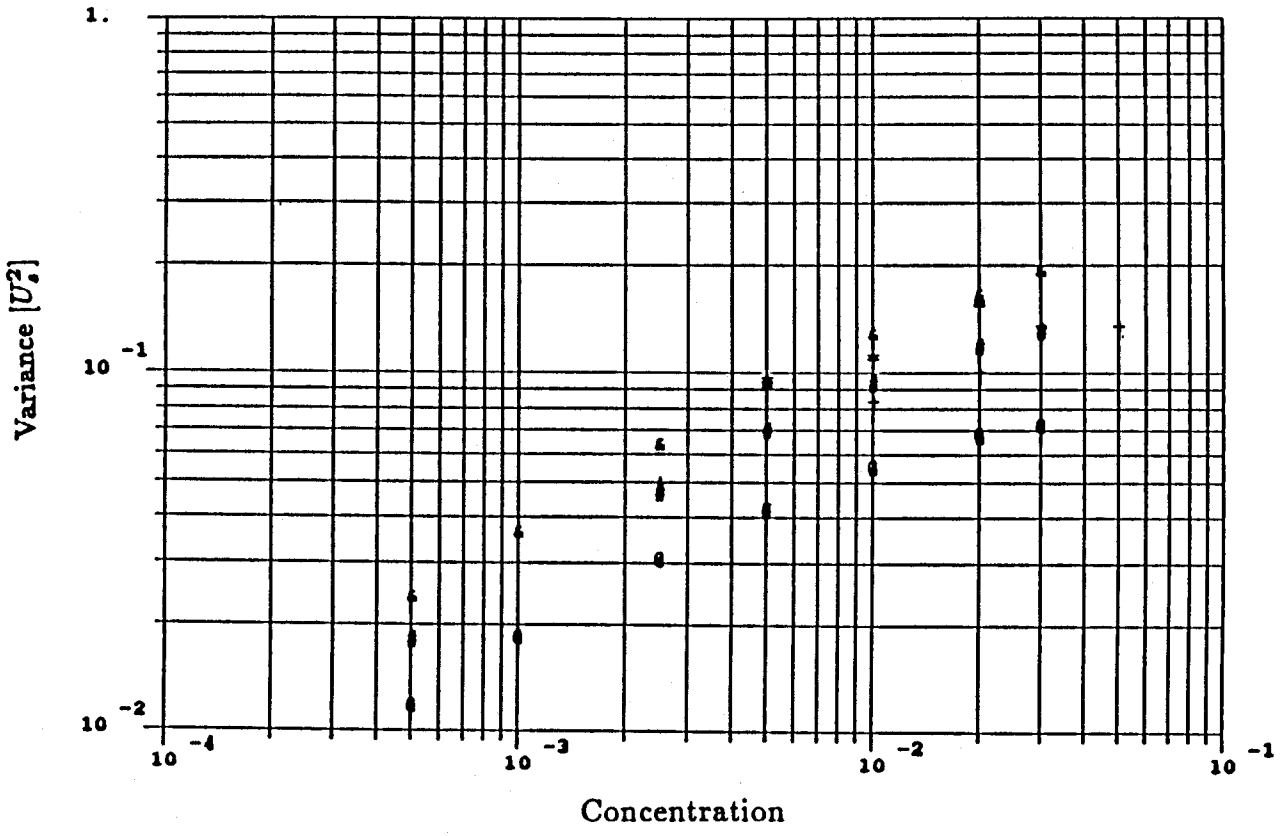

Figure 4.35 Comparison between the x variance obtained using the Monte-Carlo simulator, and the molecular-dynamics-type simulator. The symbols @, #, & are from the Monte-Carlo simulations using 27, 64, and 125 particles respectively. The symbols *, +, and = are from the molecular-dynamics-type simulations for 27, 64, and 125 particles, respectively.

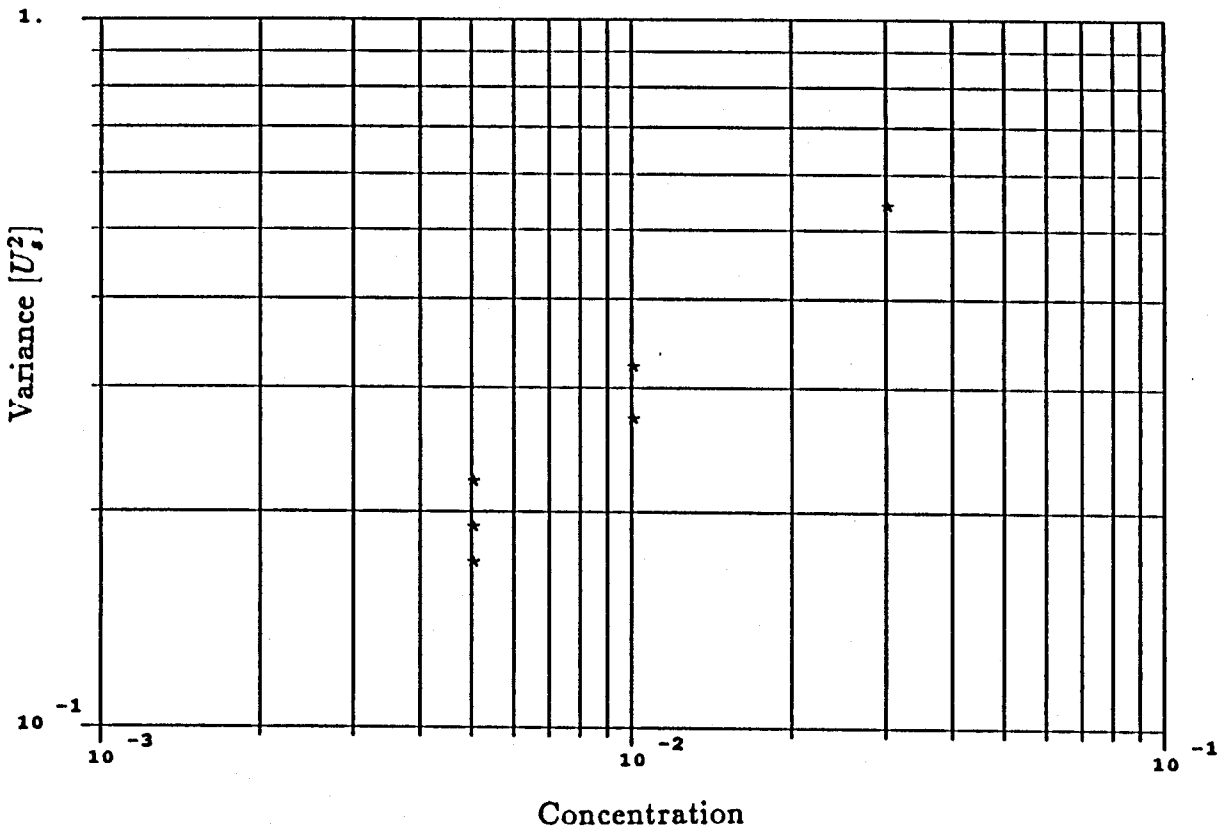

Figure 4.36 The dependence of the x variance on concentration for a suspension subjected to a dimensionless shear rate of 10.

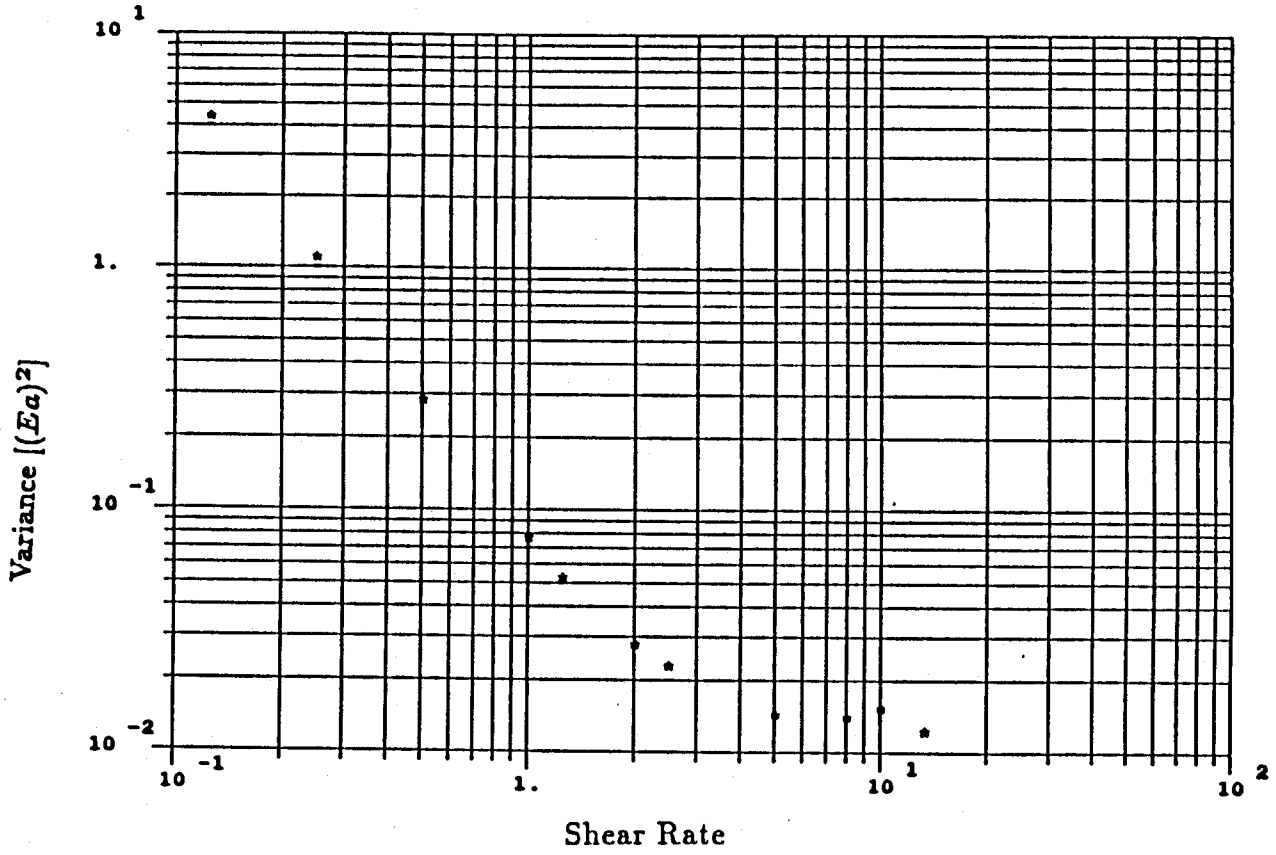

Figure 4.37 The dependence of the z variance (in units of $(Ea)^2$) on shear rate.

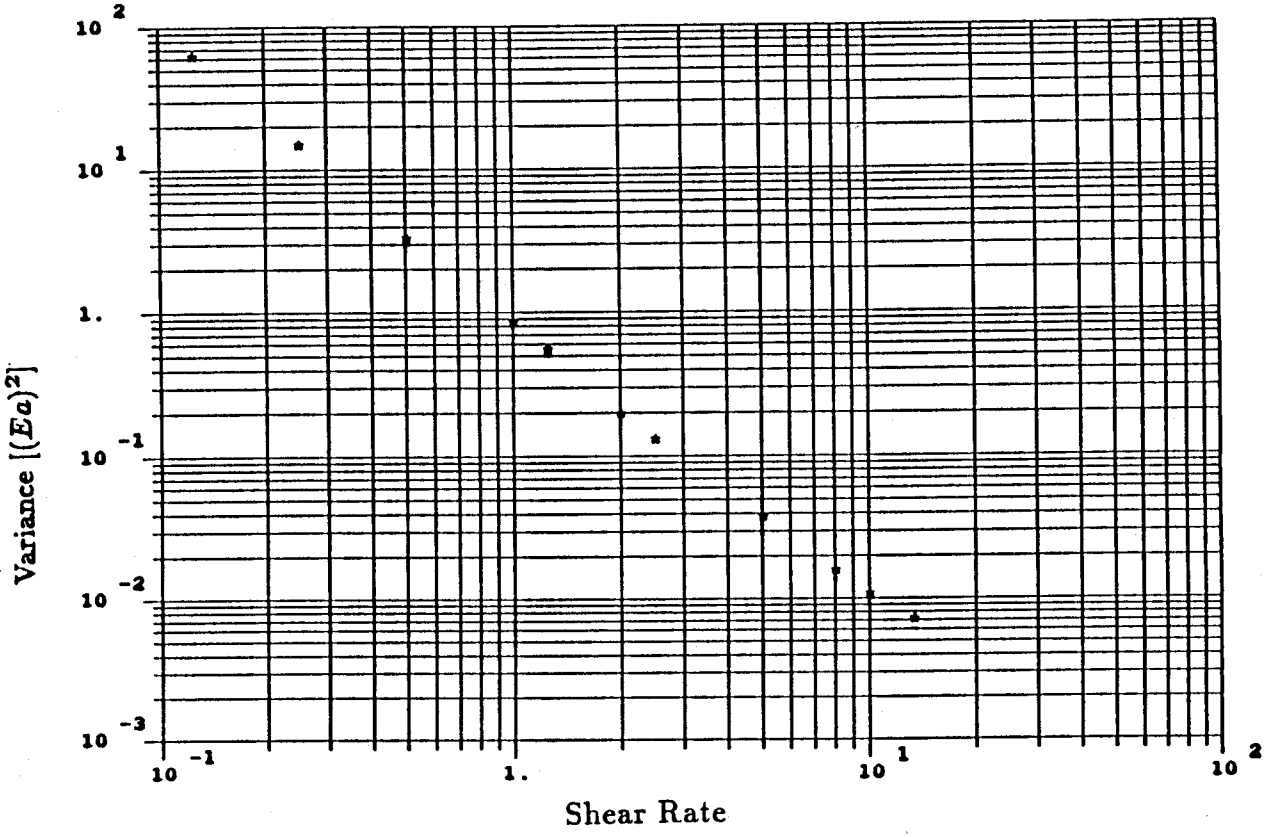

Figure 4.38 The dependence of the x variance (in units of $(Ea)^2$) on shear rate.

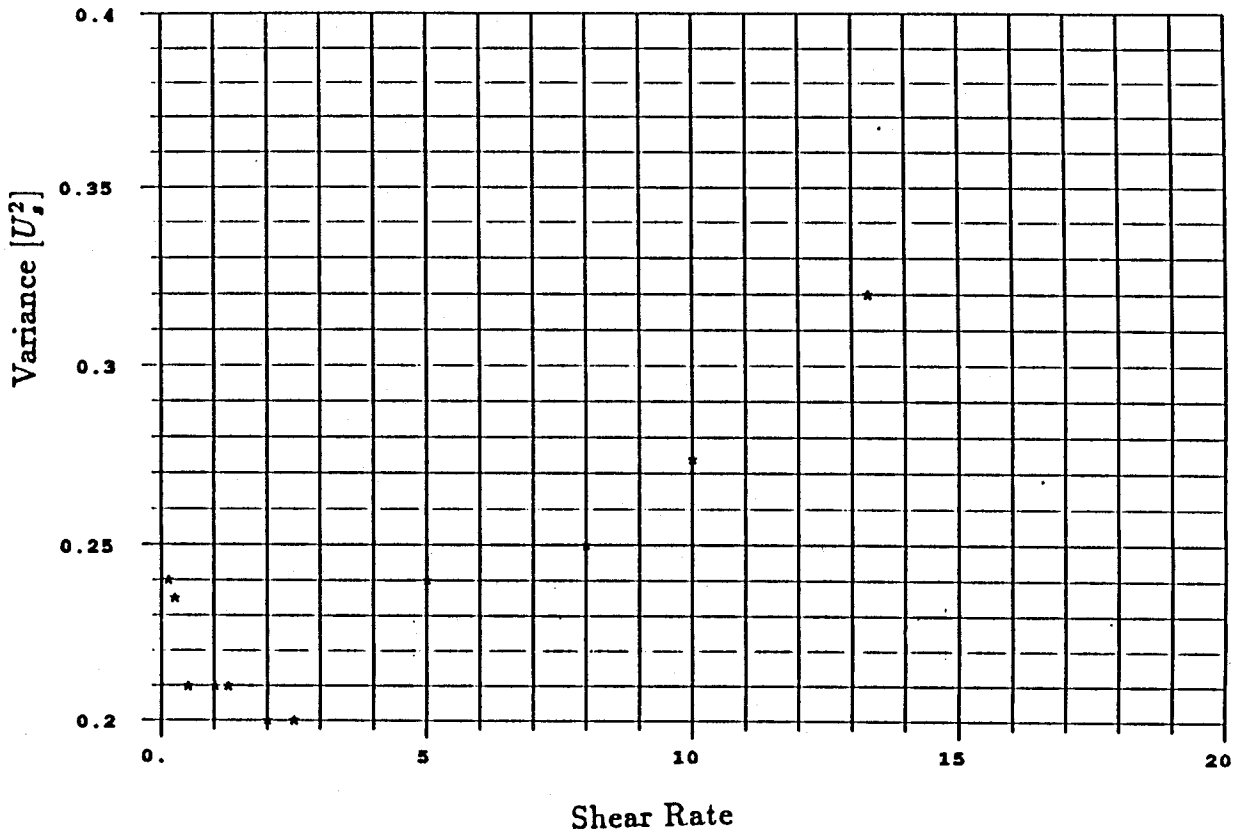

Figure 4.39 The dependence of the x variance (in units of U_s^2) on shear rate.

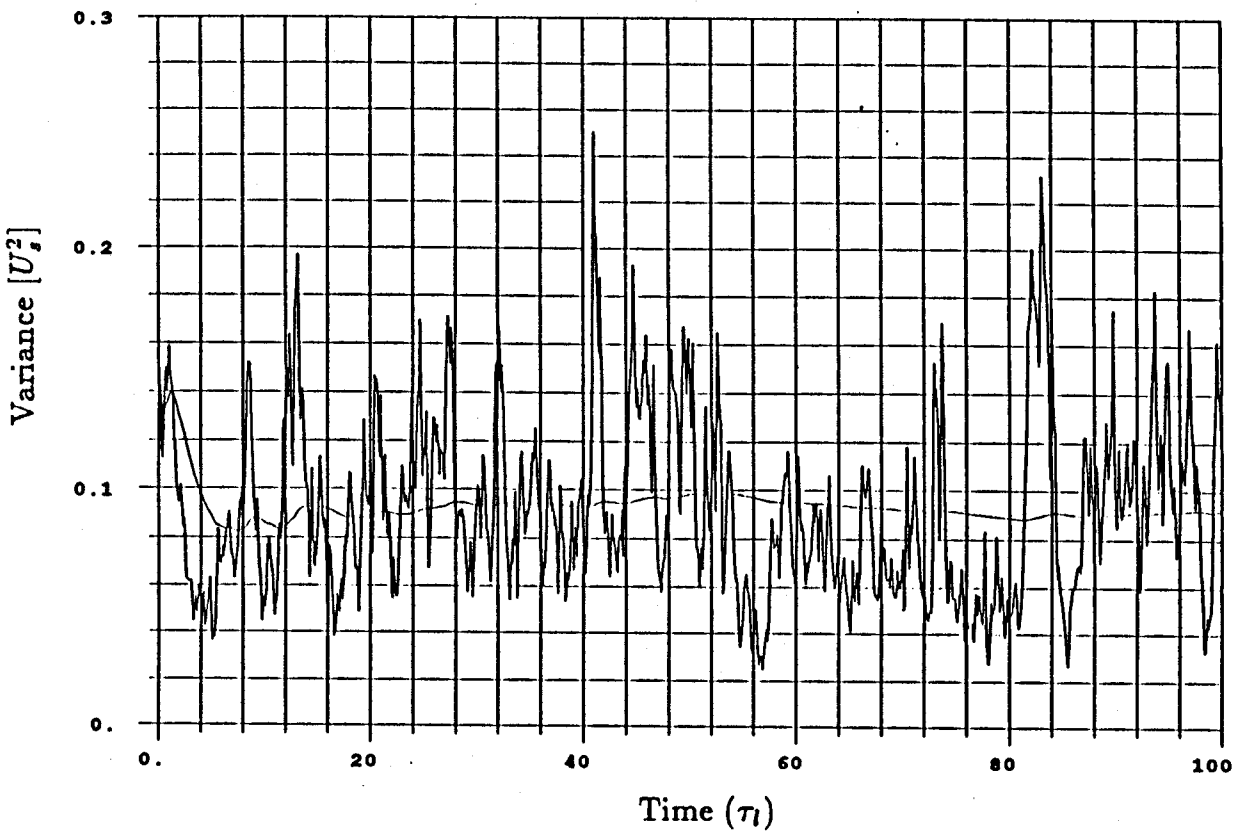

Figure 4.40 The time evolution of the x velocity variance for run q45. See table 4.6 for the simulation parameters. The smooth line is the running average of the x velocity variance.

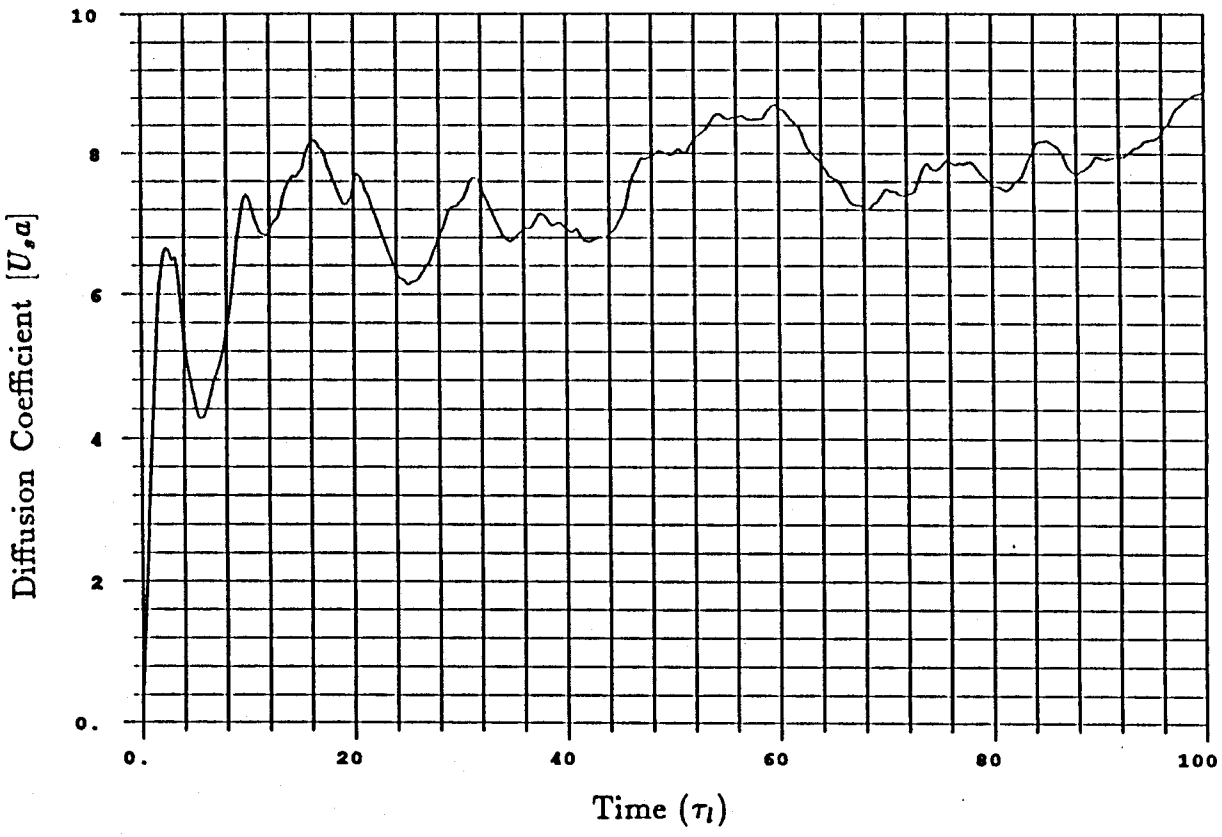

Figure 4.41 The time evolution of the x diffusion coefficient for run q45. See table 4.6 for the simulation parameters.

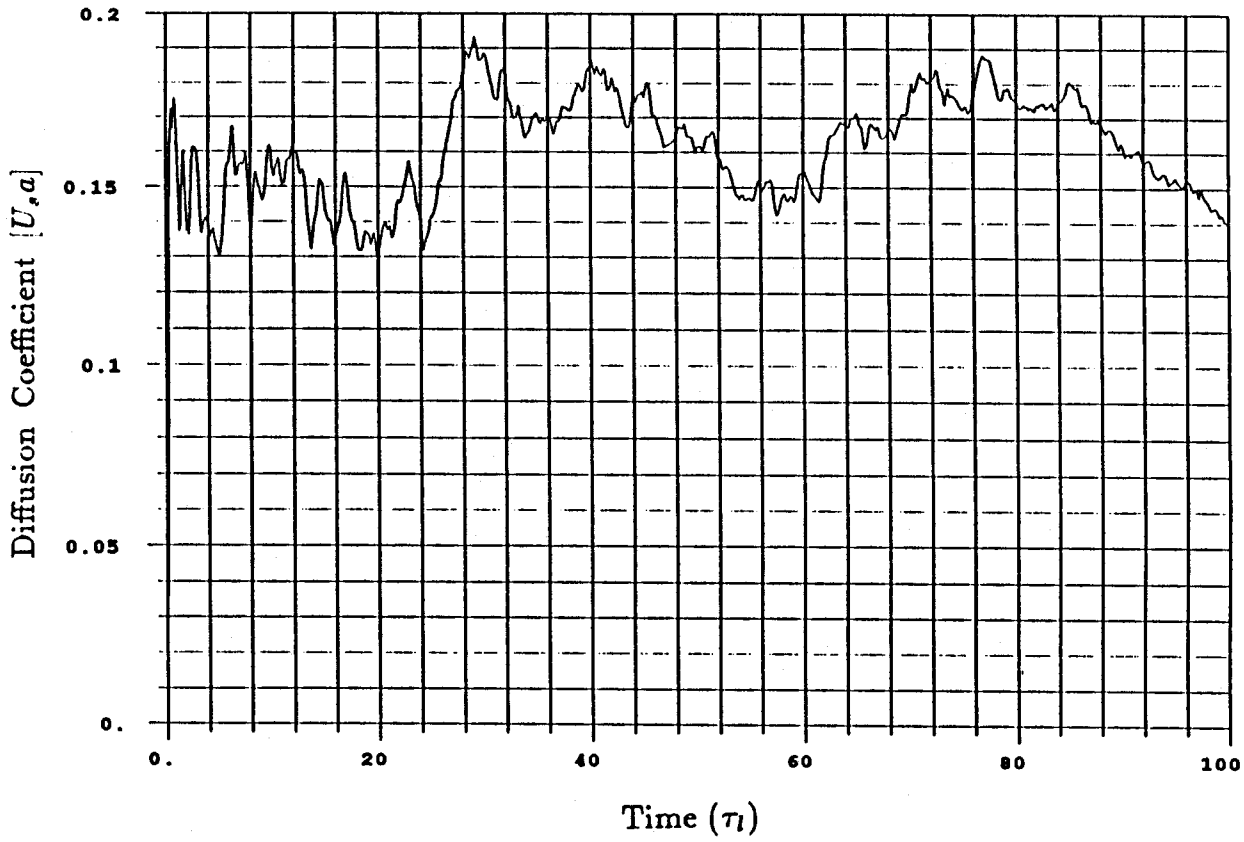

Figure 4.42 The time evolution of the y diffusion coefficient for run q45. See table 4.6 for the simulation parameters.

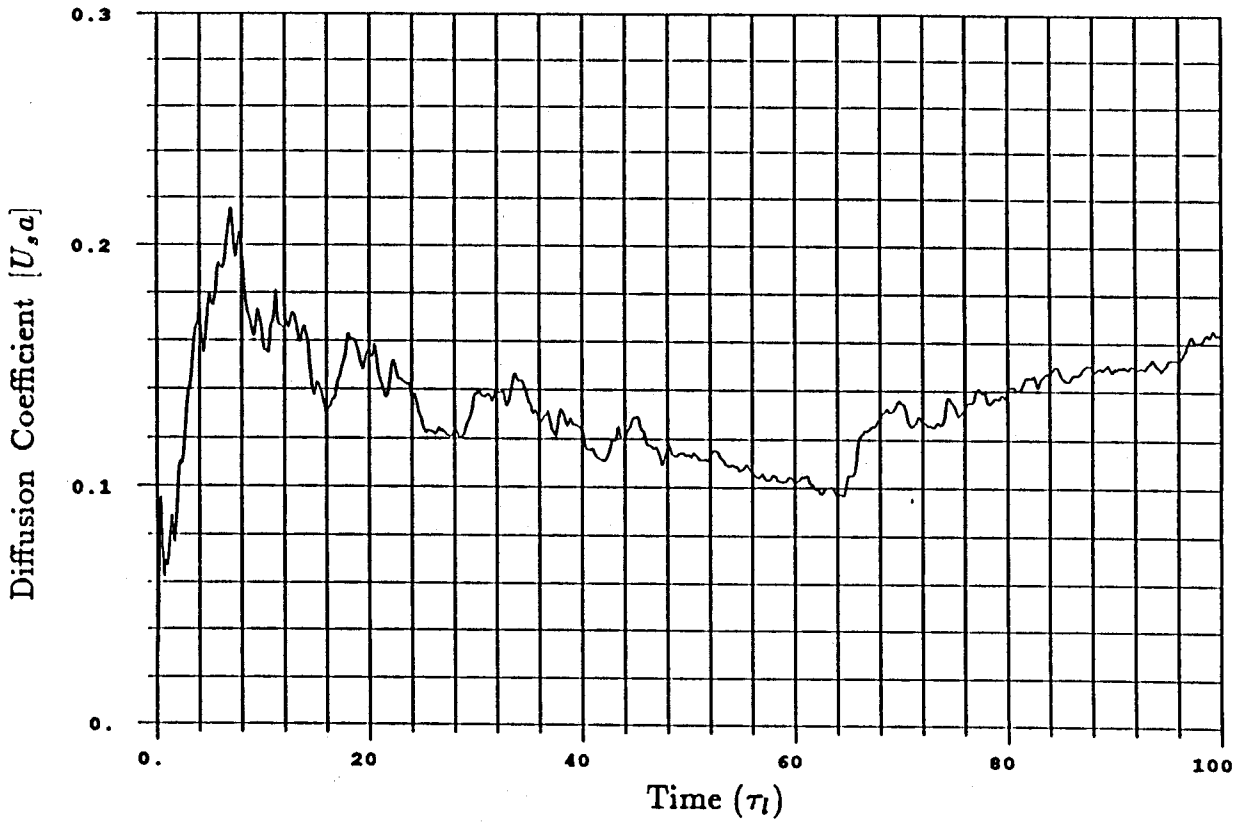

Figure 4.43 The time evolution of the z diffusion coefficient for run q45. See table 4.6 for the simulation parameters.

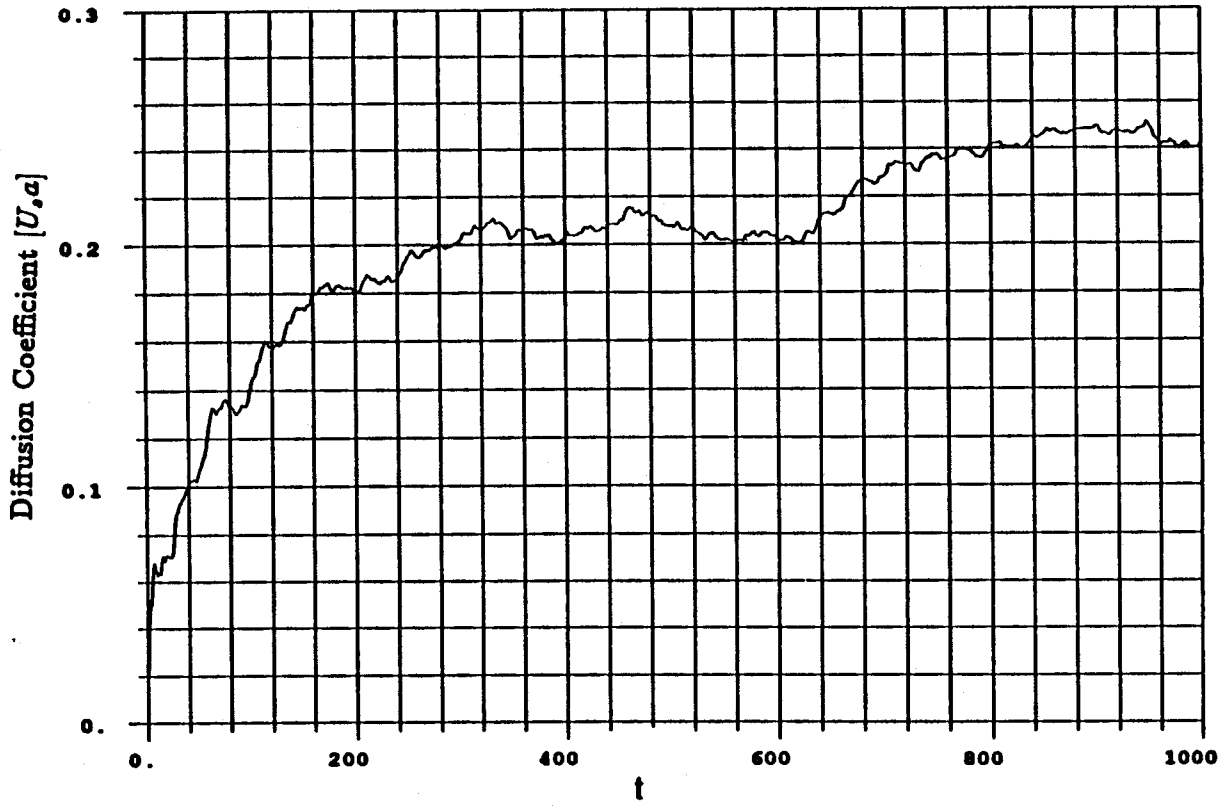

Figure 4.44 The time evolution of the x diffusion coefficient for run s62. See table 4.7 for the simulation parameters.

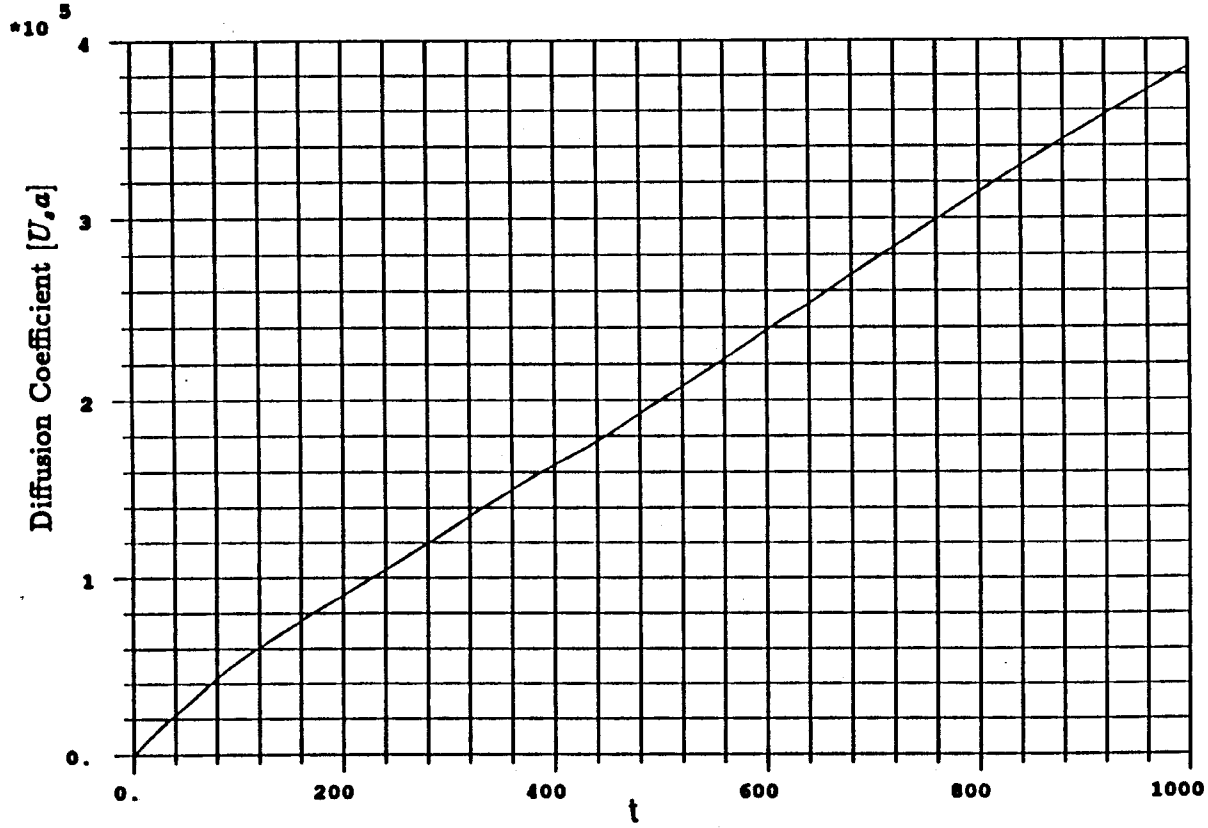

Figure 4.45 The time evolution of the y diffusion coefficient for run s62. See table 4.7 for the simulation parameters.

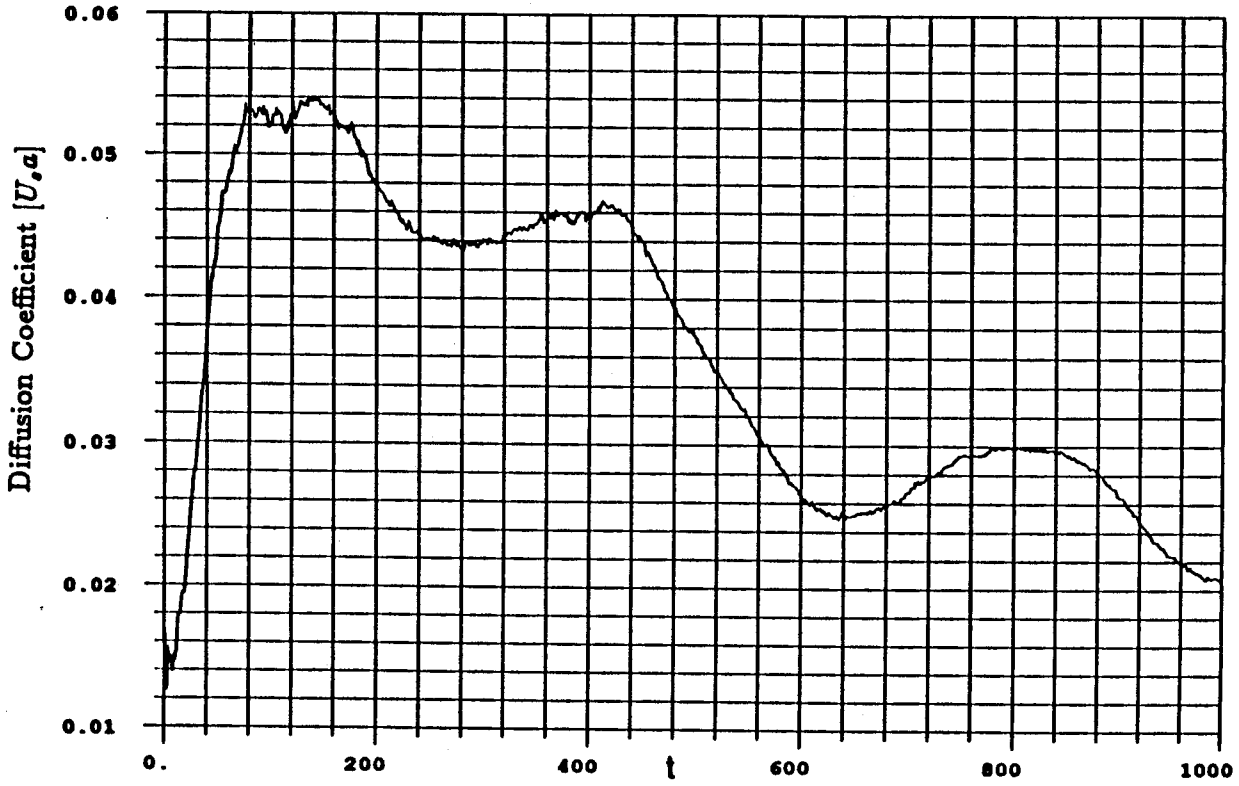

Figure 4.46 The time evolution of the z diffusion coefficient for run s62. See table 4.7 for the simulation parameters.

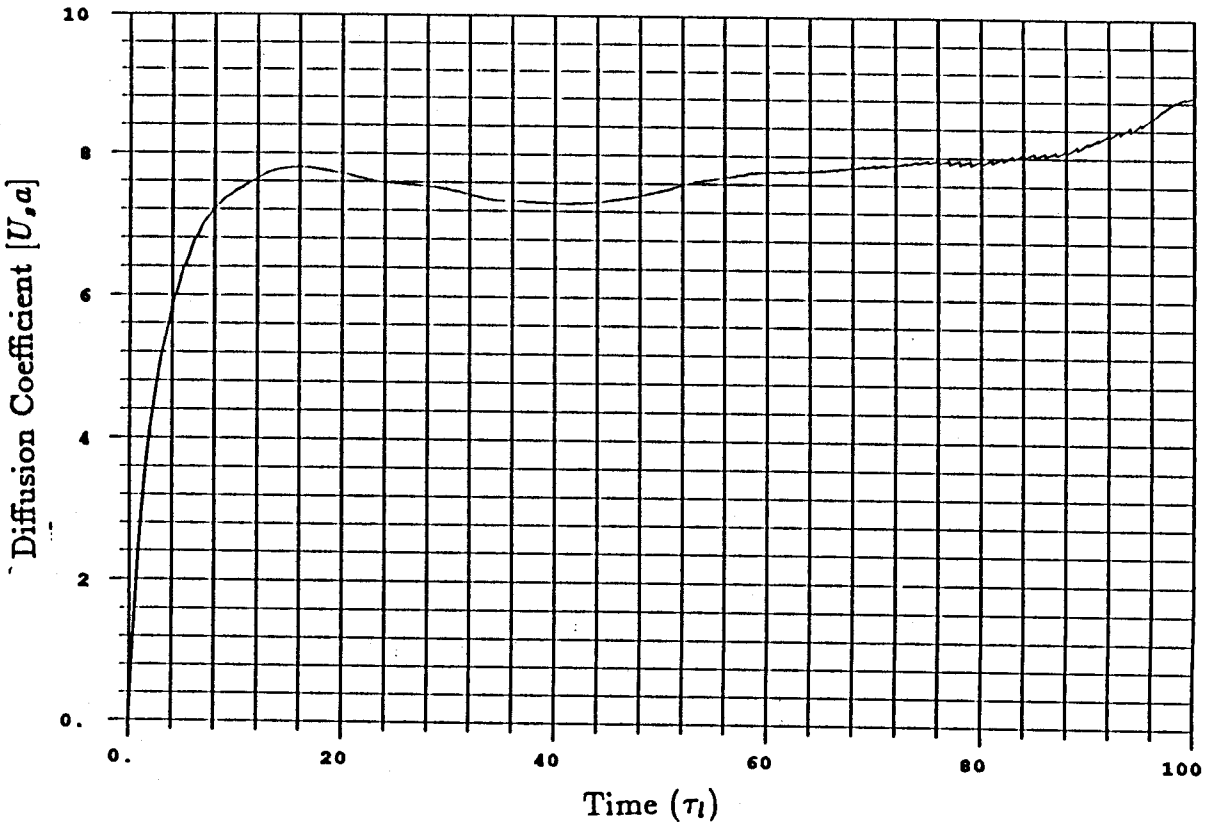

Figure 4.47 The time evolution of the x diffusion coefficient with restart for run q45. See table 4.6 for the simulation parameters.

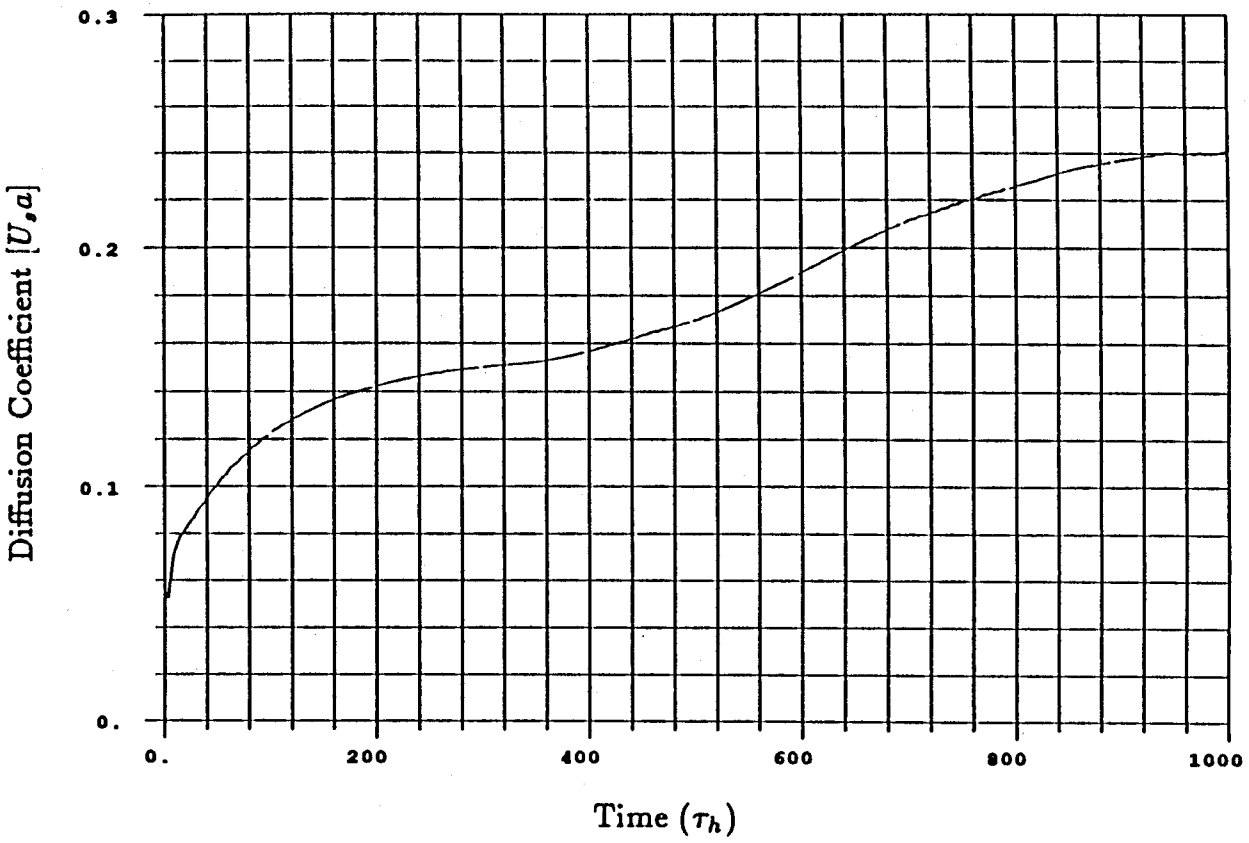

Figure 4.48 The time evolution of the x diffusion coefficient with restart for run s62. See table 4.7 for the simulation parameters.

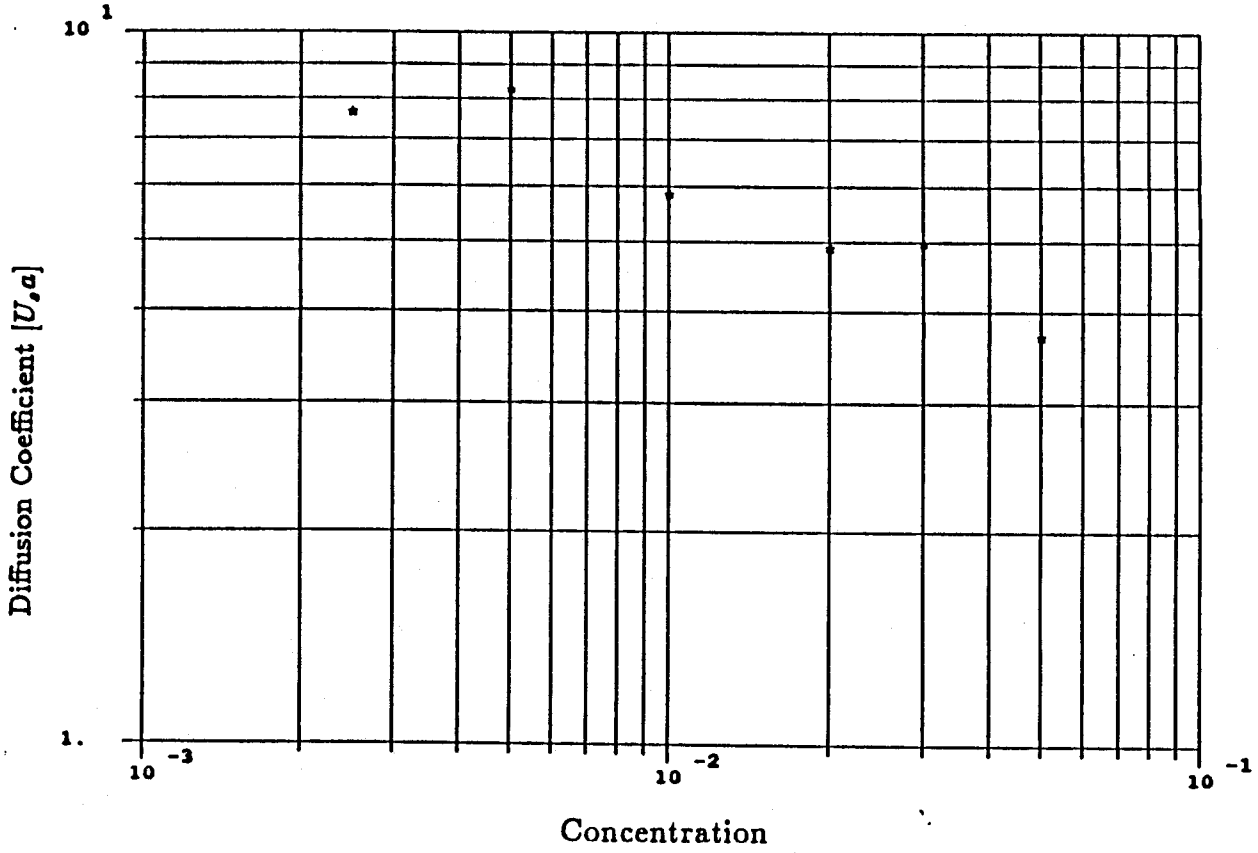

Figure 4.49 The dependence of the x diffusion coefficient on concentration. The simulations were performed using 64 particles.

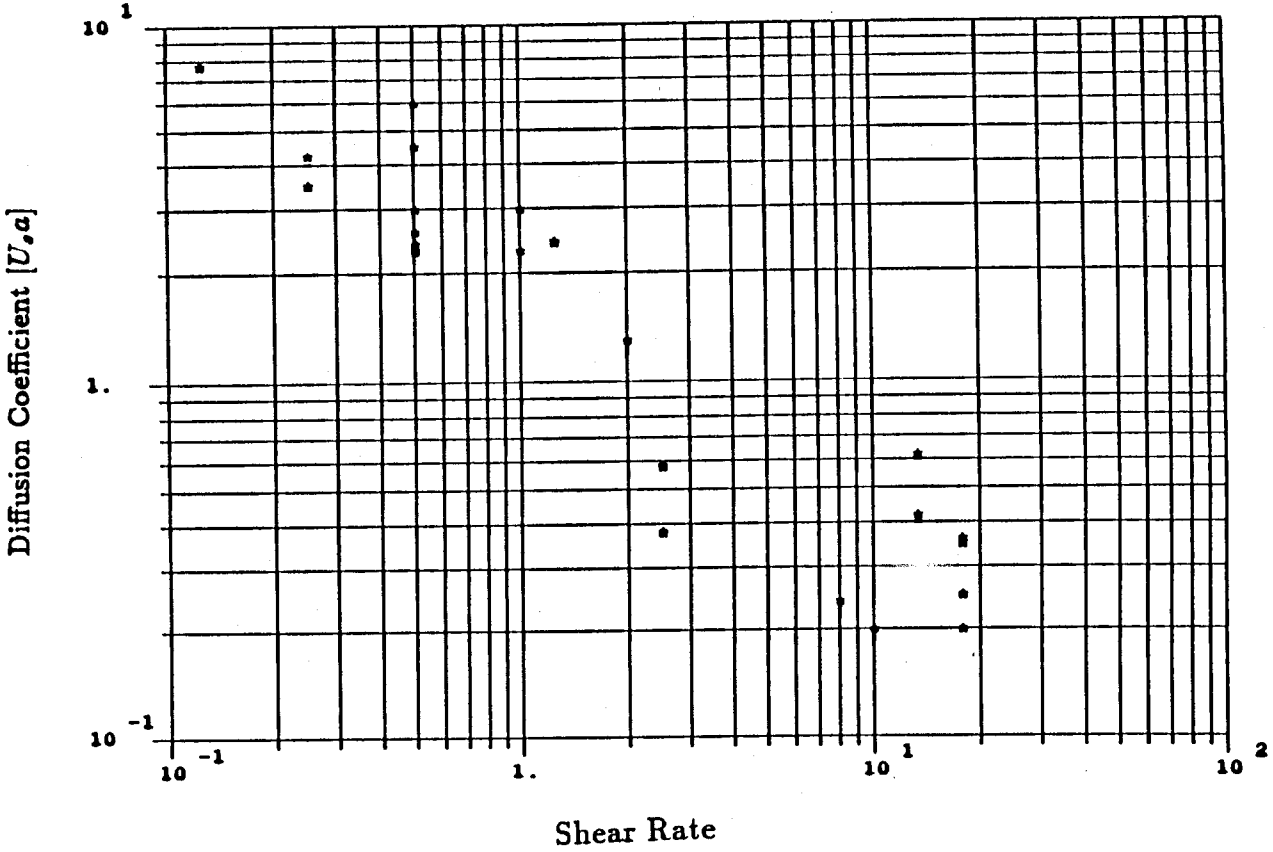

Figure 4.50 The dependence of the x diffusion coefficient on the shear rate.

5 The Effects of Hydrodynamic Dispersion on the Interpretation of Sedimentation Data

5.1 Introduction

The results from our simulator show that for both the sheared and quiescent suspensions, the sedimentation velocities vary with c rather than with $c^{\frac{1}{3}}$, and that the particle distributions do not have a length scale which depends on $ac^{-\frac{1}{3}}$. The results from our simulator also show that the suspensions behave diffusively and that one difference between the quiescent and sheared sedimenting supsensions is in their diffusion coefficients. We have pointed out that the diffusive nature of the suspension causes the interface between the suspension and the clear fluid region to spread, and thus the interface velocity is less than the sedimentation velocity in the bulk of the suspension. Therefore, in interpreting the sedimentation data, equating the measured interface velocity with the bulk sedimentation velocity is invalid. This may account for the different observed concentration dependences of the sedimentation velocity for sheared and quiescent suspensions, and for suspensions of Brownian particles. We will examine whether this is the case by using the macroscopic continuity equation to model the spreading of the interface. From this equation, the concentration profile as a function of time is determined. We will assume a value of the opaque concentration, the volume fraction at which the suspension appears opaque, and follow a point in the suspension with this concentration (i.e., the interface) as the suspension settles. The rate of fall of this interface is the apparent sedimentation velocity. We can then compare this value with those of the experiments.

5.2 The Solutions of the Continuity Equation and the Interface Velocity

The variation of the particle concentration ($\bar{c}$) in the $\bar{x}$ direction (direction of sedimentation) and in time ($\bar{t}$) is controlled by

$$\frac{\partial \bar{c}}{\partial \bar{t}} + \frac{\partial \bar{c}\overline{U}(\bar{c})}{\partial \bar{x}} = \frac{\partial}{\partial \bar{x}}\overline{\mathcal{D}}(\bar{c})\frac{\partial(\bar{c})}{\partial \bar{x}}, \tag{5.1}$$

where $\overline{U}(\bar{c})$ is the average particle velocity and $\overline{\mathcal{D}}(\bar{c})$ is the diffusion coefficient for a suspension with concentration $\bar{c}$. To simplify this problem we will choose a

reference frame moving with the velocity $\overline{U}(c_0)$ where c_0 is the bulk concentration. We nondimensionalize concentration with c_0, velocity with $[U_s - \overline{U}(c_0)]$, diffusion coefficient with $\overline{\mathcal{D}}(c_0)$, length by the thickness of the interface (l_i), and time by the time it takes for the concentration profile to become fully developed (τ_s). Equation (5.1) becomes

$$\frac{\partial c}{\partial t} + \frac{\tau_s(U_s - U(c_0))}{l_i}\frac{\partial c(U(c) - U(c_0))}{\partial x} = \frac{\mathcal{D}(c_0)\tau_s}{l_i^2}\frac{\partial}{\partial x}\mathcal{D}(c)\frac{\partial(c)}{\partial x}. \qquad (5.2)$$

Near the interface, all three terms are equally important (i.e., all the coefficients are O(1)), and therefore we expect τ_s to equal $\frac{\mathcal{D}(c_0)}{(U_s - U(c_0))^2}$ and l_i to equal $\frac{\mathcal{D}(c_0)}{(U_s - U(c_0))}$. Equation (5.2) simplifies to

$$\frac{\partial c}{\partial t} + \frac{\partial c(U(c) - U(c_0))}{\partial x} = \frac{\partial}{\partial x}\mathcal{D}c\frac{\partial c}{\partial x}, \qquad (5.3a)$$

$$t \leq 0 \qquad c = 0 \quad \text{at } x < 0 \qquad (5.3b)$$

$$= 1 \quad \text{at } x > 0,$$

$$t > 0 \qquad c = 0 \quad \text{at } x = -\infty \qquad (5.3c)$$

$$= 1 \quad \text{at } x = \infty.$$

The conditions for $t > 0$ is an idealization of a sedimenting suspension. A real suspension is finite in size, and the boundary condition should read,

$$t > 0 \qquad c = 0 \quad \text{at } x = \frac{-\overline{U}(\bar{c}_0)t}{l_i}. \qquad (5.3d)$$

At short time $\frac{-\overline{U}(\bar{c}_0)t}{l_i}$ is small, but as the experiment progresses this ratio grows and the approximation (5.3c) improves. In table 5.1 we list the ratio of $-\overline{U}(\bar{c}_0)t$ (denoted by l_e) to l_i. This ratio is greater than 40, which suggests that (5.3c) is a reasonable model for at least the latter part of the experiment.

To solve (5.3), the sedimentation velocity and diffusion coefficient are needed. For the sedimentation velocity we have chosen

$$U(c) = U_s(1.0 - \beta c). \qquad (5.4)$$

This is the form of the sedimentation velocity obtained in our simulations, and it is also the form reported for the Brownian and sheared suspension experiments. For the diffusion coefficient we have chosen

$$\mathcal{D}(c) = \mathcal{D}_0 c^{\alpha}. \tag{5.5}$$

From our simulator we find that α is between $-\frac{1}{4}$ and $-\frac{1}{3}$. There is also a possibility that the diffusion coefficient is independent of concentration at low volume fraction because it is the product of the variance and the correlation time. At low concentration, the former varies with $c^{\frac{2}{3}}$ while the latter varies with $c^{-\frac{2}{3}}$ (section 4.2). We examined three cases, $\alpha = 0$, $\alpha = \frac{1}{3}$ and $\alpha = -\frac{1}{3}$ to give us insight into the sensitivity of our results to the form of the diffusion coefficient. For the sedimentation velocity and diffusion coefficient given by (5.4) and (5.5), l_i is $\frac{\overline{\mathcal{D}}(c_0)}{U_s \beta c_0^{1-\alpha}}$, and τ_s is $\frac{\overline{\mathcal{D}}(c_0)}{U_s^2 \beta^2 c_0^{2-\alpha}}$. The continuity equation now becomes

$$\frac{\partial c}{\partial t} + \frac{\partial c(c-1)}{\partial x} = \frac{\partial}{\partial x} c^{\alpha} \frac{\partial c}{\partial x}. \tag{5.6}$$

Before proceeding to solve (5.6), let's examine the ratio of l_i to l_Δ. The latter is the difference between the distance the interface travels if all the particles settle with U_s and the distance the interface travels if all the particles settle with velocity $U_s(1.0 - \beta c)$. The ratio of l_i to l_Δ is the ratio of the error in the experimental data due to the spreading interface to the deviation from Stokes's velocity due to hindered settling. If the discrepancy among the experimentally measured sedimentation velocities is due to the spreading of the interface, then $\frac{l_i}{l_\Delta}$ will be larger for those experiments which show a sedimentation velocity which depends on $c^{\frac{1}{3}}$ (suspensions of large particles), than for those experiments which show a c dependence (sheared suspensions, and suspensions of Brownian particles). In table 5.1 we have tabulated this ratio for several experiments. In determining this ratio, we have used a value of 5.0 for β because this is the value found experimentally for Brownian particles, and it is similar to the β obtained from our simulations of non-Brownian particles. The length, l_Δ, is estimated from $\beta c_0 l_e$. The first two experiments used small Brownian particles, and their sedimentation velocities showed

a c dependence. The third experiment is Lynch's sheared sedimenting suspension experiments, and its sedimentation velocity also showed a c dependence. The final two experiments involved the quiescent sedimentation of suspensions of large particles. Their velocities depended on $c^{\frac{1}{3}}$. For each experiment we have listed its hydrodynamic diffusion coefficient, which is $6U_s a$ for a quiescent sedimenting suspension, and $0.6U_s a$ for a sheared suspension. These values are obtained from our simulations. For the first two experiments, we also included the Brownian diffusion coefficient, and in determining the interface thickness for these two cases, we have used the larger of the two. The ratio of $\frac{l_i}{l_\Delta}$ for these experiments shows the predicted trend.

One additional point to notice from table 5.1 is that the interface of a sedimenting Brownian suspension does not spread as much as the interface of a suspension of large paticles. This is counterintuitive because one imagines that small particles tend to diffuse great distance rapidly. However table 5.1 shows that this distance is small compared with the distance settled by the particles. The suspensions whose interfaces spread the most contain large particles, the kind which are not normally thought to be diffusive.

For α equal to zero, (5.6) simplifies to Burger's equation. The solution given by Whitham (1974) is

$$c = 1 - \frac{1}{1 + he^z}, \tag{5.7a}$$

$$h = \frac{2 - \mathrm{erfc}\left(\frac{1}{2}\frac{z+t}{\sqrt{t}}\right)}{\mathrm{erfc}\left(\frac{1}{2}\frac{z+t}{\sqrt{t}}\right)}, \tag{5.7b}$$

$$c = \frac{\bar{c}}{c_0}, \tag{5.7c}$$

$$t = \frac{\bar{t}}{\frac{\mathcal{D}}{(\beta c_0 U_s)^2}}, \tag{5.7d}$$

$$z = \frac{\bar{x} - (1 - \beta c_0)\bar{t}}{\frac{\mathcal{D}}{\beta c_0 U_s}}. \tag{5.7e}$$

The steady state solution is,

$$c = 1 - \frac{1}{1+e^z}. \tag{5.8}$$

Concentration profiles for several times are given in figure 5.1. We will use these profiles later to determine the interface velocity.

When α is $\frac{1}{3}$, we solve (5.4) numerically using the following finite difference method. The infinite domain of x is first mapped on to a domain between -1 and 1 by the transformation,

$$x = \frac{y}{1-y^2}. \tag{5.9}$$

Equation (5.4) now becomes,

$$\frac{\partial c}{\partial t} + \frac{(1-y^2)^2}{1+y^2}\frac{\partial c(c-1)}{\partial y} = \frac{(1-y^2)^2}{1+y^2}\frac{\partial}{\partial y}\left(c^{\frac{1}{3}}\frac{(1-y^2)^2}{1+y^2}\frac{\partial c}{\partial y}\right), \tag{5.10}$$

$$\begin{aligned} t \leq 0 \qquad c &= 0 \quad \text{at } y < 0 \\ &= 1 \quad \text{at } y > 0, \end{aligned}$$

$$\begin{aligned} t > 0 \qquad c &= 0 \quad \text{at } y = -1 \\ &= 1 \quad \text{at } y = 1. \end{aligned}$$

In (5.10) the two first order derivatives are replaced with their central difference approximations. To improve accuracy and stability, the diffusion term is approximated using the three-time-level method. In this scheme the second order derivative is replaced by the average of the central differences at the previous time step, present time step, and the next time step. Since the three-time-level method requires information at the next time step, this technique is an implicit scheme. Also because it needs information at the previous time step, this method is not self starting. To overcome the latter difficulty, the solution for the first time step is obtained using a Crank-Nicholson method. After the first time step has been taken, we convert to the three-time-level method. When the equation is finite differenced, we find that the values of the diffusion coefficient are needed between grid points, Since

the concentration between grid points are not determined, the diffusion coefficients are approximated by the average of the diffusion coefficients at the adjacent grid points. Furthermore, to maintain the linearity of the resulting set of finite difference equations, the diffusion coefficient is obtained using the values of the concentration at present time. In figure 5.2, the concentration profiles at dimensionless time of 4 obtained using three combinations of Δy and Δx (Δy of 0.04 and Δt of .001, Δy of 0.02 and Δt of 0.001, and Δy of 0.02 and Δt of 0.0001) are presented. There is good agreement between the three profiles. In generating the concentration profiles used in determining the apparent sedimentation velocity, we have used a Δy of 0.04 and a Δt of 0.001. Several concentration profiles are presented in figure 5.3. The concentration profiles differ from those of $\alpha = 0$ case in that the slope for $c > \frac{1}{2}$ is smaller, and for $c < \frac{1}{2}$ is larger. This is to be expected because the diffusion coefficient is larger for $c > \frac{1}{2}$ and smaller for $c < \frac{1}{2}$ in the $\alpha = \frac{1}{3}$ case.

When α is $-\frac{1}{3}$, the problem becomes more complex. The diffusion coefficient $c^{-\frac{1}{3}}$ approaches infinity as concentration reduces to zero. The problem, however, is still well defined because $\frac{(1-y^2)^2}{1+y^2}$ and $\frac{\partial c}{\partial y}$ both tend toward zero as c reduces to zero and the diffusion term remains bounded. However, numerically, unless the finite difference scheme accurately reproduces the rate at which $\frac{\partial c}{\partial y}$ and $\frac{(1-y^2)^2}{1+y^2}$ approach zero, and $c^{\frac{1}{3}}$ approaches infinity, the product of these terms may not be bounded. Unfortunately when we attempt to apply the three-time-level method on (5.13), we find that the finite difference scheme upsets the delicate balance between the terms $c^{-\frac{1}{3}}$, $\frac{(1-y^2)^2}{1+y^2}$, and $\frac{\partial c}{\partial y}$. At short time, the solution oscillates wildly with time. After the initial period, the solution does stabilize for a while, but at long time a kink develops in the concentration profile. These aberrant behaviors indicate that the three-time-level method is inadequate. To overcome this problem we rewrite $c^{-\frac{1}{3}}\frac{\partial c}{\partial y}$ as $\frac{3}{2}\frac{\partial c^{\frac{2}{3}}}{\partial y}$. In this form, $c^{-\frac{1}{3}}$, and $\frac{\partial c}{\partial y}$ are explicitly coupled together, and when we finite difference this term, the balance is maintained. Equation (5.10) becomes

$$\frac{\partial c}{\partial t} + \frac{(1-y^2)^2}{1+y^2}\frac{\partial c(c-1)}{\partial y} = \frac{3}{2}\frac{(1-y^2)^2}{1+y^2}\frac{\partial}{\partial y}\left(\frac{(1-y^2)^2}{1+y^2}\frac{\partial (c^{\frac{2}{3}})}{\partial y}\right). \qquad (5.11)$$

To avoid a complicated set of coupled nonlinear equations, we used an explicit finite

difference scheme to solve (5.11). The time derivative is approximated by a forward difference, and the spatial derivatives are approximated with a central difference. To examine the stability of this algorithm, we return to (5.6). It is generally believed (Ames 1977) that the stability requirement of an explicit scheme for an equation of the form

$$\frac{\partial c}{\partial t} = \frac{\partial}{\partial x}\frac{\partial c^n}{\partial x}, \tag{5.12}$$

is

$$nc^{n-1}\frac{\Delta t}{\Delta x^2} \leq \frac{1}{2}, \tag{5.13}$$

or for our problem,

$$\frac{2}{3}c^{-\frac{1}{3}}\frac{\Delta t}{\Delta x^2} \leq \frac{1}{2}. \tag{5.14}$$

Since the initial profile is a step function, c is 0 for x less than 0, and the explicit scheme is unconditionally unstable. However after several iterations, c is no longer zero, and one can choose a $\frac{\Delta t}{\Delta x^2}$ which will satisfy the stability requirement. The error introduced during the initial period of time can be viewed as perturbing our initial distribution. In practice we have found that for small time steps (10^{-7}), after 50 iterations, the profile has not deviated significantly from a step function. The stability requirement does not restrict Δt as severely as (5.13) seems to suggest. When we transform x into the y coordinate, and use a uniform Δy, we in effect are using a variable Δx in x space. As x approaches $-\infty$, the concentration is small but the Δx which we use is large. In essence we have used a variable step size explicit scheme to solve (5.13). We start the integration with step size of 10^{-8}, and then adjust Δt using the criteria

$$\mathrm{Max}\left[c^{-\frac{1}{3}}\frac{\Delta t}{\Delta x^2}\right]_{\text{all grid points}} \leq 1, \tag{5.15}$$

Furthermore we have limited the maximum value of Δt to 10^{-4}. The Δx we used is 0.02. Typically, after a dimensionless time of 0.05, Δt of 10^{-5} is sufficient. To examine the effect of the choice of the initial step size and the maximum permitted Δt, we determined the concentration profile at a dimensionless time of 0.5 using

an initial Δt of 10^{-8} and a maximum Δt of 10^{-5}, and compared this profile with that obtained using an initial Δt of 10^{-7} and a maximum Δt of 10^{-4}. The results are shown in figure 5.4. The two show good agreement. For generating the concentration profile we used an initial Δt of 10^{-8} and a maximum Δt of 10^{-4}. Several concentration profiles are shown in figure 5.5.

To determine the rate of fall of the interface, we first obtained the concentration profiles at regular intervals of time. After choosing an opaque concentration, (i.e., the interface) we find from these concentration profiles the location of the interface at regular time interval. The slope of the interface position versus time curve (IPTC) gives the rate of fall of the interface.

The concentration at which the suspension becomes opaque is low. Makhlouf (1988) had observed an interface at 0.1%. Oliver (1961) reported sedimentation velocity for concentration of 0.33%, and Buscall **et al.** (1982) reported sedimentation velocity for a volume fraction of 0.5%. These velocities were obtained by measuring the rate of fall of the interface, and therefore we conclude that an interface can be observed at these low concentrations. We have determined the apparent sedimentation velocity assuming that the suspension becomes opaque at 0.1%, 0.5% and 1.0%.

The concentration profiles are nondimensional. To compare the theoretical results with experiments, we restore units to the concentration profiles using (5.7c) through (5.7e). This transformation depends on the parameters β, U_s, $\mathcal{D}(c_0)$ and a. β was chosen to be 5.0, and the remaining parameters were chosen to model an actual experiment. To model Lynch's quiescent sedimenting suspension, we chose U_s to be 1mm/min, a to be 50 μm, and $\mathcal{D}(c_0)$ to be $6U_s a$ for a 1% suspension. Lynch did not measure the diffusion coefficient; the value $6U_s a$ comes from the results of our simulations of a 1% suspension. For α equal 0 case, a typical IPTC is shown in figure 5.6. It is for a 3% suspension, and each of the curves in the graph is for a different opaque concentration. Figure 5.6 shows that the interface velocity, i.e., the slope of the curve, decreases with decreasing opaque concentration. An argument against our explanation that it is the spreading interface which causes

the discrepancy among the experimental data is that if the spreading interface is important, then the IPTC should show significant curvature. This is because the slope of the curve, which is the interface velocity, is equal to the bulk sedimentation velocity (a constant), minus the velocity due to the spreading interface which decays to zero with time. If the latter is important then significant curvature should be observed. The fact that the experimentally obtained IPTC show no curvature implies that the spreading interface is unimportant. Figure 5.6 however shows that this is not true; the IPTC shows only a slight curvature (which can be hidden by the scatter in the experimental data), and yet, as we shall see, the interface velocity deviate significantly from the bulk sedimentation velocity.

In figures 5.7 through 5.9 the interface velocity dependence on c is shown. In obtaining the interface velocity, we need to decide over which portion of the curve to measure the slope. This is because the curvature of IPTC changes with time, and hence the interface velocity will depend on which portion of the curve is used. In Lynch's experiments, the suspension was allowed to stand for awhile after mixing had stopped before the interface positions were recorded. His experiments typically lasted between ten and twenty minutes. To mimic this, we discard the inital part of the curve and also the part of the curve beyond twenty minutes. The interface velocity is obtained from measuring the slope of the remaining portion of the curve. Since the length of the initial period we should discard is not known, we chose three lengths of time and observed how the interface velocity is affected by the choice. Figures 5.7, 5.8, and 5.9 are obtained from discarding the first two minutes, the first four minutes, and the first seven minutes of the IPTC, respectively. Varying this time increases the interface velocity at high bulk volume fractions, but it does not affect the interface velocity at low volume fraction significantly. From these figures we observe that for an opaque concentration of 0.1% the interface velocity falls close to the $(1 - c^{-\frac{1}{3}})$ correlation. For an opaque concentration of 0.5%, the interface velocity still deviates significantly from the correlation $(1. - 5.0c)$, but for the opaque concentration of 1.0%, the deviation is negligible. We repeated the same set of calculations for α equal $\frac{1}{3}$ and $-\frac{1}{3}$. Figures 5.10 through 5.12 show

the interface velocity dependence on concentration for α equal $\frac{1}{3}$, and figures 5.13 through 5.15 show the interface velocity dependence on concentration for α equal $-\frac{1}{3}$. (For each α we again obtain three velocity curves corresponding to measuring the slope between two minutes and twenty minutes (figures 5.10, 5.13), four minutes and twenty minutes (figures 5.11, 5.14), and seven minutes and twenty minutes (figures 5.12, 5.15).) The interface velocity for α equal $-\frac{1}{3}$ is slightly higher than for α equal 0 case, but otherwise the two are similar. The interface velocity for α equal $\frac{1}{3}$ is slightly lower than for α equal 0 case, but again the two are similar. It thus appears that the interface velocity is insensitive to the value of α, at least for α between $-\frac{1}{3}$ and $\frac{1}{3}$.

In chapter 4, we pointed out that the simulator underestimates the diffusion coefficient. We therefore doubled the diffusion coefficient and examine how this affects the interface velocity. We only performed this study for α equal 0. Figures 5.16 through 5.18 show that the interface velocity is lower than when the diffusion coefficient is $6U_s a$, especially at large volume fractions. For an opaque concentration of 0.1%, the interface velocity lies below the $(1 - c^{\frac{1}{3}})$ correlation.

We next turn our attention to Lynch's sheared sedimenting suspension experiment. The particle radius again is 50 μm and the Stokes velocity is 1mm/min. From our simulator the diffusion coefficient is $0.6U_s a$. The interface velocity dependence on concentration is shown in figure 5.19. The interface velocity does not deviate from the bulk sedimentation velocity.

Finally, we model a suspension of small particles. In particular, we will examine the experiments of Chen , and Schachman (1955). In their experiments, they used 0.13 μm particles with U_s of 5.6x10^{-3} mm/min and a Brownian diffusion coefficient of $160.0U_s a$. The experiments were terminated after the particles had settled over one centimeter which translates to 36 hours. Figure 5.20 shows the interface velocity dependence on concentration. There is little deviation from the bulk sedimentation velocity.

5.3 Conclusions

We have found that interface spreading is negligible for suspensions of Brownian

particles, and for sheared suspensions. For these two cases, the interface velocity and the bulk sedimentation velocity are the same. For a quiescent sedimenting suspension of large particles, this is not true. We have found that the interface velocity differs from the bulk sedimentation velocity not only in the magnitude but also in its is dependence on concentration. For this case the two velocities should not be equated. These results, however, hinge on the opaque concentration which is not known with precision, and therefore these conclusions should be considered tentative only. In the future, when sedimentation velocity measurements are made, one needs also to ascertain that the interface spreading is negligible so as to avoid misinterpreting the sedimentation velocity data.

Experiments	a (μm)	Brownian Diffusion Coefficient (cm^2/s)	Hydrodynamic Diffusion Coefficient (cm^2/s)	Thickness of Interface (l_i) (cm)	Total Distance Settled by Interface (l_s) (cm)	l_s/l_i	l_i/l_Δ
Chen and Schachman (1955)	.13	$1.6x\,10^{-8}$	$6x\,10^{-10}$	.002	1	500.	.04
Buscall (1982)	1.55	$1.4x\,10^{-9}$	$3x\,10^{-8}$	.001	2	2000.	.01
Lynch (sheared) (1985)	51	–	$1.8x\,10^{-5}$	.003	2	667.	.03
Lynch (quiescent) (1985)	51	–	$1.8x\,10^{-4}$	.03	2	67.	.3
Oliver (1961)	80	–	$4.5x\,10^{-3}$	.05	2	40.	.5

Table 5.1 Relative importance of interface spreading to hindered settling. a is the particle radius, and l_Δ is the difference in the distance traveled by the interface if it moves with U_s, and if it moves with $U_s(1-\beta c)$.

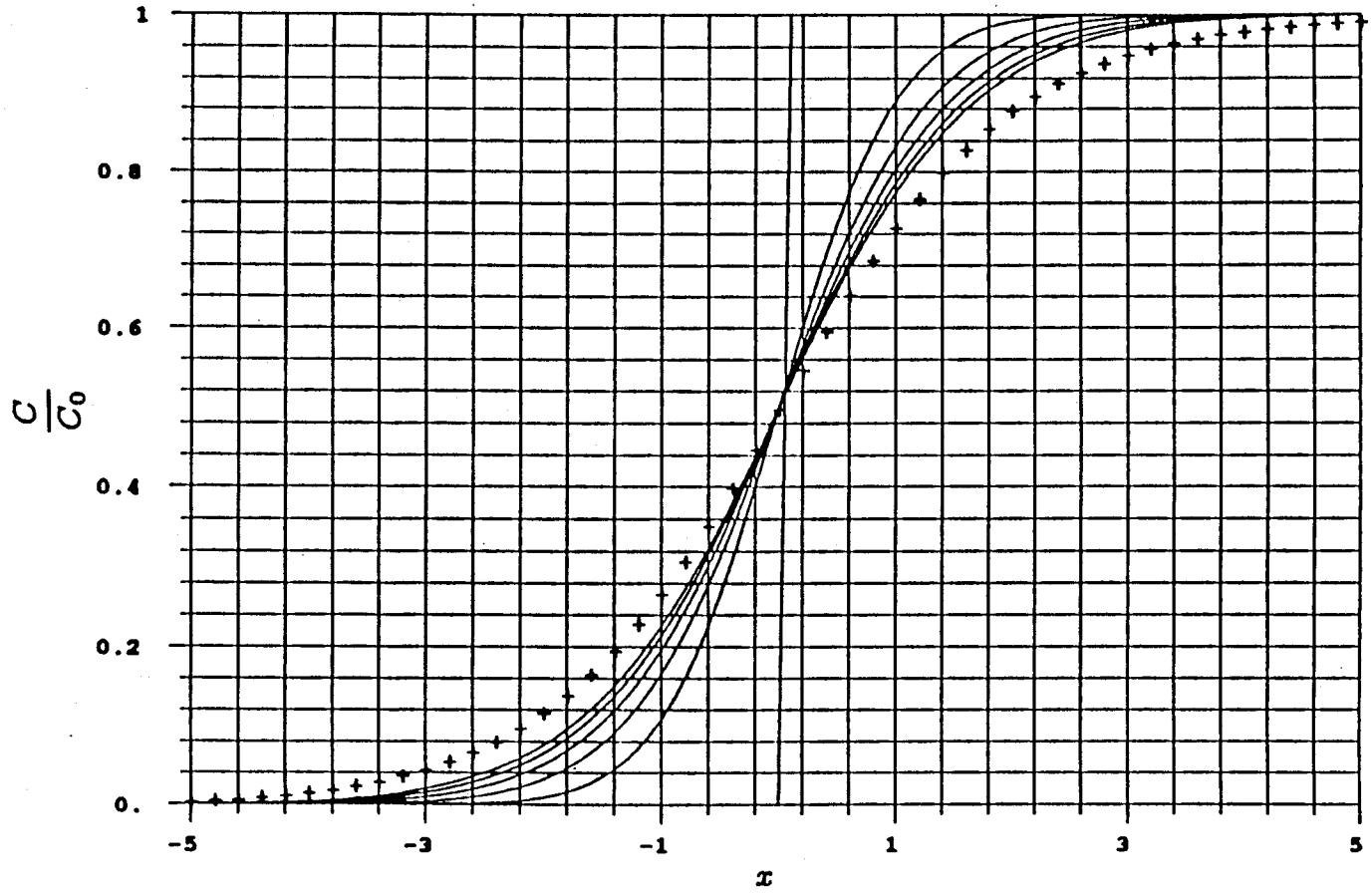

Figure 5.1 Concentration profiles in the reference frame moving with $(1.0 - 5.0c_0)$. The diffusion coefficient is independent of concentration. The solid lines are profiles that are 0.5 time units apart starting with $t = 0$, and the + symbols are the steady state profile.

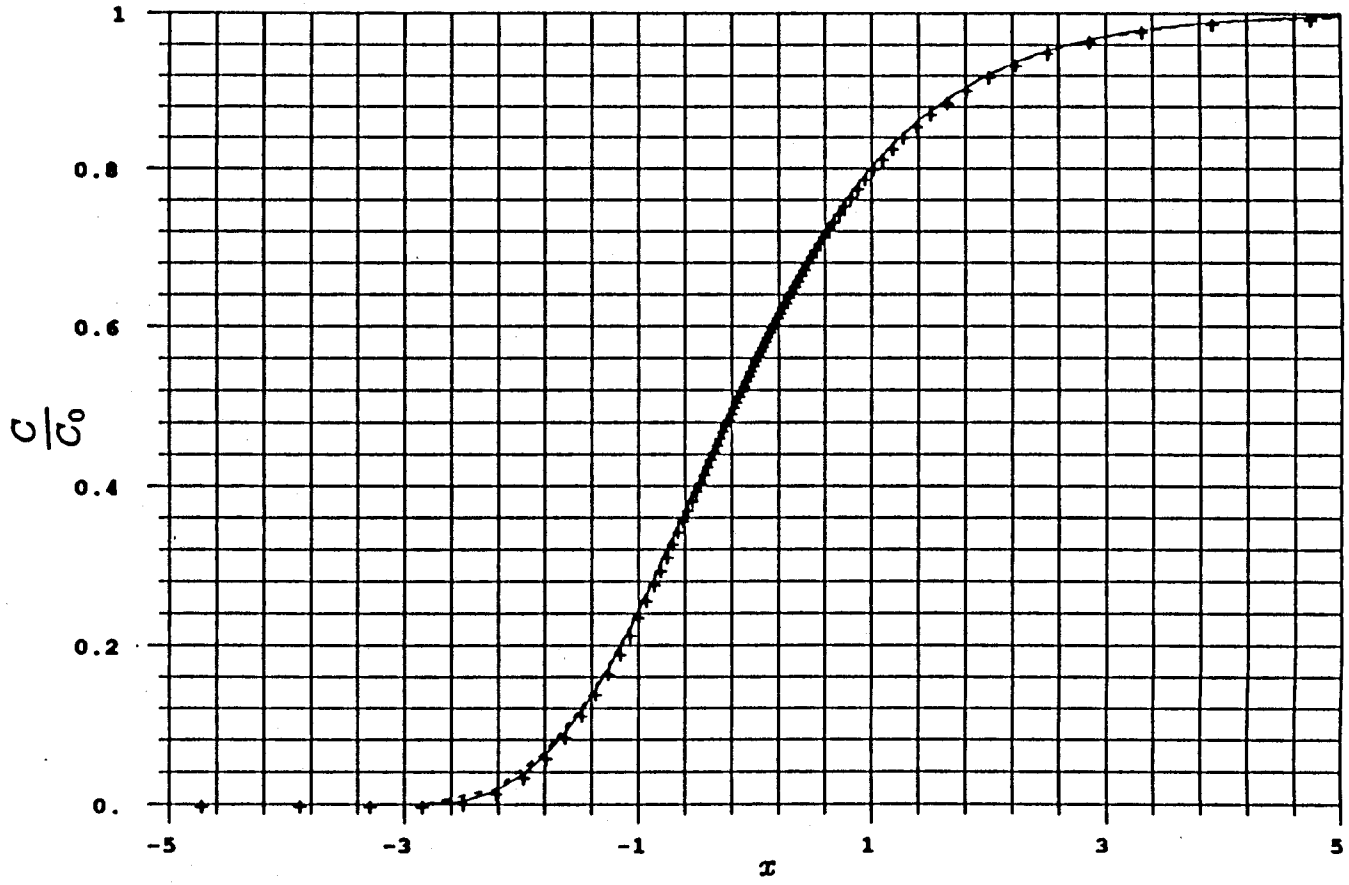

Figure 5.2 Concentration profiles obtained using three combinations of Δt and Δy. The diffusion coefficient varies with $c^{\frac{1}{3}}$. The + symbols are the result for Δt=0.001 and Δy=0.02. The dotted line is the result for Δt=0.001 and Δy=.04. The solid line is the result for Δt=0.0001 and Δy=0.02. These profiles are at a dimensionless time of 1.0.

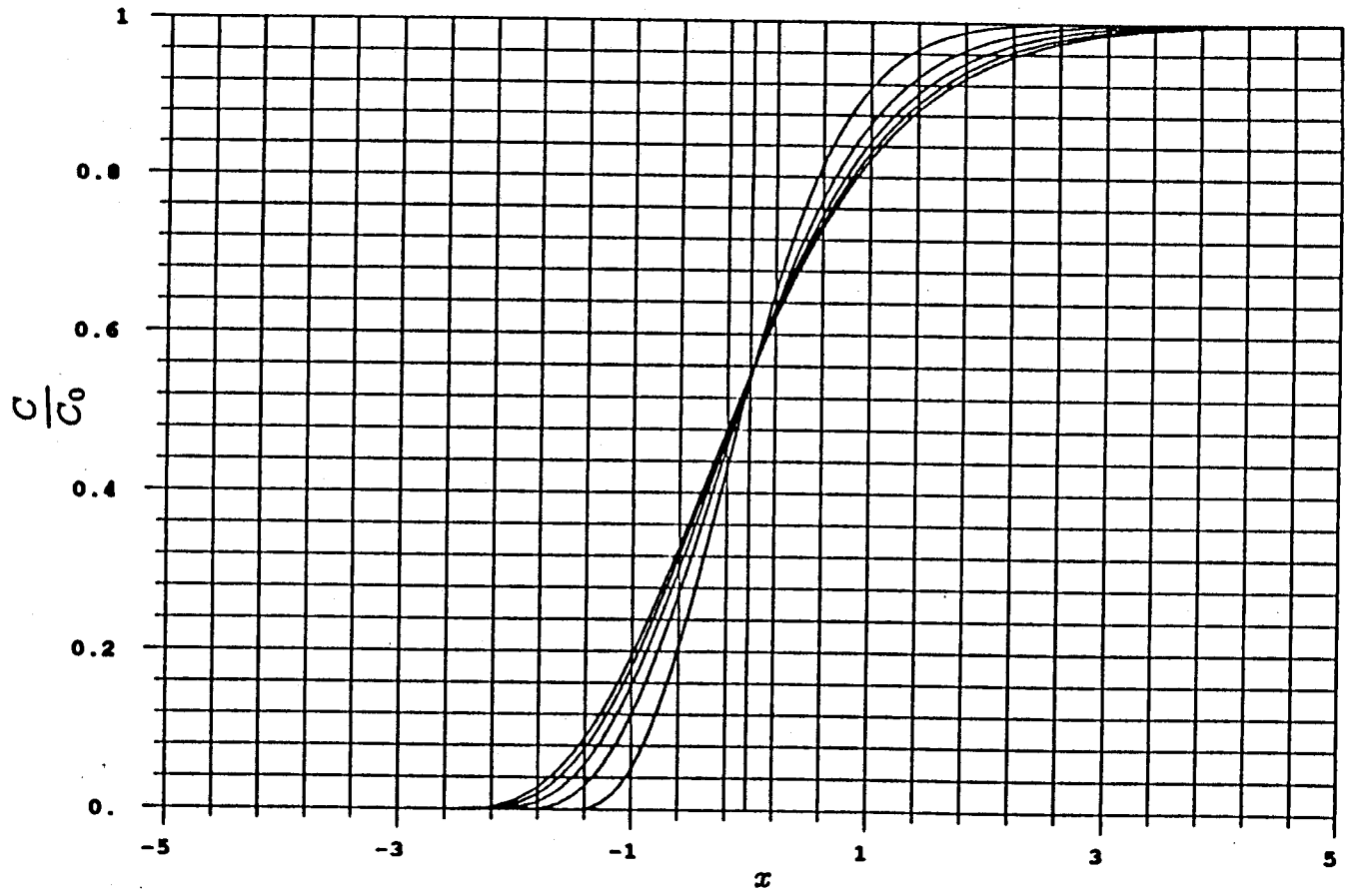

Figure 5.3 Concentration profiles in the reference frame moving with $(1.0 - 5.0c_0)$. The diffusion coefficient varies with $c^{\frac{1}{3}}$. The solid lines are profiles that are 0.5 time units apart starting with $t = 0$.

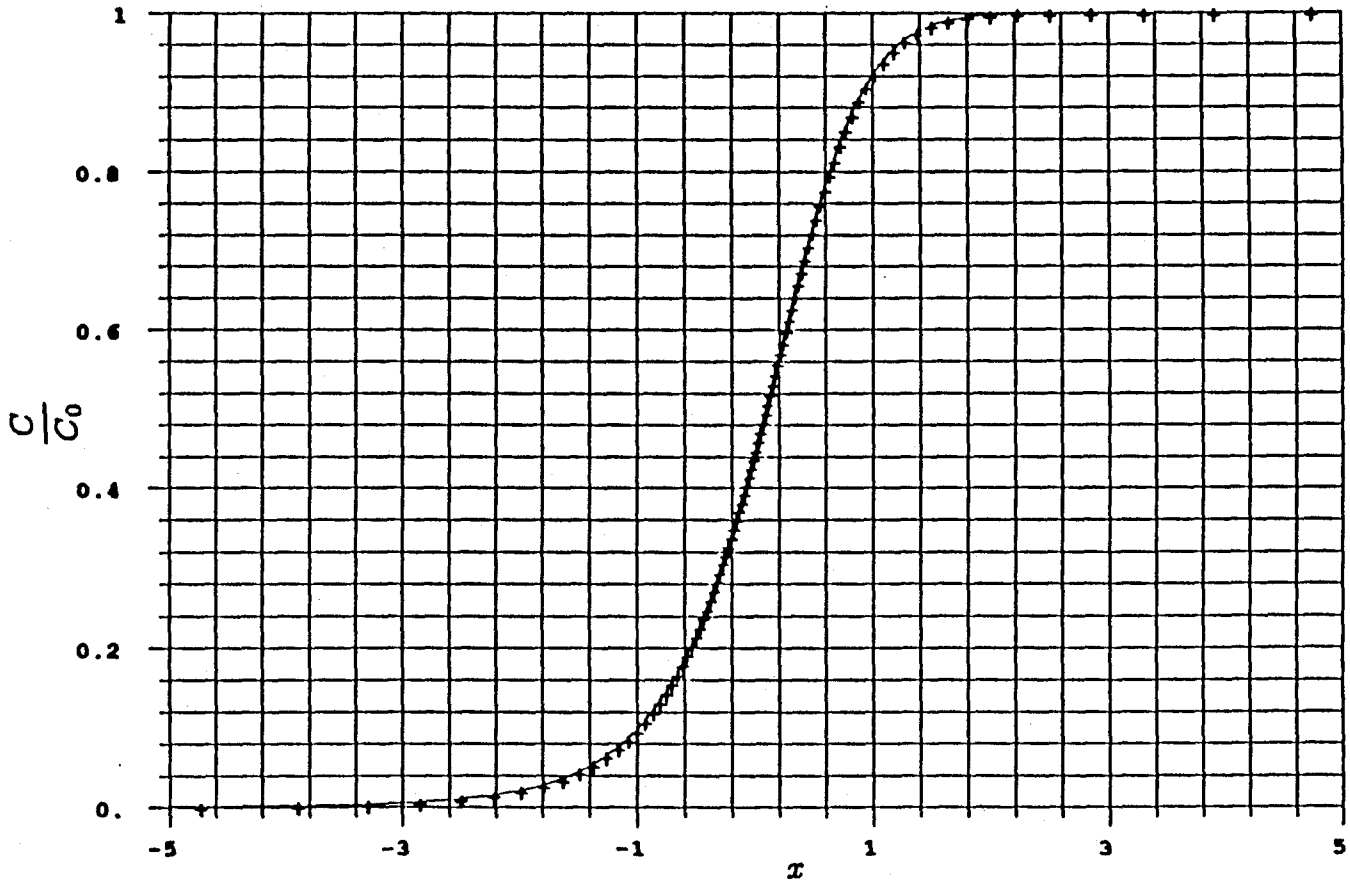

Figure 5.4 Concentration profiles obtained using two combinations of starting Δt and maximum values of Δt. The + symbol is the result for a starting Δt of 10^{-8} and a maximum Δt of 10^{-5}. The solid line is the result for a starting Δt of 10^{-7} and a maximum Δt of 10^{-4}. Δx is 0.02. These profiles are at dimensionless time of 4.0.

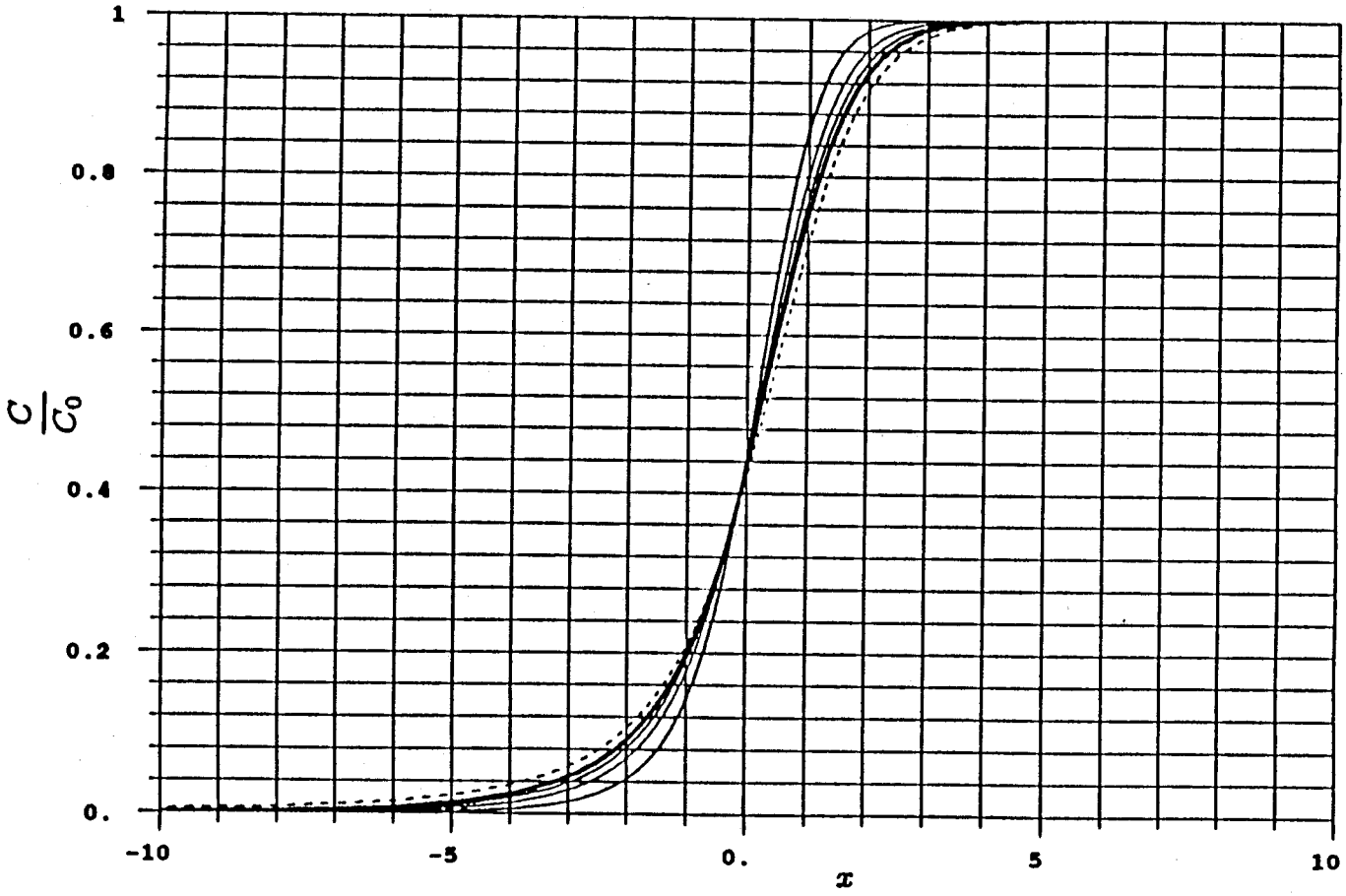

Figure 5.5 Concentration profiles in the reference frame moving with $(1.0 - 5.0c_0)$. The diffusion coefficient varies with $c^{-\frac{1}{3}}$ and is equal to $6.0U_s a$ for a 1% suspension. The solid lines are profiles that are 1.0 time units apart starting from t=0. The dashed line is at a dimensionless time of 40.0.

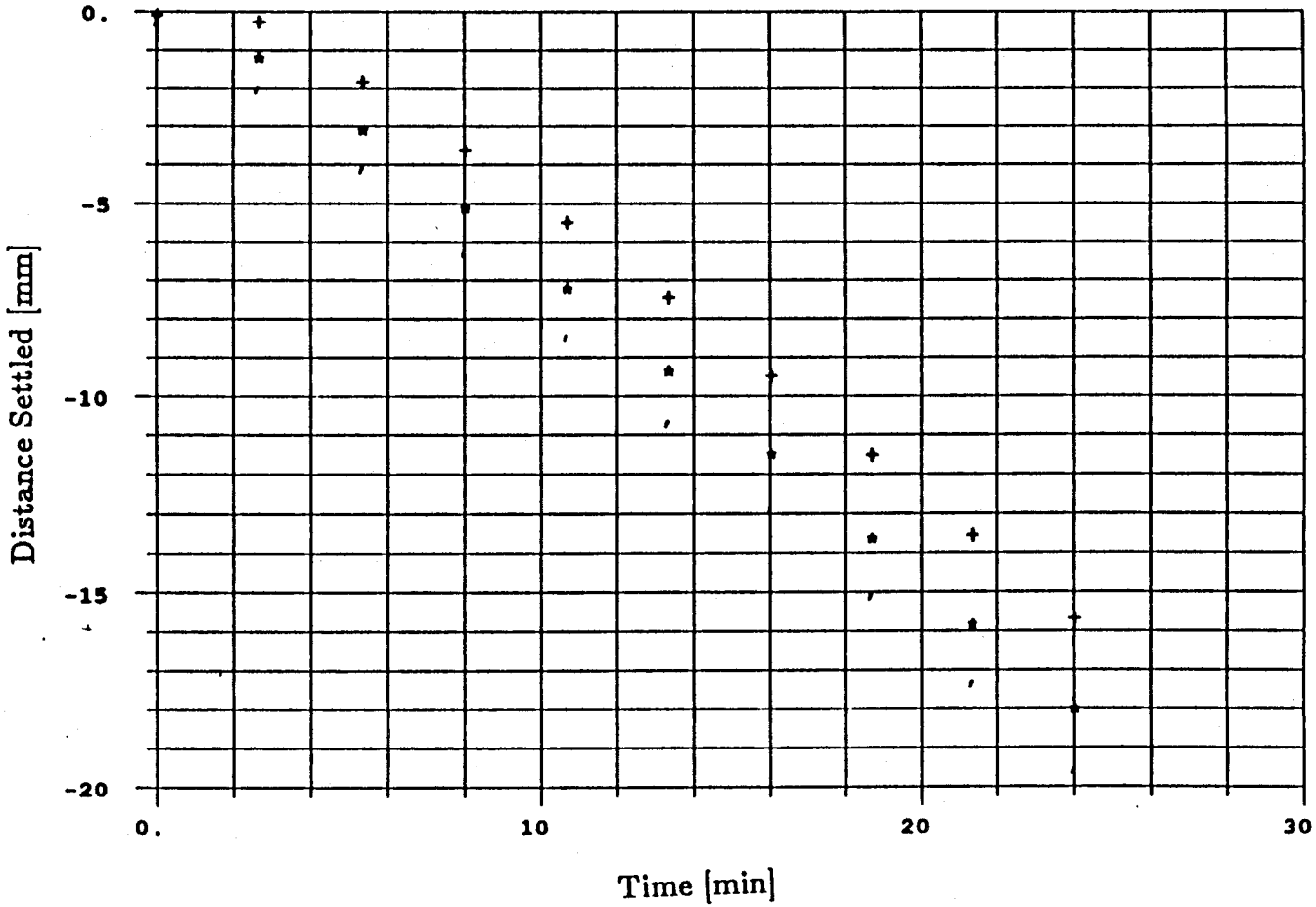

Figure 5.6 The interface positions as a function of time. The particle radius is 50μm, the sedimentation velocity is 1 mm/minute, and the concentration is 3%. The + symbols are for an opaque concentration of 0.1%. The * symbols are for an opaque concentration of 0.5%. The ' symbols are for an opaque concentration of 1.0%. The diffusion coefficient is independent of concentration, and is equal to $6U_s a$.

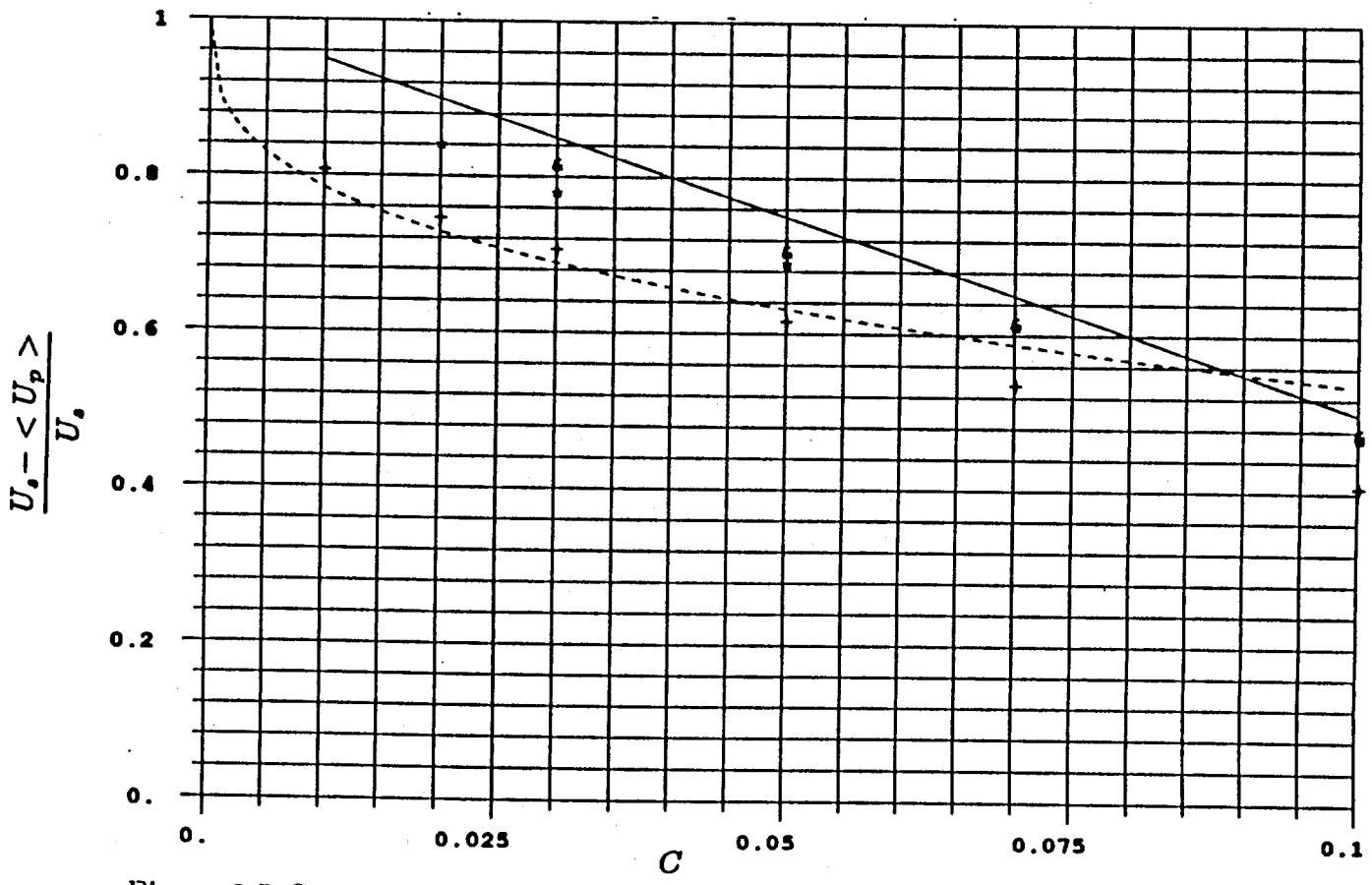

Figure 5.7 Concentration dependence of the sedimentation velocity. The diffusion coefficient is independent of concentration, and is equal to $6U_s a$. The slope is taken from the interface versus time curve between t=2.0 and t=20.0. The solid line is the correlation $(1.0 - 5.0c)$. The dotted line is the correlation $(1.0 - c^{\frac{1}{3}})$. The + symbols are for an opaque concentration of 0.1%. The * symbols are for an opaque concentration of 0.5%. The & symbols are for an opaque concentration of 1.0%.

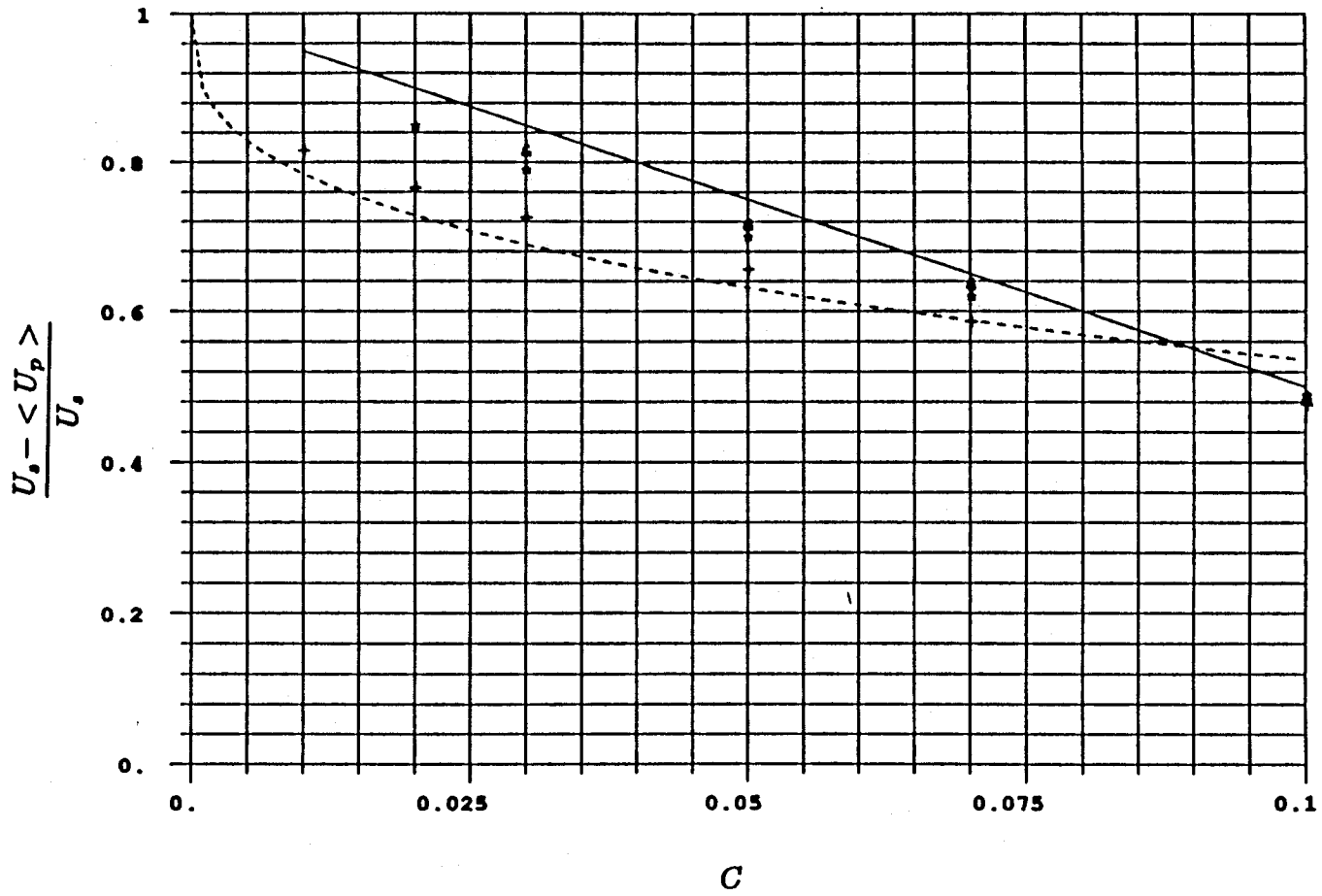

Figure 5.8 Concentration dependence of the sedimentation velocity. The diffusion coefficient is independent of concentration, and is equal to $6U_s a$. The slope is taken from the interface versus time curve between t=4.0 and t=20.0. The solid line is the correlation $(1.0 - 5.0c)$. The dotted line is the correlation $(1.0 - c^{\frac{1}{3}})$. The + symbols are for an opaque concentration of 0.1%. The * symbols are for an opaque concentration of 0.5%. The & symbols are for an opaque concentration of 1.0%.

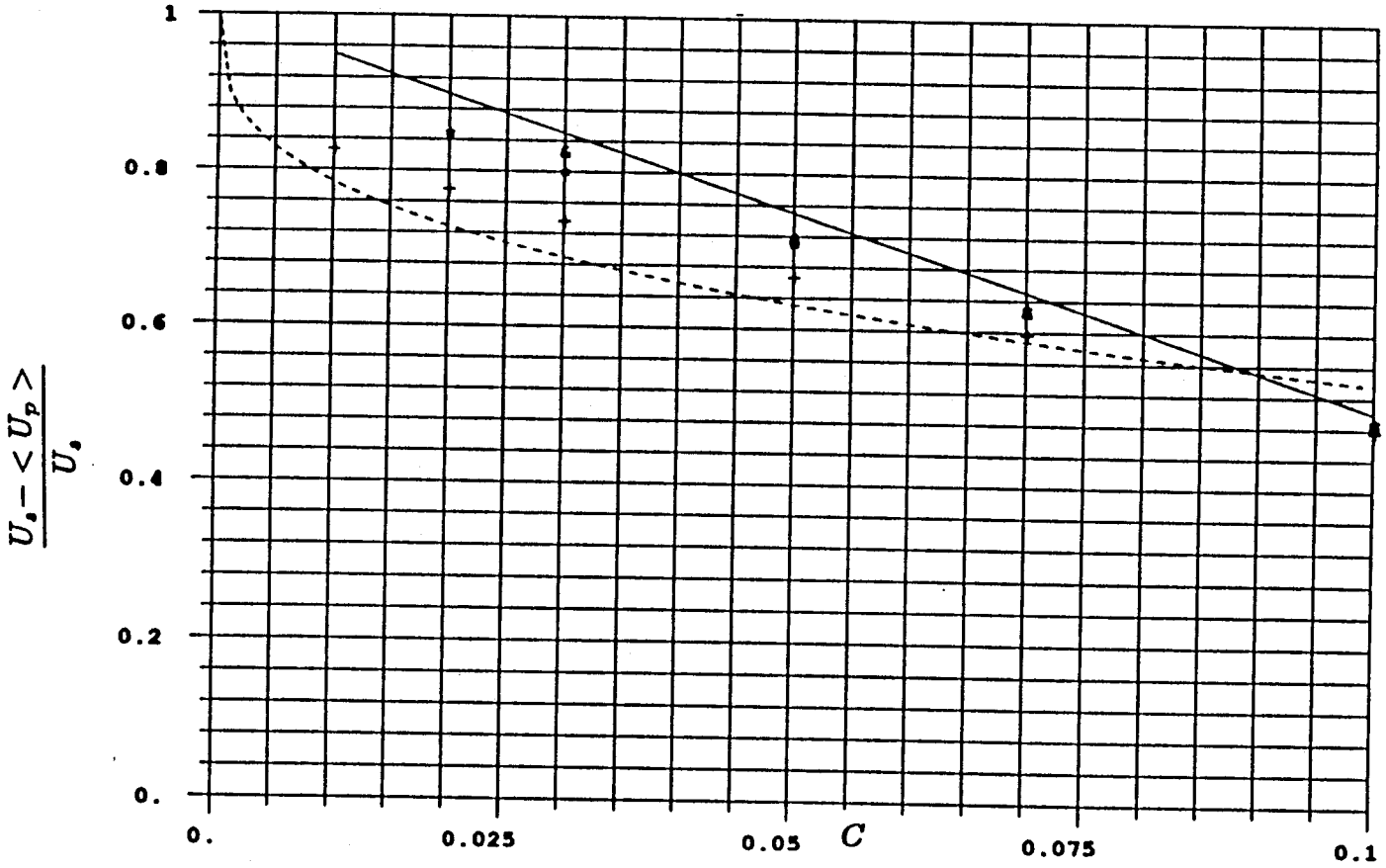

Figure 5.9 Concentration dependence of the sedimentation velocity. The diffusion coefficient is independent of concentration, and is equal to $6U_s a$. The slope is taken from the interface versus time curve between t=7.0 and t=20.0. The solid line is the correlation $(1.0 - 5.0c)$. The dotted line is the correlation $(1.0 - c^{\frac{1}{3}})$. The + symbols are for an opaque concentration of 0.1%. The * symbols are for an opaque concentration of 0.5%. The & symbols are for an opaque concentration of 1.0%.

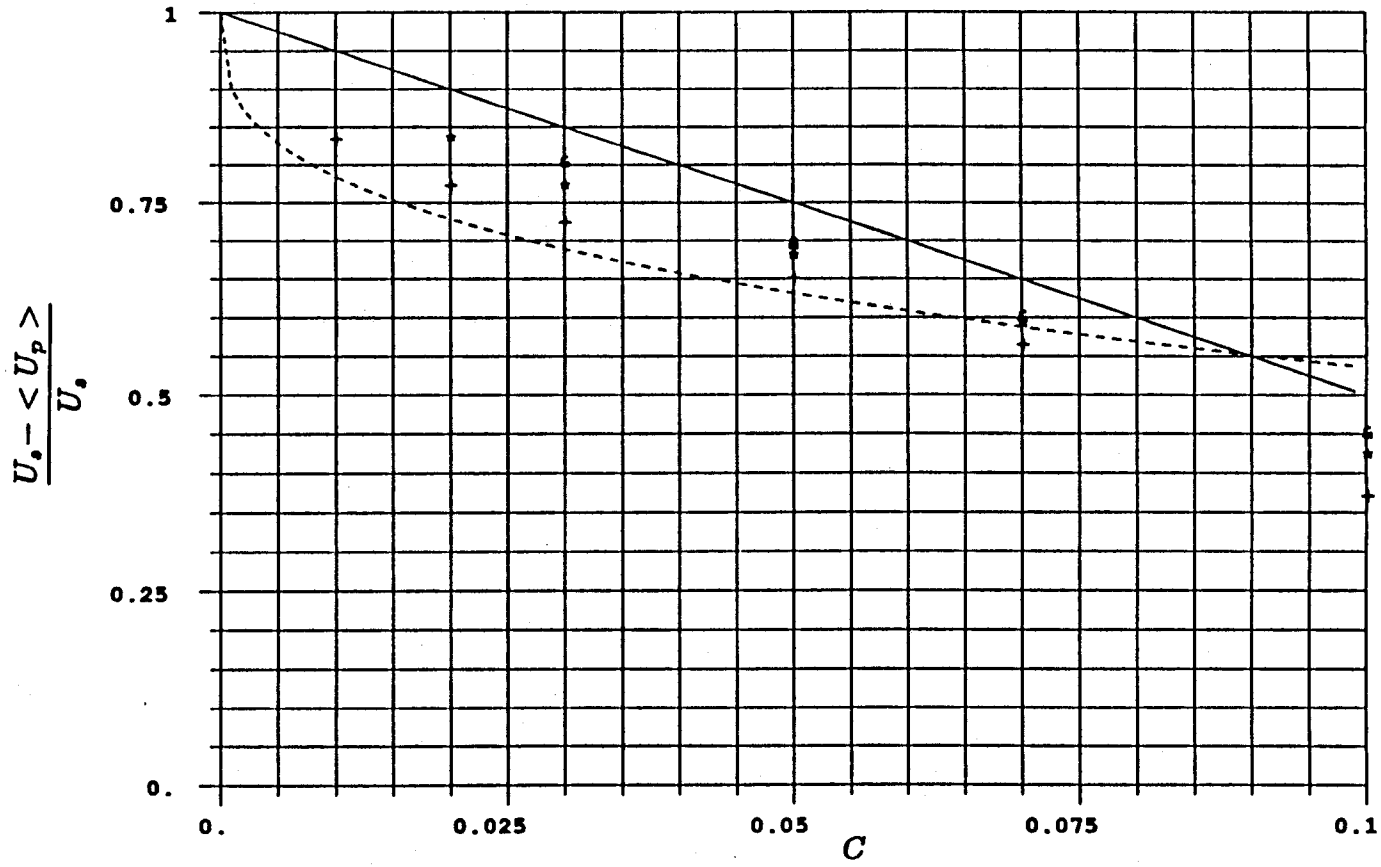

Figure 5.10 Concentration dependence of the sedimentation velocity. The diffusion coefficient varies with $c^{\frac{1}{3}}$, and is equal to $6U_s a$ at a concentration of 1%. The slope is taken from the interface versus time curve between the t=2.0 and t=20.0. The solid line is the correlation $(1.0 - 5.0c)$. The dotted line is the correlation $(1.0 - c^{\frac{1}{3}})$. The + symbols are for an opaque concentration of 0.1%. The * symbols are for an opaque concentration of 0.5%. The & symbols are for an opaque concentration of 1.0%.

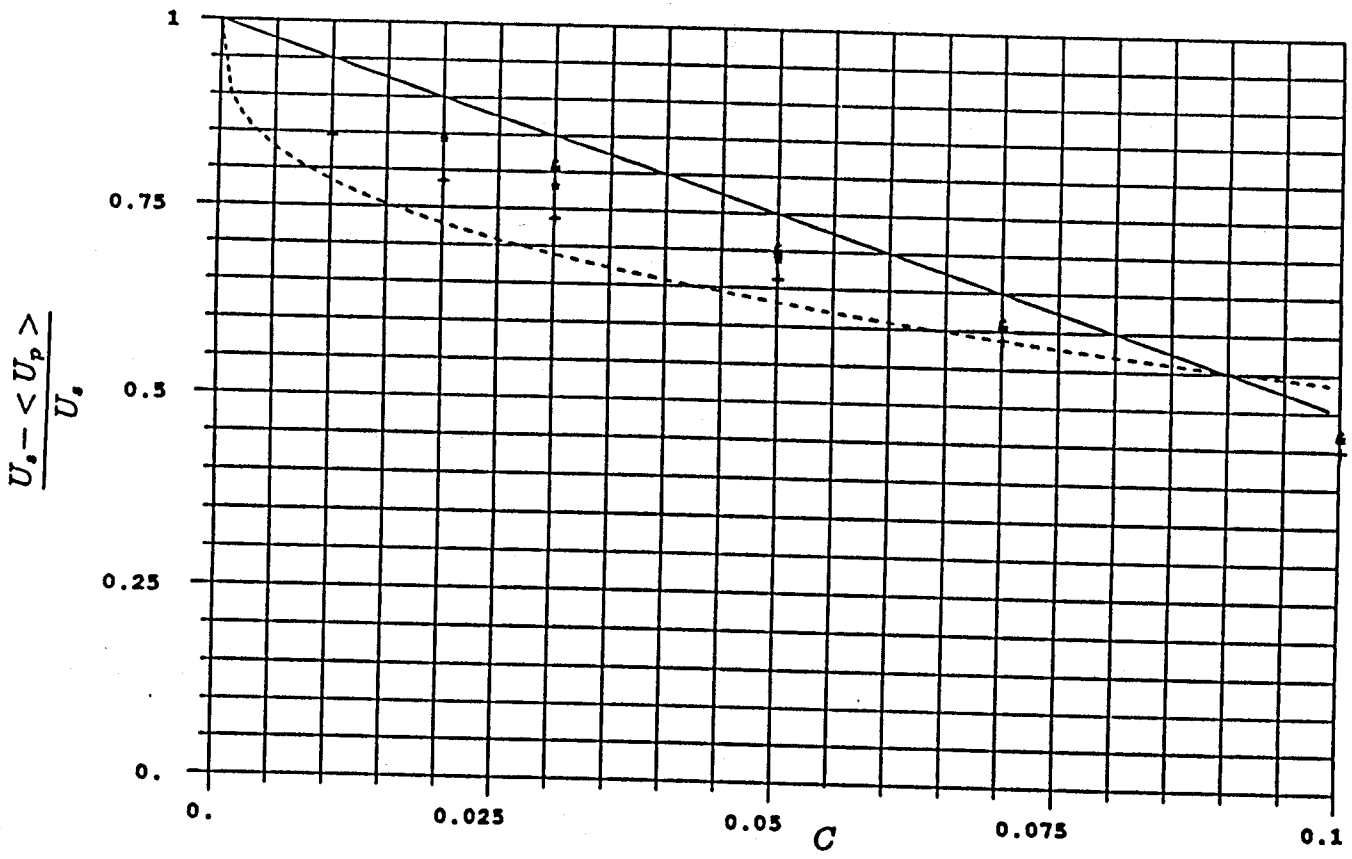

Figure 5.11 Concentration dependence of the sedimentation velocity. The diffusion coefficient varies with $c^{\frac{1}{3}}$, and is equal to $6U_s a$ at a concentration of 1%. The slope is taken from the interface versus time curve between the t=4.0 and t=20.0. The solid line is the correlation $(1.0 - 5.0c)$. The dotted line is the correlation $(1.0 - c^{\frac{1}{3}})$. The + symbols are for an opaque concentration of 0.1%. The * symbols are for an opaque concentration of 0.5%. The & symbols are for an opaque concentration of 1.0%.

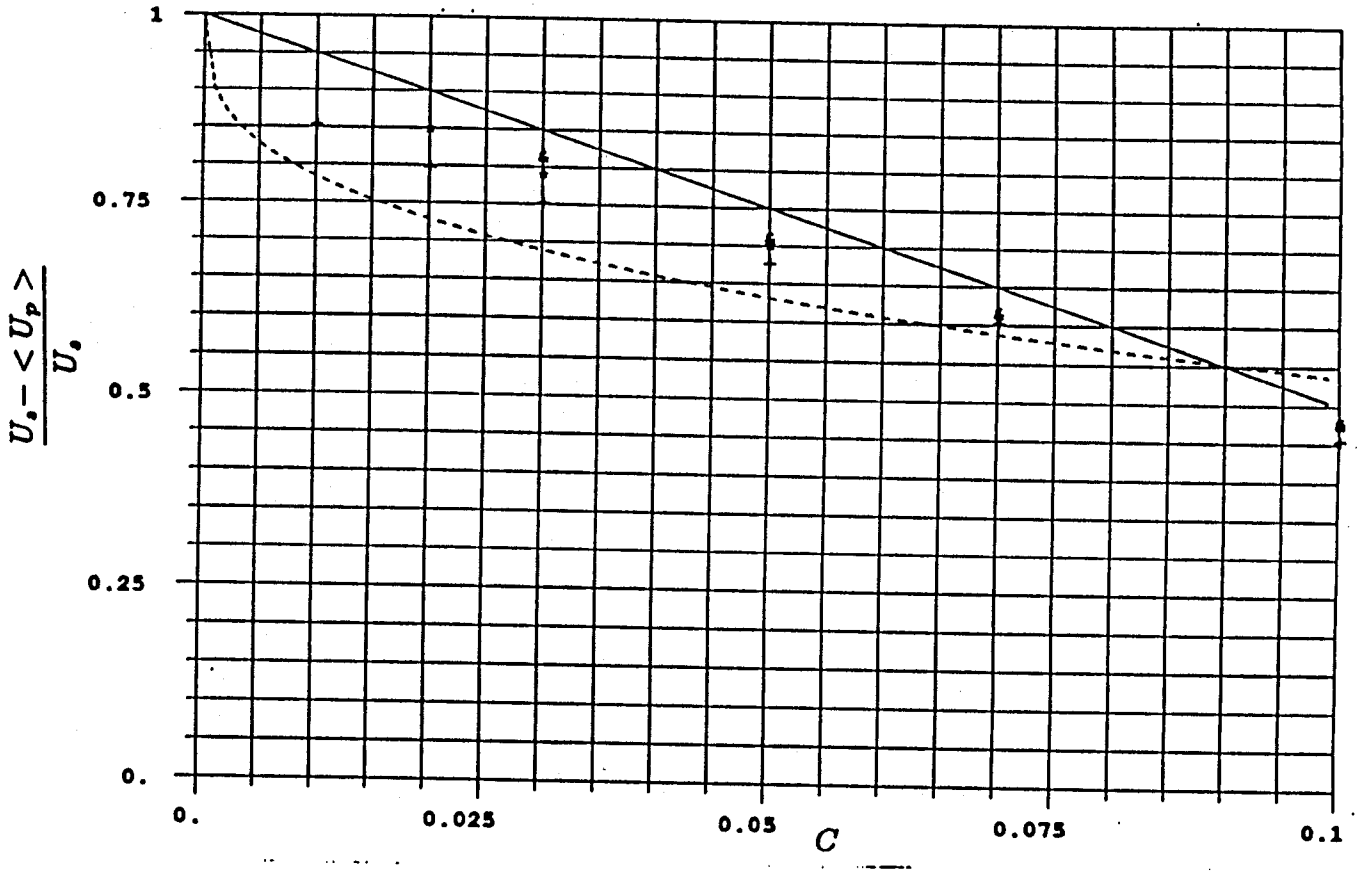

Figure 5.12 This is the concentration dependence of the sedimentation velocity. The diffusion coefficient varies with $c^{\frac{1}{3}}$, and is equal to $6U_s a$ at a concentration of 1%. The slope is taken from the interface versus time curve between the t=7.0 and t=20.0. The solid line is the correlation $(1.0 - 5.0c)$. The dotted line is the correlation $(1.0 - c^{\frac{1}{3}})$. The + symbols are for an opaque concentration of 0.1%. The * symbols are for an opaque concentration of 0.5%. The & symbols are for an opaque concentration of 1.0%.

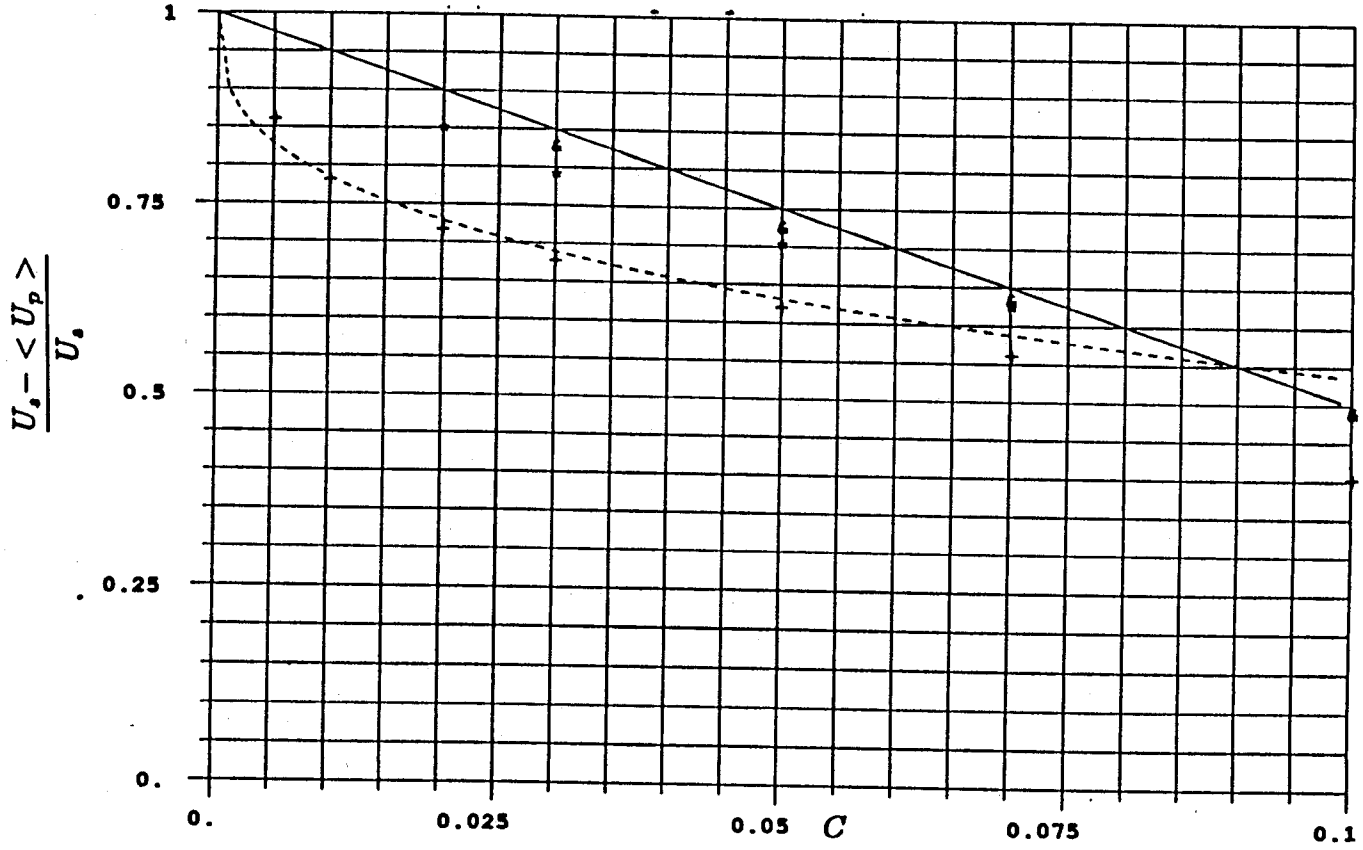

Figure 5.13 This is the concentration dependence of the sedimentation velocity. The diffusion coefficient varies with $c^{-\frac{1}{3}}$, and is equal to $6U_s a$ at a concentration of 1%. The slope is taken from the interface versus time curve between the t=2.0 and t=20.0. The solid line is the correlation $(1.0 - 5.0c)$. The dotted line is the correlation $(1.0 - c^{\frac{1}{3}})$. The + symbols are for an opaque concentration of 0.1%. The * symbols are for an opaque concentration of 0.5%. The & symbols are for an opaque concentration of 1.0%.

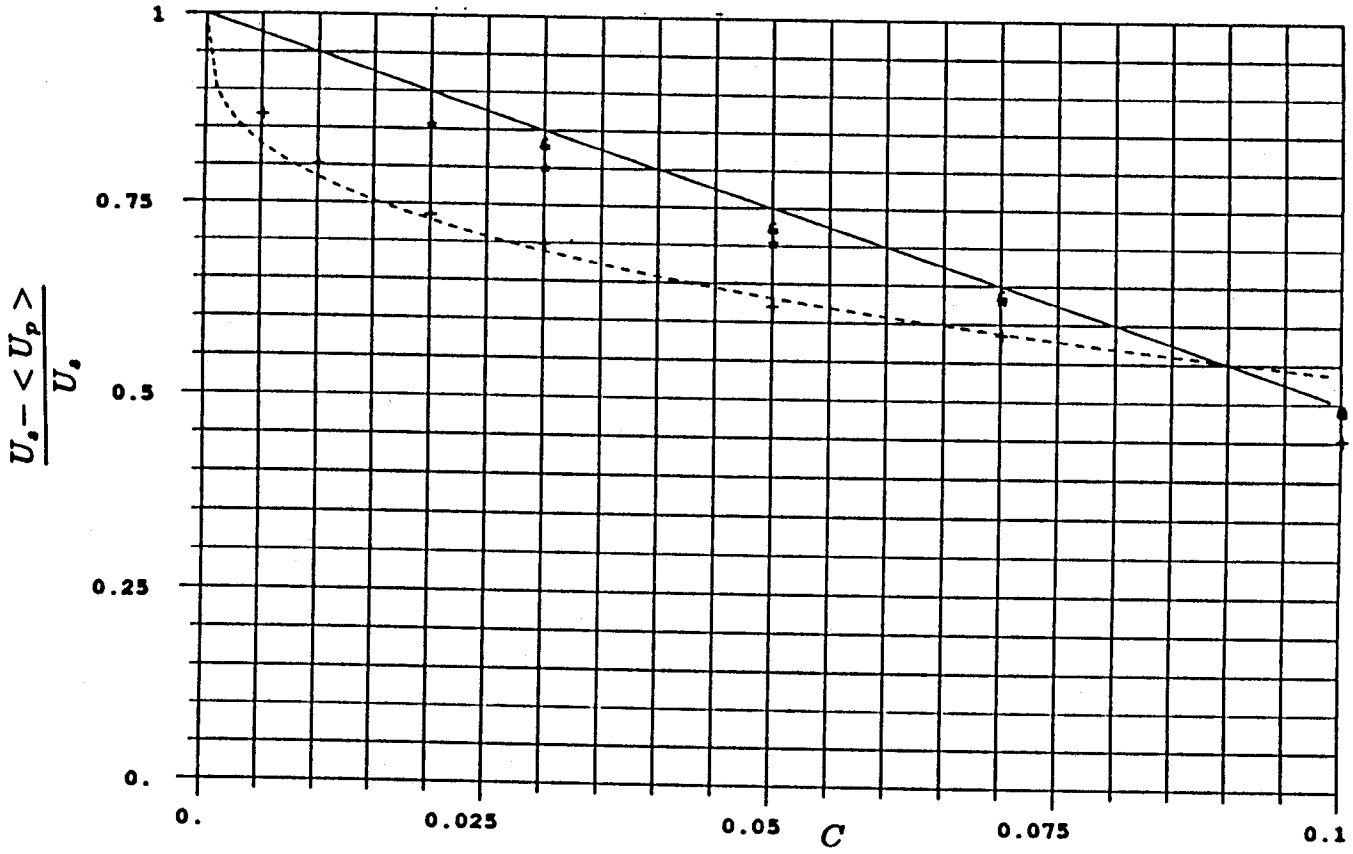

Figure 5.14 This is the concentration dependence of the sedimentation velocity. The diffusion coefficient varies with $c^{-\frac{1}{3}}$, and is equal to $6U_s a$ at a concentration of 1%. The slope is taken from the interface versus time curve between the t=4.0 and t=20.0. The solid line is the correlation $(1.0 - 5.0c)$. The dotted line is the correlation $(1.0 - c^{\frac{1}{3}})$. The + symbols are for an opaque concentration of 0.1%. The * symbols are for an opaque concentration of 0.5%. The & symbols are for an opaque concentration of 1.0%.

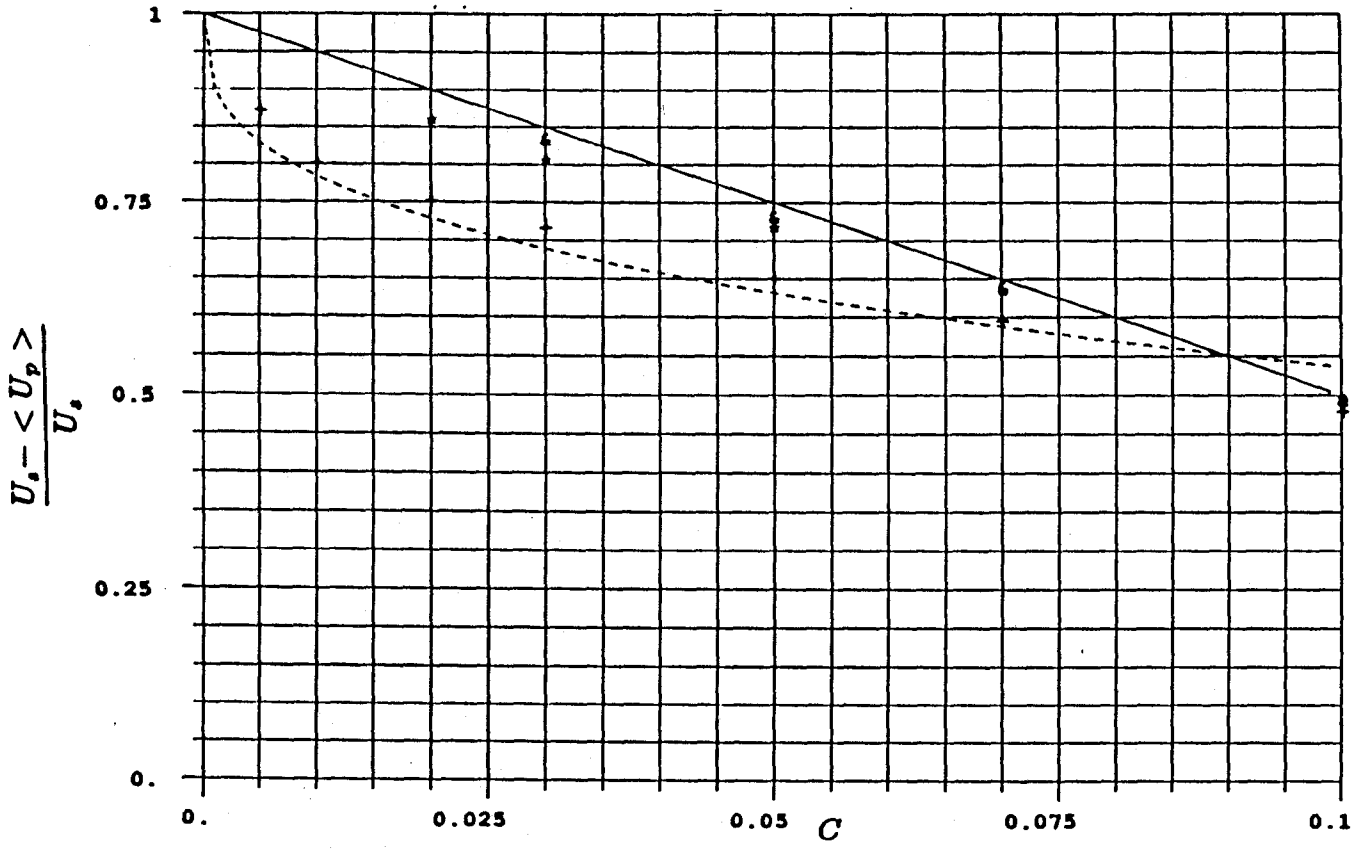

Figure 5.15 This is the concentration dependence of the sedimentation velocity. The diffusion coefficient varies with $c^{-\frac{1}{3}}$, and is equal to $6U_s a$ at a concentration of 1%. The slope is taken from the interface versus time curve between the t=7.0 and t=20.0. The solid line is the correlation $(1.0 - 5.0c)$. The dotted line is the correlation $(1.0 - c^{\frac{1}{3}})$. The + symbols are for an opaque concentration of 0.1%. The * symbols are for an opaque concentration of 0.5%. The & symbols are for an opaque concentration of 1.0%.

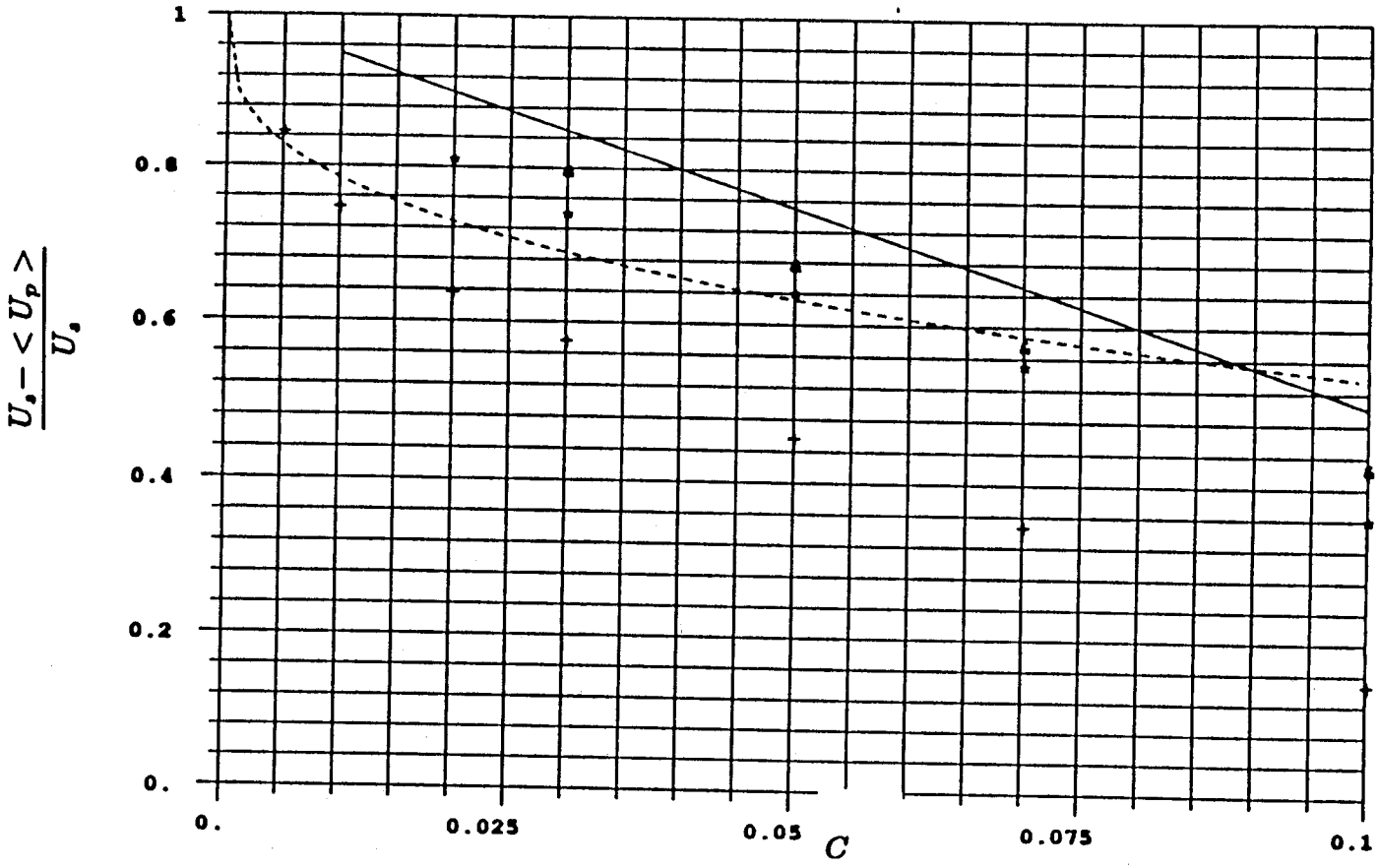

Figure 5.16 Concentration dependence of the sedimentation velocity. The diffusion coefficient is independent of concentration, and is equal to $12U_s a$. The slope is taken from the interface versus time curve between the t=2.0 and t=20.0. The solid line is the correlation $(1.0 - 5.0c)$. The dotted line is the correlation $(1.0 - c^{\frac{1}{3}})$. The + symbols are for an opaque concentration of 0.1%. The * symbols are for an opaque concentration of 0.5%. The & symbols are for an opaque concentration of 1.0%.

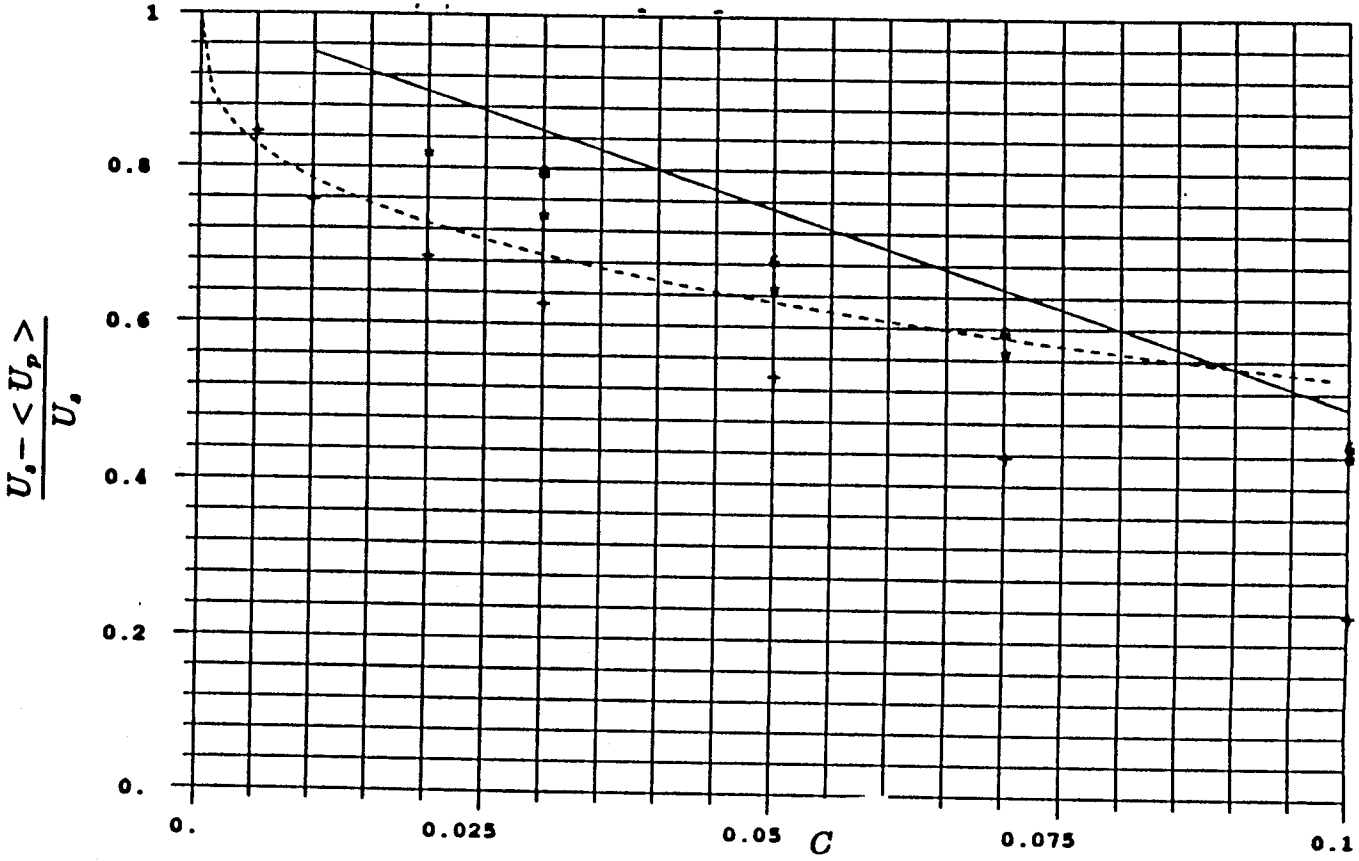

Figure 5.17 Concentration dependence of the sedimentation velocity. The diffusion coefficient is independent of concentration, and is equal to $12U_s a$. The slope is taken from the interface versus time curve between the t=4.0 and t=20.0. The solid line is the correlation $(1.0 - 5.0c)$. The dotted line is the correlation $(1.0 - c^{\frac{1}{3}})$. The + symbols are for an opaque concentration of 0.1%. The * symbols are for an opaque concentration of 0.5%. The & symbols are for an opaque concentration of 1.0%.

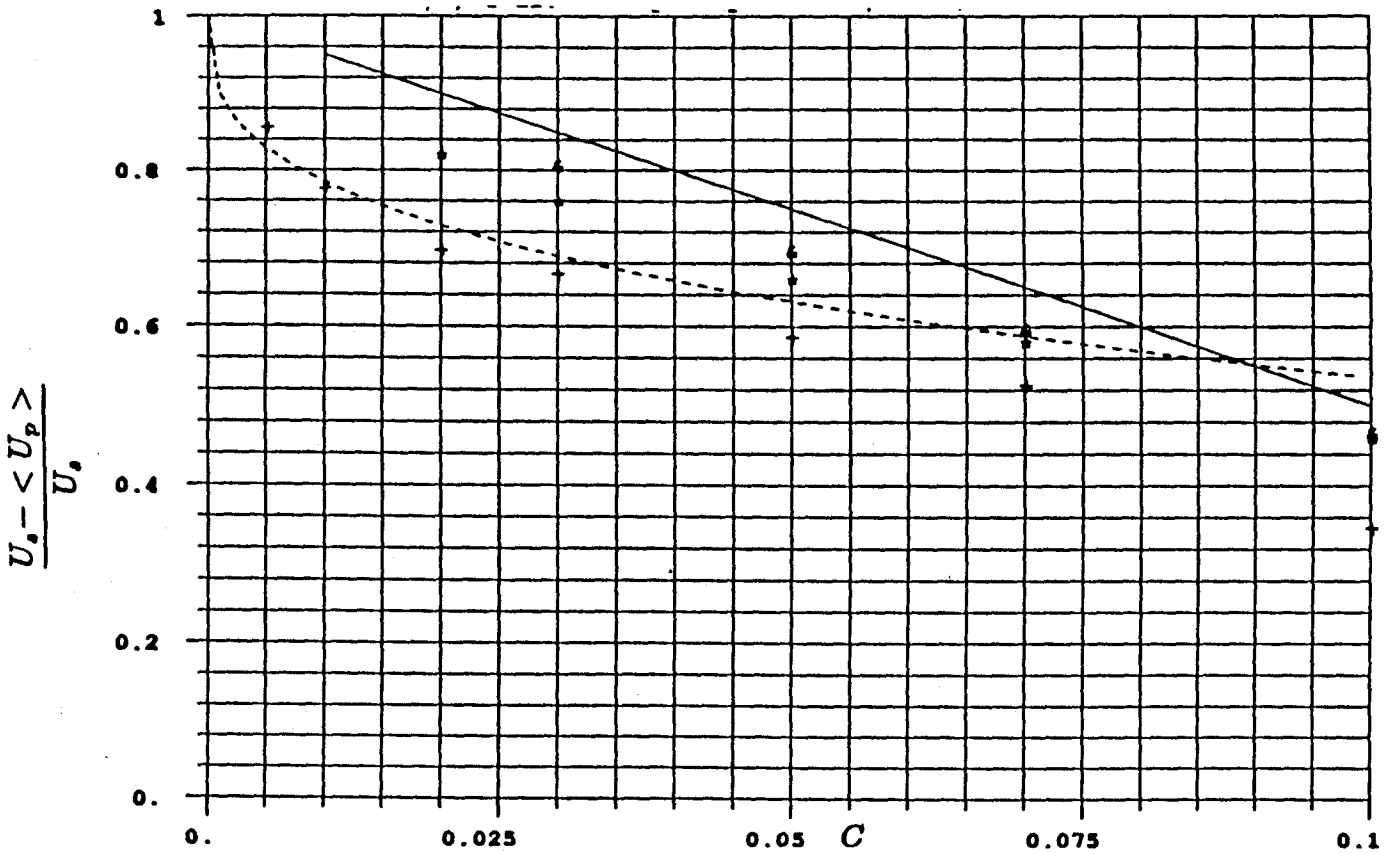

Figure 5.18 Concentration dependence of the sedimentation velocity. The diffusion coefficient is independent of concentration, and is equal to $12U_s a$. The slope is taken from the interface versus time curve between the t=7.0 and t=20.0. The solid line is the correlation $(1.0 - 5.0c)$. The dotted line is the correlation $(1.0 - c^{\frac{1}{3}})$. The + symbols are for an opaque concentration of 0.1%. The * symbols are for an opaque concentration of 0.5%. The & symbols are for an opaque concentration of 1.0%.

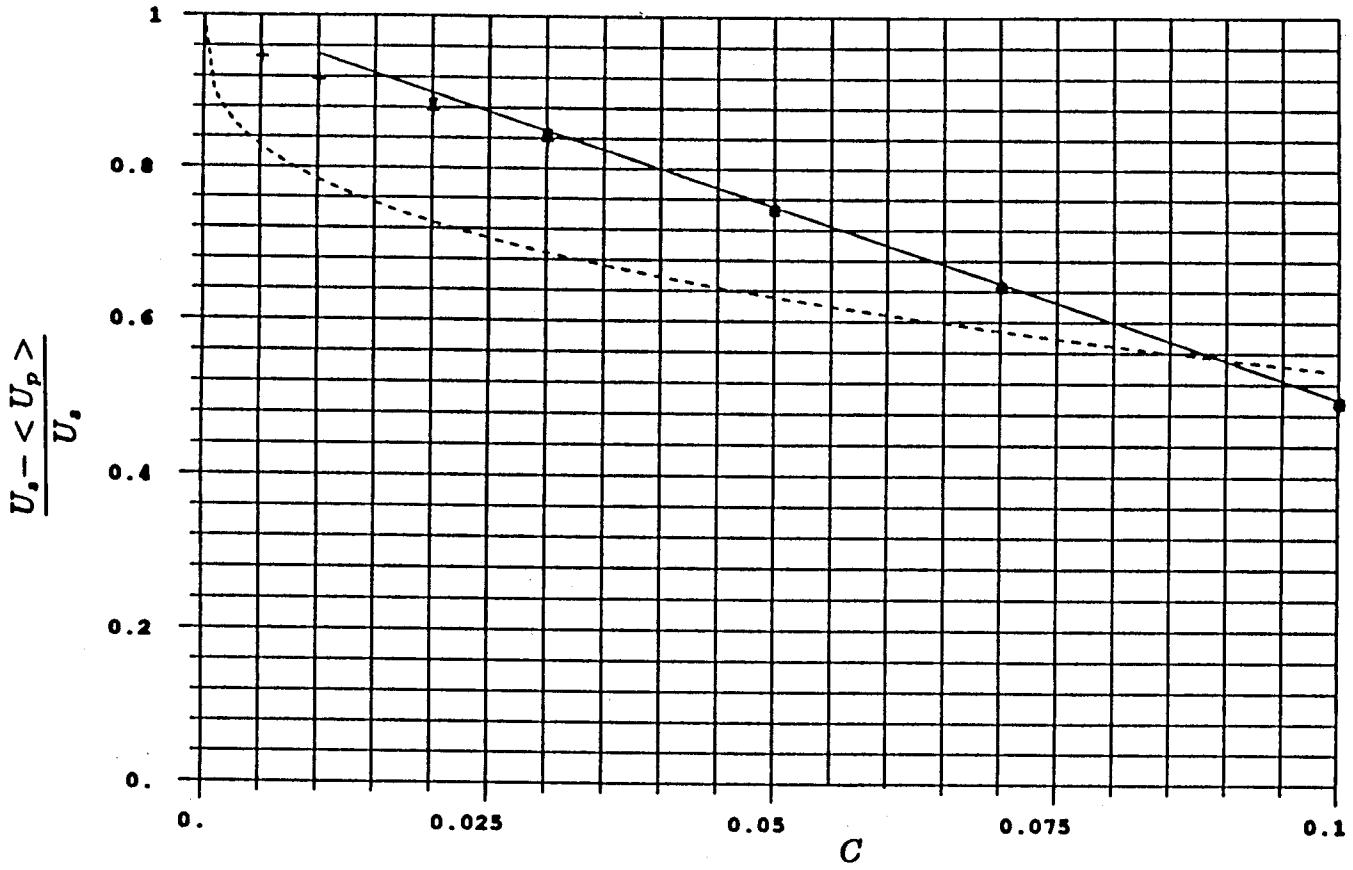

Figure 5.19 Concentration dependence of the sedimentation velocity for a sheared suspension. The diffusion coefficient is independent of concentration, and is equal to $0.6U_s a$. The slope is taken from the interface versus time curve between the t=2.0 and t=20.0. The solid line is the correlation $(1.0 - 5.0c)$. The dotted line is the correlation $(1.0 - c^{\frac{1}{3}})$. The + symbols are for an opaque concentration of 0.1%. The * symbols are for an opaque concentration of 0.5%. The & symbols are for an opaque concentration of 1.0%.

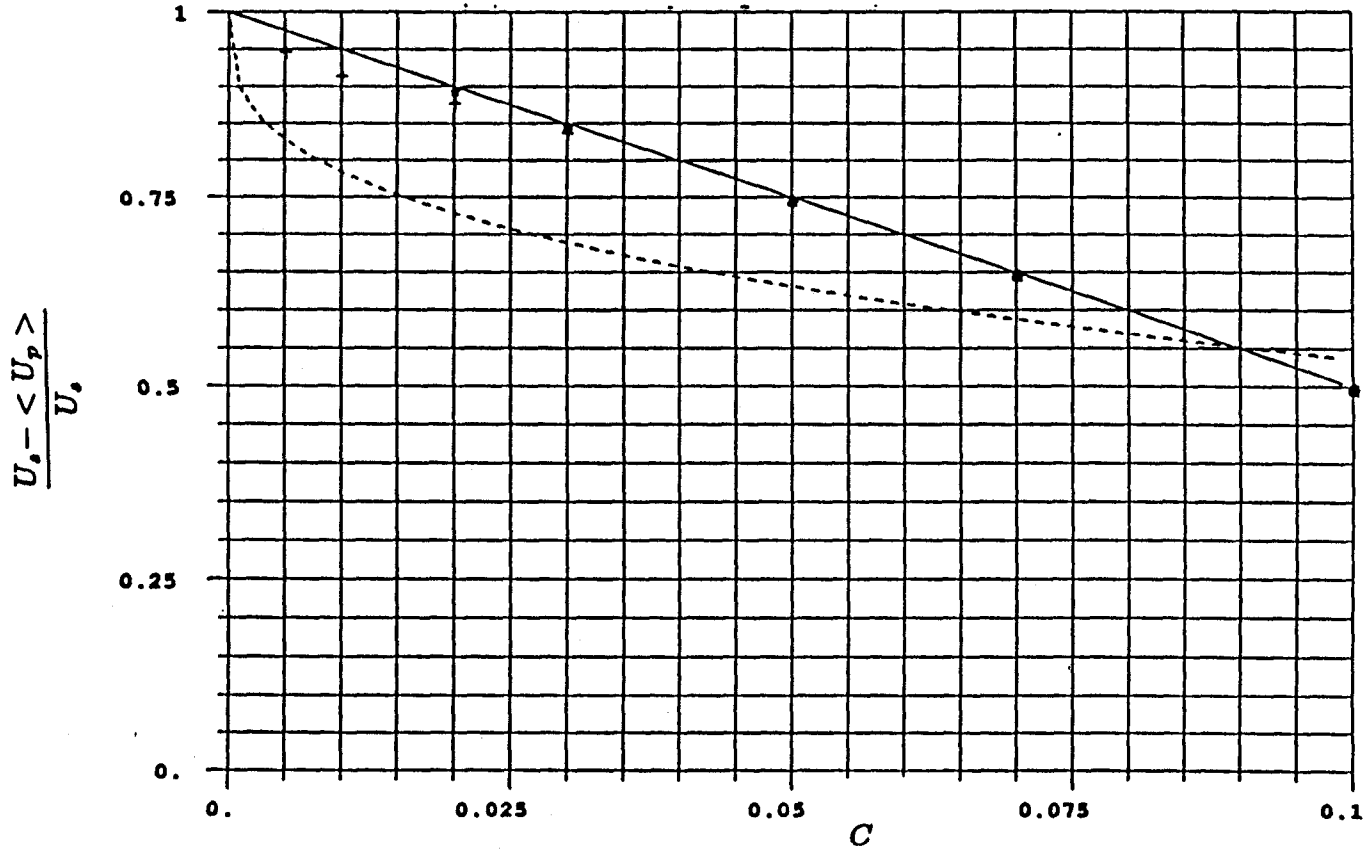

Figure 5.20 Concentration dependence of the sedimentation velocity for a Brownian suspension. The diffusion coefficient is independent of concentration, and is equal to $160U_s a$, the Stokes's velocity is $5.6x10^{-3}$, and the particle radius is $0.13\mu m$. The slope is taken from the interface versus time curve between the t=2.0 and t=20.0. The solid line is the correlation $(1.0-5.0c)$. The dotted line is the correlation $(1.0-c^{\frac{1}{3}})$. The + symbols are for an opaque concentration of 0.1%. The * symbols are for an opaque concentration of 0.5%. The & symbols are for an opaque concentration of 1.0%.

References

Ames, W. 1977 *Numerical Methods for Partial Differential Equations.* Academic Press.

Anderson, T.B. and Jackson, R. 1967 A Fluid Mechanical Description of Fluidized Beds. *I&EC Fundamentals* **6**, 527.

Arp, P.A., Mason, S.G. 1977 The Kinetics of Flowing Dispersions. *J. Colloid Interface Sci.* **61**, 21.

Barnea, E. and Mizrahi, J. 1973 A Generalized Approach to the Fluid Dynamics of Particulates. *The Chemical Engineering J.* **5**,171.

Batchelor, G.K. 1972 Sedimentation in a Dilute Dispersion of Spheres. *J. Fluid Mech.* **52**, 245.

Batchelor, G.K. 1982 Sedimentation in a Dilute Polydisperse of Interacting Spheres. Part 1. General Theory. *J. Fluid Mech.* **119**, 379.

Batchelor, G.K. and Green J.T. 1972 The Hydrodynamic Interaction of Two Small Freely-Moving Spheres in a Linear Flow Field. *J. Fluid Mech.* **56**, 375.

Batchelor, G.K. and Green J.T. 1972 The Determination of the Bulk Stress in a Suspension of Spherical Particles to Order C^2. *J. Fluid Mech.* **56**, 401.

Batchelor, G.K. and Janse Van Rensburg, R.W. 1986 *J. Fluid Mech.* **166**, 379.

Batchelor, G.K. and Wen C.W. 1982 Sedimentation in a Dilute Polydisperse of Interacting Spheres. Part 1. Numerical Results. *J. Fluid Mech.* **124**, 495.

Beenakker, C.W.J. 1986 Ewald Sum of the Rotne-Prager Tensor. *J. Chem. Phys.* **85**, 1581.

Beenakker, C.W.J. and Mazur, P. 1985 Is Sedimentation Container-Shape Dependent? *Physics of Fluids* **28**, 3203.

Beenakker, C.W.J. and Mazur, P. 1985 On the Smoluchowski Paradox in a Sedimenting Suspension. *Physics of Fluids* **28**, 764.

Brady, J. and Bossis, G. 1985 The Rheology of Concentrated Suspension of Spheres in Simple Shear Flow by Numerical Simulation. *J. Fluid Mech.* **93**, 705.

Buscall, R., Goodwin, J.W., Ottewill, R.H. and Tadros, T.F. 1982 The Settling of Particles Through Newtonian and Non-Newtonian Media. *J. Colloid Interface Sci.* **85**, 78.

Burgers, J.M. 1941 On the Influence of the Concentration of a Suspension upon the Sedimentation Velocity. *Proc. Koningl. Akad. Wetenschap. (Amsterdam)* **44**, 1177.

Caflisch, R.E. and Luke, J.H.C. 1985 Variance in the Sedimentation Speed of a Suspension. *Physics of Fluids* **28**, 756.

Dabros, T. 1985 A Singularity Method for Calculating Hydrodynamic Forces and Particle Velocities in Low-Reynolds-Number Flows. *J. Fluid Mech.* **156**, 1.

Chen, P.Y. and Schachman, H.K. 1955 Studies on the Validity of the Einstein Viscosity Law and Stokes's Law of Sedimentation. *J. Polymer Sci.* **16**, 19.

Davis, R.H. and Acrivos, A. 1985 Sedimentation of Noncolloidal Particles at Low Reynolds Numbers. *Ann. Rev. Fluid Mech.* **17**, 91.

Drew, D.A. 1983 Mathematical Modeling of Two Phase Flow. *Ann. Rev. Fluid Mech.* **15**, 261.

Durlofsky, L., Brady, J.F. and Bossis, G. 1987 Dynamic Simulation of Hydrodynamically Interacting Particles. *J. Fluid Mech.* **180**, 21.

Feuillebois, F. 1984 Sedimentation in a Dispersion with Vertical Inhomogeneities. *J. Fluid Mech.* **130**, 145.

Ganatos, P., Pfeffer, R. and Weinbaum, S. 1978 A Numerical-Solution Technique for Three-Dimensional Stokes Flows, with Application to the Motion of Strongly Interacting Spheres in a Plane. *J. Fluid Mech.* **84**, 79.

Happel, J. and Brenner, H. 1965 *Low Reynolds Number Hydrodynamics.* Prentice-Hall.

Jeffrey, D.J. 1974 Group Expansions for the Bulk Properties of a Statistically Homogeneous, Random Suspension. *Proc. R. Soc. Lond. A.* **338**, 503.

Jeffrey, D.J. and Onishi, Y. 1984 Calculation of the Resistance and Mobility Functions for Two Unequal Rigid Spheres in Low-Reynolds-Number Flow. *J. Fluid Mech.* **139**, 261.

Kim, S. and Mifflin, R.T. 1985 The Resistance and Mobility Functions of Two Equal Spheres in Low-Reynolds-Number Flow *Physics of Fluids.* **28**, 2033.

Kops-Werknoven, M.M. and Fijnaut, H.M. 1981 Dynamic Light Scattering and Sedimentation Experiments on Silica Dispersions at Finite Concentrations. *J. Chem Phys.* **74**, 1618.

Lester, J.C. 1988 Hydrodynamic Dispersion in Concentrated Sedimenting Suspensions. Ph.D. Thesis, Calif. Inst. Tech.

Lynch, E.D. 1985 Sedimentation in Quiescent and Sheared Suspensions. Ph.D. Thesis, Calif. Inst. Tech.

Makhlouf, E.M. 1988 Determination of Microscale Ordering in Quiescent Sedimenting Suspensions by Holograhy. M.S. Thesis, Calif. Inst. Tech.

Mazaika, P.K. 1974 On the Settling Speed of Dilute Arrays of Spheres. Ph.D. Thesis, Calif. Inst. Tech.

Mazur, P. and Van Saarloos, W. 1982 Many-Sphere Hydrodynamic Interactions and Mobilities in a Suspension. *Physica* **115A**, 21.

O'Brien, R.W. 1979 A Method for the Calculation of the Effective Transport Properties of Suspensions of Interacting Particles. *J. Fluid Mech.* **91**, 17.

Oliver, D.R. 1961 The Sedimentation of Suspenison of Closely-Sized Spherical Particles. *Chemical Engineering Science* **15**, 230.

Saffman, P.G. 1973 On the Settling Speed of Free and Fixed Suspensions. *Studies in Applied Mathematics* **LII**, (2) 115.

Smith, T.N. 1968 The Spatial Distribution of Spheres Falling in a Viscous Liquid. *J. Fluid Mech.* **32**, 203.

Van Dyke, M. 1975 *Perturbation Methods in Fluid Mechanics.* The Parabolic Press.

Whitham, G. B. 1974 *Linear and Nonlinear Waves.* Wiley-Interscience.

Youngren, G.K. and Acrivos A. 1975 Stokes Flow Past a Particle of Arbitray Shape: A Numerical Method of Solution. *J. Fluid Mech.* **69**, 377.